A STUDY TO ASSESS AND IMPROVE DOSE COMPUTATIONS IN PHOTON BEAM THERAPY

Maria Mania Aspradakis, B.Sc.

PhD
The University of Edinburgh
1996

Ithaka

C. P. Cavafys (1863-1933)[1]

As you set out for Ithaka
hope your road is a long one,
full of adventure, full of discovery.
Laistrygonians, Cyclops,
angry Poseidon-don't be afraid of them:
you'll never find things like that on your way
as long as you keep your thoughts raised high,
as long as a rare excitement
stirs your spirit and your body.
Laistrygonians, Cyclops,
wild Poseidon-you won't encounter them
unless you bring them along inside your soul,
unless your soul sets them up in front of you.

Hope your road is a long one.
May there be many summer mornings when,
with what pleasure, what joy,
you enter harbours you're seeing for the first time;
may you stop at Phoenician trading stations
to buy fine things,
mother of pearl and coral, amber and ebony,
sensual perfumes of every kind-
as many sensual perfumes as you can;
and may you visit many Egyptian cities
to learn and go on learning from their scholars.

Keep Ithaka always in your mind.
Arriving there is what you're destined for.
But don't hurry the journey at all.
Better if it lasts for years,
so you're old by the time you reach the island,
wealthy with all you've gained on the way,
not expecting Ithaka to make you rich.

Ithaka gave you the marvellous journey.
Without her you wouldn't have set out.
She has nothing left to give you now.
And if you find her poor, Ithaka won't have fooled you.
Wise as you will have become, so full of experience,

you'll have understood by then what these Ithakas mean.

---

[1] **C. P. Cavafy "Collected Poems"**, Translated by E.Keely and P. Sherrard. Published in 1990 by Chatto & Windus, London

Ἓν οἶδα ὅτι οὐδέν οἶδα.

Σωκράτης (470-399 π.Χ.)

Abstract

This thesis is concerned with the calculation of dose at a point for megavoltage photon therapy. The review of dose calculation algorithms provides a comprehensive and critical analysis of the models developed to date. Emphasis is given to the dimensionality of density information utilised by these algorithms in relation to their capability of producing accurate dose information in three dimensions.

Two applications of the Monte Carlo method to radiotherapy have been studied. Namely, the generation of energy deposition kernels (EDK) and the use of the method as a benchmarking tool. EDKs represent the fractional energy deposited around a single photon interaction site. Dose distributions in homogeneous and heterogeneous media were calculated in absolute units of absorbed dose per incident photon fluence ($Gy \cdot cm^2$). Both applications were carried out using the EGS4 code system.

A superposition model was developed from *the dose deposition point of view.* Dose at a point was obtained from knowledge of the total energy released per unit mass in the medium (TERMA) and the EDK. Effective energy spectrum information was used to calculate dose for clinical beams. The performance of this model was verified in homogeneous and heterogeneous media against both Monte Carlo generated and measured data.

The necessity for computation speed is addressed. As a trade off between accuracy and speed, a method was developed which reduces the calculation time required to obtain a true three dimensional dose matrix.

Contents

List of Figures

List of Tables

Chapter 1

Introduction

1.1 The aim of radiotherapy

Radiotherapy is prescribed to cancer patients on either curative or palliative grounds. Curative (also known as radical) radiotherapy aims to decrease the number of tumour cells to a level that achieves permanent local tumour control [ICRU, 1993]. The task of tumour cell killing translates mainly to two separate problems: the biological variations present in tumour cells, such as differences in radiosensitivity and the fact that cells cannot be treated in isolation [Johns and Cunningham, 1983], [Williams and Thwaites, 1993]. Consequently, the task of the clinician is to ensure that the radiation delivered to the patient is sufficient to eliminate the cancerous cells without introducing serious complications to surrounding healthy tissues.

In vitro cellular radiobiological studies have provided radiobiologists with data for constructing mathematical models of the relationship between the dose delivered to cancerous and healthy tissues and their response [Herring and Compton, 1971], [Brahme, 1984], [Mijnheer et al., 1987]. Tumour Control and Normal Tissue Complication probabilities (TCP and NTCP respectively) follow in general sigmoidal curves and have given rise to the concept of therapeutic ratio [Johns and Cunningham, 1983]. Therapeutic ratio, according to the definition provided by Johns and Cunningham, is the ratio of the dose leading to serious complications in 50% of the patients to the dose giving tumour control in the same percentage of patients. In other words, improving radiotherapy treatment would result in an increase of the therapeutic ratio.

Accuracy requirements for radiotherapy are based on studies of the steepness of the TCP and NTCP curves [K-A. Johansson, 1982], [Mijnheer et al., 1987], [Brahme, 1988]. Reviews by Thwaites [Thwaites, 1994], [Thwaites, 1988] sum-

marise the available, general, recommendations on accuracy requirements in radiotherapy (given as one standard deviation): 3% on the absorbed dose delivered at the specification point (in most cases the centre of the target), 5% on the dose at all other points within the target and 4mm on geometric accuracy in positioning field edges and shielding blocks. According to Ahnesjö [Ahnesjö, 1991] a reasonable design criterion for dose calculation algorithms in treatment planning is to accept errors that do not significantly degrade the overall treatment accuracy.

1.2 External photon beam therapy

1.2.1 Radiotherapy treatment machines

Radiotherapy is administered as external beam therapy, or as brachytherapy, or unsealed source therapy. External photon beam therapy started using x-ray tubes of a few hundred keV. In the late 30's, megavoltage beam therapy was carried out using van der Graff generators with beam energies of 1-2MV. Cobalt-60 sources and low megavoltage (4-6MV) linear accelerators appeared in the early 50's. Medium megavoltage (6-14MV) linacs came into use in the mid 60' and higher energy beams (6-21MV) in the 70's. Even higher energies than these (up to 50MV) have been available in some accelerators since the 80's [Karzmark and Pering, 1973], [Karzmark, 1984]. New generation of linear accelerators are capable of delivering dual photon energy beams, scanned photon beams and scanned electron beams. They include automatic wedge selectors, electron filter, independent collimator jaws or multileaf collimation and portal imaging devices. Such systems are currently the tools exploited for conformal radiotherapy treatment techniques [Brahme, 1987], [Webb, 1993].

1.2.2 The use of Computer Tomography (CT)

The development of radiation oncology is not only associated with new radiation sources and technical developments, but also with the advent of new imaging modalities such as CT (computer tomography), MRI (magnetic resonance imaging) and SPECT and PET (single photon and positron emission tomography) scanners [Webb, 1993].

Computer Tomography has three applications in radiation therapy. It is used for the acquisition of patient and tumour contours, for the evaluation of the results from radiation therapy and for obtaining patient density information for use with

dose calculation models. In the case of a monoenergetic X-ray source of energy E_o, CT numbers (N_{CT}) of a given material can be related to linear attenuation coefficients using the following expression:

$$\mu(E_o) = (1 + \frac{N_{CT}}{1000})\mu_{water}(E_o) \tag{1.1}$$

where μ and μ_{water} are the linear attenuation coefficient of the material and of water respectively. CT numbers are dimensionless quantities, expressed in Hounsfield units (HU). Due to systematic errors from beam hardening and scattering in the polyenergetic X-ray sources used in CT machines, the conversion of CT numbers to X-ray linear attenuation coefficients at diagnostic energies is carried out with an accuracy of 5% in relation to the attenuation coefficient of water [Huizenga and Storchi, 1985].

In order for these linear attenuation coefficients to be of use in radiation therapy, they must be appropriately converted to represent X ray attenuation properties in megavoltage photon energies. This is not an easy task mainly because at diagnostic energies the photoelectric effect is also a significant mode of photon interaction in the medium as well as Compton scattering. At these energies the linear attenuation coefficient $\mu(E)$ of a material is approximately expressed as a function of energy as well as of effective atomic number:

$$\mu(E) = \rho_e \cdot (\sigma_{KN}(E) + k_p(Z^*)^{3.5}E^{-3}) \tag{1.2}$$

where ρ_e is the electron density, σ_{KN} is the energy dependent Klein-Nishina cross sections, k_p is a constant factor (at these energies) and Z^* is the effective atomic number of the material. It has been shown that for tissue equivalent materials with CT numbers up to 50HU, the following relationship holds for relative electron densities ρ_e^w, with an accuracy of 3% [Parker et al., 1979]:

$$\rho_e^w = 1 + \frac{N_{CT}}{1000} \tag{1.3}$$

This expression is also valid for megavoltage energies since relative electron densities for water equivalent materials, are equal to linear attenuation coefficients relative to water. For diagnostic energies and non-water equivalent materials, such as bone for which CT numbers are greater than 100HU, linear expressions between N_{CT} and ρ_e^w have been derived which depend on the CT scanner used. Appropriate expressions have also been derived for megavoltage photon beams using the mean energy of the beam [Huizenga and Storchi, 1985]. For materials

with N_{CT} between 50HU and 100HU, analogous approximations have been found to be adequate.

Huizenga and Storchi conclude that the error from converting CT numbers to electron densities for use with megavoltage beams is well within 10%. Most important though was their finding that the uncertainty in the dose distribution obtained using CT information is less than 1% at the dose maximum for photon beams. Their results strongly support early reports in favour of the use of CT scanners for megavoltage photon beam therapy planning [Geise and McCullough, 1977], [Sontag et al., 1977], [Van Dyk, 1983].

1.2.3 Procedures in treatment planning

After a clinical decision in prescribing external beam radiotherapy is made, the following steps are carried out:

- *Simulation and tumour Localisation:* The positioning of the patient at the simulator is necessary for the acquisition of the necessary anatomical data, such as external contours and external reference marks, for treatment planning. With the aid of simulators or CT scanners the following two volumes are determined. These are the Gross Tumour Volume (GTV) and the Clinical Target Volume (CTV). *The GTV is the gross palpable or visible/demonstrable extent and location of malignant growth.* The CTV is defined as *the tissue volume that contains a demonstrable GTV and/or subclinical microscopic malignant disease, which has to be eliminated* [ICRU, 1993].

- *Treatment Planning:* At the commencement of treatment planning two more volumes are defined. The Planning Target Volume (PTV) (or what was previously known as the Target Volume [ICRU, 1978]) and the Organs at Risk (OAR). The PTV is used for planning and verification of dose and is defined *to select appropriate beam sizes and beam arrangements, taking into consideration the net effect of all possible geometrical variations, in order to ensure that the prescribed dose is actually absorbed in the CTV.* The OAR are those normal tissues whose radiation sensitivity may significantly influence the way the patient is planned. Treatment planning involves the selection of beam arrangements, the computation of the corresponding dose distribution, a decision on the optimal treatment plan and finally the calculation of Monitor Units (MU).

- *Verification-Simulation:* At this stage, after CT planning, the optimal treatment plan is verified on the simulator.

- *Fabrication of treatment aids:* The fabrication of blocks, compensators or any immobilisation devices is completed after verification of the treatment plan.

- *Patient set-up and treatment:* The patient is arranged for treatment on the therapy machine together with any dose verification systems such as TLDs, diodes, film or portal imaging devices (PID).

- *Follow-up during treatment:* The response of the tumour and the patient in general as a result of the treatment is monitored.

- *After completion of treatment:* tumour control and normal tissue response are evaluated.

Prior and in addition to treatment planning procedures, there are many other necessary tasks that are carried out in order to ensure that patients receive the best possible treatment. These are all treatment machine tests, absolute dosimetric measurements, dosemeter calibrations, treatment beam calibrations in reference conditions and relative dosimetric measurements in all other treatment conditions.

The overall clinical accuracy achievable in radiotherapy depends on the cumulative uncertainties from the above procedures. Studies on estimating these involve a priori considerations of possible errors present at every process [ICRU, 1976], [K-A. Johansson, 1982], [Brahme, 1988] [Thwaites, 1988] and/or implementation of appropriate dosimetry intercomparisons and quality audit programmes [K-A. Johansson, 1982], [Urie et al., 1991], [Thwaites et al., 1992]. A value of total uncertainty of at least 6 to 7% is quoted by Thwaites [Thwaites, 1994]. Specifically for dose calculation algorithms, Anhesjö concludes that at present, an achievable accuracy between 2% to 3% does not lower the overall accuracy; nevertheless, a performance with errors of less than 1% is the ultimate goal to be sought in any future developments in these algorithms [Ahnesjö, 1991].

1.3 Photon dose computation

In radiotherapy planning, dose calculations attempt to provide the best estimate of the dose deposited in the patient. For photon beams, the energy released in the medium by a primary photon is carried away from the first interaction site and deposited by secondary particles elsewhere in the medium. Accurate modelling of photon transport should include contributions from primary and scattered photon fluences as well as the transport of secondary charged particles. The distribution of radiation within a system of absorbers and sources can be completely described by specifying the particle fluence $\Phi(\vec{r}, \vec{\Omega}, E)$ at each spatial coordinate $\vec{r}$, direction $\vec{\Omega}$ and particle energy E. The particle fluence Φ can be determined by solving the time-independent Boltzmann transport equation [Roesch, 1968]. The solution of this equation, however, is highly complex but accurate estimates can be provided using Monte Carlo techniques (see chapter 4). Monte Carlo codes would be the favoured choice if it wasn't for their long computation times which make them impractical for clinical use even with the current availability of advanced hardware installed in many radiotherapy centres.

1.3.1 Beam modelling

Beam modelling in computerised radiotherapy planning refers to the efforts of setting up formalisms for the manipulation of dosimetric data for calculating the dose at a point in the patient [ICRU, 1987]. Such dosimetric data are for a reference medium, usually water, and the distribution of dose in a patient is calculated by taking into account several factors; the patient's shape, the heterogeneous nature of the irradiated volume, any requirements for fields with irregular cross section at the patient surface or beam modulators which modify the intensity of the incident beam. No exact mathematical solution exists for the calculation of dose at a single point therefore beam modelling has been a continuous search for better and faster methods of approximation [Cunningham, 1988]. Beam models differ in the origin and format of basic dosimetric data they manipulate, in their complexity and consequently in their performance in terms of time required to complete a calculation. Beam models have been categorised in the following four groups.

Matrix models

These methods use a stored matrix of numbers, representing the relative absorbed dose on a grid of coordinate points and calculate dose at other points via interpolation. Their beam data are measured in a homogeneous water phantom for normally incident square beams and are stored using cartesian or polar coordinates on a fan line or decrement line system. All matrix methods are fast in calculating dose in a homogeneous medium and in general require a large amount of data with suitable interpolation routines. They are limited by the beam configuration for which dose measurements have been carried out. The matrix method introduced by Milan and Bentley [Milan and Bentley, 1974] is the most representative method in this category. The stored measured data consist of central axis depth dose tables (CAX data) and beam profile tables (off axis ratios, OAR). CAX data represent percentage depth dose values at several depths, for square fields typically ranging from the smallest to the largest size in steps of 2cm for a given source-to-surface distance (SSD). CAX data for an intermediate field are generated by interpolation and rectangular fields are taken into account by using the data for the corresponding equivalent square field sizes. Profile data are measured for square fields in steps of 1cm and are stored for several off axis points. Off axis ratios lie on fan lines (the central fan line coinciding with the central axis of the beam). Appropriate corrections are applied to take into account beam modifying devices (wedge filters, compensators), body shape and heterogeneities, but these models are not readily applicable to irregular fields.

Analytical beam models

Analytical beam models, widely known as *beam generating function methods*, are purely empirical methods based on a mathematical representation of beam data [van de Geijn, 1972], [Redpath and Wright, 1981]. The calculation of the relative dose value at a point results from the evaluation of a function which is given as a product of two terms which are evaluated separately. The first represents the percentage depth dose along the central axis of the beam and the second the off central axis ratio, which describes the variation of dose along a line perpendicular to the beam axis. Many workers have developed beam generating functions, the earliest by Sterling *et al.* and van de Geijn [Sterling et al., 1964], [van de Geijn, 1965] (both 3D dose calculation models), and the most recent from van de Geign [van de Geijn, 1987]. Analytical beam methods are slower than matrix models but require relatively little input data and are not restricted to a

limited selection of field sizes. Allowances for beam modifying devices, surface curvatures and inhomogeneities are performed using simple correction factors. Early analytical methods can produce three dimensional dose distributions, but use either a simple inhomogeneity correction or no correction at all.

Models based on the separation of primary and scattered radiation

Dose calculation methods belonging to this category are described as *semi-empirical methods* because the equations used in the calculation resemble those in analytical methods but the data used are derived from measurements. According to ICRU 42 [ICRU, 1987] *primary radiation* is taken to be the radiation incident on the surface of the phantom and includes photons coming directly from the target or source as well as radiation scattered from the collimators and the source or target configuration elements. Its value depends on the design and construction of the x-ray target or the gamma-ray source and the collimator system. *Scattered radiation* includes radiation emerging from primary interactions within the phantom and depends on the beam size and shape and the nature (density and atomic properties) of the phantom material that is irradiated. *Primary dose* at a point in a phantom is related to the dose in air and calculated using the concept of zero-area Tissue Air Ratio. *Tissue Air Ratio* (TAR) is the ratio of the absorbed dose rate at a given point in a phantom to the absorbed dose rate at the same point in space, but at the centre of a small amount of phantom material of mass just large enough to provide electronic equilibrium at the point of measurement [ICRU, 1976]. *Zero-area Tissue Air Ratio* is the TAR for zero field size, it is derived by extrapolating TARs for small beam dimensions to zero area and describes the attenuation of primary radiation. The history of algorithms in this category refers back to 1944 with the definition of the scatter function employed for modelling the scattered photon dose component. *Scatter function* is the ratio, expressed as a percentage, of the absorbed dose arising from scattered photons at any depth on the axis of a circular field to the absorbed dose arising from primary photons at a point on the beam axis at the depth of maximum dose [BJR, 1983]. Analogous to the scatter function, but derived from TARs, *Scatter Air Ratios* (SARs) are the quantities which describe the scattered radiation reaching a point within a phantom and are obtained by subtracting the zero-area TAR from the TAR for a given field size [Schoknecht, 1966],[Cunningham, 1972]. Furthermore, *differential scatter air ratios* (dSARs) represent the scatter reaching a point from an elemental volume

in the water medium. Modelling dose from scattered photons using functions such as SARs or dSARs involves integrating this function over the scattering volume, thus taking into account the shape of the volume [Cunningham et al., 1972], [Altschuler et al., 1985], [Bloch and Altschuler, 1995].

Three dimensional integral models

This category includes all those methods which calculate dose at a point from basic radiation principles. These include Monte Carlo methods which accurately model electron and photon transport, at the expense of very long computation times. Such methods are currently not used in clinical practice, but continuous efforts during the last few years together with advanced computer hardware, are expected to make their use possible in routine treatment planning in the near future [Mackie et al., 1990b], [Neuenschwander et al., 1995] [Kawrakow et al., 1996]. Photon dose calculation algorithms, which use Monte Carlo generated input data and the full density matrix of the patient and are considerably faster than Monte Carlo simulations, have been developed continuously within the last decade. The main representative of these is the *convolution/superposition model*, essentially a three dimensional integral of the product of primary photon energy reaching a given scattering volume in the phantom with a density scaled kernel representing the distribution of this energy around this volume. Calculation of the dose at points in a patient requires three-dimensional density information according to which primary photon intensities and kernels must be modified to allow for the presence of heterogeneities [Ahnesjö et al., 1987],[Mackie et al., 1985b], [Mohan et al., 1986].

1.3.2 Summary

To calculate the dose distribution in patients all the above models, with the exception of convolution/superposition and Monte Carlo, incorporate additional corrections to the dose in water to allow for variations in patient shape, density and for the modulation of the beam with wedges, compensators and blocks. Such algorithms are generally known as *correction-based* approaches. Dose computations based on first physics principles are known as *model-based* methods.

The new generation of highly sophisticated and versatile therapy equipment are designed to enable dose conformation to the PTV, thus aiming at achieving a strong correlation between absorbed dose, local tumour control and normal tissue complication rate. The variability in irradiation geometries required for

conformal treatments requires the storage of numerous combinations of measured factors for use in treatment planning. *Model-based* algorithms do not need such input information, and can calculate dose in units of absorbed dose per incident energy fluence. In conjunction with models which estimate head scatter and electron contamination and which relate energy fluence to monitor units, it is possible for planning systems to calculate directly dose per monitor unit from first principles and therefore not be limited by the beam configuration for which dose measurements have been carried out [Ahnesjö, 1995d]. In addition *model-based* methods account well for situations of electronic disequilibrium which are present at material interfaces and at high beam energies where secondary electron transport is not insignificant.

1.4 Aims of Thesis

The ultimate goal of this work is to improve the overall accuracy of treatment by improving the accuracy of photon dose calculation algorithms. The thesis aims to revie known algorithms in detail and to identify the best approach to date. It is envisaged that a true 3D dose calculation model will be developed which would be more accurate than conventional *correction-based* methods. It is also desirable that a method is developed which would speed up 3D dose computations.

1.5 Outline of Thesis

Chapter 2 reviews all inhomogeneity *correction-based* methods, which use limited amounts of density information for the calculation of dose at a point. Even if dose distributions from these methods can be displayed in 3D, they are not true three dimensional models. It is common to refer to individual *correction-based* dose calculation algorithms with the name of the inhomogeneity correction method they incorporate. Chapter 3 reviews separately the convolution/superposition approach, because it is a true 3D *model-based* method, calculating directly a dose distribution instead of a correction factor to be applied to dose in water. Chapter 4 is an overview of the Monte Carlo method, focusing on its applications in radiotherapy physics. Chapter 5 presents the use of the EGS4 Monte Carlo System in this thesis. Chapter 6 contains a critical assessment of what the significant components of a *model-based* algorithm should be and includes a description and verification of the 3D algorithm developed in this work. The implementation of a novel method for speeding-up 3D dose computations is discussed in Chapter 7.

Chapter 2

Inhomogeneity correction models

2.1 Introduction

The excellent reviews on inhomogeneity correction methods which appear in the literature, categorise these methods according to their ability to handle correct anatomical information [Cunningham, 1982], [Cunningham, 1988], [Purdy and Prasad, 1983], their way of modelling primary and scattered photon dose components [Wong and Purdy, 1987], or the amount of CT density information they use for 3D scattered photon dose calculations [Mohan et al., 1981], [Wong and Purdy, 1990], [Wong and Purdy, 1992]. In this chapter, inhomogeneity correction algorithms will be presented according to the dimensionality of density information they use [Purdy, 1992].

2.2 One dimensional (1D) methods

This category encompasses beam models which use only one dimensional density information for calculating the dose in a heterogeneous medium. These methods use only densities along primary photon paths and are based on a semi-infinite slab approximation. Although these algorithms are classified as 1D in terms of the amount of patient density information they use they are the most widely implemented in 3D treatment planning systems. Beam models in this category were developed before the advent of CT, but in three dimensional treatment planning systems they can use density values from CT images and display dose in three dimensions. It must be emphasised that even if all these methods generate a full 3D dose distribution they cannot be considered a correction for heterogeneities

in three dimensions [Purdy, 1992].

2.2.1 Effective Pathlength (EPL) methods

EPL methods calculate inhomogeneity correction factors using the water-equivalent or radiological depth. This is taken to be the thickness of water between the entrance surface of the patient and the calculation point which would attenuate the primary beam by the same amount as the medium [ICRU, 1976]. Basically, the water-equivalent depth is the physical depth scaled by the effective density relative to water of the medium along the primary ray.

The Effective Attenuation Coefficient method

In this simple method, the inhomogeneity correction factor at a point lying at depth d below the surface of the patient is calculated from

$$C_F = e^{\mu'(d-d')} \tag{2.1}$$

were d' is the water-equivalent depth and μ' is the effective linear attenuation coefficient for the photon energy and field size used. This coefficient is a constant derived empirically. It is usually obtained from depth dose curves by removing the inverse square law effect or from tables of TARs, thus it varies with beam area [ICRU, 1976], [Williams and Thwaites, 1993]. This method does not take into account the depth and off-axis position of the dose calculation point. It corrects dose in water by considering only the variation in density along the path between the calculation point and the source and takes no account of changes present due to particle scattering.

Ratio of Tissue-Air Ratios (RTAR) method

As the name implies, the correction factor in this method is defined to be:

$$C_F = \frac{TAR(d', r)}{TAR(d, r)} \tag{2.2}$$

with d denoting the actual depth and d' the water-equivalent depth. At depth d the radius of the field size is r and $TAR(d, r)$ is the tissue air ratio value at that depth and for that field size. This approach takes into account the field size and the depth at the calculation point, but fails to consider the lateral dimensions and the position of an inhomogeneity with respect to that point. The RTAR method was recently incorporated in a three dimensional beam model

based on the 2D Fast Fourier Transform convolutions of pencil beam kernels derived from measured profile data [Low et al., 1995] with a beam transmission array [Zhu et al., 1995]. The model was developed for 3D treatment planning, namely for modelling the penumbra near block edges and the loss of primary and scattered beam in partially blocked regions.

Effective SSD method

The effective SSD method together with the isodose shift method presented in the next section, were originally introduced and are more commonly known, as methods for correcting for the patient shape (i.e. for oblique incidence). However, they have been also used as inhomogeneity correction methods and specially the effective SSD method is known to be implemented in several commercial treatment planning systems [ICRU, 1976], [Cunningham, 1982], [Purdy and Prasad, 1983].

Instead of dividing TARs, the effective SSD approach calculates a correction factor by dividing percentage depth dose values. The correction is based on the assumption that the phantom material can be compressed or expanded (when the density of the inhomogeneity is greater or less than that of water respectively), so that one can obtain the dose value from percentage depth dose data for a homogeneous water equivalent medium [Cunningham, 1982]. The correction factor (C_F) is

$$C_F = \frac{\%dd(d', r, SSD)}{\%dd(d, r, SSD)} \left(\frac{SSD + d'}{SSD + d}\right)^2 \tag{2.3}$$

d, d', r are defined as previously and SSD is the source to phantom surface distance. This equation is derived after taking into account the change in SSD when moving the isodose chart away or towards the source direction. In most implementations, this formula does not alter the percentage depth dose to account for the divergence of the beam. Equations (2.3) and (2.2) can be shown to be the same (by using the relationship between TARs and percentage depth doses), but the two approaches are subject to different implementation, depending on whether the isodose chart is slid along the central axis ray or other individual rays, or whether the correction factor of equation (2.3) includes or not the second term which corrects for the change in SSD.

The Isodose Shift method

The isodose shift technique was introduced in order to correct manually the dose in water, hence simplifying the dose calculation in treatment planning [Greene and Stewart, 1965], [ICRU, 1976]. The correction factor in this procedure, which is individually specified for each beam energy, is derived by sliding the isodose chart only a constant fraction of the thickness $(d - d')$ of the inhomogeneity as measured along a line parallel to the central axis and passing through the point of interest. The percentage depth dose (%dd) for that depth is read-off directly and no inverse square law correction is applied:

$$C_F = \frac{\%dd(d'', r, SSD)}{\%dd(d, r, SSD)} \tag{2.4}$$

with $d'' = d - n(d - d')$, where d is the actual depth, d' the radiological pathlength. r the beam radius and SSD the source to surface distance.

Summary on the Effective Pathlength methods

Effective pathlength algorithms calculate the dose at a point in an inhomogeneous medium by altering the dose in a homogeneous water medium according to the difference between the effective radiological thickness and the actual depth of that point. This difference relates accurately to the change in primary photon fluence interacting in the medium and thus to the change of the primary component of the dose deposited, which has a predominant effect on the total dose deposited at a point. EPL methods model satisfactorily the primary dose variation (except in the build up region), however the amount of scattered radiation reaching the calculation point mainly depends on its position in the medium with respect to the inhomogeneity as well as on the size of the inhomogeneity. EPL algorithms therefore fail to account for any changes in dose resulting from scattered photons. Monte Carlo studies in layered geometries of water-lung-water and water-bone-water using a ^{60}Co beam (field size $10 \times 10cm^2$) have shown that in these cases, the dose on the central axis of the beam arising from scattered radiation is better presented by completely ignoring the inhomogeneity than applying an effective pathlength correction [Fox and Webb, 1979].

When calculating dose far away from an inhomogeneity, EPL methods give results with acceptable errors; within 2-3 %. For a complex inhomogeneity medium and for dose calculations within or in the near vicinity of an inhomogeneity, EPL methods perform with errors as high as 10 % [Sontag and Cunningham, 1977].

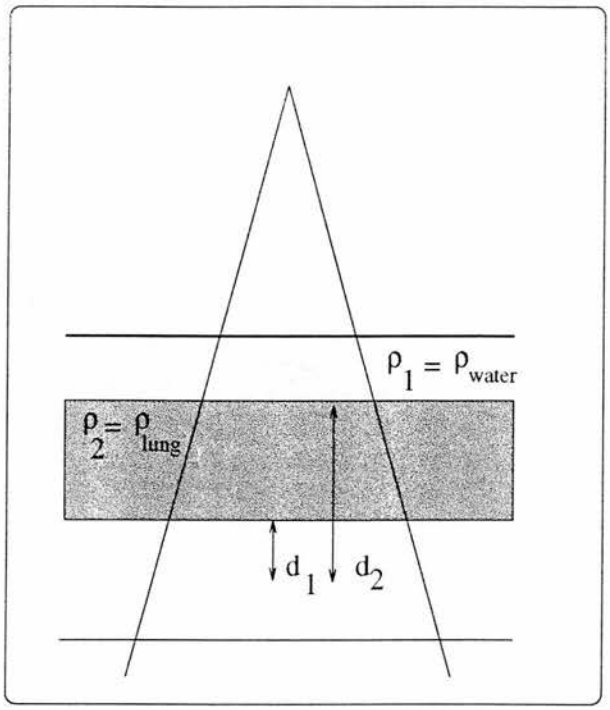

Figure 2.1: *Schematic diagram showing the irradiation geometry in the power-law method.*

Nevertheless, EPL inhomogeneity correction methods are the preferred choice for most present commercial three dimensional radiotherapy treatment planning systems due to their low memory and computation requirements [Wong *et. al.*, 1991].

2.2.2 Power-Law (BATHO) method

This method was suggested by Batho in 1964 [Batho, 1964] and since then it has undergone several further developments resulting in a variety of implementations. Together with the effective pathlength methods, it is extensively used in present-day three dimensional treatment planning systems due to its simplicity and speed, despite a number of limitations which are discussed below.

The original power-law method

The power-law method accounts for inhomogeneities by applying a correction factor based on the ratio of tissue-air ratios raised to the power of electron density relative to water. The original Batho proposal calculates the dose at points below a single inhomogeneity (e.g the lung) within water. Assuming a slab geometry representing a cross section of the chest (Figure 2.1), the inhomogeneity correction factor was defined as:

$$C_F = \frac{TAR(d_1, r)^{1-\rho_{lung}}}{TAR(d_2, r)} \tag{2.5}$$

with d_1 equal to the depth of the calculation point below the lower interface with lung, d_2 the depth of this point below the top interface of the inhomogeneity and ρ_{lung} the relative electron density of lung (set to $0.35 g/cm^3$ in the original work of Batho [Batho, 1964]). This correction factor was especially designed to take into account the position of the calculation point with respect to the inhomogeneity, while this was assumed to have an infinite lateral extent.

Experimental verifications of the above formula have been carried out for ^{60}Co irradiating several types of water heterogeneous slabs (aluminium, carbon, perspex, wood, plastic, air) and for 280kVp x rays on aluminium and foamed plastic [Young and Gaylord, 1970]. The results for ^{60}Co were considered accurate enough for most clinical situations (reported errors were within 3%), whereas results for the lower energy were considered less satisfactory but still clinically useful. Further experimental verification of the original Batho method was carried out using a 4MV photon beam [Geise and McCullough, 1977]. In this work it was shown that the Batho method predicts the dose from energies higher than 1.25MeV to within 2-3%. The success of the original Batho method, which was restricted to correcting dose in tissue-like material beneath an overlying inhomogeneous layer, encouraged its further development, leading to the generalized power-law correction factor method [Sontag and Cunningham, 1977].

The generalized power-law method

The generalized power-law method estimates the dose in cases when the calculation point lies within a non-unit density layer. It also provides a correction for those situations where the effective atomic number of the inhomogeneity differs from that of soft tissue. Referring to Figure (2.1), the expression of the generalized correction factor is defined as

$$C_F = \frac{TAR(d_1, r)^{\rho_1 - \rho_2}}{TAR(d_2, r)^{1-\rho_2}} \frac{(\mu_{en}/\rho)_{\rho_1}}{(\mu_{en}/\rho)_{\rho_2}} \tag{2.6}$$

where distances d_1 and d_2 are same as in (2.5) and ρ_2, ρ_1 are the electron densities relative to water of the inhomogeneity and the surrounding material. The second ratio in this equation is a ratio of mass absorption coefficients accounting for differences in effective atomic numbers. This expression was only designed to calculate an inhomogeneity correction factor for a geometry with three layers. This

limitation was further eliminated with the improvement suggested by Webb and Fox [Webb and Fox, 1980]. The power-law correction factor in its multiplicative form for a medium comprising of N layers of different materials is

$$C_F = \frac{(\mu_{en}/\rho)_N}{(\mu_{en}/\rho)_o} \prod_{m=1}^{m=N} \{TAR(d_m)\}^{\frac{\mu_m - \mu_{m-1}}{\mu_o}} \tag{2.7}$$

with μ_m the linear attenuation coefficient of material m, $(\mu_{en}/\rho)_N$ is the mass energy absorption coefficient of the Nth material and d_m is the distance from the calculation point to the mth point from the surface of the phantom. Sontag and Cunningham compared their generalized power-law calculations for ^{60}Co and for increasing field sizes with measurements in phantoms consisting of cork or aluminium inhomogeneities of infinite lateral extent. Webb and Fox compared their results against Monte Carlo generated dose data for ^{60}Co using bone and lung inhomogeneities with lateral extent either smaller or larger than the beam size. Both groups came to similar conclusions regarding the accuracy and the limitations of the method:

- The original and generalized power law approaches account for the contribution to dose from scattered photons only indirectly. This contribution depends on the type and geometry (lateral extent) of the material above the point of dose calculation and the energy of the primary beam. In the case of bone or lung inhomogeneities with lateral extent greater than the beam size, the dose is estimated within $\pm 2\%$. In the case of ^{60}Co irradiations, when the lateral extent of a lung inhomogeneity is less than the beam width, the power-law factors give results within $\pm 3\%$. For bone inhomogeneities the errors are large; up to 6%.

- As the photon beam energy increases (higher than that of ^{60}Co) Compton interactions become less predominant causing a decrease in the relative percentage of scatter. The generalised power-law equation assumes only Compton interactions. Therefore the accuracy of dose predicted by this method at higher energies has been questionable [Sontag and Cunningham, 1977].

- For ^{60}Co irradiation (especially for a $10 \times 10 cm^2$ field) the power-law method estimates dose within the material comprising the inhomogeneity, better than any effective pathlength approach.

- It is obvious from equations (2.6) and (2.7) that this correction factor only considers the material above the calculation point. No backscattered radi-

ation originating from the material below the point is taken into account. This results in an obvious over-estimation of dose, especially close to exit surfaces. Within low density regions Sontag and Cunningham considered this error negligible [Sontag and Cunningham, 1977].

- Electronic equilibrium is assumed throughout the irradiated medium; therefore dose near material interfaces, and for high energy beams is erroneously estimated [Mackie et al., 1985a].

The first implementation of the generalized power-law method (equation (2.7)) within a matrix beam model [Milan and Bentley, 1974] in a treatment planning system using computed tomography (CT) density data was reported by Cassell *et al.* [Cassell et al., 1981]. Assuming all interactions were Compton, CT numbers were appropriately related to electron density values relative to water [Parker et al., 1979], [Parker et al., 1980].

Enhancements to the power-law method

Wong and Henkelman [Wong and Henkelman, 1982] have demonstrated the fundamental limitations of the original and generalized Batho method through a theoretical analysis carried out on the calculation of primary and first scattered photon dose. They supported their findings with experimental verifications. According to their findings, the generalized power-law method provides an acceptable approximation to true dose below a single inhomogeneous layer with an extent larger than that of the field size and electron density less than that of tissue. In the extreme situation of a large inhomogeneity with electron density greater than tissue and large field sizes, the method has been proved to be inadequate with errors up to 10%. If the electron density of the inhomogeneity layer is greater than unity, the power law method overestimates true dose. For the calculation of dose within an inhomogeneous layer, generalized Batho corrections perform well (up to 1% error) when the electron density of the inhomogeneity is less than unity, but agreement between theory and experiment becomes progressively worse for denser layers and larger field sizes. Wong and Henkelman considered that the extension of the original method for a multilayered medium gives a poorer approximation, due to multiplication of effects, to true dose than in the case of the original two-layered geometry. This is because the contribution to dose from overlaying layers of tissue is ignored for each multiplicative factor. They suggested replacing the multiplicative rule with an additive rule for the

calculation of the correction factor, which appears to circumvent the above limitation. In any case the assumption of a multilayer geometry with extent larger than the beam cannot account for the three dimensional geometry of a patient.

Further work on the method was carried out in an attempt to improve its performance in those cases when heterogeneities have lateral extent less than that of the beam [van de Geijn and PoCheng, 1980], [Lulu and Bjärngard, 1982]. This was particularly to improve the calculation of the dose contribution from scattered photons. Lulu and Bjärngard suggested the combination of a Batho correction factor with a scatter summation technique [Day, 1950]. Their method, which was examined only for ^{60}Co beams, uses equation (2.7) unaltered for correcting dose at points which lie on the beam's central axis and when the beam width is less than that of the heterogeneity. In any other case (e.g. for heterogeneities with small lateral extent compared to the beam and for points either on or off the beam's central axis), assuming that one heterogeneous region is present, the dose is calculated separately for the homogeneous and heterogeneous regions. These dose components are added or subtracted according to the location of the calculation point. In the general case of a point lying off axis, the irradiation field is divided into subfields with the calculation point in the corner of each field. These subfields, which cover homogeneous or heterogeneous volumes, are quadrupled and converted to equivalent squares. The dose from each equivalent square is found and for those subfields which cover inhomogeneous volumes, a power-law correction is applied. Dose contributions from each equivalent square are added or subtracted to give the total dose. Comparisons of results with simulated Monte Carlo data [Webb and Fox, 1980] and measured data [Sontag, 1979] have been shown to be better than those resulting from the unmodified Batho model. Lulu and Bjärngard also pointed out that their implementation of the power-law approach can be extented to model irregularly shaped fields and irregularly shaped inhomogeneities using appropriate scatter integration methods.

Analytical calculations and comparisons with measured data have also shown that a power-law correction when defined as a ratio of Tissue Maximum Ratios (TMRs), provides estimations of dose with an improved accuracy (nearly 5%) within lung for ^{60}Co (when field sizes are different than the standard $10 \times 10cm^2$) and 6MV x rays. It was suggested replacing TARs with TMRs particularly when dose is required in low density media from large field irradiations [El-Khatib and Battista, 1984].

The power-law correction by Webb and Fox [Webb and Fox, 1980] and its

implementation by Cassell *et al* [Cassell et al., 1981] was further discussed by Siddon [Siddon, 1984]. Siddon reformulated the Webb and Fox expression (equation (2.7)) on the basis of regional identification of inhomogeneities rather than considering the passage of the photon beam through layers of tissue. The claim by Siddon on the improved efficiency of his formulation of the power-law method was further argued by Webb and Cassell [Webb and Cassell, 1985], [Siddon, 1985].

All authors mentioned previously, with the exception of El-Khatib and Battista, examined the potentialities and limitations of the generalised power-law method for ^{60}Co beams. The work of El-Khatib and Battista [El-Khatib and Battista, 1984] showed that for 6MV x rays, even when TARs where replaced by TMRs in (2.6)), the power-law correction in lung is considerably underestimated. The work of Thomas [Thomas, 1991] on water-lung-water phantom irradiations with ^{60}Co, 8MV and 16MV, confirmed this. He focused his investigation on a limitation of the power-law method which had not been accounted for by any of the previous workers. This is related to the calculation of dose near interfaces from energies greater than ^{60}Co and consequently affects dose values within low density media. Very near interfaces equation (2.6) cannot be applied directly when d_1 (Figure 2.1) is less than the build-up distance corresponding to the beam energy. In this case, one should use TMR$(0, r)$ (or TAR$(0, r)$), where r is the radius of the circular field. Cunningham [Cunningham, 1982] suggested obtaining this value by extrapolating data from greater depths. On the other hand, Cassell *et al* [Cassell et al., 1981] suggested a linear interpolation between dose at the tissue boundary and the build-up distance beyond the boundary. Thomas proved theoretically and experimentally that the above two suggestions fail to improve dose values near to and within lung. Instead, he proposed replacing TMR(d, r) with TMR$(d + d_b, r)$, where d_b is the build-up depth for the particular energy. This simple adaptation to the generalised power-law method, improves significantly its performance at high energies up to 8MV. Thomas also recommended that in the case of irradiation at even higher energies (such as 16MV) and field sizes greater than $10 \times 10cm^2$, it is preferable to use an EPL calculation instead of the power-law approach.

2.2.3 The Extended Net Fractional Dose (ENFD) method

The Net Fractional Dose (NFD) method is the most advanced up-to-date analytical beam model [van de Geijn and Fraass, 1984]. *Net fraction depth dose* (NFD) is defined as the fractional depth dose corrected for inverse square law. The model

consists of a set of exponential functions that describe the net fractional depth dose, fractional depth dose, tissue air ratio (TAR), tissue maximum ratio (TMR) and tissue phantom ratio (TPR) concepts as a function of depth and equivalent square field size. According to van de Geijn, the NFD approach describes the behaviour of collision kerma for a certain field size, along a central axis of the beam at depths beyond the electron build up in a uniform density medium and assuming lateral electron equilibrium.

The initial model, was extended (*Extended Net Fractional Dose method (ENFD)* to include corrections for inhomogeneities as well as to model interface effects [van de Geijn, 1987]. The inhomogeneity correction involves the application of O'Connor's density scaling theorem [O'Connor, 1957] assuming a medium composed of plane parallel slabs of materials of different electron densities. The two geometric parameters scaled are the depth and the equivalent square field. Corrections for the dosimetric effects of the trans-interface disequilibrium of the scattered photon fluence and the effects of incomplete longitudinal as well as lateral electron build up are applied by modifying the exponential functions which describe the downstream scatter of photons originating upstream from material interfaces (namely the peakscatter/backscatter factors) and the finite range of secondary electron transport (build-up and lateral build-up functions). These modifications are limited to the central rays or rays more than the lateral electron range away from the boundary of the beam. Experimental evaluation and comparisons with measured data and other methods (effective attenuation coefficient method and original power law method) have been carried out for ^{60}Co, 10MV and 15MV x rays in layered phantoms. It was shown that the ENFD method is accurate within 1%-2% for all energies examined regardless of the field size. At 10MV and higher energies the performance on the central axis was considered quite acceptable with errors increasing with decreasing field sizes. As expected, ENFD was shown to be superior to the original power-law method at energies higher than ^{60}Co.

2.3 Three dimensional (3D) methods

This category encompasses dose calculation methods which make use of 3D CT density information. These are the Equivalent Tissue-Air Ratio (ETAR) method, the Differential Scatter-Air Ratio method (DSAR), the Delta Volume method (DV) and the Convolution/Superposition method. They are designed to correct

for photon scattering either semi-empirically or to employ full 3D scatter ray-trace procedures. The Superposition approach is discussed separately in the next chapter. However, the Fast Fourier Transform convolution model is discussed here, since it is mainly an analytical approach employing constraints which limit the accuracy of the results in comparison to the superposition approach.

2.3.1 The Equivalent Tissue-Air Ratio method (ETAR)

Description of the original ETAR method

The dose delivered in patients is sensitive to tissue heterogeneities, therefore the dose values calculated during treatment planning are affected by the geometric outline, the relative electron density assigned to the various organs and the means by which the dose calculation algorithms account for their presence. Inaccurate delineation of tissue heterogeneity outlines can lead to severe errors in the calculated dose regardless of the degree of sophistication of the inhomogeneity correction model [Sontag et al., 1977]. Although the influence of incorrect electron density values on dose is generally less significant [Geise and McCullough, 1977], [Huizenga and Storchi, 1985] there have been cases where dose errors can be as high as 4% [Sontag, 1979]. It has been recommended that relative electron density matrices be used directly from CT and average densities be derived from these matrices regardless of the inhomogeneity correction method used. The Equivalent Tissue-Air Ratio method (ETAR) was developed as a practical method, aimed at

- making use of more accurate anatomical information, namely, the relative electron density values from CT images, and at
- improving the inhomogeneity corrections relative to the power-law approach by accounting for the lateral dimension and shape of an inhomogeneity and by taking into consideration the material below the calculation point.

Essentially, ETAR was introduced to advance the modelling of scattered photon contribution to dose at a point [Sontag and Cunningham, 1978b], [Sontag, 1979].

ETAR calculates dose in a heterogeneous medium by applying a correction factor to the dose in water. This correction factor is a ratio of TARs similar to the used in the RTAR method. The essence of ETAR lies in the application of an elegant theorem put forward by O'Connor [O'Connor, 1957] (also see section 3.4.1 in chapter 3). According to the density scaling theorem, *the dose at a point in a*

homogeneous non unit density medium can be obtained from the dose at the same point in a water medium, with all its dimensions scaled with density. This means that the TAR at a depth d in a medium of relative density ρ irradiated by a field radius r is equal to $TAR(\rho d, \rho r)$; the tissue air ratio in a unit density medium for depth ρd and field size ρr. The theorem is valid under those conditions where dose from scattered photons arises almost entirely from Compton interactions [Pruitt and Loevinger, 1982]. The application of this theorem for higher energies is questionable [Henkelman and Wong, 1981].

The ETAR correction factor is defined as

$$C_F = \frac{TAR(d', \tilde{r})}{TAR(d, r)} \tag{2.8}$$

In this expression, d' is the distance along the path of the primary photon scaled with the *average electron density* $\tilde{\rho}$ along that path and $\tilde{r}$ is the beam radius scaled with a *weighted average density* $\tilde{\rho}_r$. If the atomic number of the homogeneous medium is also different from that of water, then the above equation is modified using the mass absorption coefficients in water and the medium:

$$C_F = \frac{TAR(d', \tilde{r})_{water}}{TAR(d, r)_{water}} \frac{(\mu_{ab}/\rho)_{medium}}{(\mu_{ab}/\rho)_{water}} \tag{2.9}$$

The scaling of TARs is a two step procedure employing average density values. TAR$(d', \tilde{r})$ is taken to be the sum of two components:

$$TAR(d', \tilde{r}) = TAR(d', 0) + SAR(d', \tilde{r}) \tag{2.10}$$

Scaling the depth. The procedure of scaling involves the calculation of the average electron density along the path of the primary photon, from the source to the point of calculation:

$$\tilde{\rho} = \frac{\sum_j \rho_j}{n} \tag{2.11}$$

where ρ_j are the densities of volume elements which lie along the beam ray above the point of calculation and attenuate the primary photon fluence.

Scaling the beam radius. Scaling the beam radius involves the calculation of an average density from all those volume elements which contribute to dose from scattered photons. The scaled beam radius $\tilde{r}$ is defined as the product of the field radius in water with a weighted average density $\tilde{\rho}_r$:

$$\tilde{r} = r\tilde{\rho}_r \tag{2.12}$$

where $\tilde{\rho}_r$ is

$$\tilde{\rho}_r = \frac{\sum_i \sum_j \sum_k \rho_{ijk} W_{ijk}}{\sum_{ijk} W_{ijk}} \tag{2.13}$$

In equation (2.13), ρ_{ijk} are the densities of volume elements (i, j, k) in the irradiated medium and W_{ijk} are weighting factors dependent on the conditions of irradiation, the irradiated medium and the location of the calculation point. For each calculation point a different set of factors is required and the procedure to derive these is by no means trivial. The initial development of ETAR suggested the determination of these weighting factors using differential scatter-air ratios (dSARs) [Sontag, 1979]. This involves the calculation of two components; dose from first scattered photons and dose from multiply scattered photons:

$$W_{ijk} = \Delta S_1(d, r) + \Delta S_M(d, r) \tag{2.14}$$

The first scattered photon dose component can be calculated accurately from zero-area TARs, the Klein-Nishina probability per electron per solid angle of scatter, the number of electrons per unit volume, the linear attenuation coefficient for water for the incident primary and scattered photon energies, the average energy absorbed by primary and scattered photons and the physical density of the medium. The multiple scattered photon dose component is approximated by modifying the first calculation of dose from once scattered photons in a way that reflects the behaviour of multiple scatter. This procedure assumes that the multiply scattered photon distribution is isotropic and only average coefficients are employed for its estimation. These two steps were considered impractical for clinical implementation, therefore an empirical calculation of weighting factors was used instead.

In clinical implementations weighting factors are derived empirically as the product of two factors; thus reducing the volume summation (3D calculation) to a planar summation (2D calculation):

$$W_{ijk} = W_k W_{ij} \tag{2.15}$$

To define these two factors the irradiated volume was divided into slices (such as CT slices) and a cartesian coordinate system was set with the origin at the calculation point, its y-axis parallel to the radiation beam and the z-axis along

the parallel contiguous slices. Factor W_k, which is a function of the z position and constant with respect to the x-y directions, represents the relative importance of the kth slice's contribution to the scattered photon dose component at the dose calculation point. It is determined from the difference between two scatter-air ratios in water:

$$W_k = SAR(d_{ref}, \tilde{r_2}) - SAR(d_{ref}, \tilde{r_1}) \tag{2.16}$$

with d_{ref} arbitrarily chosen to be 10cm and $\tilde{r_1}$, $\tilde{r_2}$ the radii of equivalent circular beams which are a function of the z position of the kth slice. The calculation of these radii is presented in the appendix of the original paper by Sontag and Cunningham [Sontag and Cunningham, 1978b]. Weighting factors W_{ij} reflect the relative importance of the volume element at location (i, j) in giving rise to dose reaching the calculation point from scattered photons. These are derived in a simplistic manner assuming first and multiply scattered radiation and can be precalculated and tabulated for a given beam energy, thus speeding-up the dose calculation procedure. Using these factors, the relative electron density of equation (2.13) is calculated from:

$$\tilde{\rho}_r = \frac{\sum_i \sum_j [\frac{\sum_k \rho_{ijk} W_k}{\sum W_k}] W_{ij}}{\sum W_{ij}} = \frac{\sum_i \sum_j \tilde{\rho}_{ij} W_{ij}}{\sum_{ij} W_{ij}} \tag{2.17}$$

The quantity $\tilde{\rho_{ij}}$ replacing the square brackets, is estimated separately using a *coalescing method.* This procedure coalesces all density information from the CT-density planes on either side of the calculation plane down to a single plane located at a distance z_{eff} and with an average density $\tilde{\rho_{ij}}$. z_{eff} is defined as the position within the irradiated volume at which the scattered photon dose at a point from all the volume elements with a z-coordinate less than z_{eff} is equal to the scattered photon dose originating from all volume elements with z coordinate greater than z_{eff}:

$$z_{eff} = \frac{\sum_k z_k W_k}{\sum_k W_k} \tag{2.18}$$

Calculations of $\tilde{\rho}_{ij}$,W_k and z_{eff} need to be performed only once for each beam, whereas the calculation of factors W_{ij} and $\tilde{\rho}_r$ must be repeated for each volume element with density $\tilde{\rho}_{ij}$ on the effective scatter plane.

Performance and limitations of ETAR

Calculations with ETAR in homogeneous non-water media from ^{60}Co irradiations using variable field sizes, have shown that it performs best for small field sizes, in high density media such as Aluminium and in low density media such as cork. For large field sizes and at extreme depths the correction factor is overestimated in high density media and underestimated in low density media.

Comparisons with measured data in a heterogeneous medium irradiated with ^{60}Co, have shown that the model handles well, with an accuracy better than 2%, cases of inhomogeneities having lateral extent smaller than the beam's width and predicts exit dose values within $\pm 1.5\%$ [Sontag and Cunningham, 1978b].

The application of ETAR for beam other than ^{60}Co where interactions other than Compton (pair production and photoelectric effect) are likely to occur, has been considered by Sontag and Cunningham only with respect to the attenuation of the primary photons. They assumed that such interactions do not alter the relative importance of volume elements in producing scattered radiation. Their suggestion involved the calculation of effective depths by weighting the density of volume elements according to the fraction of the type of photon interactions that take place in the volume element. However, this assumption is not expected to improve ETAR's performance especially for higher energy beams due to its other major limitations, especially when handling situations of electronic disequilibrium.

The energy deposited at a point is due to secondary electrons. The basic assumption that dose at a given point is directly proportional to the x-ray fluence at that point may be an acceptable approximation for ^{60}Co beams, but surely not for megavoltage beams where the range of secondary electrons is even larger. For a 15MV x-ray beam this range in lung (of density $0.33 g/cm^3$) can reach up to 9cm in the forward direction and for electrons that scatter laterally it can be as long as 5cm. On the grounds of lateral electronic disequilibrium, it was shown that ETAR overestimates dose in cork along the central axis of 6MV and 15MV beams for fields as small as $5 \times 5 cm^2$ [Mackie et al., 1985a]. For inhomogeneities with small extent along the direction of the central axis of the high energy beam, dose values are overestimated due to electronic disequilibrium around media interfaces.

Calculating primary and scattered photon dose at a point separately using TARs and SARs is not always valid in the case of a heterogeneous medium, because electronic equilibrium is not always present. Extrapolation of TARs to zero-area or very large field sizes is arbitrary and imprecise.

Another limitation of ETAR relates to the application of O'Connor's density scaling theorem for photon energies higher than 1.25MeV. This theorem is strictly valid under conditions for which all scatter dose arises from Compton scattering [Henkelman and Wong, 1981], thus at beam energies resulting in secondary electrons with small ranges. However, O'Connor argues that the theorem is expected to be applicable with acceptable accuracy for 10 MV x rays in low density materials [O'Connor, 1984].

It is also an inherent modelling deficiency of ETAR that is does not consider effects from primary intensity changes on the calculation of scattered photon dose. It has been shown that the dose deposited below the lung is underestimated because of incorrect modelling of scattered photon transport reaching that region [Redpath and Thwaites, 1991], [Yu and Wong, 1993a]. A 3D implementation of the original ETAR method would fail to model irregular fields and the presence of beam modifiers. If changes in the primary intensity are not taken into account for the calculation of the weighted average density of the equivalent homogeneous medium, then the density scaling theorem is not strictly valid, subsequently foiling ETAR's attempt to model accurately dose in a non unit density homogeneous medium.

ETAR does not predict accurately the contribution to dose from scattered photons and their effect on dose in the presence of a small void in the irradiated medium [Iwasaki, 1983], [Cunningham, 1983]. A void with zero density will not produce any scattered radiation, but will alter the scattered dose reaching a point from all other volume elements in the irradiated medium. This situation, as pointed out by Wong and Henkelman [Wong and Henkelman, 1982], must be considered when designing a dose calculation model. They conclude that *any satisfactory solution to the inhomogeneity problem must be intrinsically nonlinear in its handling of individual volume elements or pixels.* It is an inherent limitation of ETAR to assume that individual point inhomogeneities act independently [Henkelman and Wong, 1981].

One of the less profound deficiencies of ETAR is that no electron contamination is accounted for when calculating surface dose, as well as assuming the patient to be completely waterlike, ignoring the presence of any high atomic number media.

The time consuming calculation of weighting factors led Sontag and Cunningham to develop the *coalescing procedure* which enabled the model to be used clinically. This reduction of the three-dimensional formulation to two-dimensional

is empirical and although this 2D ETAR implementation still performs well for most clinically encountered situations, its application in 3D radiotherapy treatment planning (3D RTP) is insufficient mainly because it does not model irregular fields. Therefore, the advantages in reducing calculation time vanish in 3D RTP because the coalescing procedure would have to be carried out for every calculation plane!

Despite its limitations in calculating accurately the dose at a point, ETAR has been the only 3D dose calculation model to date to semi-empirically correct for scattered photon dose and to be implemented in commercial treatment planning systems. The first implementation is described by Sontag and Cunningham [Sontag and Cunningham, 1978a]. Their work emphasised the improved accuracy achieved in dose calculations when using relative electron density values from CT, as well as discussing practical problems related to the use of CT in radiotherapy.

2.3.2 Modified or extended versions of ETAR

Following the introduction of ETAR, several research groups have developed dose calculation methods based on the same principles as ETAR, either introducing some simplifications in order to decrease calculation time or by extending the original algorithm to improve its versatility or overcome its limitations. The following section describes some of these approaches in chronological order.

Simplified ETAR (SETAR)

SETAR is a modification of ETAR attempting to increase the speed of the algorithm by simplifying the calculation of the weighted average density ($\tilde{\rho}_r$ of equation 2.13) [Thatcher and Palti, 1983]. Assuming that inhomogeneity corrections depend only marginally on density variations [Geise and McCullough, 1977] and that density corrections are insensitive to the depths of points located behind inhomogeneities [Young and Gaylord, 1970], Thatcher and Palti suggested representing an inhomogeneous object with one whose relative electron density equals the average density values of that object. The field size in water is scaled with a relative electron density obtained from the following formula:

$$\tilde{\rho} = \frac{V_w + V_i \rho_i f_i}{V_w + V_i f_i} \tag{2.19}$$

In this equation ρ_i represents the average density value of the inhomogeneous object i, V_w and V_i are the volumes of water equivalent and inhomogeneous parts of

the body included in the irradiated volume and f_i is an empirical factor compensating for the difference in scattered photon contribution between water equivalent body parts and a heterogeneous part. This factor depends on the beam energy and geometry. In practice, average values are assigned to f_i assuming that the irradiated volume extends longitudinally from the surface to the plane of calculation and laterally between beam edges. Volumes V_w and V_i are estimated from outlining appropriate regions in the CT images. f_i values are estimated empirically using $f_i = 0.30$ for cork (relative electron density $\rho_e = 0.29$) in order to represent regions of lung. In regions of Teflon with density $\rho_e = 1.85$ (representing bone) f_i values were taken to be ∞, equivalent to setting effective density equal to local density.

The model was verified against dosimetric data from ^{60}Co and 8MV x-ray beams incident on a water phantom including lung and bone heterogeneities with lateral extents larger and smaller than the field size ($10 \times 10cm^2$ and SSD values of 80cm and 100cm). Correction factors along the central axis calculated from an effective path length method, the power-law method and SETAR, were compared against measured data. These comparisons have demonstrated SETAR to be accurate enough in most situations encountered clinically. While ETAR was developed to benefit from 3D CT density information and generally avoids contouring heterogeneities on the calculation plane, SETAR is essentially going a step backwards by using average values for the water-heterogeneous regions. Backscatter is ignored in the calculation of relative electron density $\tilde{\rho}$ and generally this method is based on estimating f_i values by trial and error. For simple treatment planning situations such as lung treatment, where heterogeneous regions are large and well defined, the performance might appear adequate but in more complex cases such as pelvis or head and neck regions, its performance is questionable and has not been examined by the authors. All limitations of ETAR, such as no corrections for the presence of small voids or non-equilibrium conditions, exist in this model. Apart from the benefit of faster computation, this model appears to be suited for treatment planning with irregular fields but the simple manner with which volumes V_w and V_i are calculated, call into question its possible implementation in a three-dimensional treatment planning system.

Application of ETAR to Fast Reconstructor

Although the formulation of ETAR is 3D, its clinical implementation has been 2D by calculating the primary component of dose along the primary photon path on

the calculation plane and by estimating the scattered component by empirically coalescing the density information of all neighbouring CT slices into a single slice at an effective distance from the calculation plane. This coalescing procedure reduces the versatility of the model not allowing its implementation in a 3D treatment planning system, since dose calculations from irregular fields is not possible. This limitation of ETAR was the main reason for which Inamura *et al.* [Inamura et al., 1984] proposed their modified-ETAR approach.

Primary dose is calculated as in ETAR using the density scaled (effective) depth along the paths of primary photons. Scatter dose was estimated by adding contributions to dose at a point from each irregular sector j of the irradiated volume:

$$D_s = \sum_j D_j \tag{2.20}$$

Scatter dose from each sector which has sector angle θ_j s calculated using the following expression:

$$D_j = D_A(d) SAR(d', \tilde{r}) \frac{\theta_j}{2\pi} \tag{2.21}$$

$D_A(d)$ is the dose in air at the calculation point of actual depth d and $SAR(d', \tilde{r})$ is the scatter-air-ratio at effective depth d'. Scaled radius $\tilde{r}$ is obtained from:

$$\tilde{r} = \tilde{\rho}\, r_{eff} \tag{2.22}$$

Here, $\tilde{\rho}$ is a weighted average density representing the effect of a fraction of the irradiated heterogeneous volume of irregular shape to the scattered photon dose component at the calculation point. The effective radius r_{eff} of a sector of a circular field is obtained by assuming the area of the field equal to the fractional area of the irregular volume incorporating the calculation point. The formalism used for the calculation of $\tilde{\rho}$ is analogous to the original ETAR approach, but without the complicated, time consuming estimation of weighting factors. Instead of these, Inamura *et al.* arbitrarily used the exponential function $e^{-\mu t_{ijk}}$ where μ is the linear absorption coefficient of water and t_{ijk} the distance between the calculation point and each scattering element. The formula for calculating the weighted average density is :

$$\tilde{\rho} = \frac{\sum_i \sum_j \sum_k e^{-\mu t_{ijk}} \rho_{ijk}}{\sum_i \sum_j \sum_k e^{-\mu t_{ijk}}} \tag{2.23}$$

For implementing this model, special dedicated hardware (fast reconstructor) was used and the authors claimed a calculation time within 10 seconds per portal. The possibility of using a dose calculation model which accounts for scatter

variations in the medium on a 3D treatment planning system, as presented by Inamura *et al.*, is very encouraging. However, this method has not been compared with the original ETAR method or any measured data to confirm the improved accuracy claimed and to justify the replacement of weighting factors by exponential factors.

A 3-dimensional scatter correction algorithm

This algorithm [Redpath and Thwaites, 1991] is a 3D non scatter raytrace method because it does not implement explicit ray tracing procedures for the calculation of scatter. It is based on the principles of ETAR, especially in the use of a coalescing procedure for speeding up the calculation. The main improvement in this model in comparison with ETAR is that the relative scattered photon contribution (once scattered and multiply scattered photons) to a point, originating from all scattering sites in a homogeneous or heterogeneous medium, is estimated by taking into account any changes in primary dose due to the presence of beam modifying devices or inhomogeneities. Comparisons between measured data and data calculated by ETAR in situations of low or high density heterogeneities in water, confirm the importance of the primary variation influence in the calculation of the scattered dose component.

The relative dose deposited in a heterogeneous medium (normalised to dose at the maximum build-up depth) is given by the sum of primary and total scattered photon dose components:

$$DD_p = [TAR(z_{eff}, 0)PF(x, y) + S(z, r_z)C_F](\frac{SSD + d_{max}}{SSD + z})^2 \frac{1}{PSF} \qquad (2.24)$$

The calculation of relative primary dose involves the multiplication of zero-area TAR at the effective depth with a function $PF(x, y)$ which accounts for changes in primary intensity prior to entering the medium (changes due to compensators, wedges, blocks and the flattening filter), with an inverse square law correction (d_{max} is the depth of maximum buildup), and the inverse of the peak scatter factor (PSF) for each beam. From equation (2.24) it is seen that due to the presence of inhomogeneities the changes in the primary component are modelled with a radiological pathlength calculation. As mentioned in previous paragraphs modelling the primary component of the dose using zero-area TARs can be assumed to be correct for low energy photon beams but at higher energies, where secondary electron transport cannot be ignored, these algorithms are unsuitable

in regions near beam edges and material interfaces. $S(z, r_z)$ is the total amount of scattered radiation reaching a calculation point in water and is obtained from sector integration of differential scatter-air ratios. C_F is a correction factor defined as the ratio of the relative amount of scattered radiation reaching a point from all scattering sites in a heterogeneous medium to that in a water homogeneous medium:

$$C_F = \frac{\sum_{ijk}(S_{medium})_{ijk}}{\sum_{ijk}(S_{water})_{ijk}} \tag{2.25}$$

The scattered photon contribution S_{water} in a homogeneous medium is defined as

$$S_{water} = [TAR(z,0)PF(x,y)\frac{d\sigma(\theta)}{d\Omega}e^{-\mu(\theta)s}/s^2 + SAR(z,r_z)\frac{d\bar{\sigma}}{d\Omega}e^{(-\mu's)}/s^2](\frac{SSD+d_{max}}{SSD+z})^2 \tag{2.26}$$

where $\frac{d\sigma}{d\Omega}(\theta)$ is the Klein-Nishina probability of a photon being scattered through an angle θ evaluated for the mean energy of the radiation beam, $e^{-\mu(\theta)s}$ accounts for the attenuation of a once scattered photon from the interaction site to the dose calculation point and $1/s^2$ is an inverse square law correction. SAR(z,r_z) is the scatter-air-ratio at depth z with r_z being the radius of the equivalent circular field at depth z. $\frac{d\bar{\sigma}}{d\Omega}(\theta)$ is the mean Klein-Nishina scattering probability averaged over 4π. The energy of the once scattered photon has been approximately evaluated from the mean energy of the radiation beam. The second exponential, models the attenuation of multiple scattered photons for the mean energy of multiply scattered photons. The rest of the variables in equation (2.26) are the same as in equation (2.24). On the assumption that scattered radiation reaching a point depends mainly on density variations at the scattering element and along the path of scattered photons, equation (2.26) is modified to account for the presense of heterogeneities using TARs for distances scaled with the mean density between each pair of scatter and dose deposition sites and by multiplying the resulting scatter fraction with the relative electron density at the point of interaction. The relative amount of scattered radiation reaching a point in a heterogeneous medium is formulated as:

$$\begin{aligned} S_{medium} &= [TAR(z_{eff},0)(\frac{SSD+d_{max}}{SSD+d})^2 PF(x,y)\frac{d\sigma(\theta)}{d\Omega}e^{-\mu(\theta)s_{eff}}\frac{1}{s^2} \\ &+ SAR(z_{eff},r_z)(\frac{SSD+d_{max}}{SSD+d})^2\frac{d\bar{\sigma}}{d\Omega}e^{-\mu's_{eff}}\frac{1}{s^2}]\rho(i,j,k) \end{aligned} \tag{2.27}$$

This model has been implemented clinically using three ways for increasing the speed of calculation:

(a) By using a coalescing procedure similar to that suggested by Sontag and Cunningham in the original ETAR, Redpath and Thwaites considered it efficient to reduce the 3D calculation to 2D using a plane at an effective distance from the calculation plane because they assumed that the variation of scattered radiation reaching points on the calculation plane is independent of the beam energy and that more than 80% of the total scatter originates from planes at distances up to 5cm away from that plane. The effective distance from the central plane was not chosen arbitrarily as in ETAR, but was calculated by weighting the distances of all neighbouring slices with the relative amount of scattered radiation originating from them and reaching the calculation plane:

$$\bar{x} = \frac{\sum_j^n \rho_j S_j}{\sum_j S_j} \tag{2.28}$$

(b) Considering that the calculation time per field is proportional to the square of the number of points used for calculation, only a constant number of scattering points was used regardless of the patient cross section. A limit of 1000 scattering points was chosen and considered sufficient for accurate results.

(c) Furthermore, no scattered radiation was generated from points which were at a distance greater than 5cm in the lateral and forward direction from each calculation point.

This model calculates dose below air or aluminium from a 4MV beam, with errors between 1% to 3%, whereas errors from ETAR calculations can be as large as 10%. Measured data from a tangential irradiation of a water phantom with a 4MV beam were compared with calculated data from this model and ETAR. The agreement of the former was presented to be within $\pm 2\%$. Results from ETAR varied from 4% over the expected value near the central axis, to 1% over near the beam edge.

This 3D scatter correction algorithm appears to be superior to ETAR, allowing the modelling of irregular fields if the coalescing procedure is not employed. It improves the calculation of dose contributions from scattered photons and is readily suited for implementation on a 3D treatment planning system. It is akin to

ETAR in the lack of modelling surface dose, assuming no presence of high atomic number media in the patient and not accounting for electronic disequilibrium. Due to the latter, the model's performance at high energy beams is questionable.

Extension of ETAR to account for conditions of electronic disequilibrium

Dose calculation algorithms presented in previous paragraphs were not designed to model the transport of secondary electrons and accurately predict dose around media interfaces and beam boundaries. According to Woo *et al.* [Woo et al., 1990] this is due to the limited data available to these algorithms. For this reason, in their work, they abandon the assumption of local energy deposition by primary photon interactions by considering that the primary component originates from a region surrounding the calculation point with radius less or equal to the lateral distance travelled by secondary electrons. Therefore, the primary dose component in a homogeneous water medium is calculated as an integral of dose contributions from secondary electrons released from primary photon interactions. In the inhomogeneous medium a correction factor is introduced to account for the changes in primary dose, analogous to the C_F defined in the ETAR model (equation (2.8)).

Instead of modelling the relative primary dose component using zero area TAR, the relative primary dose component is calculated here using the following equation:

$$relP(d,x,y) = \frac{1}{2\pi}\int_{\theta=0}^{2\pi}\int_{r=0}^{R(\theta)} f(r,\theta)\frac{dP}{dr}[d(r,\theta),r]drd\theta \qquad (2.29)$$

The differential $\frac{1}{2\pi}\frac{dP}{dr}drd\theta$ is considered to be the primary contribution to dose from a pencil beam located at (r,θ) relative to a calculation point at (x,y) having radial and angular widths dr and $d\theta$ respectively. The limit $R(\theta)$ is set either equal to the lateral distance travelled by secondary electrons or equal to the distance from the beam edge. dP/dr represents the primary-air-ratio analogous to the differential scatter-air-ratio.

The use of primary-air-ratio requires an extended set of TARs with values for small field sizes; smaller than the smallest measured. TARs for such very small field sizes were calculated by dividing the dose in a phantom with collision KERMA (instead of the dose in air) by means of Monte Carlo techniques. With this *extended set* of TARs, the primary component can be calculated in a similar fashion to the scattered photon component; namely using a sector integration technique. These changes have been introduced in the derivation of the

ETAR inhomogeneity correction factor to incorporate electron transport modelling. The effective TAR in the medium ($TAR(d', \tilde{r})$) is calculated using the radiological pathlength d' and field radius $\tilde{r}$ scaled with the weighted average density. Weighted average density values $\tilde{\rho}$ were obtained from the known coalescing procedure (equation (2.17)). If $\tilde{r}$ is very small, between zero and the smallest radius for which measured data exist, then the TAR is looked up from the extended TAR table for small radii. In any other case, a measured TAR value is used. The density scaling of primary-air-ratios for accounting for electron transport in non water-like homogeneous media can be thought of as a first order approximation, considering that electron stopping powers are approximately linearly proportional to the electron density of the medium. The second modification introduced in this work was to replace the weighting factors with a set of pre-generated factors, stored for each beam energy, which account for once and multiply scattered photons separately.

These changes have been tested against measured and Monte Carlo generated data at beam boundaries and at interfaces of inhomogeneities and the accuracy achieved is reported to be better than 2%. The use of such an extended TAR data table would allow electron transport modelling to be also incorporated in other inhomogeneity correction algorithms such as power-law (Batho) and the Ratio of TARs (RTAR) methods. Some limitations imposed by ETAR are still present, such as the erroneous assumption of the presence of only water-like material between photon interaction and dose deposition sites and the inaccurate modelling of dose at the surface where electron contamination is not taken into account.

Implementation of ETAR using Fast Fourier Transform (FFT)

It has been noticed [Yu and Wong, 1993a] that equation (2.13) which represents the weighted average electron density at the point of calculation used for scaling the field size in ETAR, can be expressed as a convolution of the density matrix and the weighting factor matrix:

$$\tilde{\rho}(l,m,n) = \frac{\sum_i \sum_j \sum_k \rho(i,j,k) W(l-i, m-j, n-k)}{\sum_i \sum_j \sum_k \rho_o(i,j,k) W(l,m,n)} \tag{2.30}$$

Here, $\rho_o(i,j,k)$ is the density matrix of homogeneous water of the same size as $\rho(i,j,k)$. This expression can be evaluated using Discrete Fourier Transform (DFT) and circular convolution. Therefore, the three dimensional distribution of weighted average density is calculated by obtaining the Fourier Transform of the

density matrix and the weighting factor matrix, followed by their multiplication in the frequency domain and finally the inverse transformation of their product. The practical implementation of this 3D ETAR requires that the dimensionality of the FFT matrices be kept as small as possible and that the symmetry properties of FFT be used thereby halving the 3D DFT calculation matrix. Memory requirements were minimised by allowing different arrays to share the same real matrix. The calculation of a 48x48x48 density matrix of 0.5cm resolution required 1.2 Mbyte of memory and was completed within 22 seconds. The reduction in calculation time is significant; about 68 times faster than the original ETAR.

This version of ETAR improves the speed of calculation of the original implementation but no consideration has been given towards the model's inherent limitations, all of which have been mentioned in previous sections. The only exception here, is the use of weighting factors which were derived from Monte Carlo generated data. Such data include information on electron transport and therefore the use of these weighting factors is expected to perform with improved accuracy in high energy photon dose calculations.

Following the publication on the FFT implementation of ETAR, the authors proposed correcting the inability of the model to include the effects of primary intensity changes on scatter contributions, by introducing the concept of *primary fluence scaled density* [Yu and Wong, 1993b]. This idea is based on the fact that for scatter dose contributions, changes in primary photon fluence to a voxel are equivalent to changes in voxel density. This seems to be essentially what Redpath and Thwaites [Redpath and Thwaites, 1991] formulated in equation (2.27). Details on the implementation in full 3D and the performance of the modified model have not been published yet.

2.3.3 The FFT Convolution Method

FFT Convolution

The dose calculation methods described up to now use measured data in water and correct semi-empirically the dose for the presence of inhomogeneities. Their sophistication varies according to the amount of density information they use. Within the last decade, new approaches have been developed known as *convolution models*. In these models, the energy deposited in a homogeneous medium is obtained by convolving the primary photon fluence (or energy) released at an interaction site with an energy deposition kernel [Dean, 1980], [Mackie, 1983], which describes how this primary energy is distributed around that site. Imple-

mentations of these ideas are discussed in detail in the next chapter because they generally employ explicit ray-tracing procedures for scattered photons. Here, only the FFT convolution method [Boyer and Mok, 1986] will be presented in some detail. Boyer and Mok have shown in an elegant way how dose can be calculated from convolving primary fluence and kerma kernels. However, FFT convolution is a non scatter ray-trace method, due to the approximations it employs in the calculation of dose originating from scattered photons.

A convolution dose calculation is expressed by the following integral:

$$D(\bar{r}) = \int\int\int_{V'} \Phi(\bar{r}')k(\bar{r} - \bar{r}')dV' \tag{2.31}$$

where $\Phi(\bar{r}')$ is the photon fluence distribution and $k(\bar{r})$ is the interaction kernel. Convolution in the frequency domain requires the Fourier Transforms of $\Phi(\bar{r}')$, $k(\bar{r})$, which can be written as:

$$P(\omega) = \mathcal{F}\{\Phi(\bar{r})\} \tag{2.32}$$

$$H(\omega) = \mathcal{F}\{k(\bar{r})\} \tag{2.33}$$

According to the convolution theorem, the Fast Fourier Transform $T(\omega)$ of $D(\bar{r})$ can be computed by

$$\mathcal{F}\{D(\bar{r})\} = \mathcal{F}\{\Phi(\bar{r})\} \cdot \mathcal{F}\{k(\bar{r})\} \tag{2.34}$$

or

$$T(\omega) = P(\omega) \cdot H(\omega) \tag{2.35}$$

and to obtain the dose one simply takes the inverse transform of $T(\omega)$:

$$D(\bar{r}) = \mathcal{F}^{-1}\{T(\omega)\} = \mathcal{F}^{-1}\{P(\omega) \cdot H(\omega)\} \tag{2.36}$$

Details of dose calculation

The convolution method proposed by Boyer and Mok is an analytic approach based on convolving kerma (the Kinetic Energy Released by primary photon interactions per unit MAss; namely the energy imparted to charged particles) with a kerma deposition kernel. Dose at a point is due to kerma deposited by primary, first scattered and multiply scattered photon fluences. This method involves the separate convolution of the different scattering orders of photon fluences together with the appropriate kerma kernels. Especially in homogeneous media, Boyer and Mok showed that these separate convolutions can be reduced to

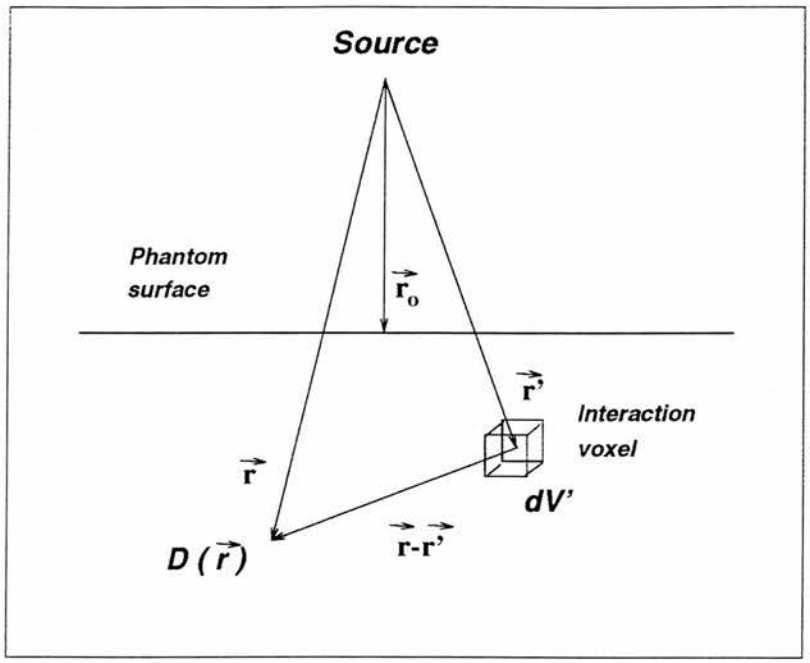

Figure 2.2: *Convolution scheme*

one single convolution between primary photon fluence and a total kerma kernel [Boyer and Mok, 1985]. The main assumptions in this model are:

- The medium is assumed to have infinite extent, because kernels have *no sense* of boundaries (this is discussed further in the next chapter).
- The kerma kernels must be kept spatially invariant so that FFT convolution can be employed.
- The patient is taken to be water-equivalent; any changes in atomic number are ignored.
- All incident photons are monoenergetic.
- The source of incident primary photons is at infinite SSD (no beam divergence taken into account).

To model dose from a polyenergetic beam, convolution must be carried out separately for each spectral component and the results are added to give the total dose in the medium. Kerma deposition kernels are calculated analytically for a water medium and are different for primary, first scattered and multiply scattered photons. Dose calculations in a homogeneous water medium allow convolution

to be performed in Fourier space because the kernels remain spatially invariant throughout the calculation. In order to benefit from the increase in calculation speed with a FFT implementation, in inhomogeneous water-like media Boyer and Mok resorted to major assumptions regarding electron scatter originating from primary interactions and the density dependent attenuation of scattered photons.

Primary Dose. In Figure (2.2) primary photon fluence at $\bar{r}$ is given by

$$\Phi_p(\bar{r}) = \Phi(\bar{r}_o)(\frac{\bar{r}_o}{\bar{r}}^2)e^{-\int_{r_o}^{r}\frac{\mu}{\rho}(\bar{s})\rho(\bar{s})ds} \tag{2.37}$$

with $\Phi(\bar{r}_o)$ the photon fluence at the phantom surface $\bar{r}_o$, $\frac{\mu}{\rho}(\bar{s})$ the mass attenuation coefficient and $\rho(\bar{s})$ the physical density at distance $\bar{s}$ from the source. The kerma (in cGy) deposited by primary photon fluence is

$$K_p(\bar{r}) = c\ \Phi_p(\bar{r})\frac{\mu_{en}}{\rho}(E_o)E_o \tag{2.38}$$

where $\frac{\mu_{en}}{\rho}(E_o)$ is the mass absorption coefficient at energy E_o and c is a factor converting $MeVg^{-1}$ to cGy (equal to $1.602 \cdot 10^{-8}$). To model accurately electron transport around $\bar{r}$, Boyer and Mok introduced a dimensionless function $f(\bar{r}-\bar{r'})$, which describes the dose deposited at $\bar{r}$ by electrons set in motion at $\bar{r'}$. This factor is derived from Monte Carlo calculations. Therefore, primary dose in a homogeneous medium can be calculated from

$$D_p(\bar{r}) = \int\int\int_{V'} \Phi_p(\bar{r'})k_e(\bar{r}-\bar{r'})dV' \tag{2.39}$$

with kerma kernel (in $cGy \cdot cm^2$):

$$k_e(\bar{r}-\bar{r'}) = c\frac{\mu_{en}}{\rho}(E_o)E_o f(\bar{r}-\bar{r'}) \tag{2.40}$$

Equations (2.39) and (2.40) do not directly show the convolution of kerma with the electron transport kernel ($f(\bar{r}-\bar{r'})$). This can be recognised from equations (2.38) and (2.40).

In a heterogeneous medium, primary dose is calculated without using the electron transport factor $f(\bar{r}-\bar{r'})$. Instead, equations (2.39) and (2.40) are replaced with the following two expressions:

$$D_p(\bar{r}) = \int\int\int_{V'} \Phi_p(\bar{r'})\rho(\bar{r})k_p(\bar{r}-\bar{r'})dV' \tag{2.41}$$

$$k_p(\bar{r}-\bar{r'}) = \rho_{e,water}\frac{d\sigma'}{d\Omega'}(\bar{r}-\bar{r'})\frac{dE}{\rho dx}(\bar{r}-\bar{r'})\frac{1}{|\bar{r}-\bar{r'}|^2} \tag{2.42}$$

In equation (2.41) $\rho(\bar{r})$ is the relative electron density at the dose deposition site. In equation (2.42) $\rho_{e,water}$ is the electron density of water, and $d\sigma'/d\Omega'$ the differential scattering cross section for the electrons in the Compton interaction. Thus, in a heterogeneous medium, primary dose is obtained by convolving an electron density-weighted-primary fluence with a primary kernel $k_p(\bar{r}-\bar{r'})$, which does not take into account secondary electron scatter and density dependent attenuation. The cross section in (2.42) is not directly a function of the scattering angle but only of vector $(\bar{r}-\bar{r'})$ and the mass stopping power $(dE/\rho dx)$ for electrons is only calculated at the end of $(\bar{r}-\bar{r'})$. The density variation along $(\bar{r}-\bar{r'})$ is not considered for the attenuation of particles along $(\bar{r}-\bar{r'})$.

Dose from first scattered photons. First scattered photon fluence is calculated from primary photon fluence and in a homogeneous medium is given by:

$$\Phi_s(\bar{r}) = \int\int\int_{V'} \Phi_p(\bar{r'}) \frac{1}{|\bar{r}-\bar{r'}|^2} \rho_{e,water}\rho(\bar{r'}) \frac{d\sigma}{d\Omega}(\bar{r}-\bar{r'}) e^{-\mu'|\bar{r}-\bar{r'}|} dV' \qquad (2.43)$$

where μ' is the linear attenuation coefficient for the energy of the scattered photons. Kerma due to first scattered photon fluence is given by:

$$K_s(\bar{r}) = \Phi_s(\bar{r}) \frac{\mu_{en}}{\rho}(E_s) E_s c \qquad (2.44)$$

Combining (2.43) and (2.44) one has

$$K_s(\bar{r}) = \int\int\int_{V'} \Phi_p(\bar{r'}) k_s(\bar{r}-\bar{r'}) dV' \qquad (2.45)$$

using the primary photon fluence at $\bar{r'}$, and the first scatter kerma kernel which is given by

$$k_s(\bar{r'}) = c\rho_e \frac{d\sigma}{d\Omega}(\bar{r'}) \frac{e^{-\mu'|\bar{r'}|}}{r'^2} \frac{\mu'_{en}}{\rho}(E_s(\bar{r'})) E_s(\bar{r'}) \qquad (2.46)$$

In a homogeneous medium, to calculate the dose from first scattered photons Boyer and Mok assumed that first scatter kerma is deposited exactly where it is released, thus excluding electron transport :

$$D_s(\bar{r}) = K_s(\bar{r}) = \int\int\int_{V'} \Phi_p(\bar{r'}) k_s(\bar{r}-\bar{r'}) dV' \qquad (2.47)$$

Contributions to dose from first scattered photons in an inhomogeneous medium involve further simplifications than those incorporated in equation (2.47). First

scattered photon fluence is now given by an expression similar to (2.43) involving an electron density-weighted primary fluence and a space variant exponential term [Boyer and Mok, 1986]. Expanding this expression in a Taylor series and neglecting the higher order terms, the following expression was obtained:

$$\begin{aligned}\Phi_s(\bar{r}) &= \int\int\int_{V'} \Phi_p(\bar{r'})\rho(\bar{r'})\rho_e \frac{d\sigma}{d\Omega}(\bar{r}-\bar{r'})\frac{e^{\mu'|\bar{r}-\bar{r'}|}}{|\bar{r}-\bar{r'}|^2}dV' \\ &+ \int\int\int_{V'} \Phi_p(\bar{r'})\rho(\bar{r'})[1-\rho(\bar{r'})]\rho_e \frac{d\sigma}{d\Omega}(\bar{r}-\bar{r'})\frac{e^{-\mu'|\bar{r}-\bar{r'}|}}{|\bar{r}-\bar{r'}|^2}\mu'|\bar{r}-\bar{r'}|dV' \quad (2.48)\end{aligned}$$

The first part of (2.48) originates from the zero-order term of the Taylor expansion series and mainly accounts for the presence of heterogeneities along primary fluence $\Phi_p(\bar{r'})$. The second part is from the second term in the Taylor series and corrects for inter-voxel attenuation. Using (2.48) and assuming that first-scatter kerma is deposited at its site of origin, dose from first scattered photons in an inhomogeneous medium is given by the sum of two convolutions:

$$D_s(\bar{r}) = D_s^o(\bar{r}) + D_s^c(\bar{r}) \quad (2.49)$$

corresponding to the zero and first order terms in the Taylor series:

$$D_s^o(\bar{r}) = K_s^o(\bar{r}) = \int\int\int_{V'} \Phi_p(\bar{r'})\rho(\bar{r'})k_s^o(\bar{r}-\bar{r'})dV' \quad (2.50)$$

and

$$D_s^c(\bar{r}) = K_s^c(\bar{r}) = \int\int\int_{V'} \Phi_p(\bar{r'})\rho(\bar{r'})(1-\rho(\bar{r'}))k_s^c(\bar{r}-\bar{r'})dV' \quad (2.51)$$

$k_s^o(\bar{r}-\bar{r'})$ in equation (2.50) is the first scatter kernel as computed for the homogeneous case (equation (2.46)) and $k_s^c(\bar{r}-\bar{r'})$ is a correction kernel, actually equal to $|\bar{r'}|\mu'(\bar{r'})k_s^o(\bar{r}-\bar{r'})$, convolved with the $(1-\rho(\bar{r'}))$ fraction of the electron-density-weighted primary fluence $(\rho(\bar{r'})\Phi_p(\bar{r'}))$.

Dose from multiply scattered photons. To model multiple (higher order) scattering, Boyer and Mok assumed that multiply scattered photon fluence is more or less isotropic, therefore multiple scattering to be modelled as a *steady-state diffusion process* described by a Helmholtz equation:

$$D\nabla^2\Phi_m(\bar{r}) - \mu''_{en}\Phi_m(\bar{r}) + \tilde{\Phi}_m(\bar{r}) = 0 \quad (2.52)$$

D is the diffusion coefficient and $\tilde{\Phi}_m(\bar{r})$ is a source distribution function equal to the number of photons per cm^2 entering the higher order scattering distribution from a once scattered photon fluence distribution. If one also assumes that multiple scatter kerma is carried away only by very low energy electrons (E_{avg}) that deposit their energy locally, then the multiply scattered photon dose component in a homogeneous medium is given by:

$$D_m(\bar{r}) = K_m(\bar{r}) = \int\int\int_{V'} \tilde{\Phi}_m(\bar{r'}) k_m(\bar{r} - \bar{r'}) dV' \tag{2.53}$$

with

$$k_m(\bar{r} - \bar{r'}) = c \frac{e^{-\frac{|\bar{r}-\bar{r'}|}{L(E_{avg})}}}{4mD(E_{avg})|\bar{r} - \bar{r'}|} \frac{\mu''_{en}}{\rho}(E_{avg}) E_{avg} \tag{2.54}$$

where L is a diffusion length. In the case of a homogeneous medium, the multiply scattered photon fluence source $\tilde{\Phi}_m(\bar{r})$ can be expressed as a convolution of primary fluence and a multiple scatter source kernel and equation (2.53) can be rewritten as a convolution of primary fluence with a composite kernel:

$$D_m(\bar{r}) = \int\int\int_{V'} \Phi_p(\bar{r'}) k_{sm}(\bar{r} - \bar{r'}) dV' \tag{2.55}$$

Dose from multiply scattered photons in an inhomogeneous medium is modelled in the same fashion as in the homogeneous case using a diffusion equation. However, it is not possible in this case to represent the dose as a convolution of primary fluence with a composite kernel $k_{sm}(\bar{r})$ as can be done for the homogeneous case. For a homogeneous phantom a total kerma kernel $k_t(\bar{r})$ can be derived simply using equations (2.39), (2.47) and (2.55):

$$k_t(\bar{r}) = k_e(\bar{r}) + k_s(\bar{r}) + k_{sm}(\bar{r}) \tag{2.56}$$

and therefore dose is calculated from:

$$D(\bar{r}) = \int\int\int_{V} \Phi_p(\bar{r'}) k_t(\bar{r} - \bar{r'}) dV' \tag{2.57}$$

In a heterogeneous medium one can only perform three separate convolutions for each dose component [Boyer and Mok, 1986].

Performance

Boyer *et al* [Boyer et al., 1988] compared convolution algorithms which employed fast ray-tracing procedures, as suggested by Siddon [Siddon, 1985], ray-tracing

look-up tables and FFT-convolution techniques. Their findings, which were dependent on the array sizes examined, show that fast ray-tracing is slower than the table look-up method by a factor of 4 to 5.5. The time required to perform a convolution calculation varied linearly with the square of the calculation matrix size. The use of FFT results in an increase in speed proportional to $NlnN$ with N being the total number of voxels in the matrix. It was further suggested that the benefit of using FFT increases with array size. Comparisons with measurements [Zhu and Boyer, 1990] have shown errors up to 7% in dose calculations at sharp density discontinuities. These errors are attributed to several factors, namely: the omission of density corrections for electrons emerging from primary photon interactions, linear scaling only of first scattered photon contributions with density at the interaction site and the first order Taylor expansion approximation of multiply scattered photon attenuation assuming the densities along photon paths to be the same as those at the initial scatter site. Central axis measurements have been shown to agree with measured data up to 1%. Although the performance of this method was hopeful when used for calculations involving multileaf collimation [Zhu et al., 1992], its simplicity in modelling scattered photon dose should be further examined and justified; as may be appreciated from the arbitrary changes in the multiple scattered photon dose component by weighting primary photon fluence with electron density [Zhu and Boyer, 1990].

2.3.4 Volume integration of Differential Scatter-Air Ratios (DSAR)

Description of the DSAR model

All 3-D scatter ray-trace methods can be considered as descendants of the differential Scatter-Air Ratio method introduced by Beaudoin [Beaudoin, 1968]. Differential Scatter Air Ratios (dSARs) describe the total relative amount of scattered radiation reaching a point from surrounding volume elements in water. $SAR(d, r_d)$, describe the relative amount of scattered radiation arriving at a point at depth d along the axis of a cylindrical beam of radius r_d at depth d, which is normally incident on a water medium. Cunningham [Cunningham, 1972] initially showed how Scatter-Air Ratios (SARs) are derived from Tissue-Air Ratios (TARs) and further how the former can be differentiated to give dSARs.

The integration of dSARs over the entire irradiated volume was first implemented by Beaudoin and later by Larson and Prasad [Larson and Prasad, 1978]. The dose at a point in a homogeneous water medium is calculated from:

$$D = D_A(d)[TAR(d,0) + SAR(d,r)] \tag{2.58}$$

where $D_A(d)$ the dose in air at that point (in the absence of the phantom). The scatter-air ratio $SAR(d,r)$ describes the absorbed dose due to all orders of scattered radiation (once-scattered and multiply scattered photons). According to Cunningham's theory [Cunningham, 1972] $SAR(d,r)$ in equation (2.58) can be replaced by the following integration

$$SAR(d,r) = \int_{\theta=0}^{2\pi}\int_{z=-\infty}^{d}\int_{r=0}^{r}(\frac{\Delta S}{\Delta V}_{water})rdrdzd\theta \tag{2.59}$$

where $(\frac{\Delta S}{\Delta V}_{water})$ is the differential scatter-air ratio in water for volume element ΔV. It was shown that dSAR in water is calculated from

$$\begin{aligned}(\frac{\Delta S}{\Delta V})_{water} = \frac{\bar{\Delta}^3 S}{r\Delta\theta\Delta r\Delta z} &= \frac{TAR(d,0)}{2\pi r\Delta r\Delta z}[\frac{SAR(z,r) - SAR(z,r-\Delta r)}{TAR(z,0)} \\ &- \frac{SAR(z-\Delta z,r) - SAR(z-\Delta z,r-\Delta r)}{TAR(z-\Delta z,0)}]\end{aligned} \tag{2.60}$$

To calculate the dose at a point in an inhomogeneous medium, equation (2.60) is modified to account for the changes in the primary and scatter component due to the presence of non unit-density inhomogeneities in the irradiated volume. TARs are modified to account for changes in primary due to relative electron density variations along the path between the source and the calculation point. Therefore, primary dose is calculated from table look up of TARs at the effective depth. SARs are modified according to:

(a) the nature (i.e. relative electron density) of each scattering volume,

(b) the variations in the primary photon fluence along the path between the source and the scattering element, and

(c) the difference in the attenuation of the secondary photon fluence between the scattering volume and the point of dose calculation.

Consequently, the amount of scatter $(\frac{\Delta S}{\Delta V})_{medium}$ reaching a point $P(x,y,z)$ in an inhomogeneous medium from a volume element ΔV at (x',y',z') is expressed as:

$$(\frac{\Delta S}{\Delta V})_{medium} = (\frac{\Delta S}{\Delta V})_{water}\frac{\rho_e(x',y',z')}{\rho_{e,water}}f_1(x',y',z')f_2(x',y',z') \tag{2.61}$$

where $\rho_e(x', y', z')/\rho_{e,water}$ is the electron density relative to water at the scattering site, f_1 is a factor describing the attenuation of the beam relative to water between source and volume element ΔV and f_2 a factor describing the attenuation of secondary photon fluence relative to water along the path between ΔV and dose calculation point. Factors f_1 and f_2 are calculated from expressions of the following form:

$$f_i(x', y', z') = e^{-\sigma(E_i)\int_{R_i}[\rho_e(\bar{r})-\rho_{e,w}]dl} \tag{2.62}$$

with $\sigma(E_i)$ the total Klein-Nishina electronic collision cross section for an incident photon energy E_i, $\rho_e(\bar{r})$ the electron density at vector point $\bar{r}$, $\rho_{e,water}$ the electron density of water and dl a path element along ray R_i. Equation (2.62) can be used for the calculation of factor f_2, that is if the electron density along the path of scattered photons is known and if the average energy of scattered radiation is assumed.

Analogous to equation (2.59), the total scatter-air ratio in the inhomogeneous medium is expressed as

$$SAR(d, R) = \int_{\theta=0}^{2\pi}\int_{z=0}^{d}\int_{r=0}^{R(\theta)}(\frac{\Delta S}{\Delta V})_{water}\frac{\rho_e(x', y', z')}{\rho_{e,w}}f_1(x', y', z')f_2(x', y', z')rdrdzd\theta \tag{2.63}$$

Performance

The DSAR method calculates dose with an accuracy of $\pm 2\%$ in simple heterogeneous geometries [Cunningham and Beaudoin, 1973],[Larson and Prasad, 1978] and can also model beam modifiers and irregular fields. Although it employs explicit 3D scatter ray-trace procedures, (a *genuine* 3D dose calculation model), and measured SARs to represent the overall scattering strength of a voxel, it has been shown that it is inaccurate when modelling the irradiation of a heterogeneous phantom with large field sizes and at low energies[Sontag, 1979]. This is because a first scatter ray-trace model is incompatible with the use of SAR data which implicitly contain contributions from multiply scattered photons [Cunningham, 1972]. In addition, as seen from equation (2.63), DSAR calculates the scatter component of dose at a point by simply adding scatter contributions from individual volume elements surrounding that point. The assumption of individual inhomogeneities acting independently and not synergistically has been proved inaccurate [Wong et al., 1981b]. When considering the

influence on the dose at a site with many small inhomogeneities (such as individual voxels in a CT array), the inhomogeneity correction algorithm must account for their mutual effects. If not, these are inferior to simplistic methods (i.e. the power-law method) when calculating dose in homogeneous non-unit density medium [Henkelman and Wong, 1981], [Wong and Purdy, 1990]. The performance of DSAR at energies higher than ^{60}Co has not been examined. It is expected that DSAR would not model dose accurately at higher energies, because at these energies photons cause secondary electrons to scatter at large distances from the interaction sites. This introduces difficulties in separating primary from scatter dose contributions using measured (extrapolated) zero area TAR and SAR respectively. An inherent limitation of the DSAR method is that backscatter is not modelled due to the difficulty in deriving explicit backscatter differential scatter-air ratios from TARs [Wong and Purdy, 1990].

2.3.5 The Delta Volume (DV) method

Larson and Prasad [Larson and Prasad, 1978] referred to their implementation of the DSAR method as the Delta Volume method due to the use of differential SARs from small (δv) volume elements. However, it is Wong and Henkelman's work which is widely known as the Delta Volume or Delta Volume II method [Wong and Henkelman, 1983], [Wong et al., 1984].

Wong *et al.* [Wong et al., 1981a] measured precisely, with specialised dosimetry apparatus and electronic instrumentation, the influence of an individual voxel on dose at a point from a Co-60 beam. An air cavity was created in a small water phantom and the associated small change in dose at a fixed point was measured and calculated analytically for various locations of the air cavity. The experiment revealed that the scattering of radiation with heterogeneous tissues could not be considered a linear process. Therefore, the inhomogeneity problem, as understood by Wong and Henkelman [Wong and Henkelman, 1983], relies on fulfilling two requirements. Dose calculation algorithms designed to give accurate results must approximate well the dose at a point in two specific geometries. These are:

1. A homogeneous water medium with a small void.

2. A homogeneous non-water medium.

Inhomogeneity correction methods (except the FFT convolution method) which use CT-based density information, fail to satisfy these two geometrical requirements. Power-law is incapable of satisfying condition (1) and adequately ap-

proximates (2); ETAR fails altogether in (1),but is designed to model (2) (using O'Connor's density scaling theorem); DSAR only approximates condition (1) and poorly accounts for (2). The DV method purported to fulfill the above requirements in addition to improving the modelling of dose from scattered photons, contrary to DSAR where all scattered photons are taken to behave as once scattered. DV was the first method to utilise theoretical dose input data.

Description of DV method

Dose at a point in a heterogeneous medium is calculated as a sum of the primary dose, an augmented first-scatter dose component and an approximate residual multiple-scatter component.

Relative primary dose is obtained similarly to the DSAR method from the knowledge of the primary intensity in air and the density along the path of the primary photons.

The calculation of the total-scatter component is the sum of the two components mentioned above. The philosophy behind scatter modelling has been well justified for a ^{60}Co beam. Wong *et al.* [Wong et al., 1981b] have studied the behaviour of second order scatter in a water medium and its contribution to dose using a semi-analytical approach for infinite field sizes and numerical integrations for beams with finite field size. They considered that, although the dose distribution from second-order scatter has similarities to that from first-order scattered photons, and predominantly originates above the calculation point, it is delivered by photons with energy less than the mean energy of once scattered photons. In addition, it is more diffuse than first-scatter, more isotropically distributed and less peaked in the forward direction. For these reasons and because photons from higher orders of scattering contribute significantly to dose at larger depths and field sizes, Wong *et al.* calculated the elemental scatter contribution to a point in a heterogeneous medium from the following expression:

$$\begin{aligned} \Delta S_i &= \rho_i[\Delta S_{1iwater} + \Delta S_{2iwater}^{small-angle}] f_{0i} f_{1i} \frac{\frac{\mu_{ab}}{\rho}_{(med)_i}}{\frac{\mu_{ab}}{\rho}_{(water)_i}} \\ &+ \frac{SAR_m(\bar{\rho}d, \bar{\rho}r)}{SAR_m(d,r)}[S_{mwater} + \sum \frac{\bar{\rho} - \rho_i}{\bar{\rho}} \Delta H_i] \end{aligned} \tag{2.64}$$

The first term in (2.64) is analogous to the DSAR method and calculates the first-scatter contribution. The augmented-first-scatter calculation in the heterogeneous medium is based on an explicit ray-tracing procedure. ρ_i is the relative

electron density of the scattering volume element ΔV_i, $\Delta S_{1i_{water}}$ corresponds to the contribution from once scattered photons in water equal to the differential Scatter-Air Ratio values and $\Delta S_{2i_{water}}^{small-angle}$ accounts for that part of second-order scatter which behaves as first-scatter. The latter was chosen to be equal to that amount of scatter dose originating from photons that had undergone a second order deflection through a small angle (less than 45°). The sum in the first parenthesis of the first term was precalculated and stored in a table of augmented-first-scatter contribution values for each volume element. Factor f_{0i} accounts for the attenuation of primary intensity from the surface to the scattering site. f_{1i} models the attenuation of first scatter in the medium and the ratio of the mass energy absorption coefficients at the dose calculation point accounts for the presence of non-water-like heterogeneities.

The second term of equation (2.64) approximates the residual multiple scatter dose component and resembles ETAR's density scaling of SAR's. In this term, $S_{m_{water}}$ represents the residual multiple-scatter dose in a homogeneous water medium and is obtained by subtracting the augmented first scatter dose from the total scatter dose given by SAR values. $\bar{\rho}$ is the mean electron density of the heterogeneous medium within the field of irradiation. ΔH_i is the residual multiple-scatter dose perturbation from a small void in volume ΔV_i. Empirical ΔH_i values are calculated as the differences of measured small dose perturbation values and from calculated augmented first scatter perturbation values in water. The measurements are taken on the central axis but are used for all points in the beam, since it has been shown that they do not vary strongly with field size or off-axis position [Wong, 1982]. It is assumed that ΔH_i (residual multiple scatter dose perturbation) values can be scaled with density $((\bar{\rho} - \rho_i)/\bar{\rho})$ and added together. This results in the total perturbation to the residual scatter dose which when added to the residual multiple scatter in water ($S_{m_{water}}$) gives the perturbed residual multiple scatter dose in a heterogeneous medium. The latter is described by the second parenthesis in equation (2.64) which ensures that constraint (1) (the effect of a small void on dose) is satisfied. The ratio of SAR's imposes the effect of non unit density heterogeneous media on the calculation of dose from multiply scattered photons, therefore ensuring that constraint (2) is satisfied.

Performance

The DV method succeeds in satisfying both constraints mentioned above, approximately calculates the multiple scatter dose component and since it is us-

ing augmented scatter values and multiple scatter perturbation values from each scattering element, it directly accounts for backscatter. It has been proposed and tested for ^{60}Co beam calculations, where all interactions are assumed to be Compton interactions and all incident photons monoenergetic. There has been no further work to improve the accuracy of the method at higher beam energies. It does not model the situation of electron disequilibrium, electron contamination at the surface or the influence on dose from heterogeneities with high atomic number.

Considerable efforts have been made to reduce the calculation time required for carrying out all scatter raytracing procedures. These efforts include employing pre-computed attenuation data, variable calculation grid for scattered photon dose [Rosenberger et al., 1984] and even the use of programmable array processors as part of the hardware system [Krippner et al., 1987]. The computational burden and the reliance on empirical data (not easily measured) have seriously impeded implementation in commercial treatment planning systems.

2.4 Summary and Conclusions

The following is a summary of the limitations present in 1D and 3D inhomogeneity correction models.

- Effective pathlength algorithms only model changes in the primary photon fluence.
- If all the enhancements on the power-law method were to be successfully incorporated in an *improved generalized power-law model*, the following can be summarised for this approach:
  - Scatter dose calculations are carried out empirically.
  - The application at energies higher than 6MV has not been examined in detail, therefore the performance of the model at these energies is questionable.
  - Contributions to dose at a point from backscattered radiation is not modelled.
  - Electron transport is not modelled.
  - Differences in atomic composition are not considered.

- The ENFD method performs better than the power-law method, especially at high energies and partly models electron transport. However, the method is limited by any restrictions in the the analytical formulations it employs and has not been widely tested.

- An *improved* ETAR model, incorporating the enhancements suggested by Woo *et al.* [Woo et al., 1990] and Yu and Wong [Yu and Wong, 1993a] has the following limitations:

  - Individual inhomogeneities are taken to act independently.
  - Electron contamination is not accounted for.
  - Variations in atomic number are not modelled.
  - True 3D implementations would be inefficient if the *coalescing procedure* is carried out for each calculation plane.
  - Dose calculations in regions with sharply varying contours such as in the head and neck, present difficulties for the *coalescing procedure.*
  - It is not yet clear how the concept of *primary fluence scaled density* [Yu and Wong, 1993b] would improve the performance of ETAR when using beam modifiers.
  - Dose contributions from backscattered radiation are not modelled.

- The FFT convolution method is a *model-based* dose calculation method and not an inhomogeneity correction algorithm. Its major limitations are:

  - Primary dose in heterogeneous media is modelled approximately since secondary electron scatter and density dependent attenuation is not taken into account.
  - The implementation of FFT techniques require that kernel arrays remain spatially invariant, thus scatter contributions are modelled approximately.
  - As all *model-based* methods, FFT should be used in conjunction with appropriate head scatter models in order to improve dose agreement with measured data (especially at depths close to the phantom surface).
  - Media with variable atomic numbers are not considered in this method.

- The limitations related to the DSAR method are:

- Contributions to dose at a point from all orders of scattering are modelled in the same manner.
- Individual inhomogeneities are treated independently and their mutual effects are not considered.
- Electron transport is not modelled, but the use of an *extended set* of TARs as proposed by Woo *et al.* [Woo et al., 1990] would eliminate this deficiency.
- Contributions to dose from backscattered radiation are ignored.

• Electron transport can also be incorporated in the DV method following the recommendation of Woo *et al.* [Woo et al., 1990]. The remaining limitations of this approach are:

- The performance of the method at high energies remains to be demonstrated.
- The presense of high atomic number media is ignored.
- Electron contamination at the phantom surface is not modelled.
- The empirical input data required are not easily obtainable.

In conclusion, it is not surprising that ETAR is the only model to be implemented clinically. It requires measured data which can be easily acquired within the hospital, and it can be potentially possible to model well primary and scatter dose within acceptable time limits.

However, conformal therapy requires the calculation of dose from modulated beams of arbitrary field sizes and it is not clear whether ETAR can be successfully modified to model irregular field irradiations. The inability of ETAR to predict increases in scatter dose due to the presence of small cavities in the medium is also a problem which will not be easy to overcome. Although the development of Woo *et al.* [Woo et al., 1990] encourages the incorporation of electron transport in ETAR, this is not yet widely implemented and it is likely that it will increase computation times. The required tables of TARs for very small field sizes must be derived theoretically employing Monte Carlo methods. This requires that a large set of such data is generated for each photon beam at each radiotherapy centre. Such a task requires that physicists at each centre are familiar with Monte Carlo techniques, have the necessary hardware to perform such simulations and are confident with the implementation of their software. In addition, since electrons

do not travel in straight lines as first-scattered photons, the application of linear density scaling of *differential primary-air ratios* is not strictly accurate and will introduce inaccuracies especially at high energies and close to media interfaces. The approximations and limitations of ETAR impose the questions: is it possible to improve its performance sufficiently for use in 3D conformal treatment planning? and, how easy is it to analyse the performance of ETAR in complex irradiation geometries, to identify and remove those modelling deficiencies which introduce errors? The latter question also applies to all those dose calculation methods (exept the FFT approach) reviewed in previous sections. The use of limited amounts of measured data, or empirical data, the lack of electron transport modelling, the implementation of various assumptions regarding the dose contributions from scattered photons and procedures such as the *coalescing* approach, impose restrictions and lead to models that cannot be reliable in any arbitrary irradiation geometry. The need for more versatile and more accurate approaches is imperative. The next chapter reviews the latest advances (*state of the art*) in photon dose modelling.

Chapter 3

The Convolution/Superposition approach

3.1 The Superposition Principle

The superposition principle states that the response of a linear system due to several inputs simultaneously applied equals the sum of its responses to each input applied separately. This principle is widely used in physics or engineering applications, such as electrodynamics and image processing. In image processing, for example, the output of a linear system can be obtained from its impulse response (point spread function) and the input using the superposition principle.

3.2 Energy deposition kernels

A kernel is a blurring function whose integral over the domain of a distribution is finite and whose functional form is invariant to shifts of space (or time). In external beam radiotherapy, energy (or dose) deposition kernels (EDK) are three dimensional distributions of energy (or dose) analogous to the impulse response used in one-dimensional electrical circuit theory or the two dimensional point spread kernel used in optical or X-ray imaging theory. The magnitude of the primary photon impulse is the energy released at each interaction site, known as TERMA (Total Energy Released per unit MAss). Energy deposition kernels are categorised according to their irradiation geometry. Those which describe the pattern of energy deposited in an infinite medium around a primary photon interaction point are known as *Point Spread Functions* (PSF). *Pencil Beam* (PB) kernels describe the energy deposited in a semi-infinite medium from a point monodirectional beam; *planar spread functions* describe the energy deposited in

an infinite medium from primary interactions in a lateral plane; *rotated pencil kernels* describe the deposition of energy due to convergent irradiation of a rotationally symmetrical phantom [Ahnesjö, 1991], [Desobry et al., 1991]. Superposition photon dose calculation algorithms use point spread functions. Pencil beam convolution algorithms have been developed which employ pencil beam kernels.

The concept of EDK in external beam irradiation was first described by Roesch [Roesch, 1958]. They were referred to as *impulse functions* and were defined in order to relate KERMA at one point with absorbed dose at surrounding points. Impulse functions were also exploited for predicting the build-up portion of depth dose curves for higher energy x-ray beams [Johns et al., 1949]. Energy deposition kernels are invaluable tools to understand qualitative aspects of dose distributions from beams of various energies. Berger used Monte Carlo generated point spread functions to calculate dose from beta-emitting radionuclides [Berger, 1969], whereas Schoknecht used pencil beam kernels (also obtained from Monte Carlo calculations) to obtain the scattered dose distribution from low energy x-ray beams [Schoknecht, 1971a], [Schoknecht, 1971b]. More recently, Dean [Dean, 1980] used PSFs from 1.25 MeV gamma rays together with experimental data from LiF thermoluminescent dosimeters, for the calculation of the relative amount of scattered dose in the irradiated medium. The Monte Carlo method is the most common method employed for the calculation of EDKs within the last decade. Several groups have carried out such calculations and obtained arrays known as *dose spread arrays* [Mackie, 1984], [Mackie et al., 1985b], [Mackie et al., 1988a], *first collision kernels* [Chui, 1985] or *differential pencil beam kernels* [Mohan et al., 1986] and *point spread functions* [Ahnesjö et al., 1987], [Ahnesjö, 1991]. Scatter kernels obtained from Monte Carlo calculations were also fitted to analytical functions to simplify their implementation [Ahnesjö and Mackie, 1987]. On the other hand, Boyer and Mok derived analytical kernels (*kerma-kernels*) calculated from the knowledge of the Klein-Nishina formulation of the differential scattering cross section[Boyer and Mok, 1985]. Iwasaki used forward and backward spread functions to calculate primary dose and scattered photon dose. These functions were derived from measured data in water (differential scatter air ratios and differential backscatter factors) [Iwasaki and Ishito, 1984],[Iwasaki, 1985]. Kernels describing primary dose distribution, were also measured for a cobalt-60 beam in a specially designed spherical shell phantom [O'Connor and Malone, 1989]. Recently, pencil beam dose kernels were determined for 6 and 25 MV x rays by fitting ana-

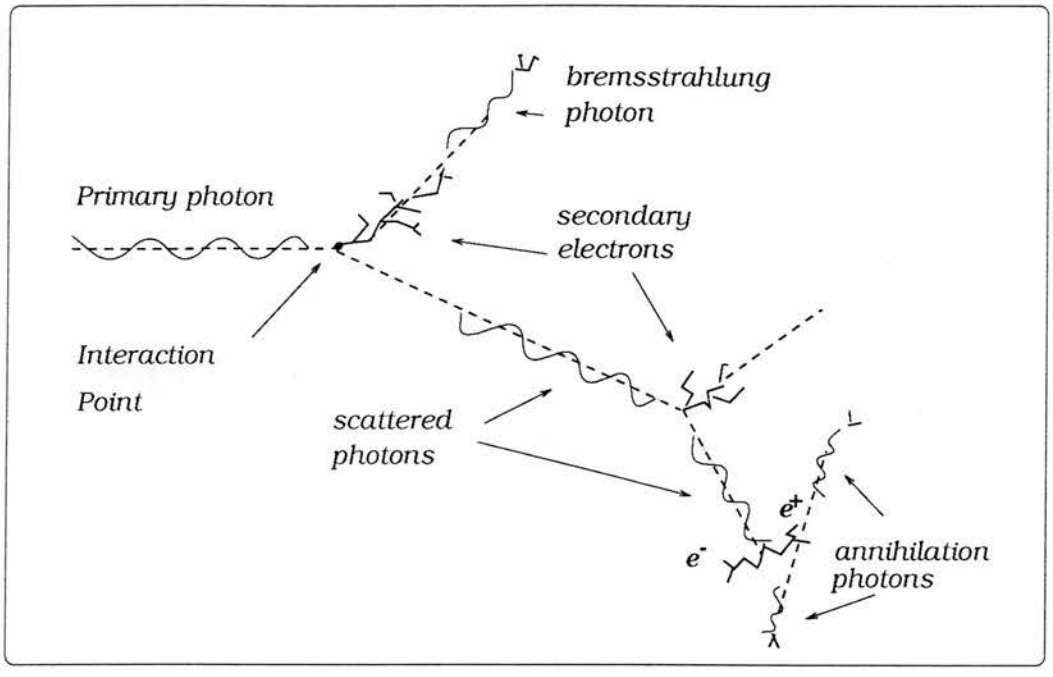

Figure 3.1: *Shower production.*

lytical models to quantities derived from broad beam data [Ceberg et al., 1996].

EDKs are calculated in a very large water medium, therefore they have *no sense* of medium boundaries, are considered *space invariant* and *non-divergent* (the trajectory of the primary photon is normal to the water-phantom surface). Kernels which are derived either by Monte Carlo methods or theoretically, are usually *monoenergetic.* Dose calculation algorithms in radiotherapy planning model x-ray beams from linear accelerators and interactions with the inhomogeneous patient geometry. Therefore in real situations, strict application of EDK is not possible and together with the time constraints imposed to achieve interactive treatment planning, several assumptions have to be employed for their implementation within a superposition algorithm.

In the following sections of this chapter, whenever EDKs are discussed the concept of PSFs is implied, unless stated otherwise. Figure (3.1) presents a shower of secondary radiations triggered at a point which experiences an impulse of primary radiation. The primary photon transfers its total energy to a Compton scattered photon and an electron. The electron, even having a relatively short range, liberates secondary electrons and bremsstrahlung photons. The scattered photon can travel a significant distance prior to interacting again. From this second Compton interaction the electron liberated slows down and deposits its energy in the medium, whereas the scattered photon interacts again further in

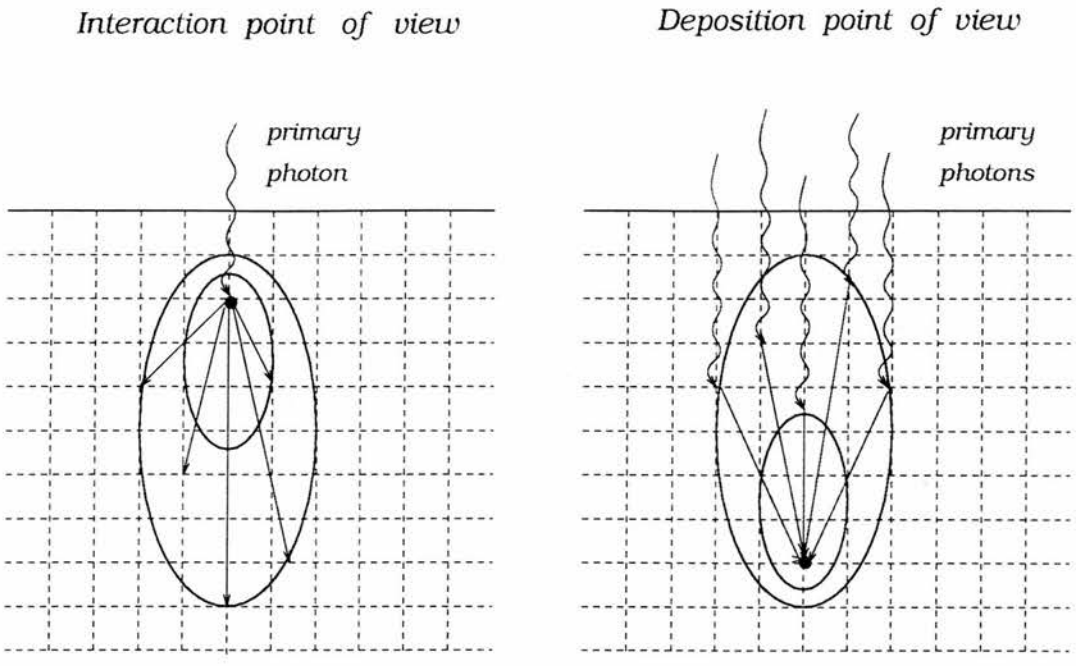

Figure 3.2: *The two different interpretations of the information carried out by EDKs according to the reciprocity principle.*

the medium with another Compton process. By keeping track of the origin of the photon (primary or scattered) which sets in motion the charged particle, different categories of EDKs can be produced. The distribution of energy due to the first secondary electron and its descendants is classified as *primary kernel.* All energy deposition which originates from the scattered photon represents the *total scatter kernel.* Total scatter kernels consist of the *first-scatter kernel,* which is essentially the energy deposited by secondary electrons emerging from the second Compton interaction. All energy deposited from the descendants of the second scattered photon are included into the *multiple-scatter kernel.* Energy deposited due to bremsstrahlung or annihilation processes can be categorised separately, but it is common practice to incorporate these in the multiple scatter kernel.

Direct experimental validation of EDK is not possible because one cannot force photon interactions to take place at a single location in an absorber. The measurements carried out by O'Connor and Malone [O'Connor and Malone, 1989] were converted to dose values around a photon interaction point by applying the reciprocity principle.

For the attenuation of any kind of radiation the reciprocity theorem states that *reversing the positions of a point detector and a point source within an infinite homogeneous medium does not change the amount of radiation detected*

[Attix, 1986]. The theorem holds strictly for regions of an infinite homogeneous material of constant mass density (*uniform isotropic medium*), in which radiation is absorbed without scatter or build-up (*uniform scatterless material.*). The above two conditions do not apply in the human body, but is was shown that *for soft tissue organ pairs in heterogeneous media, a reciprocity principle holds to an accuracy within 10% for most pairs* [Cristy, 1983]. The principle states that two regions in a human body containing the same total amount of uniformly distributed radioactivity, deliver to each other approximately the same specific absorbed dose fraction [1] [Loevinger, 1969]. Although the reciprocity principle was introduced for calculating organ dose due to internal isotopes, Mackie *et al.* applied this to the superposition of energy spread kernels with TERMA [Mackie et al., 1985b] (*dose deposition point of view approach*). This means that EDKs, as well as describing the energy deposited around a photon interaction site, also describe the distribution of interaction sites surrounding a dose calculation point. Due to this reciprocity, the comparison between theoretical energy spread kernels and measured *iso-fluence* curves was possible [Battista and Sharpe, 1992]. The reciprocity between photon interaction and dose deposition sites is schematically shown in Figure 3.2. The iso-curves illustrate the kernel.

3.3 The Superposition Method

In the superposition method, the dose at a point in water when irradiated by an x-ray beam, is calculated from the knowledge of the Total Energy Released per unit MAss (TERMA) and the distribution of the fractional mean energy imparted in small volumes around a single primary photon interaction site (PSF). This is expressed by:

$$D(\bar{r}) = \int\int\int\int T_E(\bar{s}) h_{\rho_o}(E, \bar{r} - \bar{s}) d^3s dE \tag{3.1}$$

Here, terma differential in energy T_E, is given by:

$$T_E(\bar{s}) = \frac{\mu}{\rho}(E, \bar{s}) E \Phi_E(\bar{s}) \tag{3.2}$$

where $\mu/\rho(E, \bar{s})$ is the mass attenuation coefficient of the primary photons of energy E at $\bar{s}$ and $\Phi_E(\bar{s})$ the photon fluence at $\bar{s}$ (Figure (3.3)):

[1] Absorbed fraction in target volume u which has absorbed energy from source region r, is defined as the energy absorbed in u from r, divided by the energy omitted by source region r. **Specific absorbed dose fraction** is the absorbed fraction per unit mass of target.

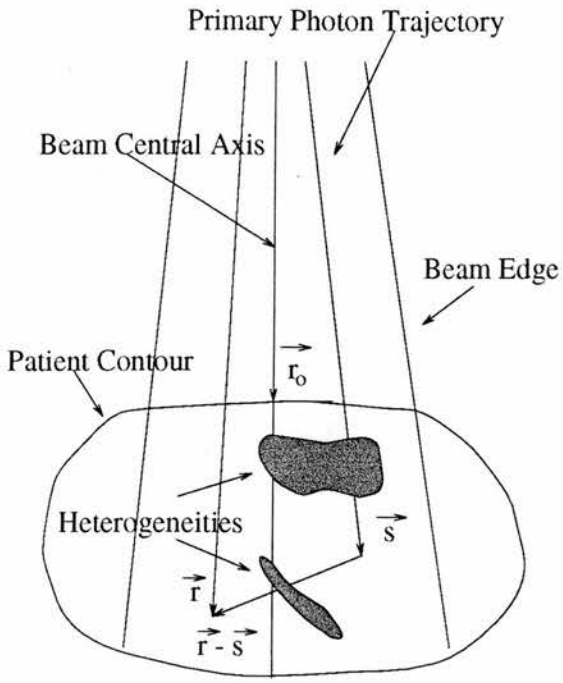

Figure 3.3: *Superposition geometry*

$$\Phi_E(\bar{s}) = \Phi_E(\bar{r_o})(\frac{r_o}{s})^2 e^{-\int_{r_o}^{s} \frac{\mu}{\rho}(E,\bar{l})\rho(\bar{l})dl} \tag{3.3}$$

$\Phi_E(\bar{r_o})$ is the primary photon fluence at a point $\bar{r_o}$ on a reference surface at the beam entrace and ρ is the density at points along the primary photon paths. The energy deposition kernel is defined in water (density ρ_o) as the fractional mean energy imparted in a small volume d^3r at $\bar{r}$ when a primary particle of energy E interacts at the origin $\bar{r} = 0$:

$$h_{\rho_o}(E,\bar{r}) = \frac{d\bar{\epsilon}(\bar{r})}{Ed^3r} \tag{3.4}$$

The conservation of energy requires the normalisation of the energy deposition kernel to be such that:

$$\int\int\int_{-\infty}^{\infty} h_{\rho_o}(\bar{r})d^3r \equiv 1 \tag{3.5}$$

In a heterogeneous medium with the same atomic composition as that of water and a density distribution $\rho(\bar{r})$, the energy deposition kernel is approximated by:

$$h(\bar{r}) \approx \frac{\rho(\bar{r})}{\rho_o} c^2(\bar{r}) h_{\rho_o}(c(\bar{r})\bar{r}) \tag{3.6}$$

where $c(\bar{r})$ is a spatially dependent scaling factor calculating the relative mean density along the line from the interaction site to the dose deposition site:

$$c(\bar{r}) = \frac{1}{\rho_o}\int_0^1 \rho(a\bar{r})da \tag{3.7}$$

a is a dimensionless variable ranging from 0 to 1. Therefore the dose at $\bar{r}$ in a non-uniform medium is approximated by

$$D(\bar{r}) = \int\int\int\int T_E(\bar{s})\frac{\rho(\bar{s})}{\rho_o}c^2(\bar{r},\bar{s})h_{\rho_o}(E, c(\bar{r},\bar{s})(\bar{r}-\bar{s}))d^3sdE \tag{3.8}$$

Here, $c(\bar{r},\bar{s})$ is calculated as $c(\bar{r})$ in equation (3.7) but replacing $a\bar{r}$ with $\bar{r}+a(\bar{s}-\bar{r})$.

3.4 Convolution/Superposition algorithms

The first implementation of this approach described the convolution of terma with a dose spread array [Mackie, 1984], [Mackie et al., 1985b]. Dose spread arrays were generated by a Monte Carlo code called MOCA, on a cartesian coordinate system. MOCA simulates all photons interactions, transports positrons as if they were electrons, employs continuous slowing down approximations and Gaussian lateral scattering for charged particles, and does not include bremsstrahlung. Primary, truncated first-scatter (TFS) and residual-first and multiple scatter (RFMS) dose spread arrays were scored separately in a cartesian geometry. Using the reciprocity principle, equation (3.1) was implemented in two ways: from the interaction point of view and from the dose deposition point of view. From the *interaction point of view*, the dose spread array contributions $h(\Delta i, \Delta j, \Delta k)$ to the entire phantom were summed over all interaction voxels (i, j, k):

$$D(i+\Delta i, j+\Delta j, k+\Delta k) = \sum_i\sum_j\sum_k T(i,j,k)h(\Delta i, \Delta j, \Delta k) \tag{3.9}$$

In this implementation, each interaction site is considered consecutively and in order to calculate the dose at a point, the convolution must be performed for the whole of the irradiated volume. In the *dose deposition point of view* implementation, the dose at voxel (i, j, k) is calculated from:

$$D(i,j,k) = \sum_{\Delta i}\sum_{\Delta j}\sum_{\Delta k} T(i-\Delta i, j-\Delta j, k-\Delta k)h(\Delta i, \Delta j, \Delta k) \tag{3.10}$$

Here, the kernel is simply *inverted* to represent the spread of interaction sites surrounding the dose calculation point (see Figure 3.2). This approach permits

the calculation of dose at a single point, without the requirement to perform convolutions at all interaction sites in the irradiated volume.

The next group to develop a superposition model used energy spread kernels known as differential pencil beams [Chui, 1985], [Mohan et al., 1986]. Differential pencil beams are defined as the fraction of a pencil beam of photons which has its first collision in a small volume surrounding a given point in water. These arrays were generated using the EGS4 Monte Carlo code [Nelson et al., 1985] on a spherical coordinate system whose origin was the point of first photon collision. The grid intervals in both radius and polar angle were chosen to follow the functional dependence of dose. Close to the origin, the intervals were chosen to be small, whereas they were set larger at distances further away from the interaction point. Differential pencil beams were not separated into components originating from different photon scattering orders. A discussion and a comparison between the dose spread array and the differential pencil beam models can be found in the literature [Mohan, 1987a].

Energy deposition kernels, named point spread functions, were also scored in voxels of cylindrical geometry in water [Ahnesjö et al., 1987]. It is in this work, that the quantity of TERMA was first clearly defined.

These three pioneering implementations of the superposition method have laid the foundations for further developments and initiated many continuing efforts within the last decade towards true three dimensional photon dose calculations employing the convolution/superposition principle. Energy deposition kernels are space invariant arrays, but, as seen from equations (3.6) and (3.8) their implementation requires the distortion of their size and shape according to density variations (equation (3.7)) within the irradiated region. The considerations that impose approximations to the superposition model are:

- The patient : Heterogeneous medium of finite extent.
- The x-ray source.
- Time constraints imposed to achieve interactive treatment planning.

The following sections will discuss these considerations and present studies carried out in order to overcome the related limitations.

3.4.1 Finite extent and tissue inhomogeneous nature of the patient

The energy deposition kernels calculated with the Monte Carlo method and used in most superposition algorithms were obtained by forcing a primary photon to interact at the centre of a very large water phantom (i.e. a sphere of $60cm$ radius) [Mackie et al., 1988a]. Therefore, these kernels have *no sense* of phantom boundaries and it is assumed that energy is conserved (equation (3.5)). The total fraction of incident photon energy deposited in the sphere was calculated for all kernels of different energies and was close to unity.

Direct superposition calculation does not account for the absence of forward scattering at the surface or the absence of backscattering at the exit surface. Ahnesjö compared dose distributions from a ^{60}Co beam, which were calculated using two different kernels [Ahnesjö, 1987]. One kernel was generated with the interaction point at the centre of the phantom and the other was constructed as the combination of two kernels. The combined kernel was composed of a kernel generated with the interaction point at the entrace surface and a kernel with the interaction at the exit surface. The difference between the two depth doses was shown to be significant only at small depths and for large field sizes, with a maximum difference of 1.6% in the build-up region and an overall difference of 0.2%.

A more detailed investigation of photon beam exit dose was carried out for ^{60}Co and 24MV beams by Woo [Woo, 1994]. This work confirmed the findings of Mohan *et al.* [Mohan et al., 1985] that a convolution calculation using an invariant kernel underestimates the dose decrease at the exit surface. This was attributed to the reduction of backscatter not being accounted for. The error was found to be smaller for the 24MV beam but increased with increasing field size. The use of pre-generated inhomogeneous kernels was suggested for accurate dose calculations at phantom boundaries.

The density problem

The patient is an inhomogeneous medium with regions which differ in electron density and atomic number. Superposition algorithms account for the presence of inhomogeneities with densities different to the density of water by calculating terma along divergent radiological beam paths and by scaling energy deposition kernels with density. The calculation of terma involves a ray-tracing procedure through voxels in the patient's CT density array [Siddon, 1985]. This is equivalent

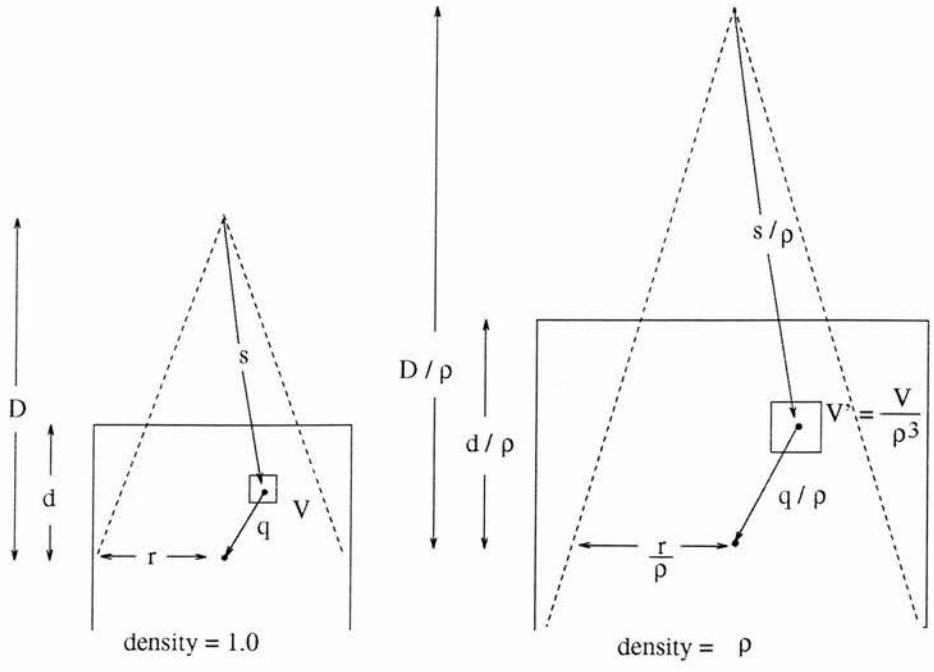

Figure 3.4: *The density scaling theorem relates the dose in a homogeneous unit density medium to that in a homogeneous, non-unit density medium.*

to the primary intensity calculations carried out in most one dimensional models. Scaling energy deposition kernels with density (or atomic number) variations between the energy release and energy deposition sites is not trivial.

The density scaling theorem. The theoretical justification of density scaling is based on the density scaling theorem formulated by O'Connor [O'Connor, 1957]. This theorem states that *the ratio of the fluence of secondary particles to that of primary particles, caused by an external source irradiating a medium in a collimated beam, is the same in two uniform media of the same composition but different density, provided geometrical distances are scaled inversely to density.* Essentially, this means that dose at points which occupy the same relative position in the two media of different density is the same. An illustration of the density scaling theorem is in Figure 3.4.

The theorem was originally developed for photon transport but was later extended to electron transport [O'Connor, 1984]. Woo and Cunningham examined the validity of this extension and found that rectilinear density scaling of secondary electron transport (i.e. primary kernels) is not accurate [Woo and Cunningham, 1990]. Their analysis showed that dose is overestimated immediately beyond air gaps and backscatter is, in general, underestimated. It

was also pointed out that although in regions where dose is greatly affected by inhomogeneities, density scaling of kernels is not so accurate, in other regions it is an acceptable approximation. Equations (3.6) and (3.7) present mathematically how density scaling of energy deposition kernels is carried out.

Scaling primary dose. As already mentioned, rectilinear density scaling of primary kernels does not model the curved path of multiply scattered secondary electrons, but considers electron paths as straight-ahead elongations. This means, that no account is taken of the perturbation in the electron fluence which occurs due to changes in the lateral deflection caused by scattering. The following two groups have worked towards improving the density scaling procedure of primary kernels by employing the Fermi-Eyges electron-scattering theory. In both cases, the calculation of primary is carried out with the improved method, whereas the scattered dose is obtained using rectilinear density scaling. Both methods are aimed at improving the performance of superposition in terms of accuracy, but are known to increase considerably calculation time.

Yu *et al.* [Yu et al., 1995] proposed replacing the primary photon beam as a source of many electron beams which are transported layer by layer. Their method, which is known as the *photon-electron cascade model*, takes into account in the calculation the scattering properties of different materials and therefore is applicable for media containing inhomogeneities with varying electron densities and atomic numbers.

On the other hand, Keall and Hoban [Keall and Hoban, 1995] extended the rectilinear density scaling method (to what was named as the *Fermi-Eyges theory (FET) scaling*), by including a factor based on the Fermi-Eyges calculated lateral planar fluence distribution. This method was only implemented for improving the calculation of primary dose in the direction of the beam axis and is reported to increase calculation time by a factor of 3. However, recently Keal and Hoban introduced the *Super-Monte Carlo (SMC)* method [Keall and Hoban, 1996]. Here, they follow a different approach for overcoming the density interface problem of superposition. Instead of correcting primary kernels, they choose to explicitly transport pre-generated Monte Carlo electron track data. Hence, their superposition algorithm is enhanced with an electron transport algorithm. Results from this approach appear promising. SMC does not account for changes in atomic number or for the hardening of the spectrum of the secondary electrons with depth and increases calculation time by a factor of 30.

Scaling scattered dose. Rectilinear density scaling is a very good approximation for first scattered photons. This is because these travel in straight lines and mass attenuation coefficients scale linearly with density. Multiply scattered photons do not follow similar pathways to those of first scattered photons. Therefore, it is expected that density scaling for multiply scattered photon kernels is not a very good approximation. For this reason, Mackie *et al.* [Mackie et al., 1985b] instead of scaling residual first- and multiple-scatter dose spread arrays with the average density along the path between interaction and dose deposition points, used the average density value for the whole irradiated medium. Since paths of multiply scattered photons are rather diffused, Boyer and Mok [Boyer and Mok, 1985] employed a diffusion theory for modelling dose from these photons. Finally, no density scaling procedure has yet been proposed for predicting the transport of bremsstrahlung and annihilation photons, since dose deposited from these particles constitutes only a very small fraction of the total dose deposited at a point.

Superposition algorithms generally are designed to use total energy deposition kernels. To overcome the limitations introduced by scaling total kernels, Mackie *et al.* [Mackie et al., 1985b] precalculated kernels at different densities, whereas Ahnesjö *et al.* used total kernels of very fine resolution, at the price of longer computation time [Ahnesjö et al., 1987].

Atomic number variations

Efforts have been carried out only by a few workers towards improving the performance of the superposition model to account for the presence of high-Z material in the irradiated medium. Sauer suggested a further twofold scaling for (spherical) energy deposition kernels generated in water [Sauer, 1994], [Sauer, 1995]. To account for the increased diffusion of electrons in the high Z material, the energy deposited in a voxel (r, θ) is calculated by averaging the energy deposited in voxels at adjacent angular positions. In addition, to consider the difference in stopping power and range between water and a high-Z material, the energy deposited in the high-Z material is calculated by scaling the radius with the mean mass stopping power ratio of the high-Z material to water along the path and by multiplying the result with the mass stopping power ratio at the energy deposition site. These modifications to the scaling of kernels were tested for simple slab geometries consisting of water and Fe and of water and Al for 5MV, 8MV and 16MV photon beams. Results were compared with experimental data and Monte Carlo generated data. It was shown, that the accuracy of the model was

significantly improved at interfaces with high-Z materials

Papanikolaou and Mackie [Papanikolaou and Mackie, 1993] chose a simple approach to account for the presence of media with different atomic numbers than that of water. They used the EGS4 Monte Carlo code [Nelson et al., 1985] to generate kernels for media of various atomic numbers, such as Al, C, Ca, Fe, Pb and bone for energies ranging from 100keV to 50MeV. Results using these kernels in a superposition algorithm have not yet been published. However, their own algorithm has been implemented in a commercial three dimensional treatment planning system and an accuracy in dose to within 3% has been claimed [Papanikolaou et al., 1995].

The *photon-electron cascade model* by Yu *et al.* which was discussed in a previous section, was also shown to model well the effect on dose due to the presence of materials with different atomic numbers [Yu et al., 1995].

3.4.2 X-ray Source

Conventional dose calculation methods utilise input originating from measured data, which inherently include any effects on dose originating from the x-ray source and the linear accelerator head in general. Convolution/superposition models are theoretical methods using only theoretical input data i.e monoenergetic kernels. Therefore, for these models it is required that spectral information is additionally taken into account. X-ray beams from linear accelerators contain photons with a broad distribution of energies. Measurements to determine the energy components of an x-ray spectrum are not simple. Alternatively, some used Monte Carlo methods for simulating the production of x rays in the target [Mohan et al., 1985],[Mohan, 1987b] as well as for quantifying the effects on dose from scattered photons or contaminant electrons originating from other components in the accelerator's head [Petti et al., 1983a], [Petti et al., 1983b], [Chaney et al., 1994].

Beam hardening

For superposition applications, it is not necessary to have a very precise knowledge of the spectral distribution. However, representing the energy spectrum with a single (mean) energy, therefore calculating a monoenergetic TERMA distribution, does not result in accurate depth dose values [Metcalfe et al., 1989]. Effective bremsstrahlung spectra which represent a good description of the energy distribution of the beam at the phantom surface and which can be

used by superposition models have been reconstructed using numerical methods [Ahnesjö and Andreo, 1989], [Sauer and Neumann, 1990]. These involve minimising, at depths greater than the maximum penetration depth of contaminant charged particles, the difference between a set of measured depth dose distributions and a weighted sum of monoenergetic depth dose distributions precalculated using Monte Carlo kernels. The weights yielding the minimal deviation define the spectrum.

Superposition/convolution is influenced by the polyenergetic nature of the incident photon beam and by the fact that photons at different energies in the primary beam have different attenuation coefficients and probabilities of interaction. EDKs generated for a spectrum of energies are known as polyenergetic EDKs. Two parts in the superposition calculation are influenced by changes in the spectrum with depth:

- terma; because the mean energy of the beam increases with depth.
- EDK; because (a) the increase of the mean energy of secondary electrons, results in energy deposition further from the interaction site and (b) the proportion of primary photon energy transferred to secondary electrons increases as the mean energy of the beam increases. This means that, beam hardening results in an increase in the total fractional energy in the primary kernel and a decrease of the total fractional energy in the scatter kernel.

Beam hardening is fully accounted for when superposition is carried out separately for each energy component (equations (3.1) and (3.8)). This is known as the *direct summation* or *components* superposition. Significant gain in computational speed and storage needs are possible when the integration over energy is made in advance. Several approaches have been implemented, where the energy dependence of the terma and EDKs is translated into a depth dependence. These are known as the *single polyenergetic approaches.*

Mackie *et al* [Mackie et al., 1987] proposed using the surface spectrum for the calculation of an effective mass attenuation coefficient by weighting mass attenuation coefficients with respect to energy fluence :

$$\frac{\bar{\mu}}{\rho}(\bar{s}) = \frac{\int \frac{\mu(E)}{\rho} \Phi_E E e^{-\frac{\mu(E)}{\rho}\bar{s}} dE}{\int \Phi_E E e^{-\frac{\mu(E)}{\rho}\bar{s}} dE} \tag{3.11}$$

Φ_E is the fluence differential in photon energy and $\mu(E)/\rho$ the mass attenuation coefficient for photons with energy E. Effective polyenergetic terma is obtained from:

$$\tilde{T}(\bar{s}) = \frac{\bar{\mu}}{\rho}(\bar{s})\bar{E}(\bar{s})\Phi(\bar{s}) \tag{3.12}$$

where $\bar{E}(\bar{s})$ is the effective energy of the beam at $\bar{s}$ calculated by weighting with energy fluence. If $\Phi(\bar{s})$, $\Phi(\bar{r_o})$ are the photon fluences at $\bar{s}$ and $\bar{r_o}$ respectively (Figure 3.3), then fluence at $\bar{s}$ is given by:

$$\Phi(\bar{s}) = \Phi(\bar{r_o})(\frac{r_o}{s})^2 e^{-\int_{r_o}^{s} \frac{\bar{\mu}}{\rho}(\bar{l})\rho(\bar{l})dl} \tag{3.13}$$

Polyenergetic EDKs were calculated using the energy spectrum at a reference depth, weighted with respect to energy fluence. The use of the same polyenergetic kernel in both the dose deposition point of view and the dose interaction point of view is not strictly valid due to the differences in the energy fluence spectrum in the two implementations [Papanikolaou et al., 1993].

A similar method was carried out by Metcalfe *et al.* [Metcalfe et al., 1990] for deriving polyenergetic EDKs. However, polyenergetic terma was obtained by integrating over energy at each depth. In these two approaches depth hardening of the polyenergetic EDK was considered to cause no significant errors in percentage depth dose calculations. Metcalfe *et al.* concluded that terma is the major factor in determining the shape of the calculated dose distribution because fractional energy values in the EDKs fall off rapidly with distance from the EDK origin. Therefore, in polyenergetic beams, it is important to include spectral information in the terma distribution.

Ahnesjö [Ahnesjö, 1989] used surface spectra to calculate both polyenergetic kernels and effective attenuation coefficients for terma. Approximate terma distributions were obtained using the mean linear attenuation coefficient for the medium present at each depth weighted with the spectrum at the surface. Polyenergetic EDKs were calculated as weighted sums of monoenergetic kernels:

$$h(\bar{r}) = \frac{1}{\Psi(\bar{r_o})} \sum_i \Psi_i h(E_i, \bar{r}) \tag{3.14}$$

where $\Psi(\bar{r_o})$ the energy fluence at the surface $\bar{r_o}$ and Ψ_i the energy fluence of energy interval ΔE_i:

$$\Psi_i = \int_{\Delta E_i} \Psi_E(\bar{r_o})dE \tag{3.15}$$

Dose values from single polyenergetic superposition were further multiplied with a depth dependent correction factor to correct for beam hardening. This factor was defined to be the ratio of dose calculated in water using the direct summation approach, to the dose in water from the single polyenergetic calculation.

Papanikolaou *et al.* [Papanikolaou et al., 1993] calculated polyenergetic terma using equations (3.11) and (3.12). Unlike equation (3.14), polyenergetic EDKs corresponded to terma-weighted spectrum-averaged kernels. Beam hardening effects on the polyenergetic kernel were accounted for by applying a depth and beam dependent correction factor. This factor was calculated from linear fitting to the ratio of depth dose curves from a direct summation calculation and a single polyenergetic superposition, for any megavoltage beam.

Hoban *et al.* [Hoban et al., 1994] carried out a thorough investigation on the influence of beam hardening on EDKs. They discuss that ideally, unique EDK should be used for each depth of primary photon interaction. Polyenergetic primary and scattered kernels were calculated separately for a surface spectrum and weighted with terma (as opposed to energy fluence) so that the variation in attenuation coefficient with energy is taken into account. These were further corrected with depth by accounting for the change in the fraction of primary photon energy transferred to secondary electrons as the beam hardens (i.e the ratio of kerma to terma at each depth normalised to the respective ratio at the phantom surface).

Later, Hoban [Hoban, 1995] continued his research on the effect of beam hardening on single polyenergetic superposition. Beam hardening translates to an (almost linear) increase of the mean primary photon energy with depth and the consequence of this is shown to be a linear increase of the ratio of collision kerma to terma with depth. Through a comprehensive study for a 6MV beam, Hoban compared results from the *components approach* with three different *single polyenergetic superposition* methods. The first single polyenergetic superposition was carried out using terma (calculated as suggested by [Metcalfe et al., 1990]) and terma-weighted primary and scatter kernels. It was shown, that this calculation, underestimates primary dose and overestimates scattered dose. The second superposition was carried out in terms of collision kerma, convolving collision kerma with kernels representing fractional energies normalised to collision kerma. This approach is accurate for primary dose but underestimates scattered dose. In the third superposition, primary dose was calculated in terms of collision kerma and scattered dose using the the difference between terma and collision kerma. This

last method was shown (theoretically and experimentally) to calculate correctly both dose components. This conclusion is a significant improvement for single polyenergetic superposition.

Off-axis beam softening

The x-ray beam quality varies with off-axis distance as well as with depth. Spectral variations of beam quality as a function of radius, usually characterised in units of HVL in water, have been reported by several workers [Hanson and Berkley, 1980], [Lutz and Larsen, 1984]. Various methods have been suggested for correcting dose calculations to account for these variations [Hanson et al., 1980], [Kepka et al., 1985]. Mohan *et al.* used the information on the angular distributions of photons generated by Monte Carlo techniques to compute transmitted energy fluence values through columns of water of different thicknesses and which were further used to determine half-value layers [Mohan et al., 1985]. Recently, is has also been confirmed that off-axis beam quality variations depend on the material of the flattening filter [Zefkili et al., 1994]. Sets of attenuation measurements were obtained on the central axis and off-axis, with and without the presence of the flattening filter and with and without correcting for the scatter generated within the mini-phantom used for the measurements. It is suggested that such measurements are carried out for each linear accelerator and used in dose calculations. Since, superposition is a theoretical method which calculates dose from first principles, off-axis spectral variations should be taken into account.

Photon and electron contamination

Photon contamination from treatment heads is widely known as *head scatter or collimator scatter.* It encompasses x rays which are produced in the head of the accelerator by inelastic collisions of primary- and higher- order electrons in the target and other head components (primary collimators, beam flattening filter, wedges, and secondary collimators) and by scattering of primary and higher-order x rays [Nilsson and Brahme, 1981], [Chaney et al., 1994]. Chaney *et al.* analysed the sources of off-focus radiation and suggested that appropriate *extended source* models are developed to account for its effects which are mainly related to the field size and the collimator settings.

For a 15MV beam, Mohan *et al.* have found that 2.8% of photons emerging from the treatment head have scattered from the primary collimator,

whereas 3.5% have scattered from the flattening filter. They also found that head scatter increases the width of the penumbra by 2mm at the depth of 5.0cm[Mohan et al., 1985]. Boyer first suggested accounting for this, by blurring the terma distribution using a Gaussian function with an empirically determined spread [Boyer, 1986], [Battista and Sharpe, 1992]. Mohan *et al.* [Mohan et al., 1986] implemented a sector integration of the angular distribution of primary photons (generated by the EGS4 Monte Carlo code) over a range of angles "seen" by the computational point, to compute relative primary fluence at points near boundaries of blocks and collimators.

Ahnesjö split head scatter modelling into three separate problems. An analytical model (*truncated cone source distribution model*) was developed to describe the distribution of scattered photons from the flattening filter and assess their influence on the dose distribution [Ahnesjö, 1994]. Modelling scatter from collimators was based on integrating scatter kernels around the field edge. Total collimator scatter kernels were derived (using EGS4) and parameterised as functions of beam energy before being used to obtain collimator scatter distributions for broad beam geometries [Ahnesjö, 1995b]. Transmission and scatter from beam modulators was modelled from first principles using first scatter theory [Ahnesjö, 1995c].

An approach by Sharpe *et al.* combines an *extrafocal source model* with a superposition algorithm for calculating the shape of the penumbra in beam profiles and dose-per-monitor-unit calibration factors (output factors) [Sharpe et al., 1995].

Electron contamination refers to those electrons which scatter within the accelerator collimation system and in the air between the treatment head and the patient. These reach the patient surface, contributing to surface dose and affecting the shallow portion of dose distributions [Mackie and Scrimger, 1982], [Petti et al., 1983a]. The lateral distribution of these electrons has been modelled by a Gaussian pencil beam distribution [Nilsson, 1985], whereas the depth dependence has been described by an exponential [Mackie, 1984]. However, there has been no complete model to date to encompass dose contributions from contaminant electrons in any convolution/superposition calculation.

Beam divergence

Primary photons emanating from a finite size source in a linear accelerator, cross the patient surface in divergent directions. For divergent beams, in contrast to parallel beams, there is an increased inverse square reduction of the non central-

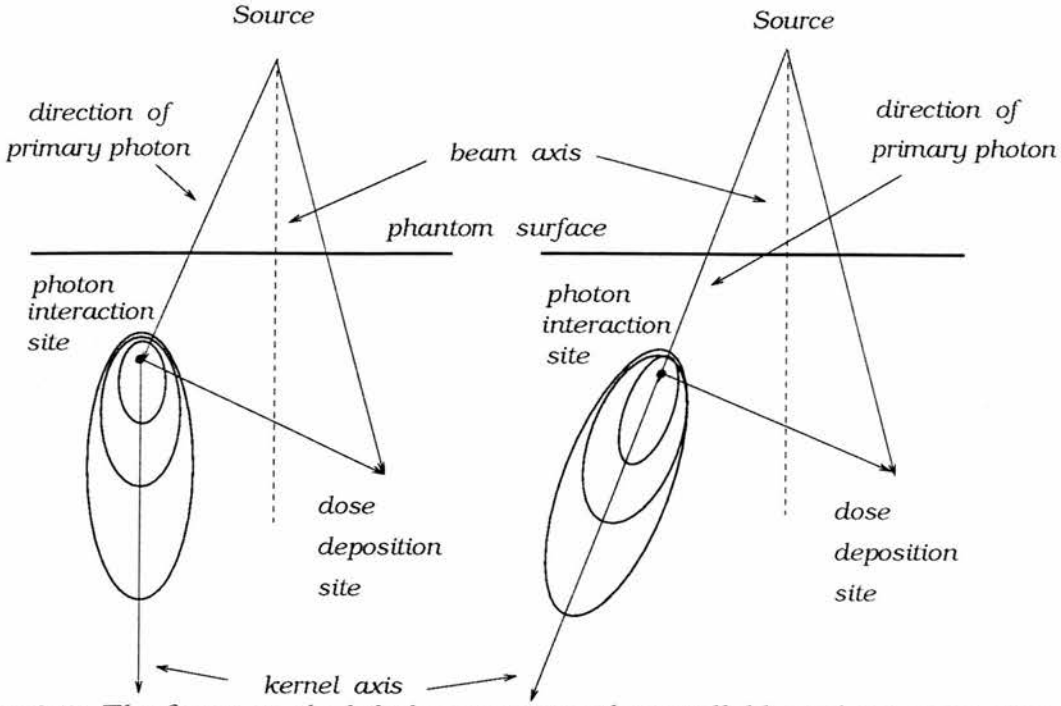

Figure 3.5: *The figure on the left demonstrates the parallel kernel approximation, whereas on the right, the kernel axis is aligned with the direction of the primary photon.*

axis primary photon fluence, a linear increase of each field dimension with depth and a spatial invariance of the EDKs. Beam divergence is illustrated in Figure 3.5. The problem of kernel alignment with direction of the primary photons was first mentioned by Mackie *et al.* [Mackie et al., 1985b]. They found that for 15MV x rays and for a field of $20 \times 20cm^2$ at a source to surface distance of 100cm, the accuracy in the calculations of Tissue Maximum Ratio (TMR) values on the central axis is improved by less than 1% up to a depth of 20cm when kernels are aligned to the divergent primary photon trajectories. Mackie *et al.* have carried out a kernel tilting procedure during superposition which increases calculation time. They conclude that not modelling this aspect of beam divergence is not important for simple irradiated geometries, but is expected to be more significant in phantoms with more complex heterogeneities.

Ahnesjö [Ahnesjö, 1987] computed a correction factor along the central axis, defined as the ratio of dose calculated with properly tilted kernels to the dose calculated without kernel tilting. He found that for SSD of 80cm this factor was 0.956 at a depth of 25cm for a $20 \times 20cm^2$ ^{60}Co beam.

A detailed study on the validity of parallel kernel approximation was carried out by Sharpe and Battista [Sharpe and Battista, 1993]. They computed dose

distributions using parallel and tilted kernels for monoenergetic photon beams (2,6,10 MeV), for different SSDs (50, 80, 100 cm) and field sizes (5×5, 15×15 and $30 \times 30 cm^2$). They found that in combinations of extreme cases such as small SSD, large field size and high energy, errors above 3% are likely to be observed. For example, for 10 MeV photons and a field size of $30 \times 30 cm^2$ at SSD of 50cm, the dose maximum is overestimated by up to 4.4%. Nevertheless, they concluded that *using parallel kernels was an acceptable approximation for most clinical situations encountered in external beam radiotherapy.*

3.4.3 Speed improvements

Dose calculation with superposition is an acceptable approximation to the computationally intensive, and therefore clinically unacceptable, Monte Carlo calculations. Although faster than Monte Carlo, superposition methods are slow for interactive treatment planning. This section presents various implementations of the convolution/superposition method which aim to increase calculation speed.

Fast Fourier convolution methods

The application of Fast Fourier Transforms was advanced by Boyer *et al.* [Boyer and Mok, 1984], [Boyer and Mok, 1985], [Boyer and Mok, 1986], [Boyer et al., 1991]. Their work, unlike others [Metcalfe et al., 1989], involved the convolution of primary photon fluence with kerma kernels. FFT implementations impose significant approximations when modelling secondary electron transport in heterogeneous media, namely kernels are treated as spatially invariant impulse functions. For this reason, this approach was discussed in the previous chapter, together with those dose calculation models which are classified as three-dimensional non scatter raytrace methods. If N is the number of voxels in a dose calculation volume along one side, the number of operations required by a convolution/superposition calculation is proportional to $N^7/2$, whereas Fast Fourier Transform methods require a number of operations proportional to $3N^3 log_2 N$ [Bracewell, 1984]. This gain in computation time, is at the expense of accuracy loss, especially in cases of electronic disequilibrium. Details on the FFT implementation and on timing benchmarks can be found in [Boyer, 1984], [Field and Battista, 1987], [Boyer et al., 1988].

Special Techniques

The *collapsed cone convolution* method [Ahnesjö, 1989] has succeeded in reducing the number of computations of dose for N^3 points to a value proportional to N^3, as well as still accounting for the presence of inhomogeneities. The constant of proportionality is explained below. Polyenergetic energy deposition kernels are analytically parametrised by an exponential over the square of the radius:

$$\frac{h_{water}}{\rho}(r,\theta,\phi) = \frac{A_\theta e^{-a_\theta r}}{r^2} + \frac{B_\theta e^{-b_\theta r}}{r^2} \tag{3.16}$$

where (r,θ,ϕ) refers to a spherical coordinate system and A_θ, a_θ, B_θ and b_θ are functions of the scattering angle θ and the accelerating potential. The first term describes the energy imparted as primary dose and the second, the energy imparted as scattered dose. These polyenergetic kernels are convolved with terma. All energy released by primary photons into coaxial cones of equal solid angle from volume elements on the cones axis is rectilinearly transported, attenuated and deposited in elements on that axis (i.e. cones are *collapsed* onto their axes). The irradiated medium is constructed as a lattice of lines, representing cone axes which intersect each calculation point from different directions. The analytic representation of the kernels as exponential factors allows convolution integrals to be evaluated along each cone axis using recursive formulae. These recursions pass each calculation point once per direction and if calculations are carried out for all points on each cone axis sequentially, the total number of operations required to calculate dose to N^3 points is proportional to N^3. Kernel scaling for the heterogeneous medium is performed during calculation. The number of cone axes used defines the constant of proportionality mentioned previously and therefore computation speed. The collapsed cone convolution method has been verified against Monte Carlo generated dose distributions for several accelerating potentials and for slab and mediastinum-like phantom geometries. The agreement with Monte Carlo data is very good. Deviations occur at media interfaces and in regions of low density, since rectilinear density scaling does not model secondary electron transport. The method is best suited for "bulk" dose calculations on regularly spaced cartesian matrixes.

Another approach, in which the angular directions at which ray-tracing is carried out can be restricted, was proposed by Reckwerdt and Mackie [Reckwerdt and Mackie, 1992]. They used a *run-length ray-tracing* technique, where ray-tracing along the path between photon interaction and dose deposi-

tion sites is carried out in such a way that results are reused for all voxels lying along that path. This algorithm reduces the number of computations in a N^3 scattering volume from $N^7/2$ to $M \cdot N^4/2$, where M is the number of angular directions traced around each scattering site. The increase in speed is reported to be comparable to that of the collapsed cone method.

Use of special hardware

As the availability of advanced hardware increases, it is likely that eventually, such systems will become available in a clinical environment, thus enabling to carry out fast, computationally intensive dose calculations such as superposition or even Monte Carlo simulations [Murray et al., 1989]. This possibility has been investigated with a superposition algorithm implemented on a multicomputer platform using up to eight transputers connected in parallel [Murray et al., 1991]. The superposition algorithm used was that of Metcalfe [Metcalfe et al., 1989]. Terma was calculated using Siddon's ray-tracing method [Siddon, 1985] and energy deposition kernels were generated with EGS4 [Nelson et al., 1985] in homogeneous media and for different densities. The algorithm was implemented on the multicomputer by means of a master/worker network. Terma was calculated by the master task. The workers performed superposition having access to the stored density array and the set of different kernels. It is beyond the scope of this review to discuss the finer details of the implementation of transputer arrays which are discussed at length in the original paper. Here, it is sufficient to mention an example of the performance of such a system in terms of time. Superposition of a $16 \times 16 \times 68$ kernel with a $16 \times 16 \times 60$ terma distribution using eight INMOS T800 transputers, requires 62.4 seconds. This time reduces linearly with the number of processors used.

Pencil beam models

Pencil beam models can be considered as approximations to superposition algorithms, where basically the integration of energy deposition kernels over depth is carried out in advance (a "pre-convolution" over depth). Pencil Beam kernels describe the energy deposited in a semi infinite medium from a point monodirectional beam (pencil beam). Pencil beam dose calculation algorithms calculate dose by convolving the in-air energy fluence (or fluence) distribution with an appropriate pencil beam kernel. If $\Phi(a, b)$ is the relative primary photon fluence distribution at off central axis positions a and b and $K(x - a, y - b, d)$ the pencil

beam kernel at $x - a$ and $y - b$ and depth d, the dose distribution at this depth is calculated from

$$D(x, y, d) = \int\int \Phi(a, b) K(x - a, y - b, d) da db \tag{3.17}$$

Irregular field shapes and fields with blocks and compensators are easily modeled if the incident beam is taken to consist of pencil beams incident on the phantom surface.

Pencil beam kernels have been obtained in a water medium using Monte Carlo methods for monoenergetic or polyenergetic linear accelerator pencil beams [Mohan and Chui, 1987]. Because of the axial symmetry of pencil beam kernels, Mohan and Chui used a cylindrical scoring geometry within EGS4. Alternatively, the same authors derived pencil beam kernels by deconvolving parallel broad beam profiles with rectangular functions [Mohan and Chui, 1988]. This deconvolution approach requires that the kernels across the field are invariant (i.e. assuming the beam quality does not vary across the field) and that a two dimensional kernel is a product of two one-dimensional kernels.

According to Eklöf *et al.* [Eklöf et al., 1990], pencil beam kernels can be calculated in a straightforward manner from an integration of monoenergetic point spread functions (PSF) (which were scored in a cylindrical geometry [Ahnesjö et al., 1987]):

$$p(r, z) = \int h(r, z - z') \mu e^{-\mu z'} dz' \tag{3.18}$$

In this convolution integral, μ is the linear attenuation coefficient of the monoenergetic primary photons and z' the depth of the primary interaction. Polyenergetic pencil beam kernels can be obtained in the same manner as polyenergetic PSFs; namely by weighting monoenergetic kernels with spectral weights. Ahnesjö *et al.* [Ahnesjö et al., 1992] have analytically parameterised polyenergetic pencil beam kernels (these derived from monoenergetic pencil beam kernels according to an estimate of the energy spectrum) as the sum of two exponentials over the cylindrical radius:

$$\frac{p}{\rho}(r, z) = \frac{A_z e^{-a_z r}}{r} + \frac{B_z E^{-b_z r}}{r} \tag{3.19}$$

Here, $\frac{p}{\rho}(r, z)$ is the energy fraction deposited per unit mass at radius r and depth z in a cylindrical coordinate system and A_z, a_z, B_z and b_z are functions of depth. Since pencil beam kernels are symmetric around the radius of the pencil beam

direction, they can be discretised into cross-sectional profiles along depth, and the calculation of dose in the medium will be from the two dimensional convolution of the relative incident photon fluence matrix and kernel profiles at a series of depths. Pencil beam data have also been derived from a combination of measured data (central axis depth dose curves and profiles at depths) and calculated data (phantom scatter factors) [Storchi and Woudstra, 1996].

Pencil beam convolution methods can be carried out either analytically [Ahnesjö et al., 1992] or using Fast Fourier Transforms [Mohan and Chui, 1987] or Fast Harley Transforms [Bortfeld et al., 1993]. Pencil beam models can be fast enough for interactive treatment planning. The calculation of dose in homogeneous media is generally accurate. Pencil beam models based on FFT and FHT techniques use spatially invariant pencil beam kernels and do not incorporate corrections for photon and electron transport. Therefore to calculate dose in heterogeneous media with acceptable accuracy, they must be used together with a conventional inhomogeneity correction method.

An exception, is the work of Ahnesjö *et al.* [Ahnesjö et al., 1992]. In heterogeneous media, primary dose is calculated using pencil beam parameters for the radiological depth and scattered photon dose is obtained by applying a correction factor based on a one dimensional convolution of the scatter fluence along the beam path. Dose is weighted by the energy fluence distribution to describe the beam compensation. Dose due to contaminant particles is described by a separate pencil beam and is added to the final dose. This is the only pencil beam model correcting photon transport in heterogeneous media. Its performance has been examined in the case of a mediastinum geometry. Dose values along the central axis of the beam (between the two lungs) deviate from Monte Carlo calculated values by up to 5% for ^{60}Co and 4MV x rays, due to the incorrect modelling of scattered photon dose. Corrections for electron transport are not incorporated, therefore dose values within low density media are overestimated by up to 14% for high energy beams (18MV x rays) [Knöös et al., 1995].

3.5 Summary and Conclusions

This chapter has presented the convolution/superposition method and complements the previous chapter in reviewing the progress towards true three dimensional photon dose computations. The main characteristics of superposition models are summarised as follows:

- Primary Dose: Electron transport is modelled. Physically the most accurate model requires the use of primary energy deposition kernels (primary PSFs) and a strictly accurate solution necessitates the implementation of an electron transport theory.

- Scatter Dose: Dose from scattered photons is modelled from first principles and not empirically. It is possible to calculate separately dose from different scattering orders, thus improving the calculation of dose contributions from multiply scattered photons.

- Dose from backscattered particles: The use of kernels generated by primary interactions forced in the centre of a large water medium is approximate at phantom edges. Especially at exit surfaces, it has been suggested to use kernels generated at such surfaces.

- High atomic number media: It is possible to model the influence on dose from high Z materials by appropriately scaling the kernels.

- Accurate implementation of scaling procedures for kernels ensures that inhomogeneities are not considered to act independently and their mutual effects are taken into account.

- Electron contamination modelling as well as modelling contributions from head scatter can be carried out independently (either by Monte Carlo methods or by analytical approaches) and incorporated into any superposition code.

- Nature of x-ray beam: The polyenergetic nature of x-ray beam must be taken into account. Strictly accurate computations require that superposition is carried out for each spectral component (*components method*). Acceptable approximations require that beam hardening and off-axis softening are modelled in the polyenergetic TERMA and EDK distributions (*single polyenergetic superposition*).

- Calculation speed: The problem of large computation times is encountered by implementing FFTs, special programming techniques (*collapsed cone convolution*, *run length ray-tracing*) or hardware and by convolving pencil beam kernels instead of point spread functions (*pencil beam models*).

From the overview on *correction-based* methods presented in section 2.4 in chapter 2 and the above, it is obvious that a *model-based* method based on the

superposition principle provides better solutions to the inhomogeneity problem, which are theoretically justified and not empirical. The superposition approach performs better than any conventional dose calculation method since the 3D dimensional nature of the patient is a prerequisite input and because all this information is used for the calculation of dose at a point.

The accuracy of results from superposition depends on various modelling aspects which determine how well the code simulates physical reality. These can be of great significance, such as the polyenergetic nature of the x-ray beam, or less important as the use of kernels generated under full scatter conditions at exit surfaces. There are parameters (*"degrees of freedom"*) which determine how well a superposition algorithm performs. These are characteristic of the different implementations. For example, in the *collapsed code convolution* or the *run length ray-tracing* software, the accuracy in the estimation of dose at a point depends on the number of cones or steps along the photon paths respectively that are considered in the computation. Obviously, these are modified mainly to increase computation speed. It must be also noted that superposition calculations using separately primary and scatter kernels, are more accurate. This is obvious in high energy beams and at media interfaces, where secondary electrons travel significantly long distances and cross media boundaries. In this case linear density scaling procedures are not sufficient.

There is scope for further development in the superposition approach. There is a need to understand and further investigate the balance between the clinically required accuracy and the various approximations that can be introduced in the physical modelling. There is also need to improve electron transport modelling in those cases where primary dose is calculated separately using primary kernels without significantly increasing calculation times. Furthermore, is it always necessary to obtain detailed dose information in all sites within the patient? Should all dose information on the 3D matrix originate from superposition? It is clear now that the *best* method to investigate and follow-up here is one based on the superposition approach. Such a model mainly requires:

1. The use of energy deposition kernels.

2. The possibility of comparing model results given in absolute units with data also in the same units.

3. Finally, information on the energy spectra of the clinical x-rays beams; so that is possible to compare calculated values with measured data.

The first two items suggest that Monte Carlo techniques should be facilitated. The third item can also be obtained using Monte Carlo methods. However, since superposition does not require detailed information on the spectral distribution, one might consider other, simpler solutions to this problem. The next chapter attempts to provide a brief summary of the essence of the Monte Carlo method and its application in radiotherapy physics.

Chapter 4

The Monte Carlo method

4.1 Introduction

Many reviews on the principles and applications of the Monte Carlo method in medical radiation physics have been published to date [Meyer, 1954], [Raeside, 1976], [Turner et al., 1985], [Nahum, 1988a], [Williamson, 1989], [Murray, 1990] and [Mackie, 199 The most recent by Andreo [Andreo, 1991], is an update to the early work by Raeside and is currently the best, almost complete, source of information on the basic aspects of the method, on practical considerations of Monte Carlo algorithms, and on applications of photon and electron transport in matter within the different areas of medical radiation physics, such as nuclear medicine, diagnostic x-ray physics, radiotherapy physics, dosimetry and radiation protection, microdosimetry and electron microscopy. Various codes available in the public domain, such as ETRAN, EGS, MCNP, MORSE_CG and ITS are presented together with their evolution and improvements. The reader obtains a critical analysis of their capabilities and limitations. Future trends, like inverse Monte Carlo methods, vectorisation of existing codes and calculations carried out using parallel processors are also mentioned.

This chapter aims to provide a concise outline of the Monte Carlo method as a mathematical technique and to present how the method is used for solving problems in radiation transport physics. For extensive details and references, the reader is referred to the reviews and original articles mentioned above and to those given in the following sections. Since the EGS4 Monte Carlo system was employed in this thesis, it is felt necessary to include a brief description of this code in order to familiarise the reader with the concepts and terminology used within the following chapters.

4.2 What is Monte Carlo?

Monte Carlo is a mathematical technique employed to achieve random sampling of a known probability distribution with the aid of randomly generated numbers. In the context of radiation transport, Monte Carlo techniques are those which simulate the random trajectories of individual particles using machine-generated (pseudo-) random numbers to sample from the probability distributions governing the physical processes involved.

In 1873 a paper by Hall [Hammersley and Handscomb, 1964] was the first known to be published on the calculation of constant π. Mathematicians performed experiments in which a needle was thrown in a random (haphazard) manner onto a board ruled with parallel straight lines (*Buffon needle problem*). The ratio of the number of times the needle landed parallel to the lines to the number of trials (namely the probability of hitting a parallel line), was proportional to the number 3.1416 (π), if one continued the trials long enough and threw the needle in a truly random fashion [McCracken, 1955]. In 1901 Lord Kelvin suggested applying the Monte Carlo Method for solving the Boltzmann equation and in 1908 the famous statistician W. S. Gosset (Student) used the method for estimating the correlation coefficient in his t-distribution. However, systematic development of Monte Carlo techniques began only around 1944, by John von Neumann, Stanslas Ulam and Enrico Fermi who worked on a secret Los Alamos research project named "Monte Carlo" involving direct simulation of random neutron diffusion in fissile material. Due to their work, scientists became aware of the possibilities, potentialities and applications of the Monte Carlo method. Since then, Monte Carlo methods have been used extensively among physicists for evaluating complex multidimensional integrals and for solving integral equations not amenable to analytic solution. Such algorithms have provided physicists with:

- an alternative method of attacking a problem
- a "bridge" between theory and experiment, and
- the performance of experiments which cannot be done in the lab.

The Monte Carlo method has been employed in scientific and engineering applications, as well as in economics and business studies.

Solutions to scientific problems are generally obtained using analytical or numerical methods. Analytical methods provide solutions to problems directly from

their mathematical representation in the form of formulas. Numerical methods essentially give approximate answers to problems, obtained as a result of substituting numerical values for the variables and parameters in the problems. The Monte Carlo method belongs to the latter type. It is a stochastic simulation technique involving sampling stochastic variates from probability distributions [Rubinstein, 1981]. The Monte Carlo method can be understood in terms of the black box diagram in Figure (4.1) [Morin, 1988].

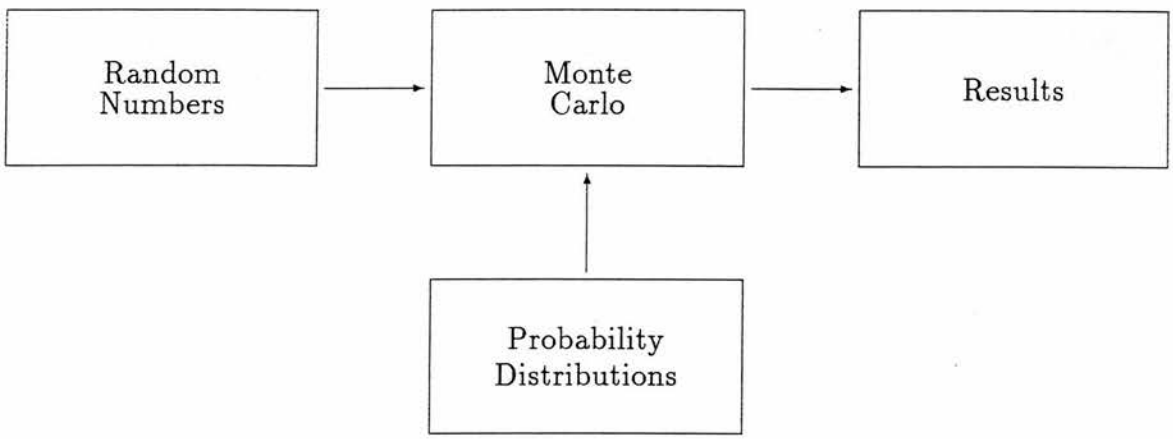

Figure 4.1: *Black box illustration of the Monte Carlo technique.*

4.2.1 Random Numbers

As shown in Figure 4.1, a prerequisite for the sampling of probability distributions is the use of random numbers. Random numbers are simply random variables uniformly distributed between zero and one. A high quality random number sequence is a long stream of numbers with the characteristic that the occurrence of each number in the sequence is unpredictable and that the stream of digits of the sequence pass certain tests designed to detect any departures from randomness. Random numbers can be obtained from tables, physical sources, such as electronic noise and from algorithms, known as *Random Number Generators (RNGs)*. The latter give numbers which are not truly random (pseudo-random) but are uniformly distributed between the unit interval, are statistically independent and reproducible. RNGs used in Monte Carlo simulations are mainly *congruential generators*. These produce a non-random sequence of numbers utilising a recursive formula based on calculating the residues modulus of a linear

transformation [Rubinstein, 1981]. The fundamental congruence formula can be expressed as:

$$X_{i+1} = (aX_i + c)(\text{mod } m),\ i = 1, ..., n \tag{4.1}$$

where a (*multiplier*), c (*increment*) and m (*modulus*) are non-negative integers. The modulus is set equal to 2^k on a computer using a binary digit system with k being the number of bits in the integers of the computer. The first value given to X_i is called the *seed* of the sequence $\{X_i\}$. The random numbers in the interval $(0, 1)$ can be obtained from

$$R_i = \frac{X_i}{m} \tag{4.2}$$

Equation 4.1 is the formula used with the type of generators called *mixed* or *linear congruential generators.* Variations of this formula lead to subsets of congruential generators such as the widely used *multiplicative random number generators* or the *additive congruential generators.*

A pitfall of RNGs is that after the production of a certain number of distinct elements (known as the *period* of the RNG), the sequence begins to repeat itself. Anyone using a RNG must ensure that its use does not exceed its full period Furthermore, it is important to put the RNG through certain statistical tests prior to its use, in order to check its randomness (namely the independence and uniformity of the pseudorandom number sequence) [Morin et al., 1979]. A description of such tests is given by Rubinstein [Rubinstein, 1981] and Morin *et. al.* [Morin, 1988].

4.2.2 Sampling from probability distributions

Random variables are those quantities which cannot be specified without the use of a probability law. A random variable X is defined as *continuous* when it has a continuous distribution taking any values between the limits x_1 and x_2. It is defined as *discrete* when it can take only a countable number of distinct values $x_1, x_2, ...$ Considering only continuous variables, the probability (*probability distribution function)* that a continuous random variable X lies within an interval (a, b) is defined as:

$$P = Prob(a < X < b) = \int_a^b p(x)dx \tag{4.3}$$

p(x) is the differential probability distribution (*probability density function (PDF)*) of X. *Cumulative Probability distribution (CPD)* is the probability that a random variable has a value not exceeding a prescribed value x^*:

$$CPD : P(x) = \int_a^{x^*} p(x)dx \tag{4.4}$$

while

$$\int_a^b f(x)dx = 1$$

CPD has values between 0 and 1. Therefore for a given random number **R**, it is possible, if the probability density is known to calculate a value for the random variable X. There are mainly three techniques used for generating random variates from probability distributions: the *inversion method*, the *acceptance-rejection method* and combinations of these two (*mixed methods*). Detailed description of these is documented elsewhere [Rubinstein, 1981],[Bielajew, 1993b].

In the *inversion method*, a value for random variable X is calculated from a PDF, by selecting a random number **R** and equating it to the CPD. An application of *the inversion method* relevant to radiation transport is the problem of sampling the random distances travelled by photons between interactions. This process is governed by the exponential probability law. According to this law, the probability (PDF) that a photon experiences no interactions after being transported a certain distance x is given by

$$PDF(x) = \mu e^{-\mu x},\ 0 < x < \infty \tag{4.5}$$

The respective CPD is

$$CPD(x) = \int_0^x \mu e^{-\mu x} dx = 1 - e^{-\mu x} \tag{4.6}$$

Choosing a random number **R** uniformly distributed over (0,1) and solving the following for x:

$$\mathbf{R} = 1 - e^{-\mu x} \tag{4.7}$$

one obtains the distance x (in numbers of mean free paths, (MFP's)) to an interaction :

$$x = -\frac{1}{\mu} ln(1 - \mathbf{R}) \tag{4.8}$$

or

$$x = -\frac{1}{\mu} ln(\mathbf{R}') \tag{4.9}$$

In some problems, calculation of the CPD is mathematically complicated. In such cases *the acceptance-rejection method* is used. This method consists of sampling a random variable from an appropriate distribution and subjecting it to a test to determine whether or not it will be acceptable for use. The method requires the $PDF(x)$ to be bounded over [a,b] and its maximum value $PDF_{max}(x)$ to be known. The method requires the normalisation of $PDF(x)$ with $PDF_{max}(x)$ which creates a new $PDF'(x)$ with a maximum of 1. The sampling procedure requires the repetition of the following steps:

1. Generation of two random numbers $\mathbf{R_1}$ and $\mathbf{R_2}$ within [0,1].

2. Use of $\mathbf{R_1}$ to calculate a value for x^* from $x^* = a + (b - a)\mathbf{R_1}$ and the respective $PDF(x^*)$.

3. Use of $\mathbf{R_2}$ for the following check:
   If $\mathbf{R_2} \leq PDF'(x^*)$ then the value of x^* is accepted (sampled). If not, the value of x^* is rejected and another set of random numbers is generated.

Mixed methods are essentially a combination of the previous two techniques. It is necessary that the PDF can be expressed as the product of two functions:

$$PDF(x) = f(x)g(x) \tag{4.10}$$

one of which is invertible and can be normalised over (a,b) ($\int_a^b f(x)dx = 1$) and the other ($g(x)$) has a known maximum value PDF_{max}. The sampling procedure involves:

1. Generation of two random numbers $\mathbf{R_1}$, $\mathbf{R_2}$

2. Application of the inversion method to sample a random variate x^* from $CDF^{-1}(\mathbf{R_1})$ of $f(x)$.

3. Use of the rejection method on g(x) with x^* . This requires the generation of a third random number $\mathbf{R_3}$ to assess whether x^* is accepted or not.

An example of the application of mixed methods in radiation transport is the simulation of Compton scattering. As described by Raeside [Raeside, 1976], in order to sample the wavelength of the scattered photon, the Klein-Nishina formula (which yields the probability that the photon scatters into a wavelength range λ' and $\lambda' + d\lambda'$) is decomposed into two products of probability density functions. With the aid of a random number, one of the two products is sampled

using the rejection method and using a second random number together with the inversion method the wavelength λ' of the scattered photon is determined. Substituting this value of λ' in the Compton wavelength shift formula, a value of the scattering angle θ is calculated. The sampling of the azimuthal angle simply requires sampling over the uniform distribution $p(\phi) = 1/2\pi$.

4.2.3 The Monte Carlo solution

Whether or not the Monte Carlo method can be applied to a given problem does not depend on the stochastic nature of the system to be studied, but on the ability to formulate the problem in such a way that random numbers may be used to obtain the solution [James, 1980].

The Monte Carlo solution of a function T(s) in a system involves repeatedly sampling from the probability density function describing the behaviour of the system over space Σ . Each value of s is a (possibly) multidimensional array describing the state of the system (these arrays are called particle histories in radiation transport). The mean value of T(s) over space Σ is:

$$< T >= \int_{\Sigma} T(s)p(s)ds \tag{4.11}$$

Function $p(s)$ is a probability density function giving the probability that the state of the system lies between s and $s + ds$. Monte Carlo methods provide an *estimate* $\bar{\mathrm{T}}$ of the *true mean* $< T >$ by randomly selecting N samples $\{s_i\}_{i=1}^{N}$ from p(s). The Monte Carlo estimate $\bar{\mathrm{T}}$ is given by

$$\bar{T} = \frac{1}{N}\sum_{i=1}^{N} T(s_i) \tag{4.12}$$

$T(s_i)$ is called the *Monte Carlo estimator* or *scoring function* and defines the contribution of each random variable s_i to the quantity of interest. The statistical goodness of the estimate $\bar{\mathrm{T}}$ depends on the sample size N and on the variance associated with estimator T(s):

$$\sigma^2 = \int_{\Sigma}(< T > -T(s))^2 p(s)ds \tag{4.13}$$

According to the central limit theorem, for a large number N of independent estimators $T(s_i)$ with a true mean $< T >$ and a variance σ^2, the distribution of the calculated mean $\bar{\mathrm{T}}$ tends to a Gaussian (normal) distribution (of mean $< T >$ and variance $\sigma'^2 = \sigma^2/N$). In other words, $(\bar{T} - < T >)/(\sigma/\sqrt{N})$ is approximately normally distributed with a mean of zero and a variance of one.

This suggests that the Monte Carlo estimate of the mean $\bar{T}$ approximates the true mean:

$$\lim_{N\to\infty} \bar{T} =< T > \tag{4.14}$$

and that the precision in the Monte Carlo estimation of the true mean increases with the square root of the sample size.

Efficiency of a Monte Carlo calculation is defined as

$$\epsilon = \frac{1}{\sigma^2 t} \tag{4.15}$$

where t denotes the computing time required to obtain a result associated with a variance σ^2. Increasing sample size N in order to improve accuracy (i.e. reduce variance σ^2) would result in long computations, and conceiving ways of decreasing t is not always a profitable solution. Rather, ways have been devised for decreasing σ^2 using *variance reduction techniques.* These are non-analogue sampling and scoring techniques, either modifying the estimator to efficiently use the information available from randomly sampled histories (*analytical averaging, expected value* and *statistical estimation methods*) or techniques which bias the sampling from the probability distributions describing the simulated system in order to emphasise those events which contribute to the estimate $\bar{T}$. The latter are known as *importance sampling methods.* When using a variance reduction technique a fair game is maintained in the simulation by associating each history with a *weighting factor* which corresponds to the relative probability that the history simulated would actually occur. The first general review on such techniques was published by Kahn [Kahn, 1954] who pointed out that the variance reduction technique used for a particular simulation depends upon the probability model and introduces greatest gain in efficiency when it is designed by exploiting specific details of the simulated problem. Extensive reviews on these techniques have been also published by McGrath and Irving [McGrath and Irving, 1975], Carlsson [Carlsson, 1981], Lund [Lund, 1981], Hammersley and Handscomb [Hammersley and Handscomb, 1964] and Rubinstein [Rubinstein, 1981].

4.3 The Monte Carlo solution to the radiation transport problem

4.3.1 The Boltzmann Transport equation

Radiation transport within a system of absorbers and sources is a linear statistical phenomenon because particles generally do not interact with each other. As in many other systems in statistical physics, the time-independent Boltzman transport equation describes the fluence for any combination of sources and boundary conditions. From a knowledge of particle fluence it is possible to derive other dosimetric quantities such as dose under the condition of electronic equilibrium:

$$D(\mathbf{r}) = \int\int E\Phi_E(\mathbf{r},\mathbf{\Omega},E)(\frac{\mu_{en}}{\rho})d\Omega dE \tag{4.16}$$

where $\Phi(\mathbf{r},\mathbf{\Omega},E)$ is the particle fluence at spatial coordinate $\mathbf{r}$, direction $\mathbf{\Omega}$ and particle energy E. (μ_{en}/ρ) is the mass energy absorption coefficient and $d\mathbf{\Omega} = sin\theta d\theta d\phi$.

According to Williamson [Williamson, 1988] the time-invariant Boltzmann transport equation can be formulated as

$$\mathbf{\Omega}\nabla\Phi(\mathbf{r},\mathbf{\Omega},E) = -\mu(E)\Phi(\mathbf{r},\mathbf{\Omega},E) + S(\mathbf{r},\mathbf{\Omega},E) + \int\int \Phi(\mathbf{\Omega}',E')\mu(\mathbf{\Omega},E|\mathbf{\Omega}',E')d\Omega dE \tag{4.17}$$

Here, $\Phi(\mathbf{r},\mathbf{\Omega},E)$ defines the number of particles that cross per unit time through a unit area of a surface perpendicular to direction $\mathbf{\Omega}$ and $S(\mathbf{r},\mathbf{\Omega},E)$ is the source distribution of primary particles. $\mu(E)$ is the linear attenuation coefficient, namely the probability per unit pathlength of any interaction between the particles and the medium and $\mu(\mathbf{\Omega},E|\mathbf{\Omega}',E')$ is the differential cross section per unit path length, that is, the probability that a particle will change from state $(\mathbf{\Omega}',E')$ to state $(\mathbf{\Omega},E)$. The derivation of (4.17) assumes random distribution of scattering sites in the medium and that particles do not interact with themselves. Polarisation or anisotropy of the radiation is ignored. The solution of equation (4.17) and subsequently equation (4.16) for an unbounded absorber (away from medium boundaries or radiation sources) has been carried out using analytic or semi-numerical methods. In the case of a medium with finite extent the Monte Carlo method offers a satisfactory solution. When the Boltzmann equation is expressed in its integral form it is revealed that radiation transport is a Markov process. This has been demonstrated by Williamson [Williamson, 1988] by expressing fluence Φ in equation (4.17) in orders of scattering:

$$\Phi = \sum_{n=1}^{\infty} \Phi_i \tag{4.18}$$

With Φ_i representing fluence of the ith scattered particles, the Boltzmann transport equation can be modified to calculate the particle fluence for each scattering order within a medium of sources and absorbers. After some straightforward mathematics the integral form of the Boltzmann transport equation is re-written in terms of collision density $\Psi(\mathbf{r}, \mathbf{\Omega}, E)$. $\Psi(\mathbf{r}, \mathbf{\Omega}, E)$ represents the number of photons with state $(\mathbf{r}, \mathbf{\Omega}, E)$ entering a collision per unit volume, steridian, energy and time. Finally, the integral form of the Boltmann transport equation is:

$$\Psi(\mathbf{r}, \mathbf{\Omega}, E) = \sum_{n=1}^{\infty} \int\int\int \Psi^n(\mathbf{r}', \mathbf{\Omega}', E') P(\mathbf{r}, \mathbf{\Omega}, E | \mathbf{r}', \mathbf{\Omega}', E') dR' d\Omega' dE' + \Psi^1(\mathbf{r}, \mathbf{\Omega}, E) \tag{4.19}$$

with

$$\Psi^1(\mathbf{r}, \mathbf{\Omega}, E) = \int_0^{\infty} \mu(E) e^{-\mu R} S(\mathbf{r} - R\mathbf{\Omega}, \Omega, E) dR \tag{4.20}$$

These two equations state that the only source of n times scattered particles with energy E and direction Ω are the (n-1) times scattered particles scattering into the state $(\mathbf{\Omega}, E)$ somewhere along the line $\mathbf{r}' = \mathbf{r} - \mathbf{\Omega} R$. $P(\mathbf{r}', \mathbf{\Omega}', E' | \mathbf{r}, \mathbf{\Omega}, E)$ is a conditional probability density function showing that the probability of a particle experiencing its nth collision at $(\mathbf{r}, \mathbf{\Omega}, E)$ is given by a conditional transition probability which depends solely on the particle's state prior to its (n-1)th collision:

$$P(\mathbf{r}, \mathbf{\Omega}, E | \mathbf{r}', \mathbf{\Omega}', E') = \mu(E) e^{-\mu(E)|r - r'|} \frac{\mu(\mathbf{\Omega}, E | \mathbf{\Omega}', E')}{\mu(E')} \delta[\frac{(\mathbf{r} - \mathbf{r}')}{|\mathbf{r} - \mathbf{r}'|} \cdot \mathbf{\Omega} - \mathbf{1}] \tag{4.21}$$

where δ is the Kronecker delta function. Equation (4.21) reveals that radiation transport is a Markov process. In such processes the probability of entering a certain state depends on the last state that occurred. In radiation transport, this simply implies that in order to find the solution to the particle fluence in phase space $(\mathbf{r}, \mathbf{\Omega}, E)$ one must consider all possible random walks through that space. This essentially means that radiation transport is stochastic in nature therefore that a solution to the radiation transport problem can be obtained using the Monte Carlo method.

According to the above, in a Monte Carlo simulation of radiation transport, each particle history is fully represented by an array $[\mathbf{s}_i^j | i = 1, ..., N_i; j = 1, ..., N_j]$

of which each (vector) element denotes the state of the photon just before the ith collision:

$$\mathbf{s}_i^j = (\mathbf{r}_i^j, \Omega_i^j, E_i^j, W_i^j) \tag{4.22}$$

$\mathbf{r_i}, \Omega_\mathbf{i}$ and E_i indicate position, direction and energy. W_i represents the particle weight for that state. Using probability density functions which govern particle scattering and transport it can be easily shown that such arrays are randomly sampled from all possible trajectories given by the solution of the Boltzmann transport equation [Williamson, 1988].

4.3.2 Monte Carlo simulation of physical processes

Simulation of particle transport

The mean distance a particle of a given energy travels in the medium is known as its *mean free path* (MFP) λ and is given by

$$\lambda = \frac{M}{N_a \rho \sigma_t} = \frac{1}{\Sigma_t} \tag{4.23}$$

where M is the molecular weight of the medium,N_a is Avogadro's number, ρ the density of the medium, σ_t the total cross section per molecule and Σ_t the macroscopic total cross section. The mean free path may change as a particle moves from one medium to another or when it loses energy [Nelson et al., 1985]. The number of MFPs N_λ traversed by particles between positions x_1 and x_2 in a medium is

$$N_\lambda = \int_{x_1}^{x_2} \frac{dx}{\lambda(x)} \tag{4.24}$$

Using the inversion sampling method and a random number R between 0 and 1 (see section 4.2.2) the number of mean free paths to the next interaction is sampled from the cumulative probability distribution function

$$F(x) = 1 - e^{N_\lambda} \quad for \quad N_\lambda > 0 \tag{4.25}$$

and is

$$N_\lambda = -ln(1 - R) = -ln(R') \tag{4.26}$$

Finally to calculate the location of the next interaction one substitutes the value for N_λ from equation (4.26) in equation (4.24).

Monte Carlo codes employed for solving the Boltzmann transport equation generally utilise specific techniques for simulating the transport of charged particles. This is because the typical number of collisions experienced by electrons while slowing down in matter is considerably higher (10^5) compared to photons ($\simeq 30$) [Williamson, 1989]. The cross sections of all charged particle interactions become infinite as the transferred energy approaches zero and exact values for very large cross sections are not well known [Nelson et al., 1985]. Therefore, direct simulation of all these physical interactions is not practical. Instead, charged particle interactions are treated together in a continuous manner and cutoff energies are used to distinguish continuous and discrete interactions. The technique of combining the effects of many collisions is known as *condensed history* technique. It divides the electron history into a manageable number of steps, each one accounting for the combined effect of many individual collisions.

The simplest condensed history approach is the *continuous slowing down approximation* (CSDA) technique. In CSDA, within each charged particle step, the charged particle is assumed to lose energy continuously, such that the energy lost is a deterministic function of its total pathlength, s_j, traversed through its jth step. This method ignores multiple scattering and energy-loss straggling (i.e the fluctuations of energy loss about its mean value caused by random production of δ-rays and bremsstrahlung photons and the correlation between these energy loss events and the trajectories of the primary charged particles [Rogers and Bielajew, 1990]).

A condensed history can be presented as a sequence of vectors $\beta_j = (r_j, \Omega_j, E_j, s_j)$ with r_j denoting the position, Ω_j the direction, E_j the energy and s_j the pathlength of the charged particles. The direction Ω_j of a charged particle emerging from the jth step is sampled from one of the multiple scattering distributions. These are most commonly derived from the Molière [Molière, 1948] or the Goudsmit-Saunderson [Goudsmit and Saunderson, 1940] multiple scattering theories. The energy loss along the pathlength is calculated from the unrestricted collisional stopping power. Seltzer *et al.* [Seltzer et al., 1978], Berger and Seltzer [Berger and Seltzer, 1982], Rogers and Bielajew [Rogers and Bielajew, 1988a] and others have discussed the case of 20MeV electrons incident on a flat slab of water and have examined the resulting depth dose data using the CSDA model with or without multiple scattering and energy-loss straggling. The inclusion of the effect of multiple scattering leads to a lateral spreading of the electrons which shortens the depth of penetration of most electrons and increases the dose

at shallower depths (due to the increased fluence). Energy-loss straggling introduces a depth straggling because the actual distance travelled by electrons varies according to the energy they give up to secondaries.

Berger [Berger, 1963] divided electron transport algorithms into two categories (classes) according to the way they treat individual events that lead to bremsstrahlung photons and/or knock-on electrons.

Class I models simulate each condensed history step by grouping together the energy losses and angular deflections associated with individual events. The energy and direction of the primary electrons are not affected by the creation of secondary particles. Energy losses instead of being calculated during each multiple scattering step from CSDA are sampled from an energy straggling distribution. Scattering angles are determined from a multiple scattering distribution. Class I schemes are used in codes ETRAN [Seltzer, 1988] and ITS [Halbleib and Mehlhorn, 1984].

Class II or *'mixed procedures' models*, group together the effects of secondary particles (knock-on electrons and/or bremsstrahlung photons) with energies below a certain threshold (considered as *minor* collisions) and treat individually those interactions (*major* or *catastrophic* collisions) resulting in secondary particles with energies above the energy thresholds (production thresholds). The energy and direction of primary electrons is only affected in the case of discrete interactions. The choice of the values for production thresholds is arbitrary. For collisions involving energy transfers below some production threshold Δ the CSDA-multiple scattering condensed history approach is used. The pathlength between multiple scattering steps is calculated using the restricted stopping power L_Δ. Collisions with energy transfers greater than Δ are simulated individually and give rise to randomly sampled δ-rays or bremsstrahlung photons. The trajectories of these particles are sampled from appropriate differential cross sections. EGS4 [Nelson et al., 1985] is a representative of class II models.

Both classes use cutoff energy thresholds below which the energy of secondary particles is deposited locally. Class II algorithms are, in principle, more accurate than class I because they consider correlations between primary and secondary particles [Rogers and Bielajew, 1990]. Detailed discussion and comparisons between the two classes can be found in the literature [Rogers and Bielajew, 1990], [Rogers and Bielajew, 1988b].

Simulation of particle interactions

The interactions considered for photon simulations are usually the photoelectric effect, Compton scattering, pair production and Rayleigh (coherent) scattering. In *the photoelectric effect* a photon gives up all its energy to an electron, which is ejected from the atom with the corresponding energy less the binding energy of the electron. If an inner shell electron is knocked out then *characteristic radiation* may also be emitted when an outer shell electron drops into the vacancy in the inner shell. In *Compton scattering* a photon collides with a free electron, transferring momentum to the recoiling electron. *Pair production* occurs when a photon with energy greater than 1.02MeV interacts with the nucleus to produce an electron-positron pair. The positron may further *annihilate* to produce two 0.511MeV photons. *Rayleigh (coherent) scattering* is the (elastic) scattering of photons from atoms with no energy loss causing the entire atom to move just enough in order to conserve momentum.

Electron interactions simulated by Monte Carlo codes include Møller and Bhabha scattering, bremsstrahlung emission and positron annihilation "in-flight" and at rest. *Møller and Bhabha scattering* are collisions of electrons or positrons respectively with atomic electrons. An excited or ionised electron deposits its energy in the medium as heat. If it has sufficient energy it can be considered as a *delta ray* and carries energy a significant distance away from the interaction site. *A bremsstrahlung process* occurs when an electron or a positron are scattered by a virtual photon from the field of a nucleus together with the production of a free photon. In *positron annihilation in flight or at rest* an electron and a positron annihilate and produce two photons of energy 0.511MeV.

When a particle reaches a point of interaction an interaction process must be selected and the parameters for the product particles must be determined. The probability that a given type of interaction occurs is proportional to its cross section. If the possible interactions are numbered between 1 and n, then the ith interaction number is a random variable with distribution function

$$F(i) = \frac{\sum_{j=1}^{i} \sigma_j}{\sigma_t} \tag{4.27}$$

with σ_j the cross section of the jth type of interaction and σ_t the total cross section

$$\sigma_t = \sum_{j=1}^{n} \sigma_j \tag{4.28}$$

The F(i) are the *branching ratios.* The number of interaction to occur i, is selected by picking a random number **R** and finding the i which satisfies:

$$F(i-1) < R < F(i) \tag{4.29}$$

4.3.3 Statistical analysis and efficiency

Estimation of errors

Monte Carlo simulation of radiation transport is analogous to an experiment with the only difference that the "experiment" is carried out in the computer. There are two approaches for evaluating uncertainties [Andreo, 1991]. Following the *batch-wise* method, some Monte Carlo codes divide the total number of histories N to be simulated into n number of batches of N/n histories each, and statistical uncertainties are evaluated using the mean values of the variables scored in each batch. On the other hand, in the *history-wise* method, uncertainties are estimated using a single set of N histories, and both the quantity of interest and its squared value are scored whenever a particle is transported a given pathlength. Uncertainties are then evaluated during simulation of each history; this process is equivalent to assuming that every history is a batch of its own. Although, it has been proven that in general, the *history-wise* method gives the most efficient estimation of uncertainties ([Lux and Koblinger, 1991], [Ma, 1992]), codes such as EGS4 and ITS use the *batch-wise* approach. This is because, with sufficiently large number of histories in each batch, the results for individual batches will be approximately normally distributed and the corresponding confidence limits are easily obtained.

In the *batch-wise* approach, if the calculated quantity from the ith batch is T_i then the Monte Carlo estimate $\bar{T}$ of the true mean is obtained from:

$$\bar{T} = \frac{1}{N}\sum_{i=1}^{n} T_i \tag{4.30}$$

The variance associated with the distribution of T_i is given by

$$s_T{}^2 = \frac{1}{n-1}\sum_{i=1}^{n}(T_i{}^2 - \bar{T}^2) \tag{4.31}$$

On the assumption that the T_i are drawn from a normal distribution, the best estimate of variance σ^2 of the true mean is given by

$$s_{\bar{T}}{}^2 = \frac{s_T^2}{n} \tag{4.32}$$

The final result from the Monte Carlo calculation is written as:

$$T = \bar{T} \pm s_{\bar{T}} \tag{4.33}$$

Andreo calculated ratios of $s_{\bar{T}}$ defined as values from *batch-wise* to *history-wise* technique, and has demonstrated the dependence of the standard deviation of the mean on the number of batches n. [Andreo, 1991]. In EGS4 and ITS codes it is standard practise to use 10 batches. For $n \gtrsim 10$, one can assert that the interval $(\bar{T} - s_{\bar{T}}, \bar{T} + s_{\bar{T}})$ contains the true value of the mean in about 68% of all cases, or 95% of all cases for $\pm 2 s_{\bar{T}}$ [Rogers and Bielajew, 1990].

Variance reduction techniques

Variance reduction techniques commonly used in radiation transport simulations are categorised into three groups [Bielajew and Rogers, 1988b]. Those applied to electron transport, those concerning photon transport and a third group of general methods.

Electron specific methods

Geometry Interrogation Reduction. In a condensed-history radiation transport code electrons are transported differently from photons. Electrons travel only small distances during each electron step whereas photons can travel relatively long distances before interacting. If the distance travelled by an electron is small compared to the size of the regions in the simulation geometry, which effectively means that the electron is transported in an infinite medium, a lot of time is spent in unnecessary geometry checks. Geometry interrogation reduction can be an option in the code to allow the user to avoid such redundant geometry calls. When this option is switched on, the distance to the nearest region boundary is computed and maintained in a variable and only when this distance falls below a preset value the geometry routine is interrogated.

Zonal Discard. If the range of the electron is less than the distance to the closest scoring region boundary, the energy of the electron may be deposited in the current region. This is an approximation because the creation and transport of any bremsstrahlung photons that otherwise might have been created is ignored. The error is considered to be small [Bielajew and Rogers, 1988b].

Range Rejection. With range rejection techniques, electrons are discarded because they cannot reach some region of interest. As in zonal discard, the contribution of bremsstrahlung photons from the discarded electrons is neglected. A common application of this technique is found in simulations of energy deposition in the sensitive volume of particle detectors. In this case the user might wish to transport particles in the whole volume of the detector, but only score the quantity of interest within a certain region of the detector.

Photon specific methods

Interaction Forcing. This technique is very useful when there is a high probability that a photon will pass through a region of interest without interacting. To force photons to interact within a region, one must sample the number of mean free paths λ from a conditional probability distribution which governs the probability of the photons experiencing a collision after λ MFPs, given that they interact within an absorber of thickness Λ (measured in MFPs) [Rogers and Bielajew, 1984]. The probability distribution of a photon interaction is:

$$p(\lambda)d\lambda = e^{-\lambda}d\lambda \tag{4.34}$$

From this, we construct the conditional probability distribution

$$p(\lambda)d\lambda = \frac{e^{-\lambda}d\lambda}{\int_0^{\Lambda} e^{-\lambda'}d\lambda'} \tag{4.35}$$

with Λ the total number of mean free paths along the direction of motion of the photon to the end of the geometry. λ is restricted to $0 \leq \lambda \leq \Lambda$ and if R is a random number uniform in the range of $0 \leq R \leq 1$, then λ is calculated from,

$$\lambda = \ln(1 - R(1 - e^{-\Lambda})) \tag{4.36}$$

According to the above, forcing photons to interact within a region requires altering the probability distribution from which the MFPs will be sampled. This variance reduction technique is an *importance sampling technique* (see section 4.2.3) and because of the biased probability distribution, a weight must be assigned to each forced photon and its descendants. This weight

ensures that the photon maintains the correct amount of statistical significance compared to photons which experience no interaction forcing, in other words it ensures the "fair game" of the Monte Carlo method. The weighting of such forced photons takes the form,

$$w' = w(1 - e^{-\Lambda}) \tag{4.37}$$

with w the old weighting factor and w' the new weighting factor. The factor $(1 - e^{-\Lambda})$ represents the probability of the photon interacting before travelling Λ mean free paths.

Exponential Transform. The *exponential transform* technique is useful in surface (e.g., build-up in photon beams) or deep penetration problems (e.g., shielding calculations), where only a small proportion of photons interact in the region of interest. In the example of a photon beam normally incident on the surface of a medium, to bias the interaction probability distribution the distance λ, measured in MPFs, is shortened or extended according to,

$$\tilde{\lambda} = \lambda(1 - C\mu) \tag{4.38}$$

where $\tilde{\lambda}$ is the scaled distance, μ is the cosine of the angle the photon makes with incident photon direction and C is the scaling parameter. Therefore the interaction-probability is,

$$\tilde{p}(\lambda)d\lambda = (1 - C\mu)e^{-\lambda(1-C\mu)}d\lambda \tag{4.39}$$

The values of C are restricted by $|C| < 1$. For $C = 0$ the above equation gives the unbiased probability distribution, for $0 < C < 1$ the probability distribution is biased so that the photon pathlength in the forward direction is "stretched"("Path-length stretching"), and for $-1 < C < 0$ the pathlength is "shortened" in the forward direction ("Path-length shortening"). Sampling from the above probability distribution, the number of mean free paths to the next interaction can be shown to be,

$$\lambda = -\frac{ln(R)}{(1 - C\mu)} \tag{4.40}$$

with R a random number chosen uniformly over the unit interval $[0, 1]$. The weighting factor applied to photons which are forced to interact in this manner is,

$$w' = w \frac{e^{-\lambda C \mu}}{(1 - C\mu)} \tag{4.41}$$

where w is the old weighting factor and w' is the new weighting factor. To increase the efficiency in the build-up region of photon beams one should use $C < 0$. For such values of C it can be seen from equation 4.41 that photons which do happen to penetrate deeply will receive a very large weighting factor. If these photons subsequently backscatter into the region of interest they increase the variance considerably. A *particle splitting* technique can be then employed to avoid this.

Particle Splitting and Russian Roulette. *Particle splitting* divides large-weight particles into N particles with weights $w' = w/N$. With this, each of the resulting particles has less of an influence on the overall statistics. Furthermore, particles which emerge from the splitting with very small weights and are heading away from the region of interest, can be given the chance to be discarded by playing *Russian roulette*. *Russian roulette*, a converse process to splitting, is a way of terminating particles in regions where information is not required. In this technique a random number is generated and compared with a pre-set threshold ζ. If the random number lies above the threshold then it is discarded, whereas if it lies below, it is allowed to "survive" with a new weight $w' = w/\zeta$. Although particle splitting and Russian roulette are often used in conjunction with exponential transform, they can be employed alone in applications where the region of interest involves only a fraction of the simulated geometry. In these cases photons are set to split as they approach the region of interest and they are made to play Russian roulette as they recede.

General Methods

Secondary particle enhancement. This technique is applied to cases where one wants to study the behaviour of secondary particles in diagnostic X rays or the effect of pair production in low atomic number materials in radiotherapy. In low energies ($\approx$ 70 keV) the bremsstrahlung cross section is much smaller than the Møller cross section, so the calculation of bremsstrahlung characteristics is difficult. To decrease the variance associated with such results instead of creating just one photon after a bremsstrahlung interaction, N photons are created with weight 1/N relative to the electron's weight. The

energy and angular distributions are sampled N times and N new photons are placed on top of the particle "stack". In order to preserve the stochastic nature of the primary electron, its energy is reduced only by the energy of one of the secondary photons. Although this procedure violates the energy conservation for that primary electron, the average energy over many histories and many interaction is conserved [Bielajew et al., 1989].

Sectioning, use of pre-computed results. Sectioning is used for saving computational time and involves using results from previous Monte Carlo simulations. The method assumes that there is no interaction between the sections. This is a good approximation for simulations such as modelling a linear accelerator to study the effects of scatter originating from the head of the machine [Rogers et al., 1988], [Chaney et al., 1994]. After modelling each section of the head (starting from the source) the phase space parameters of the particles leaving that section are stored and used in following simulations to model the transport of particles through collimators and filters of the machine.

A second example of the method is the use of pre-computed fluence-to-dose conversion factors to calculate dose due to an arbitrary incident spectrum. The conversion factors are derived for monoenergetic, infinitely broad electron and photon beams incident normally on semi-infinite slabs of tissue and water [Rogers, 1984a]. Thus, calculation of dose is limited in the cases of beams which are broad and normally incident.

Geometry equivalence. According to the geometry equivalence theorem, the energy deposited from a circular beam of radius ρ_b on a circular detection region with radius ρ_d is the same as that from a circular beam with radius ρ_d on a detector region with radius ρ_b. When calculating dose in regions within a small radius using beams with radius much larger than the scoring region, very few photons are likely to reach the region of interest and deposit their energy there. Application of this theorem, allows one to calculate the central-axis depth dose for a finite-radius beam by scoring the dose in a finite region from a zero-area beam. The gain in efficiency is very large.

Geometry symmetry. Improvement in efficiency can be achieved by using some inherent symmetry in the simulation geometry. In this case one needs to perform a simulation at a portion of the geometry and assign results for the rest of the phantom according to that symmetry.

Correlated sampling. This technique is used for comparing two or more simulations, by combining the comparison into a single problem. The efficiency is increased since the direct difference is calculated instead of the separate individual quantities. The technique is also used for testing the accuracy of an approximate theory, by calculating the difference between the idealised and non-idealised situations [Kahn, 1954]. It has been applied in radiotherapy for the calculation of the correction factors for ion chambers and Fricke dosimeters [Ma, 1992], LiF TLDs [Mobit et al., 1996] and for computing the heterogeneity correction factor for a electron dose distribution in a heterogeneous medium [Holmes et al., 1993].

4.4 Applications of the Monte Carlo method in radiotherapy physics

Andreo in two review articles [Andreo, 1991], [Andreo, 1994] provides a thorough discussion on the use of Monte Carlo techniques in radiotherapy. Applications are categorised in four major groups:

Simulation of radiotherapy treatment machines. Monte Carlo modelling of the geometry configuration of ^{60}Co sources and accelerator treatment heads provides practical means for obtaining energy spectra and angular distributions of photons and electrons emerging from such machines, as well as information on the influence of their design on dose deposited in an irradiated medium [Petti et al., 1983b], [Petti et al., 1983a], [Mohan et al., 1985], [Mohan, 1988], [Udale-Smith, 1988], [Udale-Smith, 1990], [Udale-Smith, 1992], [Chaney et al., 1994].

Simulation of dosimeter response. The simulation of ionisation chambers has received considerable attention. The importance of accurate electron transport and the production of "interface artefacts" in regions which are small compared to electron step sizes has been discussed by many [Bond et al., 1978], [Nath and Bond, 1981], [Nahum, 1988b], [Bielajew, 1990a], [Bielajew, 1990b], [Rogers, 1992], [Rogers, 1993], [Ma and Nahum, 1993], [Ma, 1992], [Bielajew and Rogers, 1992b], [Mobit et al., 1996].

Calculation of physical quantities. The applications of Monte Carlo modelling which had the greatest impact on radiotherapy are those

which have provided better understanding of the physics of radiation transport. These include simulations where different interactions are "switched on or off" [Seltzer et al., 1978]; those providing the energy distribution around a single photon interaction site or a point monodirectional beam [Mackie et al., 1988b], [Andreo, 1988]; calculations of electron spectra and water/air stopping-power ratios from monoenergetic electron beams [Nahum, 1976], [Nahum, 1978] and proton beams [Medin and Andreo, 1995]; mass energy-absorption coefficient ratios [Cunningham et al., 1986] and even examinations on the effect of strong longitudinal magnetic fields on dose deposition [Bielajew, 1993a].

Treatment Planning. Basic data used for advanced three dimensional dose calculation algorithms have been generated using Monte Carlo techniques [Lax et al., 1983], [Mackie, 1984], [Mohan et al., 1986], [Ahnesjö et al., 1987]. The method is also widely used as a benchmark tool, for assessing the performance of treatment planning algorithms.

Within the last five years, considerable efforts have been directed towards true three dimensional Monte Carlo Treatment Planning (MCTP) employing patient CT density information. These include the:

- UNION code: based on EGS4 and calculating dose from photon or electrons beams [Manfredotti et al., 1990],[Manfredotti et al., 1995].
- Macro Monte Carlo (MMC) approach: based on EGS4 for 3D electron dose calculations [Mackie and Battista, 1984], [Neuenschwander et al., 1995], [Neuenschwander and Born, 1992].
- Voxel Monte Carlo (VMC) model: also developed for fast electron dose calculations [Kawrakow et al., 1996].
- OMEGA project: utilising EGS4, this collaborative investigation lead to the development of the BEAM code designed to model radiation transport through the linac heads and further utilised the MMC model for computing routinely the dose from clinical electron beams [Mackie et al., 1990b], [Rogers et al., 1995], [Mackie, 1995b].
- McRad Monte Carlo model: based on EGS4 for calculating the incident photon fluence distribution to be used directly with a superposition model [Lovelock et al., 1995].

Applications of the Monte Carlo method in brachytherapy include:

- Simulations of well detectors used for the calibration of sources [Williamson et al., 1983a].
- Simulations of encapsulated ^{226}Ra and ^{192}Ir sources [Williamson et al., 1983b] and comparisons with numerical results from the Sievert integral.
- Computation of dose distributions in water of a number of point isotropic brachytherapy sources [Webb and Fox, 1979], [Burns and Raeside, 1987]. Monte Carlo modelling of ^{125}I, with a low mean energy of $30keV$, a high attenuation coefficient and therefore a particularly steep dose gradient, is a difficult task [Dale, 1982].

4.5 The EGS4 Code System

The **E**lectron **G**amma **S**hower System, version 4 (EGS4), is a general purpose package for the Monte Carlo simulation of the coupled transport of electrons and photons in an arbitrary geometry for particles with energies above a few keV up to several TeV [Nelson et al., 1985]. This is an analog Monte Carlo program, where each and every particle is followed until it reaches its final destiny, usually an energy limit (energy cutoff) or a discard boundary. Details on the structure and the physics modelling of EGS4 can be found in the manual of the EGS4 system published by the Stanford Linear Accelerator Center (SLAC-265 Report) [Nelson et al., 1985]. The history and a general overview of EGS is very well documented in a joint report by the National Research Council of Canada (NRCC), the National Laboratory for High Energy Physics of Japan, and SLAC [Bielajew et al., 1994].

EGS4 is a collection of subroutines and block data with a flexible user interface. The entire code is written in a structured language called Mortran (Mortran3), a FORTRAN like language developed at SLAC [Cook, 1982]. Mortran3 contains a very useful macro-facility which reduces the length of the code considerably as well as increasing its flexibility. Macros provide the user with an easy and effective way of introducing changes in EGS4 itself without actually having to edit the code. Figure 4.2 includes a schematic representation of the general structure of EGS4. The EGS4 System is now available for a number of operating system environments: Unix (egs4unix_2.0) [Bielajew, 1993d], VAX/VM and Alpha/VM, IBM/VM(CMS) and DOS [Walker et al., 1992]. It can run on a large range of hardware platforms from PCs to Crays as well as on a variety of architectures [Bielajew, 1993e], scalar, parallel [Ma, 1994] and vector [Miura, 1987].

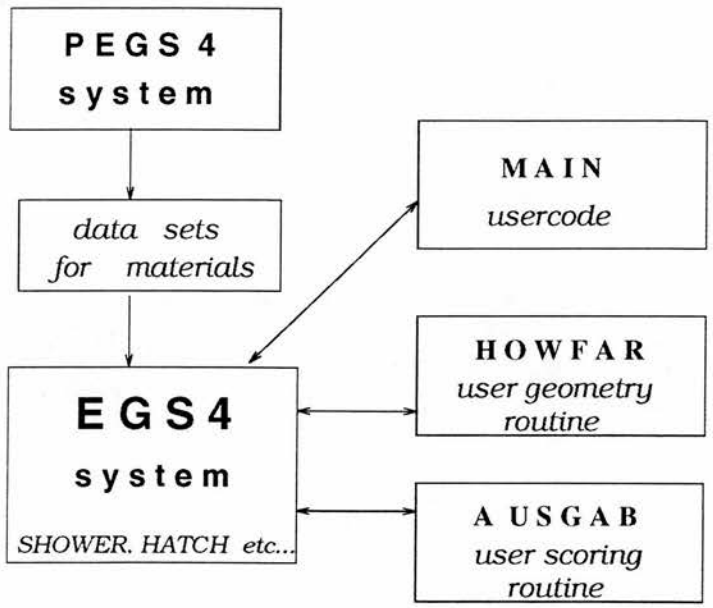

Figure 4.2: *Schematic representation of the structure of the EGS4 system*

Distributions of the system are available on tape or ftp transfer from the NRCC, SLAC or the Lanzl Institute of Medical Physics in Seattle [Bielajew, 1993d].

4.5.1 The physics in EGS4

EGS4 can simulate the radiation transport of electrons, positrons and photons in any elements, compound or mixture. The preprocessor PEGS4, creates data to be used by EGS4, using cross section tables for element 1 to 100. Photons or charged particles are transported in random steps. The dynamic range of charged-particle kinetic energies goes from a few tens of keV up to a few thousand GeV, whereas the dynamic range of photon energies lies between 1 keV and several thousand GeV. The following physical processes are considered within EGS4 [Nelson et al., 1985]:

- Bremsstrahlung production.
- Positron annihilation in flight and at rest.
- Molière multiple scattering (*i.e.*, Coulomb scattering from nuclei).
- Møller (e^-e^-) and Bhabha (e^+e^-) scattering.
- Continuous energy loss applied to charged-particle tracks between discrete interactions.

  - Total stopping power consists of soft bremsstrahlung and collision loss terms.
  - Collision loss determined by the (restricted) Bethe-Bloch stopping power with Sternheimer treatment of the density effect.
- Pair production.
- Compton scattering.
- Coherent (Rayleigh) scattering is optional.
- Photoelectric effect. The default version of the subroutine for the photoelectric effect does not include the production of fluorescent photons or Auger electrons.

4.5.2 Preprocessor for EGS4 (PEGS4)

PEGS4 is a stand-alone data preprocessing code consisting of 12 subroutines and 85 functions. The program needs to be used only once prior to simulation to obtain the media data files required by EGS4. With PEGS4 certain parameters are required as input such as atomic masses and densities. In PEGS4, two important low energy thresholds are set. `AE` is the threshold for discrete electron collision losses (delta-ray production) and `AP` is the threshold for discrete electron radiation losses (bremsstrahlung). The output is directly read by EGS4 using the subroutine `HATCH`. Details of the physical models used to calculate cross sections and the implementation of the PEGS4 routines are given in the PEGS4 User Manual (Appendix 3 of the SLAC-265 manual).

4.5.3 User written routines

The `MAIN` routine

The user must write a `MAIN` program, together with two subroutines; these three modules comprise what is known as the *usercode*. The `MAIN` program is an initialisation routine, where the user specifies the simulation geometry, the type of the incident radiation and sets energy, position and direction parameters for incident particles. The cut-off energy parameters `ECUT` and `PCUT` are set here. These are the energy limits for electrons and photons respectively, at which particle histories are terminated. These must have higher values than the corresponding secondary particle production thresholds (`AE` and `AP` respectively). In the default version

of EGS4 it is also important to set a parameter, ESTEPE. This represents the electron maximum fractional energy loss per step due to continuous energy losses [Rogers, 1984b]. Subroutine SHOWER is called once for each source particle. The order of which particles are transformed is related to the position of the particle on the stack. STACK is the common block holding variables with the information of particles currently in the shower. NP is the integer indicating the particle being pointed to, as well as the number of particles to be transported. After the simulation of NCASE source particles is complete, the arrays containing output data are analyzed and printed. Variance reduction techniques can be incorporated into the usercode (defined at the beginning of MAIN), in the form of Mortran3 macros. Such macros are available for the implementation of importance sampling, leading particle biasing, interaction forcing [Rogers and Bielajew, 1984], [Bielajew and Rogers, 1988b], particle splitting, Russian roulette *etc.*. A typical MAIN code is written in the following order [Nelson et al., 1985]:

1. Step 1: User-override of EGS4 macros. At the beginning the user specifies common blocks, declares various input variables and macros.

2. Step 2: Pre-HATCH initialisation. Medium information and energy cutoffs are given at this stage. This includes, number of materials, material names and densities, ECUT and PCUT values.

3. Step 3: Call to subroutine HATCH. Data created using PEGS4 are read by HATCH.

4. Step 4: Initialisation for HOWFAR. Geometric information for phantom is given at this stage.

5. Step 5: Initialisation for AUSGAB. Here, dose scoring arrays are initialised.

6. Step 6: Determination of incident particle parameters. At this step, the nature of incident particles, the energy and the direction of the beam with respect to the phantom surface are set.

7. Step 7: Call to subroutine SHOWER. SHOWER is called NCASE times.

8. Step 8: Output of results. The final stage involves reporting results, essentially saving calculated information in a file.

Subroutine HOWFAR

This subroutine specifies the simulation geometry and checks whether a particle will cross a boundary in its next step. EGS4 calls HOWFAR when it wishes the current particle to be transported by a distance USTEP in a straight line. If no boundaries are crossed HOWFAR returns. If a boundary is crossed, then HOWFAR identifies the new region via variable IRNEW and sets USTEP to the distance to the boundary. To speed up simulations and avoid unnecessary boundary checks in large regions the user can set variable DNEAR. This variable is set equal to the minimum distance from the particle's current position to a boundary and HOWFAR is called only when the proposed particle step length is greater than the current value of DNEAR. In that case DNEAR is updated, that is, its value is decreased by the steplength. The information returned from HOWFAR to the subroutine which calls it includes the region number at the end of the step and the steplength. It also returns a flag called IDISC, which when set to unity, determines the immediate termination of the particle history. Several auxiliary geometry routines exist for modelling planes, cylinders, cones and spheres or a combination of these (the Combinatorial Geometry (CG) [Guber et al., 1967]) and some are available together with the EGS4 code.

Subroutine AUSGAB

This routine performs the scoring of variables and parameters of interest (phase-space information, charge, energy deposited etc). AUSGAB is called by default at the beginning of a step (after HOWFAR) and at the end of a particle track. The array of flags IAUSFL makes the scoring system very flexible. The first five of these flags are set to unity in a default EGS4 simulation. The remaining twenty flags are zero by default, but can be overridden to unity (in MAIN) to allow a call to AUSGAB just before and/or after an interaction. An example of this important feature of EGS4 will be demonstrated in the following chapter. To score the energy deposited by a particle in its step, variable EDEP is used. Auxiliary subroutines can be set within AUSGAB to keep track of energy deposited or exiting the irradiated medium (subroutine ECNSV1), or the number of times energy is scored (subroutine NTALLY) or even to carry out a detailed step by step or event-by-event tracking of the simulations (subroutine WATCH).

4.5.4 Improvements/enhancements to EGS4

The report by [Bielajew et al., 1994] records a number of improvements to EGS version 4, carried out after its release in December 1985. These are included as options to the default EGS4 code and can be utilised ("switched on") by the use of flags or macros in the usercodes. Very significant is the development of PRESTA (**P**arameter **R**educed **E**lectron **S**tep **T**ransport **A**lgorithm), which changes the way electron transport is carried out [Bielajew and Rogers, 1986b]. The default EGS4 code simulates accurately electron transport but demonstrates a strong dependence on electron step size. This dependence is known as electron step-size artefact and refers to the dependence of calculated results upon arbitrary "non-physical" parameters of the electron transport, such as the value of ESTEPE. Bielajew and Rogers [Bielajew and Rogers, 1987], [Bielajew and Rogers, 1988a] have demonstrated that these artefacts occur because of (a) an inaccurate path-length correction (PLC): the default EGS4 code incorporates a PLC algorithm based on the Fermi-Eyges multiple scattering theory, which was shown to be inadequate; (b) the lack of lateral displacement during the course of an electron step: the default EGS4 code ignores lateral deflection during the course of a sub-step, therefore generally underestimating lateral diffusion; (c) the abuse of the basic constraints of Moliére's multiple scattering theory in the vicinity of boundaries describing the geometry of the simulation: existing multiple scattering theories are strictly applicable only in infinite or semi-infinite geometries. PRESTA circumvents the above using [Bielajew et al., 1994]:

1. A refined calculation of the average curvature of the electron sub-step (electron sub-step is the distance between point of deflection by multiple elastic scattering).

2. A lateral correlation algorithm, which introduces an extra lateral displacement to the sub-step correlated to the multiple scattering angle.

3. A boundary crossing algorithm which causes electron sub-steps to shorten in the vicinity of boundaries in order to eliminate the occurrence of electron transport artefacts near interfaces.

Further improvements include:

- The implementation of a long sequence random number generator. This is a new "universal" lagged-Fibonacci pseudo RNG as developed by Marsaglia

et al. [Marsaglia et al., 1990], [Marsaglia and Zaman, 1991]. It is written in Mortran3 and distributed for EGS4 by Bielajew [Bielajew, 1992], [Bielajew, 1994].

- The modelling of bremsstrahlung angular distribution [Bielajew et al., 1989].
- The creation and transport of K and L-shell fluorescent photons [Del Guerra et al., 1991].
- The transport of electrons in an electromagnetic field [Bielajew, 1988], [Bielajew, 1993a].
- The use of ICRU37 [ICRU, 1984] collision and radiative stopping powers [Duane et al., 1989].
- Improved photon cross sections from a more modern library [Sakamoto, 1993].
- A study of the photoelectron angular distribution [Bielajew and Rogers, 1986a]
- Improved angular distribution of the electron and positron emanating from pair production [Bielajew, 1991]
- Improved low-energy electron cross section modelling [Ma and Nahum, 1992].
- A study of the the validity of the small angle formalism in the Molière multiple scattering theory [Bielajew et al., 1993].
- Inclusion of electron bound effect in Compton scattering [Namito and Hirayama, 1991].
- Inclusion of Doppler broadening and linearly polarised photon scattering for simulations in the low energy range [Hirayama et al., 1994].
- Tools such as `EXAMIN` for understanding the quality of PEGS4 output, `PIF` (Prepare Input File) for creating PEGS4 input files [Karr and Bielajew, 1993] and various graphics packages that provide graphical output of particle tracks and geometries of EGS4 simulations [Bielajew, 1993c].

4.6 Summary and Conclusions

This review indicates that the Monte Carlo method is a powerful, invaluable and versatile tool in those problems where analytical techniques are inadequate.

However, it is also an imprecise technique, because it only provides statistical estimates rather than "exact" solutions. Furthermore it can be a very slow and costly way to study a problem. The diagram in Figure 4.1 does not imply that a Monte Carlo code can be considered as a *black box*. A good understanding of the problem to be simulated and of the physical processes under consideration is imperative. In addition, the randomness of the numbers from a RNG must be thoroughly tested. Results from Monte Carlo simulations, as from any experiment, have no significance if they are not associated with a value of uncertainty. Variance reduction techniques are specially designed tools for generating results with low uncertainties within a reasonably short period of time. Their use depends on the individual problem under study. Care must be exercised in their implementation in order to ensure a *"fair game"* in the Monte Carlo simulation.

The task of understanding and using software written by others is not easy. Monte Carlo codes are comprised of numerous subroutines and data files and it is important that these are well documented and tested. The EGS4 code system was chosen in this work because:

1. It is a very well documented Monte Carlo code; which provides confidence in its performance.

2. It is a continuously developing system; which means that there is expertise available for support and discussion.

3. It is a very flexible code; it gives sufficient freedom to users to model any problem by choosing the irradiation geometry and the desired quantities to be scored. Events can be switched on or off, without altering the main routines in the system.

4. EGS4 is easily obtained, since it is public domain software and can run on a variety of platforms.

The EGS4 Monte Carlo code, was chosen here for the generation of energy deposition kernels and as a benchmark tool. The usercode employed together with the necessary alterations carried out to it are discussed in the following chapter.

Chapter 5

Use of Monte Carlo for kernel generation and model benchmarking

5.1 Introduction

The discussion in chapter 3 suggested that Monte Carlo is the best tool for obtaining energy deposition kernels (namely, point spread functions) from different scattering orders. Chapter 4 has shown that Monte Carlo is the only precise method for computing dose data in absolute units of absorbed dose per incident energy fluence or per incident photon fluence. The EGS4 code system is currently the best available software used for energy deposition studies in radiotherapy. This chapter presents work carried out using EGS4 to generate kernels and on the development of a usercode suitable for benchmarking dose computations from clinical photon beams.

The generation of energy deposition kernels with EGS4 was carried out using one of the early usercodes, known as `XYZDOS`. This was the only usercode available in the public domain that could be used for this purpose. A description of `XYZDOS` will be given, followed by a discussion of the various alterations that were introduced here which lead to the modified version of `XYZDOS`, known as `XYZKERN`. Finally, results of monoenergetic kernels from `XYZKERN` will be presented.

Benchmarking of dose calculation models used clinically is imperative. The development of a new model is only justified if its results in homogeneous and heterogeneous media are compared with a best result, that is usually measured data. Conventional dose calculation models generate dose distributions in arbitrary units and therefore are only compared against relative dosimetric data. Results from convolution/superposition models can also be compared against

such measured data. This requires normalising the dose values, to the value of dose at a certain voxel. Since this is a *model-based* method, any errors related to incorrect input (namely in the TERMA distribution due to an incorrect representation of the spectrum or in the polyenergetic kernels) might cancel out in normalisation and therefore although the shape of the dose distribution might appear to be fine, the absolute dose values at points might be wrong. The use of EGS4/PRESTA for benchmarking purposes is investigated here. A new version of XYZDOS was developed (usercode XYZSIM) for use in energy deposition studies in cartesian geometries from polyenergetic photon beams.

5.2 Generation of energy deposition kernels

5.2.1 Usercode XYZDOS

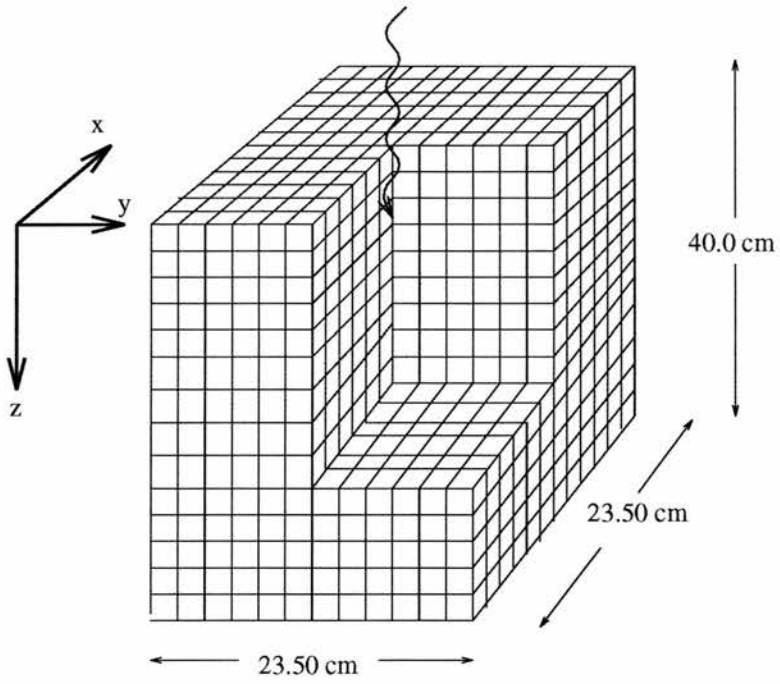

Figure 5.1: *The geometry of the simulation phantom in* XYZDOS *and* XYZKERN. *The dimensions refer to the size of the dose scoring matrix used for the generation of kernels.*

XYZDOS is an EGS4 usercode employing a three dimensional rectilinear geometry. It simulates the passage of rectangular parallel beams of photons or electrons incident on the X-Y surface at arbitrary angles. The coordinate system is right-handed with the origin set at the front left top corner of the scoring

phantom (Figure 5.1). The irradiated phantom consists of cartesian volume elements (voxels) which can be of different materials and/or varying densities. Voxel dimensions are completely variable in all three directions. This geometry is similar to that of a CT image set. This usercode was developed within EGS4 [Nelson et al., 1985] and was designed as a treatment planning example [Rogers and Bielajew, 1990]. It has been mainly used as the standard timing benchmark for EGS4 [Bielajew and Rogers, 1992a]. XYZDOS is a simple usercode, primarily not designed to study clinical dose deposition problems. Its capabilities can be summarised as follows:

1. The phantom geometry is modelled as a set of regions within a cartesian coordinate system.
2. Dose is scored in all or in a restricted number of these regions.
3. The incident photon or electron beam is set to be rectangular, parallel and monoenergetic.
4. Dose contributions are not separated into various components, i.e. only total dose can be scored.
5. It is an analog code, i.e. no variance reduction techniques are included.
6. It is not flexible in terms of allowing the user to carry out large simulations in groups, thus avoiding long runs.

As a consequence of point 3 above, XYZDOS cannot simulate beams from linear accelerators, which are divergent and polyenergetic.

For the generation of energy deposition kernels it is required that incident primary photons are forced to interact at a certain depth in water. XYZDOS does not include this option, neither has its associated subroutine AUSGAB been designed to accumulate separately energy deposited by particles originating from different orders of scattering.

Variance reduction methods which could improve the statistics or decrease calculation time are also not present.

Simulation of a large number of histories is necessary when it is desirable to obtain data with low uncertainty values. In this case extensive CPU time is required and even if the simulation is the only process running, it can take a number of weeks to complete. This is not ideal, since a lot of work can be lost if, for whatever reason, the computer is brought down before the results of the simulation are written to disk.

5.2.2 Version XYZKERN

To be able to generate energy deposition kernels using XYZDOS, a number of appropriate changes and enhancements had to be introduced. The following sections refer to the various changes incorporated into the PRESTA version of XYZDOS, which uses the long sequence pseudo-random number generator [Bielajew, 1992], [Bielajew et al., 1994]. This modified code was named XYZKERN.

Recently, however, and after this work was complete, Rogers *et al.* published their development of the BEAM code which was used in conjunction with their new version of XYZDOS known as DOSXYZ [Rogers et al., 1995]. They report that DOSXYZ simulates polyenergetic, divergent beams, uses variance reduction techniques such as those related to geometry symmetry and correlated sampling and is designed to "re-use" phase-space data as often as required to improve the statistical precision of the results. However, DOSXYZ is not available in the public domain.

Primary photon forcing

To transport photons (subroutine PHOTON), the default EGS4 code calculates the photon's mean free path GMFP (the mean distance a photon would travel in a particular medium) and samples the number of MFP's (DPMPF) the photon would travel prior to experiencing a collision (see section 4.3.2 in chapter 4). Thus, the distance to the next interaction is:

$$\texttt{TSTEP} = \texttt{GMFP} \times \texttt{DPMFP} \tag{5.1}$$

and the straight line step length USTEP for the photon in set equal to TSTEP. The photon's coordinates X(NP), Y(NP), Z(NP) are updated from the knowledge of USTEP and the direction cosines. For photons within the irradiated medium the value of DPMFP is updated from:

$$\texttt{DPMFP} = \texttt{AMAX1}(0, \texttt{DPMFP} - \frac{\texttt{USTEP}}{\texttt{GMFP}}) \tag{5.2}$$

That is, the value of DPMFP is chosen to be the maximum of 0 and the difference between the previous value of DPMFP and the number of MFPs within the current value of USTEP. If the resulting DPMFP is larger than a very small number (variable $EOSGMFP set to 10^{-6}), an interaction can take place.

For source (primary) photons, the initial value of DPMFP is calculated at the beginning subroutine PHOTON from the following macro:

```
{$SELECT-PHOTON-MFP;} WITH
{$RANDOMSET RNNO35;DPMFP=-ALOG(RNNO35);}
```

Namely, the default of this macro translates to the natural logarithm of a random number as formulated in equation (4.9), in section 4.2.2 of chapter 4. RANDOMSET RNNO35 is the macro generating a random number, in this case named RNNO35.

For generating kernels it is required that source photons "appear" at the desired interaction depth, so they are not transported prior to interacting. This essentially involves avoiding the execution of the initial part of subroutine PHOTON (see flow diagram in SLAC-265, pages 222-226, [Nelson et al., 1985]). To do this $SELECT-PHOTON-MFP is overwritten at the beginning the usercode. It is clear that if $SELECT-PHOTON-MFP is altered to set DPMFP to zero for incident photons, then TSTEP and USTEP will be also zero, the coordinates of the photon will remain the same and a new random number will be chosen to sample an interaction. This is done elegantly by using a photon forcing counter, NFTIME. Integer variable NFTIME is declared in COMMON block COMIN/USER-VARIANCE-REDUCTION/ which will be discussed in the next section. NFTIME is initialised to zero in the usercode prior to the start of a shower production (i.e. prior to the call to SHOWER). A photon is forced to interact only if NFTIME is zero. This is possible only for source photons, since NFTIME is set to one after forcing the primary photon to interact. All this is done with the following macro replacement:

```
REPLACE{$SELECT-PHOTON-MFP;} WITH

 {;IF(NFTIME=0)[DPMFP=0.0; NFTIME=1;]
   ELSE[
      NFTIME=NFTIME+1;
      $RANDOMSET RNNO35; IF(RNNO35.EQ.0.0)[RNNO35=1E-30;]
      DPMFP=-ALOG(RNNO35);
   ]
  }
```

XYZDOS requires that the user specifies the field size by giving the minimum and maximum values of the field in the x and y direction. It is also required that the user specifies the angles of incidence between the parallel beam and the phantom surface. To simulate a beam with field size larger than zero, incident particle

coordinates are sampled within that field prior to initiating particle transport. If the minimum and maximum x and y values of the field are set to zero, the beam size is set to zero by default. This defines a pencil beam of particles incident on the phantom surface along the phantom's axis of symmetry. In XYZDOS, the z-coordinate of incident particles ZIN, is set to 0cm, namely at the phantom surface. For the generation of kernels in XYZKERN, ZIN was set equal to ZINTPT. This is a new (real) variable representing the z-coordinate value, in centimeters, of incident particles. It is declared in a separate COMMON block:

```
REPLACE {;COMIN/PFORCE/;} WITH {;COMMON/PFORCE/ZWIDTH,ZINTPT;}
```

ZWIDTH is a variable assigned to be equal to the voxel size along the z-direction. The user can choose any value for ZINTPT greater or equal to zero and less or equal than the maximum length of the phantom. For the generation of kernels the voxel size was set equal to $0.5 \times 0.5 \times 0.5 cm^3$. Primary photons were forced to interact at 5.25 cm, which is the center of the voxel located with front face at the depth of 5.0 cm. This depth was considered sufficient for scoring any energy deposited due to backscattered secondary radiation for the photon energies examined.

Photon interaction forcing

Photon interaction forcing was discussed in chapter 4 (section 4.3.3). It was introduced as an option in XYZKERN mainly for the case of high energy kernels, when the probability of high energy photons escaping without interacting increases. Interaction forcing is implemented together with primary photon forcing in the $SELECT-PHOTON-MFP macro. It is based on the general purpose macro written by Rogers and Bielajew [Rogers and Bielajew, 1984], which can be used with any EGS4 geometry. As seen from equations (4.36) and (4.37) (in chapter 4) the only difficulty lies in the calculation of the total number of mean free paths each photon must traverse before leaving the medium. Rogers and Bielajew simply calculate this by carrying out a fake transport through all regions along the photon's line of flight, while calling HOWFAR each time the particle moves to a different region. Appendix A.1 lists the $SELECT-PHOTON-MFP macro as implemented in XYZKERN. It is invoked at each call to subroutine PHOTON, whenever the photon's energy is above the pre-defined cutoff limit (PCUT).

To use this macro several additional variables must be declared and used. In

default EGS4 the COMMON block COMIN/USER/ is left empty for users to include their own declarations. The egs4unix_2.0 version supplied by the National Research Council of Canada provides users with a selection of useful COMMON block overrides (stored in file nrcc4mac.mortran). One of these, is the following override of COMIN/USER/:

```
REPLACE {;COMIN/USER/;} WITH
{;COMIN/USER-STEP-CONTROLS,USER-VARIANCE-REDUCTION,USER-MISC/;}
```

For photon interaction forcing in XYZKERN the following COMMON block is used:

```
REPLACE {;COMIN/USER-VARIANCE-REDUCTION/;} WITH
{;COMMON/USERVR/GWAIT,IFORCE,NFMIN,NFMAX,NFTIME;}
```

Photon interaction forcing of photons can be "switched on" in the usercode, by assigning the value of unity to the integer variable IFORCE. For a value of zero, no interaction forcing is in effect. Integer variables NFMIN and NFMAX specify the minimum or maximum number of photon interactions for which photon forcing is "switched on or off". For this work, NFMIN was set to 1 and NFMAX to 4. As seen in $SELECT-PHOTON-MFP in Appendix A.1, the real variable GWAIT is the probability of interaction (factor $1-e^{-\Lambda}$ in equations (4.36), (4.37), chapter 4). The weight of forced photons is adjusted by this factor. In essence, photon interaction forcing is achieved by appropriately adjusting (reducing) the number of MFPs of photons and by weighting the relative importance of the interaction i.e. by weighting the secondary particles with their probability of occurrence.

Energy conservation checks

Two energy conservation checks are considered in the generation of EDKs. The first is to ensure that energy is conserved due to the implementation of photon interaction forcing and the second to check whether the integral energy in the kernels is calculated correctly.

Energy conservation during photon interaction forcing. Interaction forcing techniques work by causing interactions to happen and then weighting the results by the probability of interaction. Therefore, the total energy deposited in the medium will be the same as the total energy deposited when no interaction forcing is implemented. An explicit check on energy conservation is required to

verify that interaction forcing is carried out correctly. This means that the fraction of incident energy deposited in the medium and the fraction escaping, must add up to unity.

After a forced interaction, the weight of the photon as well as that of resulting particles will be WT(NP) $\times$ GWAIT. WT(NP) is the weight of the forced photon and GWAIT the probability of interaction. If the energy of the photon prior to forcing is E(NP), then the energy of the forced photon will be WT(NP) $\times$ GWAIT $\times$ E(NP). Forcing assumes that one is not interested in those photons with probability 1 $-$ GWAIT, i.e. those which do not interact. Therefore, these "virtual" escape photons have weight WT(NP) $\times$ (1 $-$ GWAIT) and energy WT(NP) $\times$ (1 $-$ GWAIT) $\times$ E(NP). To keep track of this energy the following declaration was included in COMMON block COMIN/USER-MISC/:

```
COMMON/USERMI/GTWOLD, VIRTGE
```

Variable GTWOLD is used only within the forcing macro and is assigned the value of the weight of the photon. VIRTGE is a real variable holding the energy value of the "virtual" escape photon after each forcing.

At the beginning of a simulation three real variables are initialised to zero. VIRTGE, EVIRT and ELOST. The latter two are declared within COMMON block COMIN/SCORE since they are used in MAIN and in AUSGAB. EVIRT is the total energy of all those "virtual" escape photons whereas ELOST is the energy of all those photons which are discarded after a request from HOWFAR. Setting the appropriate IAUSFL flags (mentioned in 4.5.3 in chapter 4) to unity in MAIN, allows calls to AUSGAB just prior to pair production, Compton and photoelectric interactions and bremsstrahlung production. These flags are IAUSFL(16), IAUSFL(18), IAUSFL(20), IAUSFL(7), respectively. During these calls, EVIRT accumulates the values of VIRTGE and the latter is re-set to zero. The energy of discarded particles EDEP is also accumulated in AUSGAB through variable ELOST:

$$\text{ELOST} = \text{ELOST} + \text{WT(NP)} \times \text{EDEP} \tag{5.3}$$

Therefore, at the end of a simulation the sums of EVIRT and ELOST are used to compute the total fraction of incident energy escaping the medium. The total fraction of energy deposited in the medium is easily calculated from the 3D energy deposition array for each batch of incident photons.

Check on kernel integrals. This check was carried out following the recommendation by Boyer [Boyer, 1988]. Boyer discussed the relationship between linear attenuation coefficients and energy deposition kernels using the concepts of *integral dose* and *kernel integral*. His conclusions are summarised as follows.

Integral dose is defined as the volume integral over all space of the product of dose with an infinitesimal mass element $dm = \rho dV$ [Attix, 1986]:

$$\Sigma = \int_V D(\bar{r})\rho dV \tag{5.4}$$

The conservation of energy requires that

$$\Sigma = \Sigma_p + \Sigma_s \tag{5.5}$$

where Σ_p, Σ_s the primary and scatter integral dose components, and

$$\Sigma = (h\nu) \tag{5.6}$$

where $h\nu$ is the energy of the incident photon.

Kernel integral is defined as the integration over the (total) kernel $k(\bar{r})$[1]:

$$< \tilde{k} >= \int_V k(\bar{r})\rho dV \tag{5.7}$$

and for a point source emitting isotropically monoenergetic photons of energy $h\nu$, it is easily shown [Boyer, 1988] that the kernel integral is equal to the product of the linear attenuation coefficient and the integral dose:

$$< \tilde{k} >= \mu \cdot \Sigma \tag{5.8}$$

Since the integral dose per photon is the quantum energy carried by the primary photon (equation (5.6)), the kernel integral can be also written as:

$$< \tilde{k} >= \mu \cdot (h\nu) \tag{5.9}$$

This product represents the energy lost per unit mean free path and essentially is the average rate of energy loss into the medium by photon attenuation per unit penetration distance.

The energy deposition kernel can be represented as the sum of a primary and a scattered photon kernel:

$$k(\bar{r}) = k_p(\bar{r}) + k_s(\bar{r}) \tag{5.10}$$

[1]Here the kernel is defined in units of dose per distance and represents the dose deposited at $\bar{r}$ around a single photon interaction site located at $\bar{r} = 0$.

and so can the kernel integral:

$$< \tilde{k} >=< \tilde{k}_p > + < \tilde{k}_s > \tag{5.11}$$

Equating (5.9) and (5.11) and considering that the linear attenuation coefficient can be expressed by the sum of an absorption μ_{en} and a scattering component μ_s:

$$\mu = \mu_{en} + \mu_s \tag{5.12}$$

one obtains the following relationships for the primary and scatter integral kernels:

$$< \tilde{k}_p >= \mu_{en} \cdot (h\nu) = \frac{\mu_{en}}{\mu} < \tilde{k} > \tag{5.13}$$

$$< \tilde{k}_s >= \mu_s \cdot (h\nu) = (\mu - \mu_{en}) \cdot (h\nu) = \frac{(\mu - \mu_{en})}{\mu} < \tilde{k} > \tag{5.14}$$

or

$$\frac{< \tilde{k}_p >}{< \tilde{k} >} = \frac{\mu_{en}}{\mu} \tag{5.15}$$

and

$$\frac{< \tilde{k}_s >}{< \tilde{k} >} = \frac{\mu - \mu_{en}}{\mu} \tag{5.16}$$

Assuming that all the energy released in the medium is deposited within the medium, equations (5.15) and (5.16) formulate that the the sum of fractional energies in primary and scatter kernels are equal to μ_{en}/μ and $(1 - \mu_{en}/\mu)$ respectively. This comprises a useful check for verifying the generation of primary and scatter kernels. Examples of such checks are presented in section 5.2.5.

Changes in AUSGAB

XYZKERN was employed for generating total energy deposition kernels and total scattered photon kernels. Their difference approximately equals the primary energy deposition kernel; energy due to bremsstrahlung or annihilation photons is included into the total scattered photon kernel.

The user has full control over scoring in AUSGAB. Subroutine AUSGAB in XYZDOS has the most basic format a scoring routine could have. Variable EDEP (in COMMON/EPCONT/) holds the energy of the current particle on the stack. For particles within the medium and with non zero EDEP, this energy is accumulated in the energy scoring array DOSEIS(I,J,K,IS,IT). I,J,K determine the current voxel position, IS is the batch number this particle belongs to and IT indicates the energy component scored. The maximum number of energy components is set

in MAIN using macro $ITMAX. In XYZDOS, $ITMAX = 1, IT = 1 and AUSGAB stores in DOSEIS(I,J,K,IS,1) all the energy deposited in the medium, i.e. total dose. For this work $ITMAX is set to 3, so DOSEIS stores total energy (IT = 1), total scattered photon energy (IT = 2) and energy deposited due to bremsstrahlung and annihilation photons originating from secondary charged particles (IT = 3).

To separate and score energy from particles originating from different scattering orders, it is necessary to "label" particles so their history can be followed. Array variable LATCH (contained in COMMON/STACK/) can be utilised for this purpose. LATCH can be set for any particle on the "stack" of particles being transported and is passed on to all its progeny (EGS4 manual page 111, TUTOR 5, [Nelson et al., 1985]). LATCH is implemented through two macro overrides (included among other NRCC macros in nrcc4mac.mortran). The macro overrides are :

```
REPLACE {;COMIN/STACK/;} WITH
{;COMMON/STACK/$LNG(E,X,Y,Z,U,V,W,DNEAR,WT,
  IQ,IR,LATCH($MAXSTACK)),LATCHI,NP;$ENERGY PRECISION E;}
```

and

```
REPLACE {$TRANSFER PROPERTIES TO # FROM #;} WITH
{X{P1}=X{P2};Y{P1}=Y{P2};Z{P1}=Z{P2};
IR{P1}=IR{P2};WT{P1}=WT{P2};}
DNEAR{P1}=DNEAR{P2};LATCH{P1}=LATCH{P2};}
```

LATCH is set just after particles are created and this is done within AUSGAB. EGS4 permits the user to change the default simulation by replacing macros at various positions. This was demonstrated in the previous section when calls to AUSGAB prior to interactions were necessary. Here, calls to AUSGAB must be carried out just after collisions take place so that particles are given the appropriate flag. To permit these calls, the following IAUSFL elements are set to unity in MAIN (step5: initialisation for AUSGAB) :

- IAUSFL(17) (IARG = 16, pair production)
- IAUSFL(19) (IARG = 18, Compton interaction)
- IAUSFL(21) (IARG = 20, photoelectric interaction)
- IAUSFL(8) (IARG = 7, bremsstrahlung production)

- IAUSFL(14) (IARG = 13, positron annihilation)
- IAUSFL(15) (IARG = 15, positron annihilation at rest)

IARG is the argument which indicates the situation under which AUSGAB is called. The process in brackets corresponds to those after which AUSGAB calls are required. LATCHI is defined as the initial value of LATCH and is set to zero at the start of each history. Appendix A.2 contains a listing of subroutine AUSGAB as implemented in XYZKERN. The rationale behind these changes can be summarised as follows:

- FLAG1 identifies particles descending from the secondary electrons including bremsstrahlung or annihilation photons emerging from these. FLAG2 identifies first scattered photons and their descendants, and FLAG3 is set to separate bremsstrahlung and/or annihilation photons originating from primary charged particles. FLAG1 is in units of LATCH, FLAG2 is in thousands of LATCH and FLAG3 is in ten thousands of LATCH.
- If the primary photon interaction is a pair production, this process will generate two particles on the stack (NP = 2). Both these particles, when AUSGAB is called, are still at the same z-position as the primary photon, therefore Z(NP) would still be equal to ZINTPT.
- If the primary photon interaction is a photoelectric effect, a secondary electron will emerge, therefore there will be one particle on the stack (NP = 1) at a depth of ZINTPT cm.
- If the primary photon interaction is a Compton interaction, a secondary electron and a scattered photon will be on the stack (NP = 2) and still at a depth of ZINTPT cm. The particle with the lowest energy is placed at the top of the history list. To assign a flag to the top particle on this list one must find out its charge IQ(NP). If this is the electron, FLAG1 is set on the top of the stack, whereas if it is a photon, then FLAG2 is set on the top of the stack.
- The energy deposited from descendants of bremsstrahlung or annihilation photons (in-flight or at rest), which originate from primary charged particles, should be included in the total scatter component. FLAG3 is set for these photons; their energy is saved separately at the end of the simulation (in MAIN) and added to total scatter.

- Since EDEP is the energy of the current particle, the actual energy scored (FTMP) in DOSEIS(I,J,K,IS,1), DOSEIS(I,J,K,IS,2) and DOSEIS(I,J,K,IS,3) is equal to EDEP weighted according to the particle's weight WT(NP). This is important when photon interaction forcing is "switched on".

Accumulation of phase-space data from independent runs

XYZDOS simulates the passage of source particles in the medium and stores energy values (in MeV) in array DOSEIS(I,J,K,IS,IT). This array includes the energy deposited within each voxel from each batch of histories and each scattering order as requested by the user. The reason for dividing the number of particle histories into batches was discussed in section 4.3.3 in chapter 4. Variable IS takes values from 1 to 10 and DOSEIS is the set of "raw" data which are analyzed after the completion of the simulation. The final energy values are stored in array DOSE(I,J,K,IT) and the corresponding uncertainty values are kept in DOSEUN(I,J,K,IT). In XYZDOS, the conversion of energy to dose (matrix DOSE) and the calculation of dose uncertainty values (DOSEUN) is carried out once after the completion of the simulation. In XYZDOS, DOSEIS is not stored to disk.

Accumulation of phase-space data from independent runs requires that information from DOSEIS is available to the next simulation of the same "experiment". In this work, XYZKERN was further modified to store and re-use DOSEIS. These changes have been introduced in a similar manner as in subroutine INPUTS.MORTRAN in usercode DOSRZ. DOSRZ will be described in one of the following chapters, since it was used for benchmarking the superposition algorithm. A separate subroutine called XYZINIT was written to carry out the following tasks:

1. Determine whether the current run is a new or a re-started simulation.

2. Set the number of new histories and the new initial random numbers required by the random number generator.

3. Set the flag which requests the storage of DOSEIS in MAIN.

4. Initialise DOSEIS in the case of a new simulation.

5. In the case of a re-started run, to read-in DOSEIS, the number of histories already simulated and the total energy leaving the phantom from previous simulations.

XYZINIT is called in MAIN during the determination of incident particle parameters (step 6). The new number of histories is divided into 10 batches. Just after the completion of these batches DOSEIS is written to a file. Also stored in the file are the total number of histories simulated (the sum of those from the previous and those from the current process) and the total energy that escaped the medium during all runs. DOSEIS contains energy information from all histories (old and new). The calculation of the fractional incident energy deposited, assigned to variable DOSE, is carried out by dividing through by the total energy reaching the primary photon interaction point. In XYZDOS, values in DOSE represent dose per unit incident fluence, i.e. $Gy \times cm^2$. In XYZKERN, DOSE holds fractions of incident energy deposited.

Geometry symmetry

Kernels have a rotational symmetry about an axis defined by the incident photon direction. Due to this symmetry, when generating kernels on a rectilinear geometry it is not necessary to score and store the whole output matrix. It is sufficient to only score/store data from one quadrant. Furthermore, since each quadrant can be mirrored to its midline, one only needs the information from half the quadrant. XYZKERN was modified accordingly, in order to reduce disk space requirements.

5.2.3 Simulation parameters

Phantom geometry

By definition, energy deposition kernels must be generated in an infinite medium, so that almost all energy is deposited within the medium. Mackie *et al.* chose a 60 cm radius sphere with the interaction at its centre [Mackie et al., 1988b]. For this work, the phantom was a parallelepiped comprising of cubic voxels of 0.5 cm. The length of the phantom in the x and y dimensions was 23.50 cm and the z dimension was 40.0 cm (see Figure 5.1). The interaction point was set at the depth of 5.25 cm in the medium and along the direction of the primary photon. The medium was water with density $1.0 g/cm^3$. The density, the relative proportion of H and O together with the energy cutoffs are specified in the PEGS4 input file. An example of this file used for the generation of 6MeV kernels is shown in Table 5.2.

```
COMP
 &INP NE=2,RHO=1.0,PZ(1)=2,PZ(2)=1 &END
WATER1                          H2O
H  O
ENER
 &INP AE=0.561,UE=1000.0,AP=0.05,UP=1000.0 &END
TEST
 &INP &END
PWLF
 &INP &END
DECK
 &INP &END
```

Figure 5.2: PEGS4 *input file used for 6MeV kernels*

EGS4 simulation parameters

The choice of parameters were based on those suggested by Mackie *et al.* [Mackie et al., 1988b]:

1. EI: Incident photon energy. Kernels were generated for energies between 0.1-20MeV.

2. NCASE: Number of incident photon histories. At least 10^6 need to be considered. Enough to reduce statistical uncertainties down to an acceptable value (about $\pm 0.5\%$ at the interaction voxel)

3. ESTEPE: Maximum fraction of electron kinetic energy lost per step via continuous energy loss, set to 0.2 for all kernels (total and total-scatter).

4. Energy thresholds and cutoffs (in MeV). These are:

   - ECUT'=ECUT-0.511: Global electron kinetic energy cut-off.
   - AE'= AE-0.511: Global secondary electron production kinetic energy threshold.
   - PCUT: Photon energy cut-off.
   - AP: Secondary photon production energy threshold.

   ECUT' and AE' were set to 50keV for incident energies of 1.25MeV or more.

   PCUT and AP were set to 50keV for incident energies of 1.25MeV or more.

```
6 MeV Kernel          simulation title
1                     number of materials
WATER1                material 1
0.561,0.05,0.01       ECUT, PCUT, ESTEPE
-1,-1,-1              numbers of groups of regions in x,y,z directions
0.0                   initial boundary in the x-direction
0.5,47                voxel width, number of voxels in x-direction
0.0                   initial boundary in the y-direction
0.5,47                voxel width, number of voxels in y-direction
0.0                   initial boundary in the z-direction
0.5,80                voxel width, number of voxels in z-direction
0.5                   voxel width in z-direction (ZWIDTH)
0,0,0,0,0,0,0,0.0     groups of regions for which density and medium
0,0,0,0,0,0,0.0,0.0                                  are not defaults
1,47,1,47,1,80,0      lower and upper x,y,z indices for which results
0,0,0,0,0,0,0                                          are to be output
0.0,0.0               range of x-values for which beam is incident
0.0,0.0               range of y-values for which beam is incident
0.0,0.0,0.0           angle of beam to phantom axis
6.0,0,0               beam energy (EIN), charge (IQIN), IWATCH
0,1,0                 initial RNG not stored, restarted run, store data
250000,0,0,0.99       NCASE, 1st, 2nd initial RNG seed, max CPU time
5.25                  interaction depth in cm (ZINTPT)
1,1,4                 IFORCE, NFMIN, NFMAX
0,0,0,0,0.0           PRESTA inputs (IPLC, IBCA, IOLDTM, BLCMIN)
```

Table 5.1: *Example of an input file for* XYZKERN

Table 5.1 presents an example of a typical input file for XYZKERN. Appendix A.3 lists the log file printed out after the completion of the simulation with this input file.

5.2.4 Results

Monoenergetic energy deposition kernels were generated using XYZKERN for incident photon energies ranging from 1.25 to 20 MeV. XYZKERN scores and stores the total kernel and the total-scatter kernel. The following sections present the 1.25 MeV, 6.00 MeV and 20.00 MeV energy deposition kernels.

1.25 MeV kernels

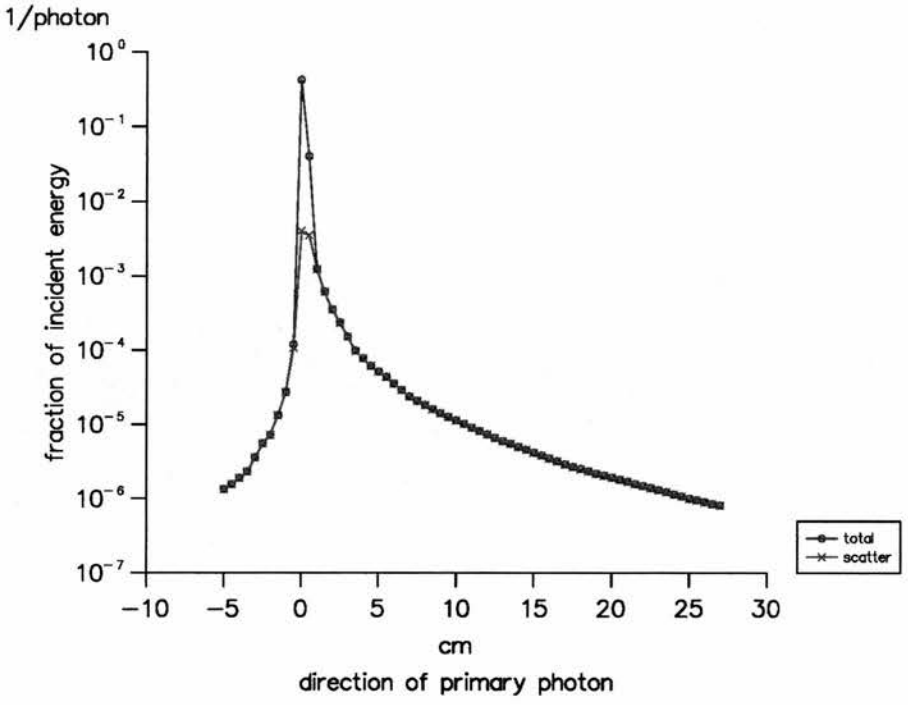

Figure 5.3: *Energy deposition kernels for 1.25 MeV: variation along primary photon direction.*

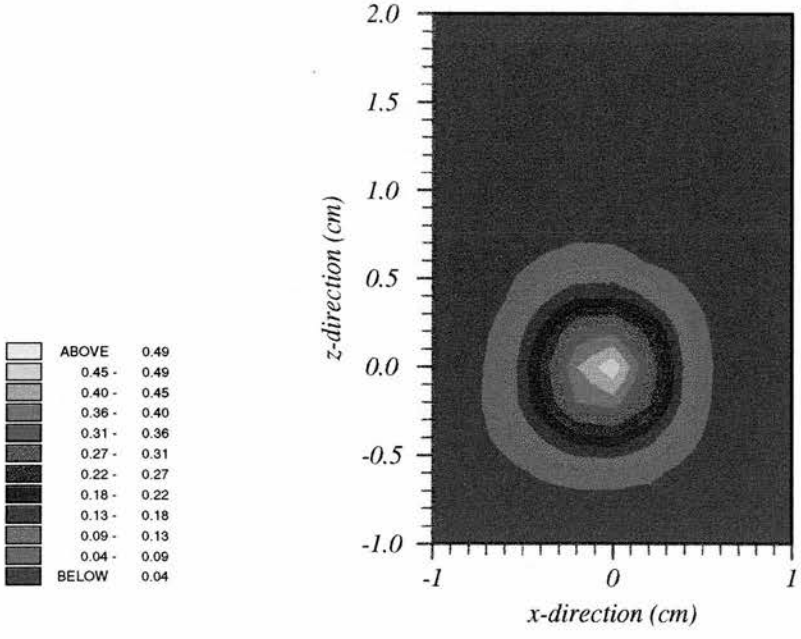

Figure 5.4: *1.25 MeV (total) energy deposition kernel: relative fractional energy values normalised to the value at the interaction voxel.*

Figure 5.3 presents the variation of total and total-scatter kernels along the direction of the primary photon (z-direction), from 1.25MeV primary photons. At this energy, secondary electrons would have a maximum range or rather less than 1.0cm and this is confirmed in the figure above. Figure 5.4 shows the same kernel in an isoline format on the plane which includes the primary photon direction (z-axis). Here, the primary photon interacts at point $(x, z) = (0, 0)$ (incident from the lower part of the graph). The distribution of energy deposited around the interaction point is almost symmetrical. The maximum energy deposition is very close to the interaction point, which justifies the lack of secondary electron transport modelling for this energy, in conventional photon dose calculation algorithms.

6.00 MeV kernels

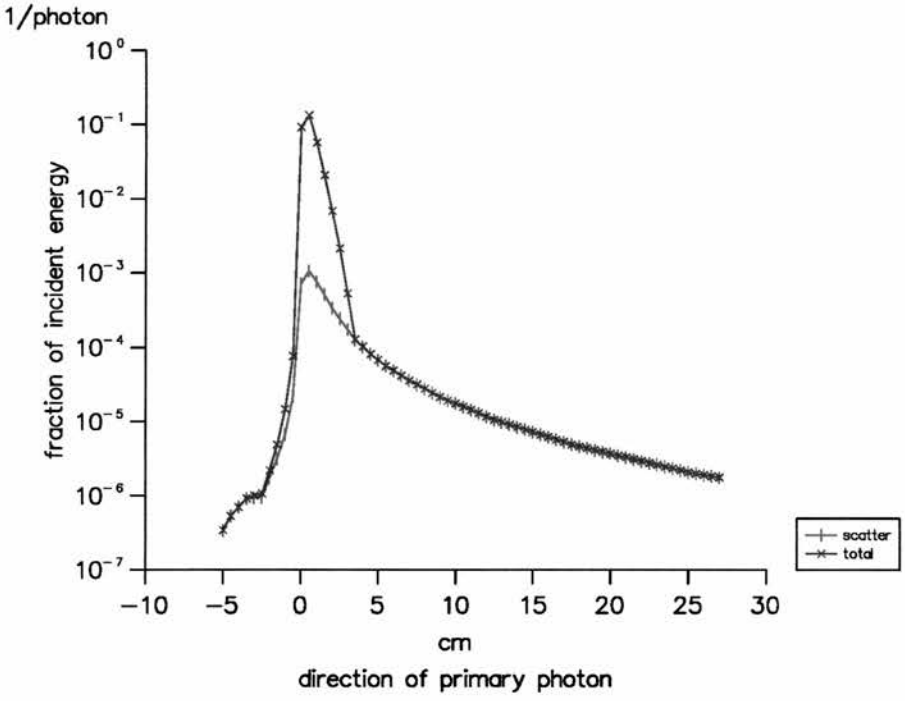

Figure 5.5: *6.00 MeV energy deposition kernels: variation along primary photon direction.*

The variation of energy deposited along the direction of the primary photon from 6MeV photons is shown in Figure 5.5. The extent of the total kernel in the forward direction is almost 3cm. This is mainly due to the range of the secondary electrons, namely the primary kernel component. Scattered photon energy comprises a significant portion of the total kernel. Any lack of electron transport modelling in this energy will introduce errors in the calculated dose,

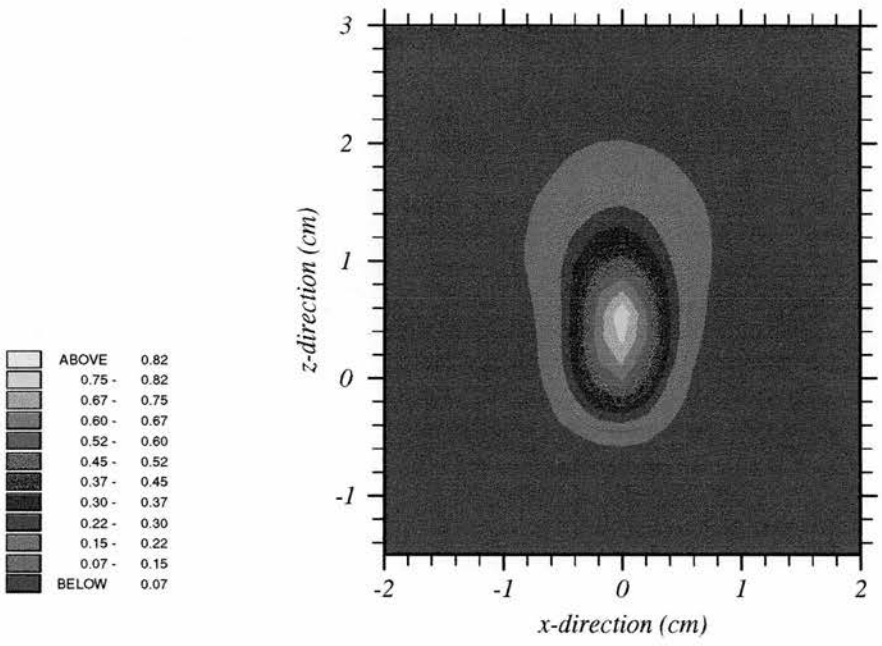

Figure 5.6: *6.00 MeV "primary kernel" in an isoline format. Fractional energy values are normalised to the value of "primary" at the interaction voxel.*

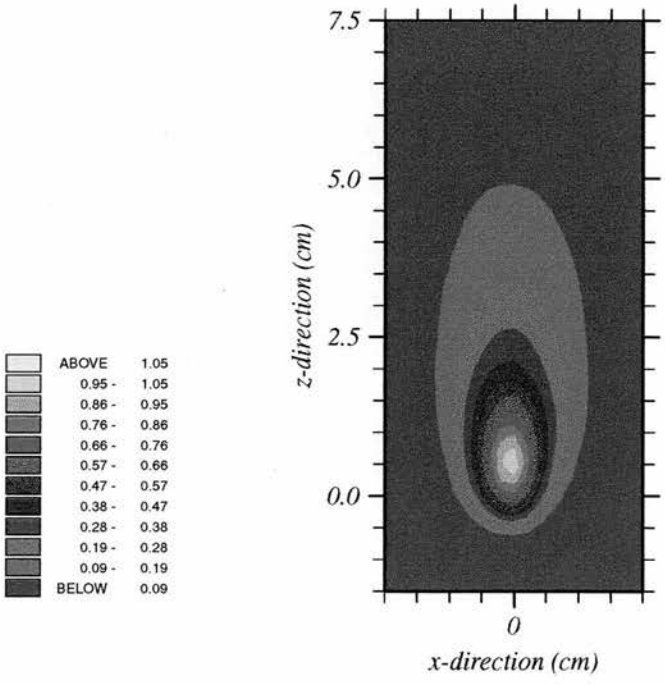

Figure 5.7: *6.00 MeV scatter kernels. Fractional energy values are normalised to the value of scatter at the interaction voxel.*

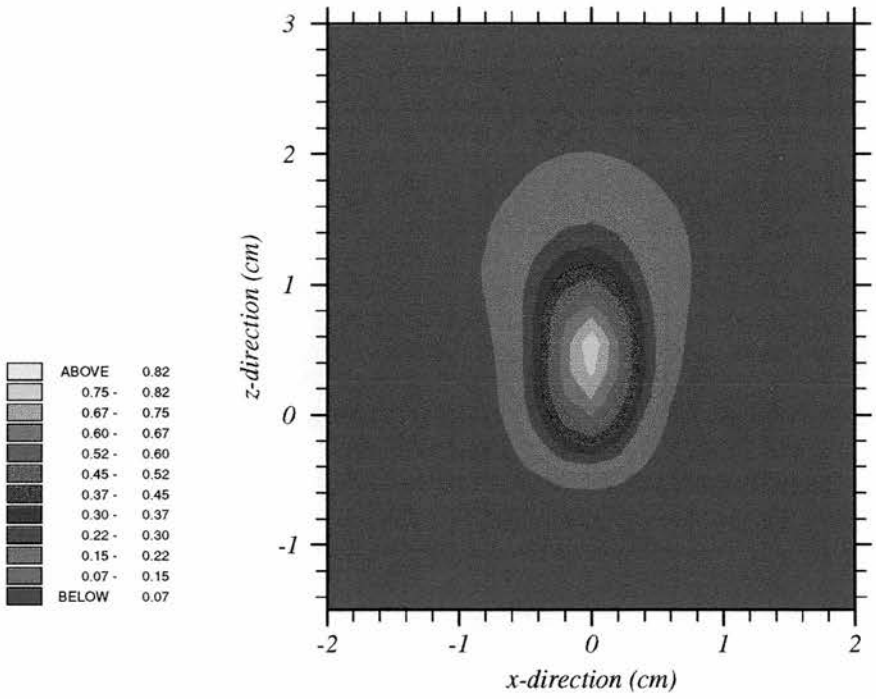

Figure 5.8: *6.00 MeV total kernel. Fractional energy values are normalised to the value of total at the interaction voxel.*

especially in low density media. Figures 5.6, 5.7 and 5.8 present the primary, total-scatter and total 6MeV kernel as an isoline distribution. The shape of the primary kernel was obtained by subtracting the total-scatter kernel from the total. This is not exactly accurate, since energy contributions from secondary electrons with very low energy are assigned to the scatter component. However, these contributions are very small. The resulting "primary kernel" in isoline format still appears to dominate the shape of the total kernel. The fractional energy distribution in the total-scatter kernel is elongated in the forward direction.

20.0 MeV kernels

In the case of incident photons of 20 MeV, secondary electrons would travel in the forward direction in water distances up to 10 cm (Figure 5.9). In Figure 5.9 it is seen that down to 12 cm from the interaction point the fractional energy in the total kernel results from both primary and scattered fractional energies; whereas beyond that depth energy contributions are almost entirely due to scatter. The distribution of energy deposited due to scattered photons is mainly in the forward direction as shown in Figure 5.11. Direct comparison between the the isoline graphs (5.10, 5.11, 5.12) is not possible because they are normalised to each component's maximum value. The primary kernel isoline distribution

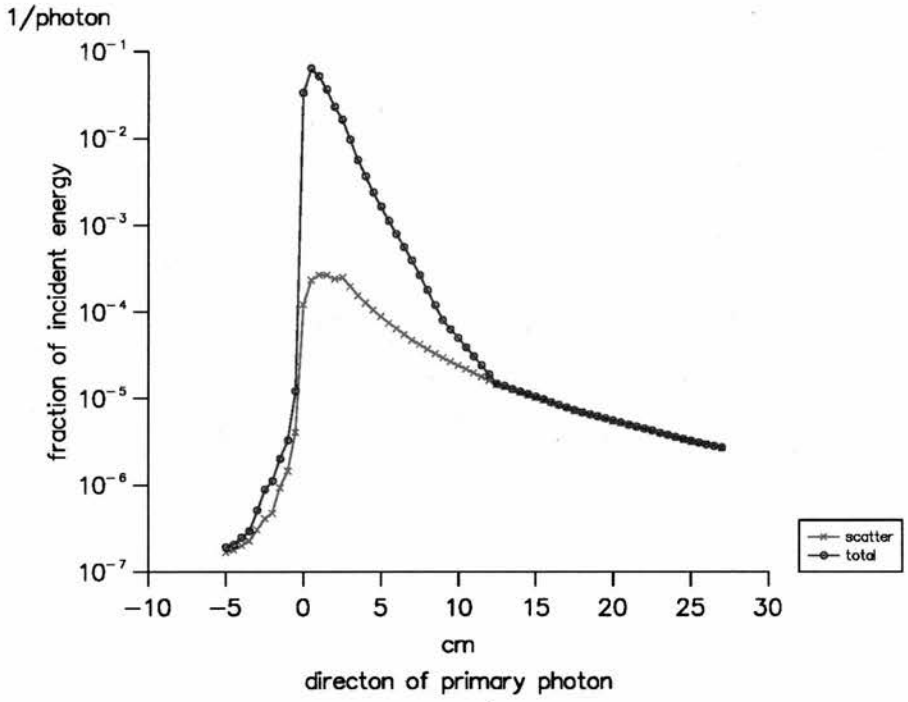

Figure 5.9: *20.0 MeV energy deposition kernels: variation along primary photon direction.*

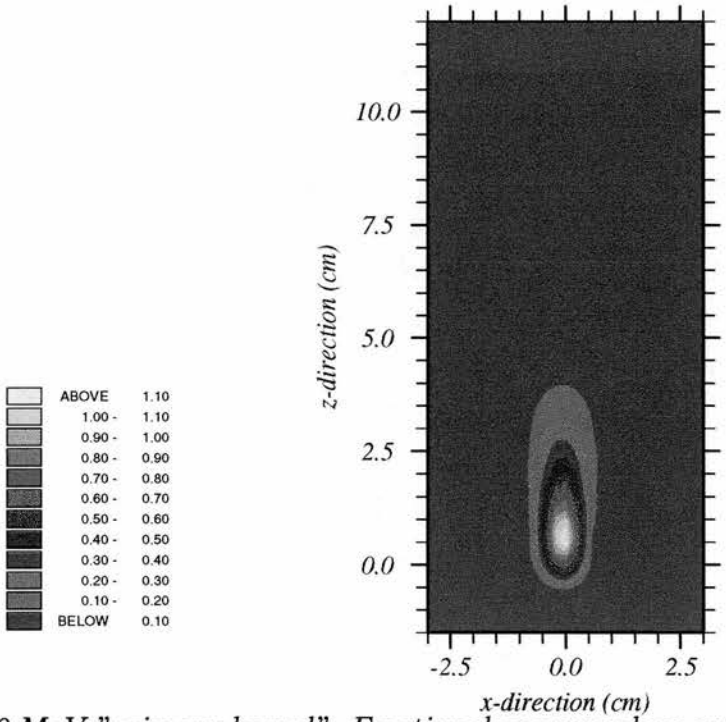

Figure 5.10: *20.0 MeV "primary kernel". Fractional energy values are normalised to the value of "primary" at the interaction voxel.*

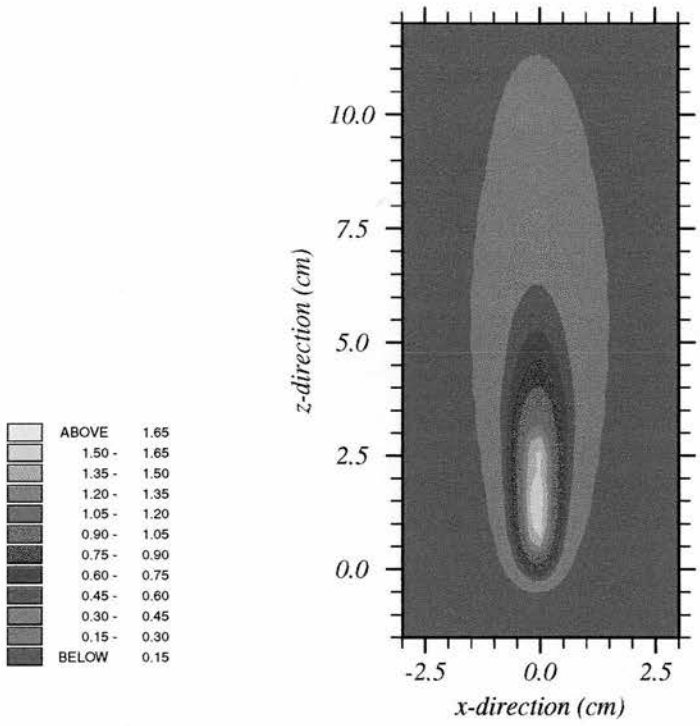

Figure 5.11: *20.0 MeV scatter kernel. Fractional energy values are normalised to the value of the total-scatter kernel at the interaction voxel.*

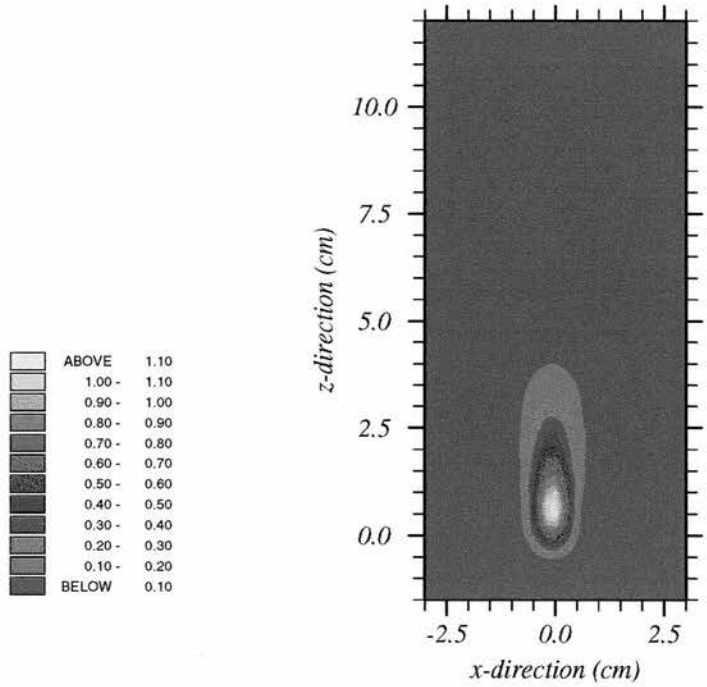

Figure 5.12: *20.0 MeV total kernel. Fractional energy values are normalised to the value of the total kernel at the interaction voxel.*

(Figure 5.10) was derived in the same way as that for the 6MeV (Figure 5.6).

5.2.5 Discussion

The values of kernel integrals are presented in Tables 5.2 and 5.3 following the conclusions from section 5.2.2.

Energy (MeV)	1.25	6.00	20.00
$\mu(cm^{-1})$	0.06413	0.0277	0.0181
$\mu_{en}(cm^{-1})$	0.02966	0.0180	0.0139
μ_{en}/μ	0.46245	0.6510	0.7644
$1-\mu_{en}/\mu$	**0.5375**	**0.3489**	**0.2355**

Table 5.2: *Linear attenuation and linear absorption coefficients for 1.25, 6.00, 20.00 MeV photons.*

Energy (MeV)	1.25	6.00	20.00
$\int k$	0.7867	0.8240	0.8699
$\int k_s$	0.3179	0.1709	0.0989
$\int k_{escape}$	0.2133	0.1759	0.1300
$\int k_p$	0.4690	0.6508	0.7621
$\int k_s + \int k_{escape}$	**0.5312**	**0.3468**	**0.2289**
$\int k + \int k_{escape}$	1.0000	0.9999	0.9999

Table 5.3: *Integral fractional kernel values from total, total-scatter and primary kernels and the total fractional energy escaping the phantom for primary photon energies of 1.25, 6.00, 20.0 MeV.*

Table 5.2 holds the values of μ and μ_{en} for energies 1.25 MeV, 6.00 MeV, 20.00 MeV [Hubbell, 1982] The two bottom lines display the ratio and differences seen in equations (5.15) and (5.16). Table 5.3 holds the following integral kernel values:

- $\int k$: is the total fractional energy scored and stored in the medium.
- $\int k_s$: is the total fractional energy scored and stored in the medium from scattered photons (including energy originating from bremsstrahlung or annihilation photons descending from secondary electrons).
- $\int k_{escape}$: is all the fractional energy escaping from the irradiated medium.

- $\int k_p$: is the fractional energy deposited as primary dose, which was calculated from: $\int k - \int k_s$.

- $\int k_s + \int k_{escape}$: is the sum of all energy from particles contributing to the scatter component of the kernel. The energy escaping the medium is considered to originate from scattered photons.

- $\int k + \int k_{escape}$: is the final energy conservation test. Namely, the sum of the fractional energy deposited in the medium and the fraction of the primary photon energy that leaves the phantom.

From Table 5.3 it is seen that during the generation of 1.25, 6.00 and 20.0 MeV kernels the primary photon energy is conserved, i.e. values of $\int k + \int k_{escape}$ are almost unity. A comparison of respective values between Tables 5.2 and 5.3 indicates that the separation in primary and scatter kernels is consistent with the theory (section 5.2.2).

If comparisons were to be carried out between kernels generated with `XYZKERN` and EGS4/PRESTA and those generated by Mackie *et al.* [Mackie et al., 1988b] who have used EGS4 without PRESTA, one should expect to identify variations which would be attributed to differences in the modelling of electron transport (see section 4.5.4 in chapter 4). Differences will be present mainly in primary kernels that are scored and stored on a matrix with a fine resolution and especially from high energy primary photons. The results presented here do not allow comparisons like these to be carried out. Mainly, because primary kernels were not seperately scored. Also because the kernels were scored in voxels sizes of $0.5 \times 0.5 \times 0.5 cm^3$ which are rather large compared to the size of electron step in low and medium energies. Nevertheless, any future work to generate sets of EDKs with EGS4, no matter what usercode and coordinate system, should use the PRESTA option.

5.3 Benchmarking against EGS4

Two EGS4 usercodes were available for benchmarking photon dose calculations. The following two sections present these codes.

5.3.1 Usercode `XYZSIM`

As discussed in section 5.2.2, usercode `XYZDOS` was altered in order to enable the generation of energy deposition kernels. It was also realised that `XYZDOS` could not

simulate the dose deposition in a medium from a divergent polyenergetic beam. Therefore, along with XYZKERN version XYZSIM was created. XYZSIM carries most of the significant alterations introduced in XYZKERN with a few more in addition. These are summarised as follows:

1. Photon interaction forcing: identical to that in XYZKERN.
2. Energy conservation check: as in XYZKERN.
3. The option of accumulating phase-space data from independent runs using subroutine XYZINIT.
4. Changes in AUSGAB which permit the separate scoring of the total-scatter component of dose (see Appendix B.1).
5. The choice of monoenergetic or polyenergetic beam: XYZDOS simulates only rectangular parallel monoenergetic beams. Appendix B.2 includes and explains the various changes incorporated to enable the input and use of an energy spectrum.
6. The option of parallel or divergent beam. XYZDOS randomly samples the coordinates of particles at the phantom surface (XIN,YIN,ZIN) and requires as input the angles of the beam to the phantom axes. From these angles the direction cosines of incident particles are computed. In the case of a rectangular beam incident normally on the surface of a phantom, it is very simple to model beam divergence. The code was set to require the source to surface distance (SSD). Since only rectangular beams are to be modelled, the X, Y coordinates of the intersection of the beam's central axis with the phantom surface are derived (XBEAM,YBEAM). From these, it is straightforward to compute the distance of each point (XIN,YIN,ZIN) from the point source and accordingly alter the direction cosines.

The above alterations, enable the use of XYZSIM for irradiations with polyenergetic divergent beams.

5.3.2 Usercode DOSRZ

DOSRZ is a usercode, written in NRCC and now provided together with the standard distribution of the EGS4 package. This code simulates the passage of an electron or photon beam in a finite, right cylindrical geometry. The main characteristics of this usercode are summarised as follows:

- The irradiated phantom is a cylinder which is defined by a number of planar and cylindrical coordinates. Each cylindrical region can be composed of different material. The user can specify whether dose is scored in all or just some of these regions.

- The energy of the incident beam is specified as a monoenergetic or a polyenergetic beam. For this work, subroutine `ENSRC.MORTRAN` was replaced by a modified version in order to use the spectral information provided by `SPEC_ANA` (see Appendix B.2).

- The source configuration can be selected by the user. Available options include parallel and point sources originating from the side or the front of the cylinder. Isotropically irradiating sources embedded in regions within the cylinder can also be modelled.

- The user sets the number of histories as well as a time limit for the execution and the desired statistical limit to be reached.

- In each of the dose scoring regions, both the total dose and the total dose less that due to stopped or discarded particles is scored. Further options allow total dose to be separated into contributions from particles entering the scoring region from different directions.

- Various transport controls can be set by the user. These include `ESTEPE`, `ECUT`, `PCUT`, `SMAX` (the maximum step size), range rejection parameters, option to include Rayleigh scattering or x-ray fluorescence and others.

- Several variance reduction techniques are implemented. These are photon interaction forcing, exponential transform, particle splitting, Russian roulette and range rejection.

- The user can select the format and degree of detail in the output.

- The current version of `DOSRZ` also scores pulse height distributions in an arbitrary volume made up of any number of regions.

`DOSRZ` uses a geometry symmetry for scoring and stores results in a two dimensional array defined by radius and depth. In cylindrical geometries the voxel size increases with radius, and in homogeneous media so does the mass of the voxels. Increasing the mass in the voxel, means more energy deposition and hence less uncertainty in the result. Uncertainties on voxels along the central axis should be

slightly higher at voxels off axis. The net flow of particle current away from the central axis complements the reduced energy deposition along the central axis. The use of such an efficient code is very advantageous. Mainly because one can obtain results with low uncertainties, fast, while running less memory intensive processes.

5.3.3 Discussion

The development of XYZSIM was carried out after realising that there was no user-code available that would simulate the energy deposited from clinical, divergent, polyenegetic beams in a complex heterogeneous medium described on a cartesian coordinate system.

For benchmarking results from other calculation models in realistic irradiation geometries, codes such as XYZSIM are invaluable. However, there is still a drawback with XYZSIM. The code does not yet incorporate variance reduction techniques (other than photon interaction forcing) which could improve the efficiency of simulations. The difficulty in efficiently using XYZSIM is displayed in Figures 5.13 and 5.14. Figure 5.13 presents total dose and total-scatter dose values along the central axis of a beam with field size of $10. \times 10. cm^2$ incident on water at an SSD of 100.0 cm. The energy spectrum information for this beam was for a 4MV X-ray beam. The spectral data used in these simulations were derived from those published by Mohan *et al.* [Mohan et al., 1985]. Figure 5.14 displays total dose profiles at various depths from the same simulation. Simulations were carried out for a total of 17 million histories. As seen from these figures the resulting dose curves for this large number of photon histories are rather noisy. The uncertainty in the voxel with the maximum total dose is $\pm 3.12\%$! It is obvious that further simulations of photon histories are necessary to improve statistics.

Dose values generated in a geometry with constant voxel sizes, have large uncertainties at larger depths and further away from the beam's central axis. This is because primary photon fluence at such positions is reduced, therefore the number of primary photons interacting within voxels is small. Although XYZSIM permits the use of variable cartesian voxel size, in order to generate results on a fine calculation grid with low uncertainties at certain regions (such as along the beam's central axis), variance reduction techniques appropriate to the simulated problem are essential. Alternatively, it would be necessary to have sufficient computing power or time to wait for the completion of many millions of particle histories. The development of such variance reduction techniques is beyond the

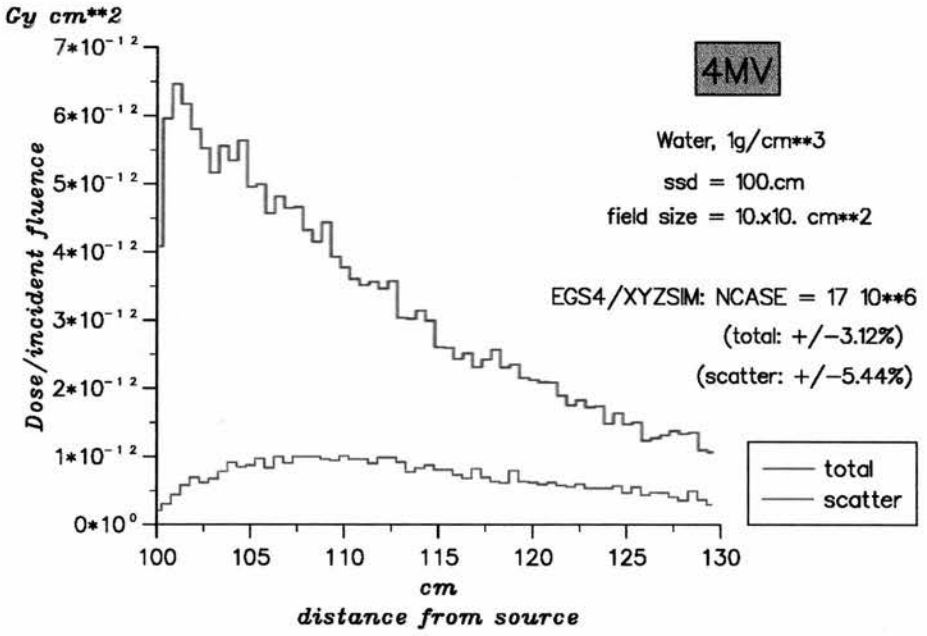

Figure 5.13: *Depth dose distributions of total dose and total scattered dose from a 4MV beam in water.*

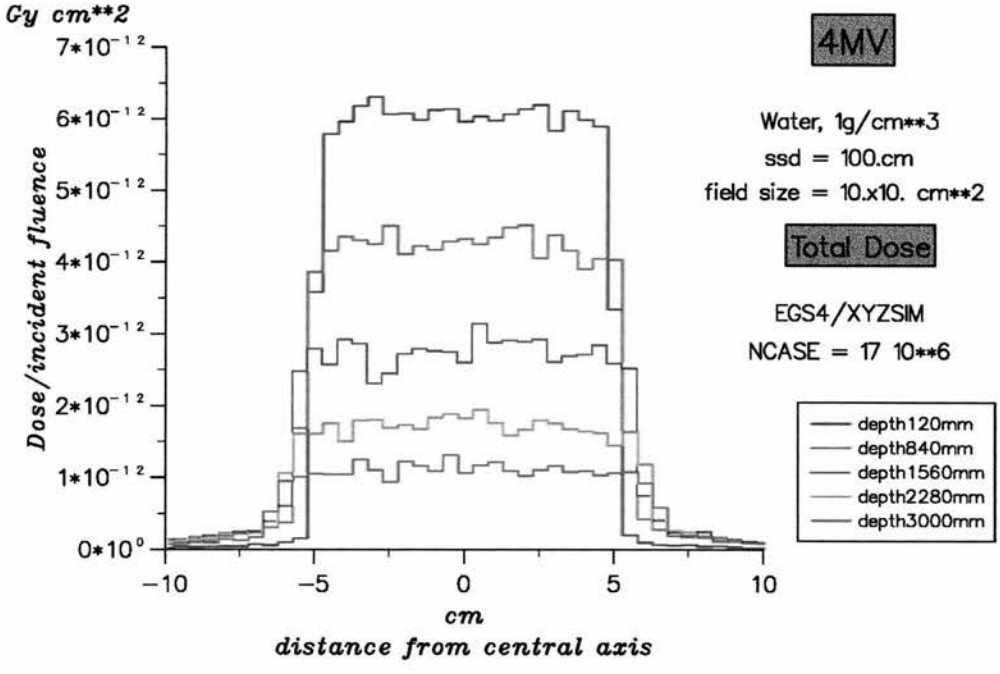

Figure 5.14: *Profiles of total dose at various depths (1.20cm, 8.40cm, 15.60cm, 22.80cm and 30.0cm) from a 4MV beam in water.*

scope of this thesis. Due to the limited computing power and time available for this work, it was decided that verifications of superposition calculations in simple geometries against Monte Carlo generated data should be carried out using DOSRZ.

5.4 Summary and Conclusions

5.4.1 Energy deposition kernels

This chapter described the generation of energy deposition kernels using the XYZKERN usercode. Figures 5.3, 5.5, 5.9, display kernel distributions (total and total-scatter components) along the direction of the primary photon from primary photons with energies 1.25 MeV, 6.00 MeV, 20.00 MeV. In these graphs, the kernels are in units of fractional incident energy deposited in cartesian voxels of size $0.5 \times 0.5 \times 0.5cm^3$. Figure 5.4 displays an isoline distribution of the 1.25 MeV total-kernel containing the direction of the primary photon. Values are normalised to the value at the interaction voxel, therefore the isolines present relative values of fractional energies. In the same manner, Figures 5.6, 5.7, 5.8, 5.10, 5.11, 5.12, display primary, scatter and total kernels for 6.00 MeV and 20.00 MeV kernels.

Choice of a suitable coordinate system

Energy deposition kernels have been generated using the Monte Carlo method on several coordinate systems (see section 3.4 in chapter 3). The following analyses the advantages and disadvantages from the use of these systems.

1. *Cartesian coordinate system.* This coordinate system was one of the first used for scoring kernels [Mackie, 1984].

   - *Advantages:* Scoring kernels on a Cartesian coordinate system is in general easy to comprehend and since CT density data and terma distributions are also stored on such a system, cartesian EDK are simple to implement in a superposition algorithm. Especially for calculations of dose in homogeneous or simple heterogeneous media it is only a matter of straightforward look-up of kernel values instead of time-consuming ray-tracing.
   - *Disadvantages:* The constant voxel size in Cartesian kernel matrices restricts their use only with terma and for dose matrices of the same

resolution. To use these kernels in any other calculation grid necessitates that these are rebinned in the new Cartesian voxel size. This might not be as complicated as rebinning kernels from other geometries (cylindrical [Rathee et al., 1993] or spherical [Mackie, 1993]). However, it requires that each time Cartesian kernels with resolution different from that of the stored kernels are required, the kernels should be rebinned to the desired voxel size, using a separate calculation. An algorithm for this rebinning, might introduce additional uncertainties in the values of the rebinned kernels.

2. *Cylindrical coordinate system.* Anhesjö *et al.* use EDKs which were scored and stored in a cylindrical geometry [Ahnesjö et al., 1987]. EDKs in cylindrical coordinate systems are easy to generate since the homogeneous water medium is cylindrically symmetric and energy values can be stored for varying combinations of depths from the interaction point and radii from the direction of the primary photon. The choice of such a scoring geometry is a compromise between geometries based on cartesian and spherical coordinate systems.

3. *Spherical coordinate system.* The choice of a spherical grid is most suited to the shape of the EDKs, because kernels are spherically symmetric entities, therefore they need only to be scored and stored in voxels defined by polar angular and radial intervals (see Figure 6.5). A spherical geometry was initially used by Mohan *et al.* [Mohan et al., 1986] and later by [Mackie et al., 1988b]. Although the Monte Carlo algorithm which generates spherical kernels is generally more complex than those used for cartesian or cylindrical studies, spherical kernels are more flexible to use, especially in terms of density scaling (see section 6.5.3).

In this work, the generation of EDKs using EGS4/PRESTA with usercode `XYZKERN` on a cartesian coordinate system provided in depth understanding of the physics and problems related to the generation of kernels. These cartesian kernels were successfully implemented within a superposition algorithm developed from the *interaction point of view.* However, it was concluded that the use of a superposition algorithm which is capable of modelling irradiation geometries with a dose matrix of potentially variable resolution, necessitates the flexibility provided by the use of spherical EDKs. Therefore, the model developed for this work, presented and verified in the next chapter, employs monoenergetic

EDK taken from the set of spherical kernels generated with EGS4 by Mackie *et al.* [Mackie et al., 1988b].

5.4.2 Model benchmarking

Any future development of clever variance reduction techniques or an increase in computing power, would enable `XYZSIM` to be used for simulations of radiation transport in more realistic situations, namely in patients, since this usercode is designed on a cartesian geometry thus permitting the use of density information from CT. Due to the advantage in generating, in a reasonable time, dose values with low uncertainties when using `DOSRZ`, this usercode was used for all benchmarking simulations in irradiation geometries that were rotationally symmetric. Such results are presented in the next chapter.

Chapter 6

A single polyenergetic superposition model

6.1 Introduction

The purpose of this chapter is to present and describe in detail the superposition model developed for this thesis. The foremost aim is to develop a 3D scatter ray trace model that would calculate dose at a point from first principles. Secondly, it was understood that this algorithm would allow the implementation of suitable approximations for optimising computation time. The following considerations are employed:

1. *Superposition in terms of terma*: The recent work by Hoban [Hoban, 1995] (also see review in chapter 3) demonstrates (for a 6 MV beam) the initial suggestion by Ahnesjö [Ahnesjö, 1991], according to which the most accurate way to perform superposition is by using collision kerma with primary kernels for the calculation of primary dose and the difference between terma and collision kerma with total-scatter kernels for the calculation of scatter dose. Such an implementation, although faster than the components method, would still be slow and therefore impractical for clinical use. Hoban concludes that the least accurate way to perform single polyenergetic superposition is in terms of terma. However, many workers have used this approach Ahnesjö *et al.* [Ahnesjö et al., 1987], Mackie *et al.* [Mackie et al., 1987], Ahnesjö [Ahnesjö, 1989] and Papanikolaou *et al.* [Papanikolaou et al., 1993]. The superposition code developed in this work, performs superposition in terms of terma (as it was considered the most practical choice) and accounts for beam hardening of the photon spectrum according to methods suggested by the above authors. The use of collision

kerma is physically more rigorous but the use of terma and a beam hardening correction, as seen in the graphs that follow, result in the same accuracy for the irradiation geometries examined.

2. *Single polyenergetic superposition*: As discussed in chapter 3 (section 3.4.2), superposition calculations for a clinical beam can be performed in two main ways. Either with the *components method*, where superposition is carried out for each spectral component, or the *single polyenergetic method*, where terma and kernel are approximate arrays weighted appropriately using energy spectrum information. The former approach is more accurate and requires longer computation times than the latter. In order to get acceptable calculation speed, the implementation of the single polyenergetic method was the most practical choice.

3. *Dose deposition point of view*: To obtain a detailed representation of the 3D dose distribution, the resolution of the calculation matrix should be as fine as that of the density matrix provided from CT. However, the larger the number of calculation points, the longer the time the algorithm requires for the calculation. An optimum number of calculation points should be used, and this necessitates the development of a flexible code, which enables the rigorous calculation of dose at individual points, such as points on a nonuniform grid. For this reason, the superposition algorithm was implemented from the *dose deposition point of view* (see chapter 3, section 3.2 and Figure 3.2).

4. *Dose per incident photon fluence (in Gy cm^2)*: The fundamental quantity for describing photon fields is the energy fluence, differential in energy, or simply energy fluence [Ahnesjö, 1995a], since this quantity is directly proportional to the output of a linear accelerator. Results from superposition are usually given in terms of dose per unit incident energy fluence (in cm^2g^{-1}) [Ahnesjö, 1989], [Ahnesjö, 1991]. Here, dose values are expressed in dose per incident photon fluence simply because the EGS4 usercodes employed for comparisons are designed to calculate dose in these units.

6.2 Reconstruction of bremsstrahlung spectra

A numerical reconstruction method based upon depth dose data measured in water was used to derive bremsstrahlung spectra. This is the method developed

by Sauer and Neumann [Sauer and Neumann, 1990]. Their code was installed on Edinburgh University's ERCVAX system (running VAX/VMS version V5.5).

6.2.1 The numerical reconstruction method

According to the publication by Sauer and Neumann [Sauer and Neumann, 1990], this method is based on the assumption that measured depth dose data, $D_Q(z)$, for a certain beam quality can be thought of as a superposition of monoenergetic depth dose curves, $D_n(z)$, with the same field size and source to surface distance:

$$D_Q(z) = \sum_{n=1}^{\infty} \Psi_n \cdot \Delta E_n \cdot D_n(z) + C(z) \tag{6.1}$$

Here, z is the depth in water, n the number of discrete energies E_n, ΔE_n the width of the individual energy bins and $C(z)$ the dose due to contaminant electrons from the accelerator head and the air between the target and the water surface. If the monoenergetic depth dose data are normalised with respect to the incoming energy fluence, then the coefficients Ψ_n represent the energy fluence spectrum. Energy fluence coefficients are normalised so that:

$$\sum_{n=1}^{\infty} \Psi_n \cdot \Delta E_n = 100\% \tag{6.2}$$

A least squares fit method is employed to minimise the difference between measured and calculated depth dose data, expressed as χ^2:

$$\chi^2 = \sum_{i=1}^{I} \sigma_i^{-2} [D_Q(z_i) - \sum_{n=1}^{N} \Psi_n \Delta E_n D_n(z_i) - C(z_i)]^2 \tag{6.3}$$

i refers to each measurement point, I being the total number of points, σ_i the uncertainty of each dose point and N the total number of energy bins. The fitting algorithm is based on a Wolfe reduced gradient method, which solves optimisation problems with arbitrary linear or nonlinear constraints. The following constraints are implemented in the optimisation algorithm:

1. All energy bins have positive values:

$$\Psi_n \geq 0 \quad for \ all \ n \tag{6.4}$$

2. Fluence in a pure bremsstrahlung spectrum with no characteristic peaks is expected to increase up to a modal energy and then decrease monotonically:

$$\Psi_n \leq \Psi_{n+1} \quad for \;\; n < n_{modal} \tag{6.5}$$

$$\Psi_n \geq \Psi_{n+1} \quad for \;\; n \geq n_{modal} \tag{6.6}$$

3. Ψ values are confined to an upper limit:

$$\Psi_n \leq \frac{100\%}{0.5 \cdot (E_{max} - E_{thres})} \quad for \;\; all \;\; n \tag{6.7}$$

where E_{thres} is the threshold energy due to filtration of the low energy photons (set at 0.5MeV) and E_{max} corresponds to the accelerating potential. This upper limit however, is usually not reached.

Smoothing of the spectral distribution is carried out by weighted averaging of adjacent energy bins. Dose due to contaminant electrons is modelled by a quadratic function of the depth from the surface.

Sauer and Neumann calculated monoenergetic depth dose curves using the kernels and convolution software provided by Mackie *et al.* [Mackie et al., 1985b], [Mackie et al., 1988b]. These curves were for source to surface distance of $100cm$ and field size of $10 \times 10cm^2$ and were provided together with the code for reconstructing spectra.

6.2.2 Description of code

The hierarchy of files comprising the spectrum reconstruction software (written in FORTRAN), as installed on the VAX computer is shown in Appendix C. `SPEC_ANA` is the main program which handles the input, calls the optimisation routine `GRGA` and outputs the results. Routine `GRGA` calculates the fitting variables so the 'goal-function' (χ^2) has its absolute maximum. The chi-square function is defined by `PHIX`, the gradient is defined by `GRADFI`, the constraints are defined within `CPHI` and the derivatives of the constrains are set by routine `JACOB`.

6.2.3 Reconstructed spectra

Measured depth dose data used with this software were for source to surface distance of $100cm$ and for field sizes of $10 \times 10cm^2$. Measurements have been carried out with silicon semiconductor diodes and were checked and confirmed with cylindrical ionisation chambers or parallel plate chambers [Thwaites, 1995].

The following sections present the reconstructed spectra for 4MV, 9MV, 6MV and 16MV beams. No explicit uncertainty analysis was carried out for the reconstructed spectra presented here. Sauer and Neumann [Sauer and Neumann, 1990] have investigated the uncertainties involved with the use of their software using the graphical $\chi^2 + 1$ method suggested by Rogers [Rogers, 1979]. They found that in the reconstructed spectra, one standard deviation of the energy fluence values is within $\pm 10\%$ of the peak value.

4MV spectrum

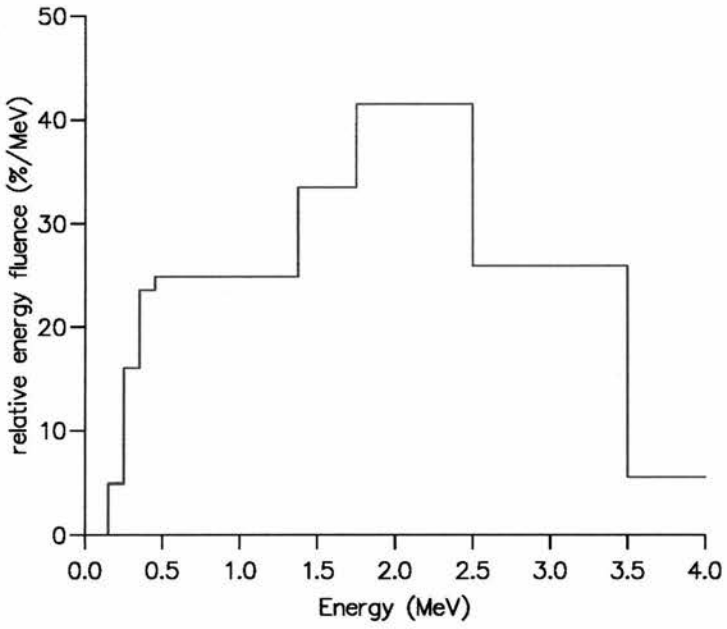

Figure 6.1: *Dynaray4, 4 MV spectrum.*

Figure 6.1 shows the relative fluence differential in energy reconstructed using depth dose data from a Dynaray4 (4MV) treatment machine. The reconstruction software produced the lowest value for χ^2 at a mean energy of about 2.0 MeV. As seen from this graph the total energy fluence is normalised to 100%.

9MV spectrum

Figure 6.2 shows the relative fluence differential in energy reconstructed using depth dose data from a Dynaray10 (9MV) machine. Here, the lowest χ^2 value is generated for a mean energy of about 4.0 MeV.

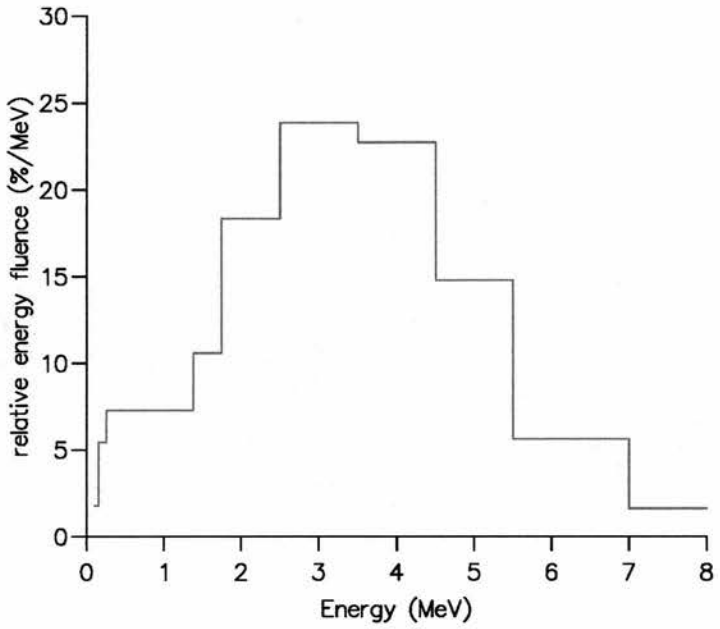

Figure 6.2: *Dynaray10, 9 MV spectrum.*

6MV spectrum

The 6 MV beam from an ABB CH6 linear accelerator has the spectral distribution shown in Figure 6.3. The most accurately reconstructed energy spectrum (corresponding to the minimum value of χ^2) results in a maximum energy fluence occurring at an energy bin that is different (less) than the mean energy. Slightly higher values of χ^2 gave spectra with maximum fluences at energies closer to the mean energy ($\sim 2.0MeV$); however, since the superposition model is not sensitive to an exact representation of the energy spectrum, it was not considered necessary to compare results from the slightly different spectra.

16MV spectrum

The reconstructed 16 MV beam from an ABB CH20 linac, is presented in Figure 6.4. The minimum χ^2 was given at a mean energy of 5.0 MeV.

6.3 Spherical energy deposition kernels

The spherical energy deposition kernels were generated at the National Research Council of Canada in Ottawa by Alex F. Bielajew and David W. O. Rogers in collaboration with Rock Mackie at the Allan Blair Clinic in Regina, Canada and

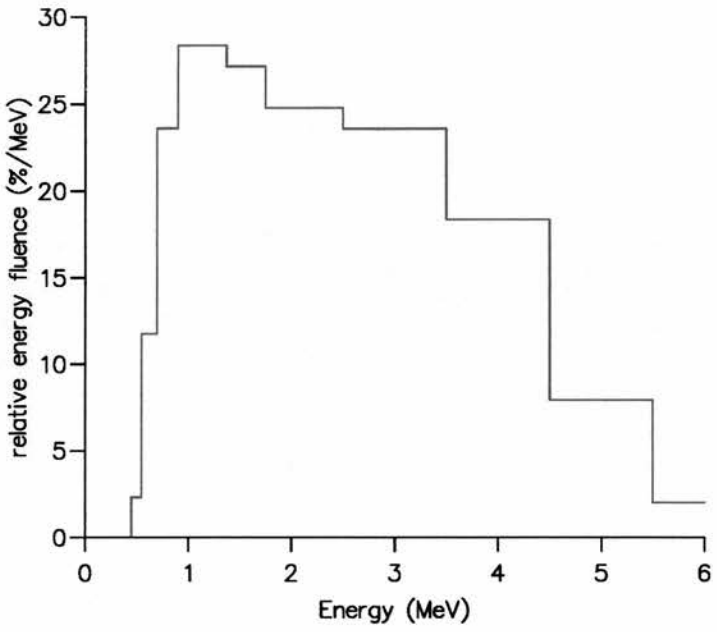

Figure 6.3: *ABB CH6, 6 MV spectrum.*

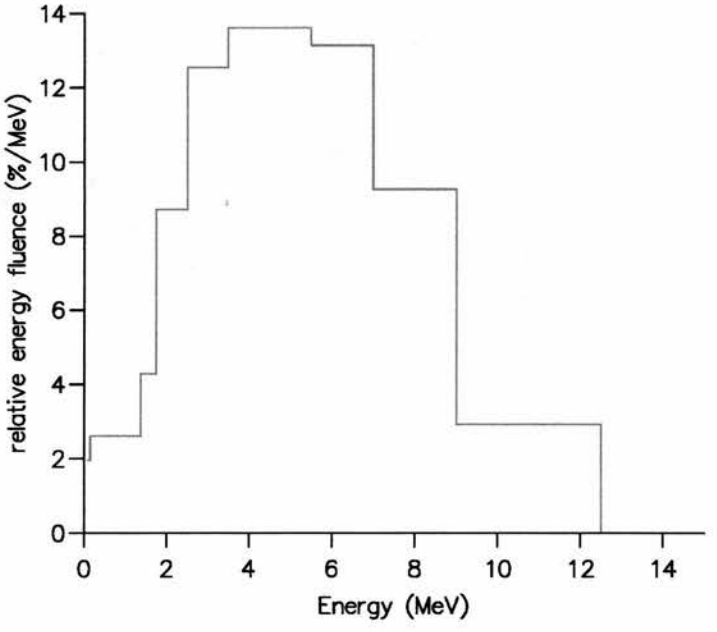

Figure 6.4: *ABB CH20, 16 MV spectrum.*

Jerry J. Battista at the Cross Institute in Edmonton, Canada. The software and documentation to use these kernels is the Copyright of Rock Mackie.

EGS4 with usercode SCASPH was used for setting up a spherical water phantom (radius of 60 cm) and for scoring and storing the fractional energy deposited in spherical volume elements due to the interaction of monoenergetic primary photons at the centre of this sphere. Figure 6.5 illustrates a voxel in the spher-

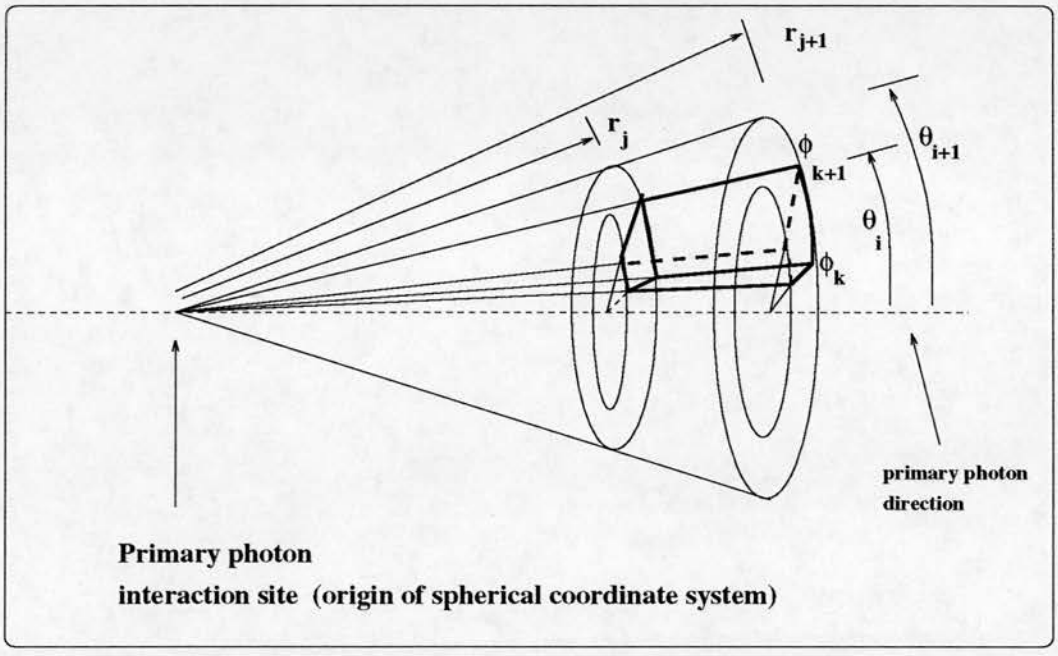

Figure 6.5: *The spherical volume element*

ical water phantom as defined by Mackie *et al.*. The kernel $h(\bar{r}, \theta, \phi)$ exhibits a rotational symmetry about the direction of the incident photon. Therefore these kernels were scored and stored as $h(\bar{r}, \theta)$ matrices with variable radial spacing and constant angular spacing of 3.75°. The spacing of radii was small at distances close to the primary interaction site and larger further away (smallest spacing was 0.05cm and largest was 10 cm). The data provided by Mackie *et al.* comprise 23 files with monoenergetic kernel information corresponding to energies from 0.1MeV to 50 MeV as well as two files containing the radial spacing (normal or enhanced) of the kernels. Each kernel file includes all information on the shower production from a primary photon interacting at the centre of the sphere. In addition, routines are also provided for manipulating these data, namely for extracting the various kernel components (primary, first-order scatter, second-order

scatter etc), or for enhancing the radial resolution (by a factor of two).

6.4 Photon spectrum consideration: beam hardening

Consideration of changes in the photon spectrum essentially refer to modelling the effect of beam hardening. Here it is based on suggestions by Ahnesjö [Ahnesjö, 1987] and Mackie *et al* [Mackie et al., 1987], according to which the energy dependence of the mass attenuation coefficient is translated to a depth dependence. Using the energy spectrum at the surface, the effective mass attenuation coefficient is calculated by weighting with respect to energy fluence (equation 3.11 in chapter 3) as a function of distance from the source $\bar{s}$:

$$\frac{\bar{\mu}}{\rho}(\bar{s}) = \frac{\int \frac{\mu}{\rho}(E)\Phi_E E e^{-\frac{\mu}{\rho}(E)\bar{s}} dE}{\int \Phi_E E e^{-\frac{\mu}{\rho}(E)\bar{s}} dE} \tag{6.8}$$

Φ_E is the photon fluence at energy E and $\mu/\rho(E)$ the mass attenuation coefficient for photons of this energy.

6.4.1 Polyenergetic terma distribution

The approximate polyenergetic terma distribution was calculated simply as the product of the effective mass attenuation coefficient and the energy fluence distribution (refer to Figure 3.3 and equation (3.2) in chapter 3):

$$\bar{T}(\bar{s}) = \frac{\bar{\mu}}{\rho}(\bar{s})\ \Psi(\bar{s}) \tag{6.9}$$

The energy fluence distribution $\Psi(\bar{s})$ is defined as:

$$\Psi(\bar{s}) = \bar{E}(\bar{s})\ \Phi(\bar{s}) \tag{6.10}$$

Fluence $\Phi(\bar{s})$ is

$$\Phi(\bar{s}) = \int \frac{d\Phi_E(\bar{s})}{dE} dE \tag{6.11}$$

and the effective energy values $\bar{E}(\bar{s})$ along the depth are energy values weighted with photon fluence:

$$\bar{E}(\bar{s}) = \frac{\int E \frac{d\Phi_E(\bar{s})}{dE} dE}{\int \frac{d\Phi_E(\bar{s})}{dE} dE} \tag{6.12}$$

Therefore equation (6.9) is replaced by:

$$\bar{T}(\bar{s}) = \frac{\bar{\mu}}{\rho}(\bar{s})\bar{E}(\bar{s})\Phi(\bar{s}) \tag{6.13}$$

where photon fluence at $\bar{s}$ is usually defined in terms of the photon fluence at the phantom surface multiplied by an inverse square correction accounting for the divergence of the beam and a factor for exponential attenuation (equation (3.13) of chapter 3). According to the work of Papanikolaou *et al.* [Papanikolaou et al., 1993], the divergence correction factor, when applied at the dose deposition site instead of the terma calculation site, corrects for the alignment of kernels along the direction of the primary photons (further details in section 6.5.4). Therefore, at the stage of calculating the terma distribution, $\Phi(\bar{s})$ in equation (6.13) can be replaced by the product of a (pre-calculated) attenuation factor and the fluence at the phantom surface [Papanikolaou et al., 1993].

$$\Phi(\bar{s}) = \bar{F}(\bar{s})\Phi(\bar{r}_o) \tag{6.14}$$

$\Phi(\bar{r}_o)$ is the photon fluence at the reference depth, here the phantom surface. $\bar{F}(\bar{s})$ for a particular beam is defined as:

$$\bar{F}(\bar{s}) = \frac{\int e^{-\mu d}[\frac{d\Phi_E(\bar{r}_o)}{dE}]dE}{\int[\frac{d\Phi_E(\bar{r}_o)}{dE}]dE} \tag{6.15}$$

where d is the depth in the medium. Finally, terma at $\bar{s}$ is calculated from:

$$T(\bar{s}) = \frac{\bar{\mu}}{\rho}(\bar{s})\bar{E}(\bar{s})\bar{F}(\bar{s})\Phi(\bar{r}_o) \tag{6.16}$$

The incident photon fluence distribution at the phantom surface can be known from simulating radiation production and transport within the treatment head of the linear accelerator [Rogers et al., 1995] [Lovelock et al., 1995]. The phase-space parameters of particles on the phantom surface can be further used as input to Monte Carlo or appropriately designed superposition models. Here, photon fluence at the phantom surface is modelled with a step function which has a value of unity within the radiation field and zero outside.

6.4.2 Polyenergetic energy deposition kernel

Accurate superposition should employ energy deposition kernels representative of the energy spectrum of the beam. On the other hand, the energy spectrum

changes with depth and the calculation and use of a polyenergetic kernel at each depth is not practical.

Polyenergetic kernels for megavoltage beams were calculated using the spectral distribution at the phantom surface by weighting with energy fluence (see equation (3.14) in chapter 3) [Ahnesjö, 1989]. It is not strictly accurate to use a polyenergetic kernel obtained using the spectrum at a certain depth, at other depths. This is because as the mean energy of the spectrum increases with depth, (a) the mean energy of secondary electrons depositing energy increases, thus their range of travel from the interaction site increases, and (b) the ratio of collision kerma to terma increases, that is the total fractional energy in the primary and scatter kernels increase and decrease respectively. The change in the range of secondary electrons results in a change in the shape of the kernel (particularly for the primary kernel). The variation in kernel shape as the beam hardens is not taken into account here, and according to Hoban [Hoban, 1995] this is not an important factor. However, the almost linear increase of the ratio of collision kerma to terma is modelled by applying a kernel depth hardening correction factor [Papanikolaou et al., 1993].

Calculation of kernel depth hardening correction factor

This depth dependent correction factor K_{CF} is derived separately for each x-ray beam by performing a simple linear fit to the ratio of depth dose values calculated by the components approach (discussed in section refsec:beamhardening) to those calculated by the single polyenergetic method:

$$K_{CF}(z) = a + b\ z \tag{6.17}$$

To calculate fitting paramenters a and b, the following steps were carried out for each beam energy:

1. Monoenergetic depth dose curves were calculated with superposition for each component of the energy spectrum. These values represent absorbed dose per unit incident fluence (in $Gy\ cm^2$).

2. The weighted sum of these curves is obtained using the photon fluence spectrum:
$$D(\bar{r}, MV) = \int \frac{D(\bar{r}, E)}{\Phi(\bar{r}_o)} \frac{d\Phi(\bar{r}_o)}{dE} dE \tag{6.18}$$

3. The components to polyenergetic superposition dose ratio was derived.

Energy MV	Slope b	Intercept a
4	0.005332	0.950222
6	0.002745	0.966797
9	0.006274	0.954483
16	0.007324	0.932721

Table 6.1: *Fitting parameters for evaluating kernel depth hardening correction factors*

4. These ratios were fitted to a line using appropriate fitting routines [Press et al., 1992]

Table 6.1 lists the values of fitting parameters a and b of equation (6.17) for the four photon beams. Figures 6.6 and 6.7 present the respective ratios and their linear fits. The importance of including a kernel depth hardening correction factor will be demonstrated in one of the following sections.

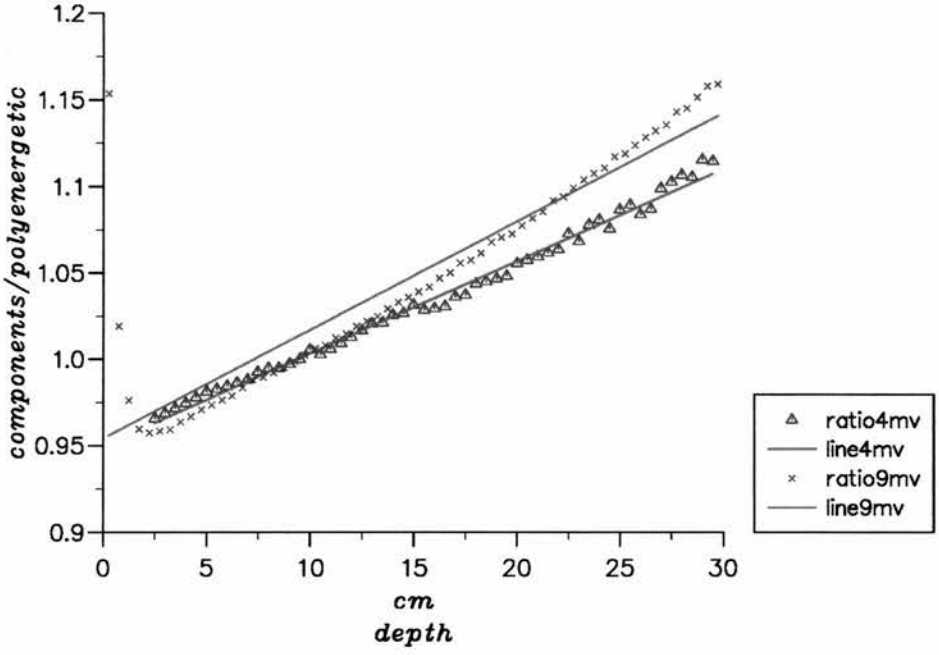

Figure 6.6: *Ratio of the components depth dose data to the single polyenergetic depth dose data for the Dynaray 4MV and 9MV beams.*

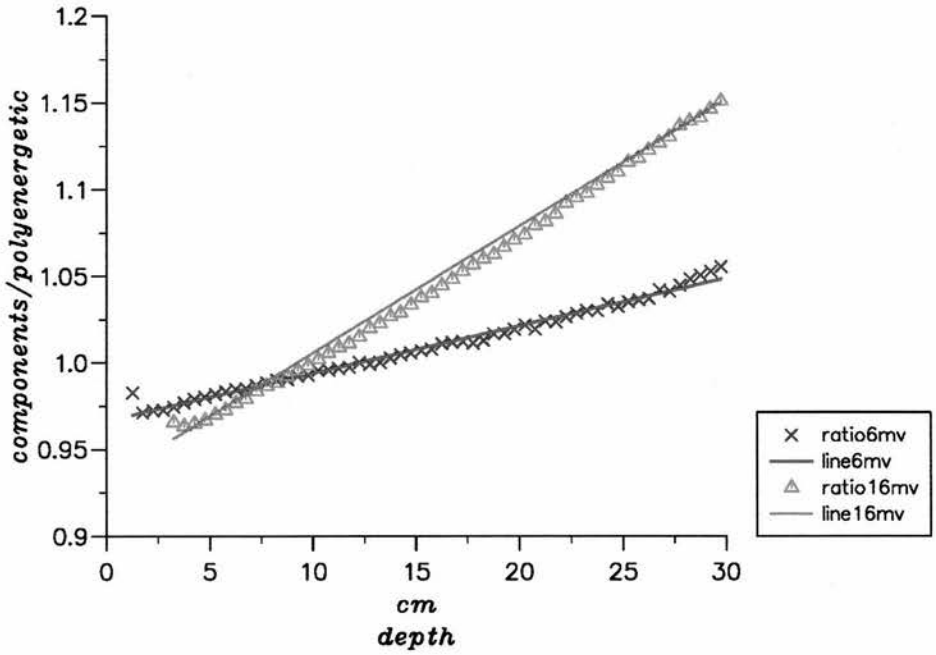

Figure 6.7: *Ratio of the components depth dose data to the single polyenergetic depth dose data for the ABB 6MV (CH6) and 16MV (CH20) beams.*

6.5 Dose calculation scheme

6.5.1 Geometry of model

The superposition model calculates the dose distribution on a Cartesian matrix. The origin of the coordinate system is set at the radiation source, the collimators define the beam in the x and y directions and depth is in the z-direction. The beam's central axis is set to run through the centre of voxel $(x, y) = (0, 0)$ at the phantom surface. Collimator, gantry or couch rotations are not modelled.

6.5.2 Variable input and calculation

The following describe the order with which some important variables are set and calculated.

Input of various variables

At first, variables such as source to surface distance (SSD), voxel size, and number of calculation points to be considered are set accordingly.

3D density distribution

A 3D density matrix is interactively set up for a homogeneous medium or a simple geometry (such as a phantom consisting of slabs of different materials). This involves specifying the dimensions and the density values of the irradiated medium. More general heterogeneous phantoms, such as CT data, are read-in from a named file.

3D terma distribution

Following the assignment of the density matrix, control is handed over to the subroutine performing the calculation of the terma distribution. Initially, this involves the calculation of a 2D array describing the relative energy fluence distribution on the phantom surface (the in-air profile). If the incident beam is monoenergetic then relative terma is calculated using the density distribution, the in-air profile and the mass attenuation coefficient for this energy. In the case of a polyenergetic beam, precalculated values of the effective mass attenuation coefficients and effective energies at each depth are used instead. These are obtained once and for all for each x-ray beam and stored separately on disk. The algorithm traces divergent ray-lines from the phantom surface down through the thickness of the phantom. The number of rays passing through the surface voxel is specified by the user, and at the end of the calculation a normalisation of terma to the number of rays passing each voxel is carried out to account for the fact that, due to divergence, a smaller number of rays passes though voxels at larger depths.

Kernel input

The appropriate monoenergetic or polyenergetic kernel is read-in separately and manipulated so that instead of describing the fractional energy deposited in each spherical voxel it represents the amount of energy released up to a certain radius at each angle. The reason for this will be obvious from the following sections.

Superposition procedure

The 2D pattern for calculating dose at a point with superposition is schematically simplified in Figure 6.8. The calculation of dose at a point on the calculation matrix, is essentially an integration of all dose contributions from surrounding interaction voxels. The red isolines represent the distribution of interaction centers

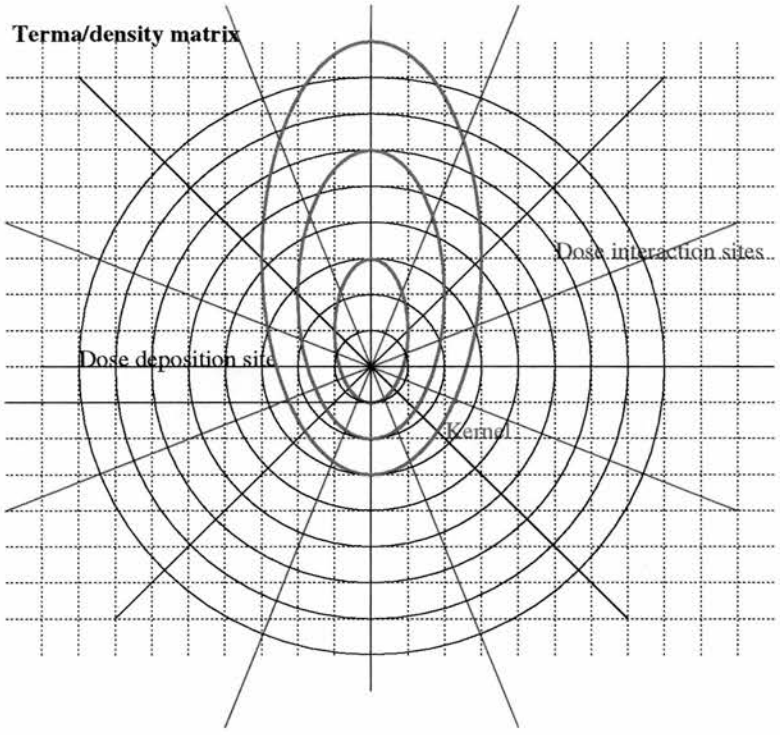

Figure 6.8: *An illustration of the way superposition of terma with a kernel is carried out.*

around the point, i.e. this is the kernel matrix inverted for implementation in the dose deposition point of view. The combination of circles and solid lines in black defines an arrangement of spherical interaction voxels around the dose calculation point and the intersections of dashed lines are the centres of the cartesian terma voxels. The number of interaction centres to be considered is set by the user by specifying the number of radii as well as the separation between them. Namely, the centre of each dose deposition voxel is the origin of a spherical coordinate system, where the polar angular increments are set equal to those defined by the spherical kernels. azimuthal angles are set arbitrarily by the user. The number of steps in the radial direction is set at the beginning of the run, but is "dynamically" altered during calculation. This was necessary in order to ensure that energy contributions resulting from particles scattered at lower depths and in the forward direction are adequately taken into account. The blue lines represent the directions on which interaction centers are to be considered. These lie at the center of each voxel and the corresponding terma values are taken to represent the average terma from each spherical voxel. Therefore, the energy contributions reaching a dose deposition site are transported along the axes of cones defined around that site. This resembles the basic idea in the *collapsed cone* convolution method by Ahnesjö [Ahnesjö and Andreo, 1989]. All results presented in the next sections

were obtained by using radial steps equal to 0.25 cm (this is variable `radstep`, discussed in detail in the next chapter), 48 angular steps in the polar directions and 48 angles in the azimuthal direction. The resolution of the polyenergetic energy deposition kernel used in all calculations was $(r, \theta, \phi) = (24, 48, 48)$.

6.5.3 Density scaling of kernels

The discrete form of equation (3.8) of chapter 3 for single polyenergetic convolution is:

$$D(\bar{r}) = \sum_{s}^{volume} \bar{T}(\bar{s}) \frac{\rho(\bar{s})}{\rho_o} c^2(\bar{r}, \bar{s}) h(c(\bar{r}, \bar{s})(\bar{r} - \bar{s})) V_{\bar{s}} \tag{6.19}$$

Here $h(c(\bar{r}, \bar{s})(\bar{r} - \bar{s}))$ represents the density scaled polyenergetic kernel and $V_{\bar{s}}$ the volume element at position $\bar{s}$. A spherical volume element is:

$$\Delta V = (\bar{r} - \bar{s})^2 \Delta r \Delta \Omega \tag{6.20}$$

and a spherical kernel can be rearranged so it represents the fractional energy absorbed between positions $(\bar{r} - \bar{s})$ and $(\bar{r} - \bar{s}) + \Delta\bar{r}$ in a medium of density ρ_o, when energy E is released at $\bar{s}$:

$$k_{\Delta r}(\bar{r} - \bar{s}) = \frac{\Delta \epsilon}{E} \tag{6.21}$$

From equation (3.4) of chapter 3 and equation (6.21) it follows that:

$$h(\bar{r} - \bar{s}) = \frac{k_{\Delta r}(\bar{r} - \bar{s})}{\Delta V} \tag{6.22}$$

Thus, in an inhomogeneous medium, $h(c(\bar{r}, \bar{s})(\bar{r} - \bar{s}))$ can be expressed as:

$$h(c(\bar{r}, \bar{s})(\bar{r} - \bar{s})) = \frac{k_{\Delta r}(c(\bar{r}, \bar{s})((\bar{r} - \bar{s}))}{c^2(\bar{r}, \bar{s})(\bar{r} - \bar{s})^2 \frac{\rho(\bar{s})}{\rho_o} \Delta r \Delta \Omega} \tag{6.23}$$

Replacing (6.23) in (6.19), the actual formula implemented in the routine performing superposition for calculating dose per incident photon fluence is:

$$\frac{D(\bar{r})}{\Phi(\bar{r}_o)} = \sum_{s}^{volume} \frac{\bar{T}(\bar{s})}{\Phi(\bar{r}_o)} k_{\Delta r}(c(\bar{r}, \bar{s})(\bar{r} - \bar{s})) \tag{6.24}$$

This means, that in order to calculate the contribution to dose at a point from a given interaction site, it is only necessary to calculate the radiological distance between the two positions, interpolate a kernel value at this (density scaled) distance and use the terma value at the interaction site. Referring back to Figure 6.8,

density scaled distances are accumulated along the blue lines, assuming the density at the interaction site to be representative of that at the spherical interaction voxel.

6.5.4 Kernel alignment to beam divergence

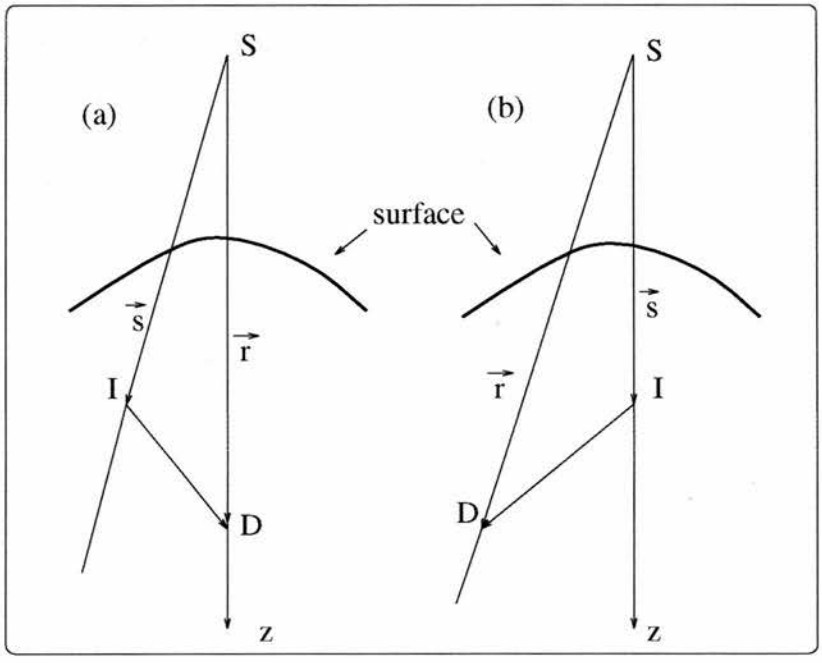

Figure 6.9: *(a) The kernel tilting "trick" applied to dose at points on the central axis of the beam, (b) at points in the periphery of the beam the trick is not valid.*

The problem of aligning the kernel with the divergent rays of the beam is dealt with here in a simple manner in order to avoid long computations. As suggested by Papanikolaou *et al.* [Papanikolaou et al., 1993] applying the inverse square correction at the dose deposition site instead of the dose interaction site appears to improve the agreement with measured data for dose values along the central axis of the beam. This *kernel tilting trick* can be explained with the aid of Figure 6.9. Generally, the alignment of the kernel with the direction of the primary photon decreases the dose at a point on the central axis of the beam. Dose deposition point D on the left of Figure 6.9 receives less dose due to an interaction at point I if the kernel at I is appropriately tilted. Ignoring kernel tilting and by applying the inverse square correction $|\bar{r}|^{-2}$ to the dose at D, where $|\bar{r}|$ is larger than $|\bar{s}|$, the dose value at D is reduced, leading to the same result as when kernel tilting is explicitly carried out. However the diagram on the right of

Figure 6.9 displays that this *trick* is not valid for points in the periphery of the beam. The application of this divergence correction to the dose deposition site, instead of to the primary photon interaction site, that is during in the calculation of terma as physically correct, compensates partially for not aligning kernels to the fan-line geometry of the beam.

6.5.5 Kernel depth hardening correction

Papanikolaou *et al.* [Papanikolaou et al., 1993] calculate this correction for the distance of each calculation point from the intersection of the beam's central axis with the phantom surface and apply the correction to the 3D dose matrix after completion of the superposition procedure. The use of this geometric distance gives accurate results in the homogeneous water medium, but inaccurate in any other case. Here, the kernel depth hardening correction factor is calculated for the radiological distance along the primary photon path within the medium. This correction is applied during the calculation of terma, where these radiological distances are obtained from ray tracing, in order to avoid an additional ray tracing procedure after the completion of superposition.

6.6 Code structure

Table 6.10 presents the layout of the superposition software in the order with which tasks are carried out. After the kernel is read in by the main routine, the six superposition loops are executed. Dose values are calculated in units of $(MeV \cdot cm^2)/g$. This can be seen from equation 6.16 considering that kernels represent fractional energy values and have no units. Since MeV/g is equivalent to $1.60210^{-10} Gy$, dose values calculated from superposition are multiplied by $1.602 \cdot 10^{-10}$ and are expressed in units of $Gy \cdot cm^2$.

6.7 Results

The verification of this dose calculation model was carried out in homogeneous or simple heterogeneous geometries via comparisons with Monte Carlo generated data. The verifications in homogeneous media were carried out for the 4MV, 6MV, 9MV and 16MV beams and in a simple heterogeneous geometry only for 4MV.

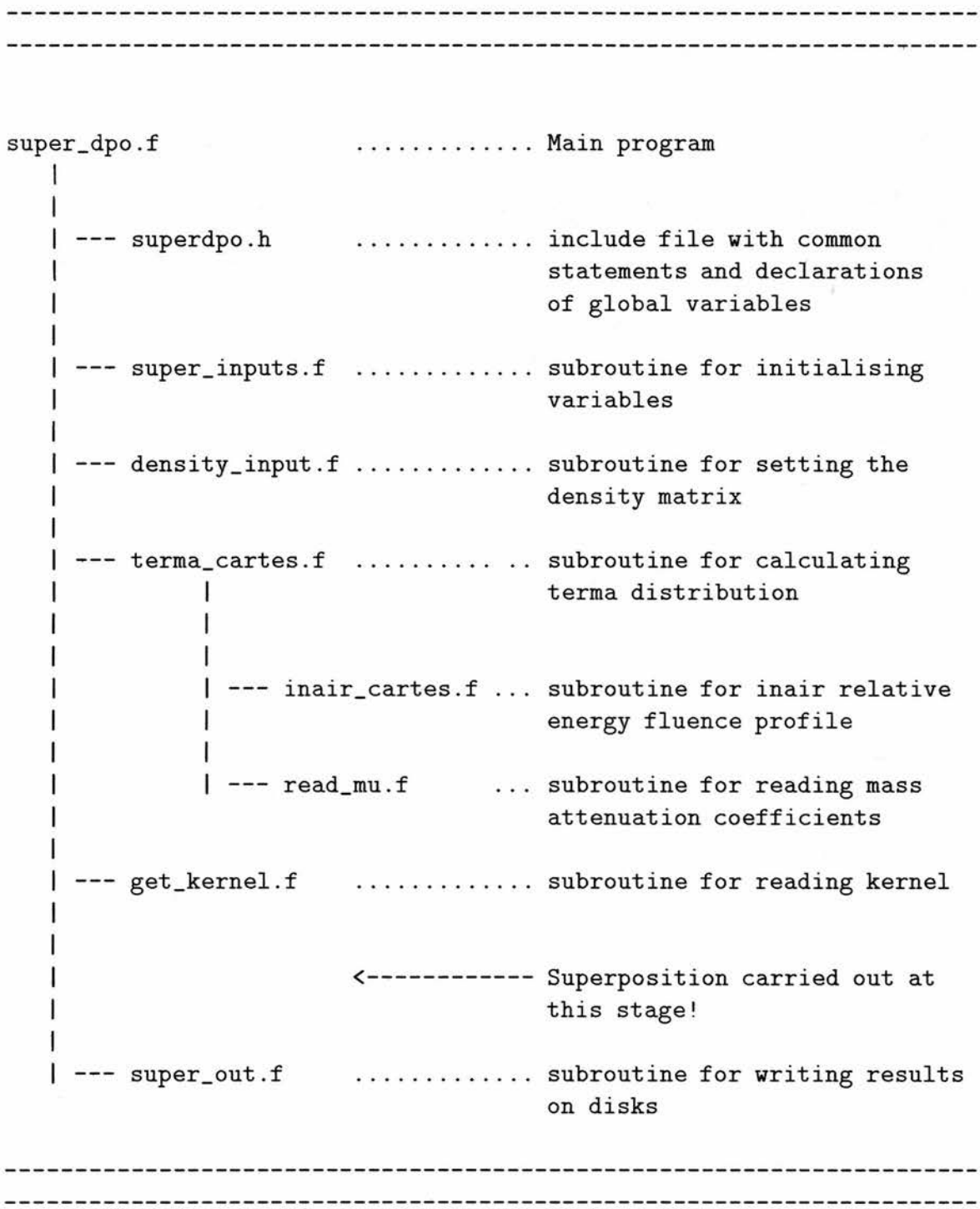

Figure 6.10: *The superposition software*

6.7.1 Monoenergetic beams in water

The performance of this superposition model for monoenergetic beams is compared against published data by Papanikolaou *et al.* assuming that the latter are in good agreement with Monte Carlo generated data [Papanikolaou et al., 1993]. Depth dose data for three beams (low, medium and high energy) are presented. The source to surface distance is 100cm and the field size is $10 \times 10cm^2$. Figure 6.11 shows the comparison for 1.25 MeV. The curve denoted as *superdpo* represents the results from this work and the curves denoted as *pap* is from the data given by Papanikolaou *et al.* A disagreement lies only in the value of dose within the first voxels of the central axis with its centre at 0.25 cm from the phantom surface.

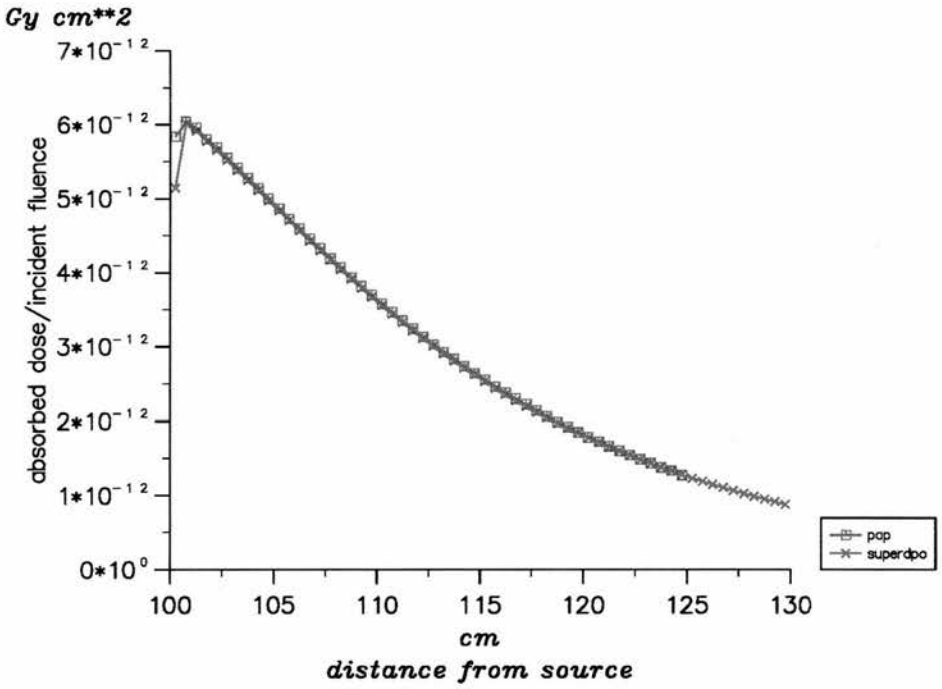

Figure 6.11: *1.25 MeV depth dose curves.*

The depth dose curves for a 6 MeV beam are shown in Figure 6.12. A small disagreement between the two curves lies in the build up region. The build up region is not an equilibrium zone and to model accurately energy deposition is not easy. An analogous performance is seen in Figure 6.13 for the 20 MeV photon beam.

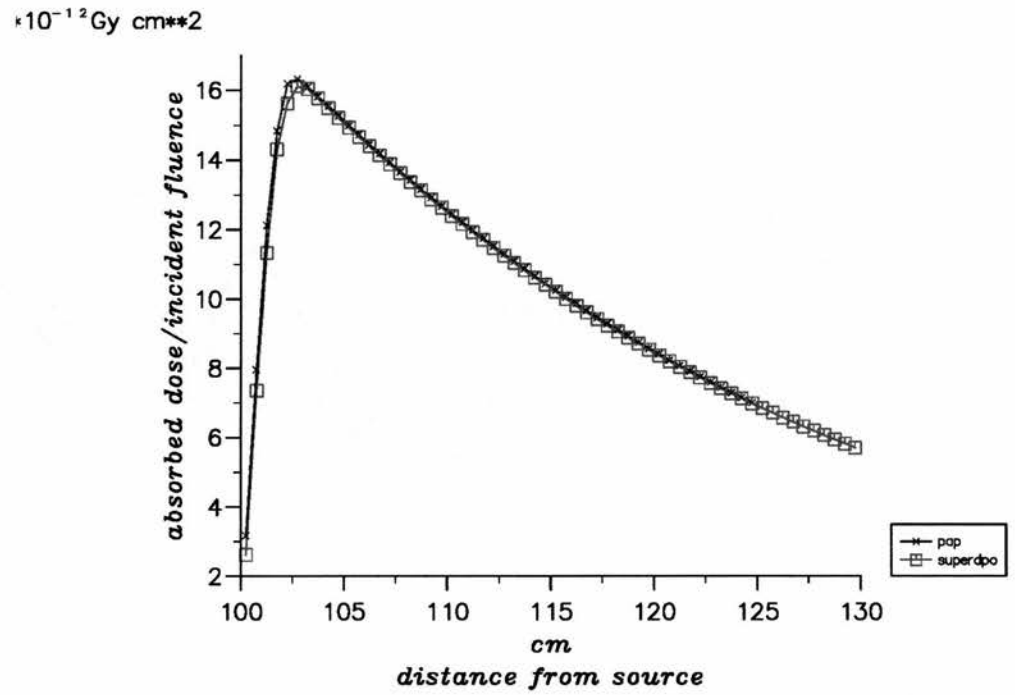

Figure 6.12: *6 MeV depth dose curves.*

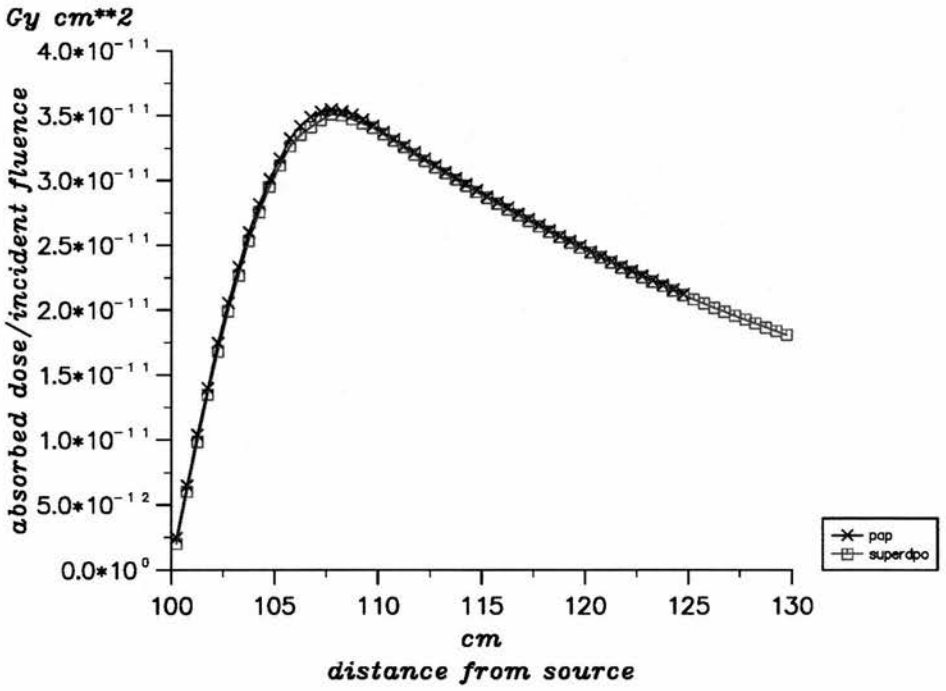

Figure 6.13: *20 MeV depth dose curves.*

6.7.2 Polyenergetic beams on homogeneous media

The performance of the single polyenergetic superposition algorithm was examined for the Dynaray 4 MV in three cases of homogeneous media. The performance of the model at higher energies (6MV, 9MV and 16MV beams) in water is also shown. All irradiations were for a diverging beam with SSD=100cm and radiation field of $10 \times 10 cm^2$ incident normally on the phantom surface. Relative incident fluence was set to unity within the field. The dimensions of the phantom were $20 \times 20 \times 30 cm^3$. The voxel size in the terma and dose matrixes was $0.5 \times 0.5 \times 0.5 cm^3$. All EGS4 data were obtained with usercode DOSRZ. The irradiated cylinder had maximum radius of 10 cm and depth of 30 cm. The equivalent radius of the beam was set to 5.58 cm. ECUT was set to 0.521 MeV and PCUT to 0.01 MeV. PRESTA was invoked and photon interaction forcing was switched on. Cylindrical voxels were separated with a step of 1.0 cm in the radius and depth direction.

Dose in water

The performance of the algorithm for water (density $1.0 g/cm^3$) is illustrated in Figures 6.14, 6.15, 6.16. In the first figure there is a comparison between EGS4

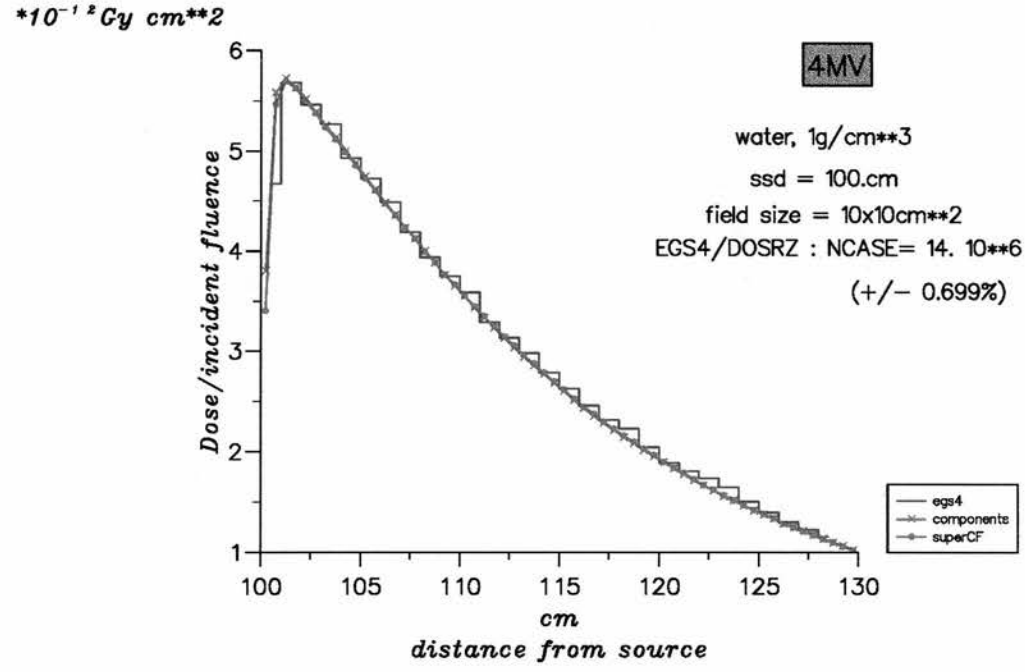

Figure 6.14: *Comparisons between EGS4, the components method and the single polyenergetic superposition approach.*

(*egs4*: staircase curve), the single polyenergetic superposition curve (*superCF*) and the depth dose curves obtained using the components method. The agreement between these curves is excellent. The components method was employed for calculating the kernel depth hardening correction factor (as explained in section 6.4.2). Figure 6.15 demonstrates why it was necessary to include this correction. Here the components calculation is compared with superposition without applying any K_{CF} correction (curve denoted as *super*) and superposition after kernel depth hardening was applied (curve denoted as *superCF*). Figure 6.16

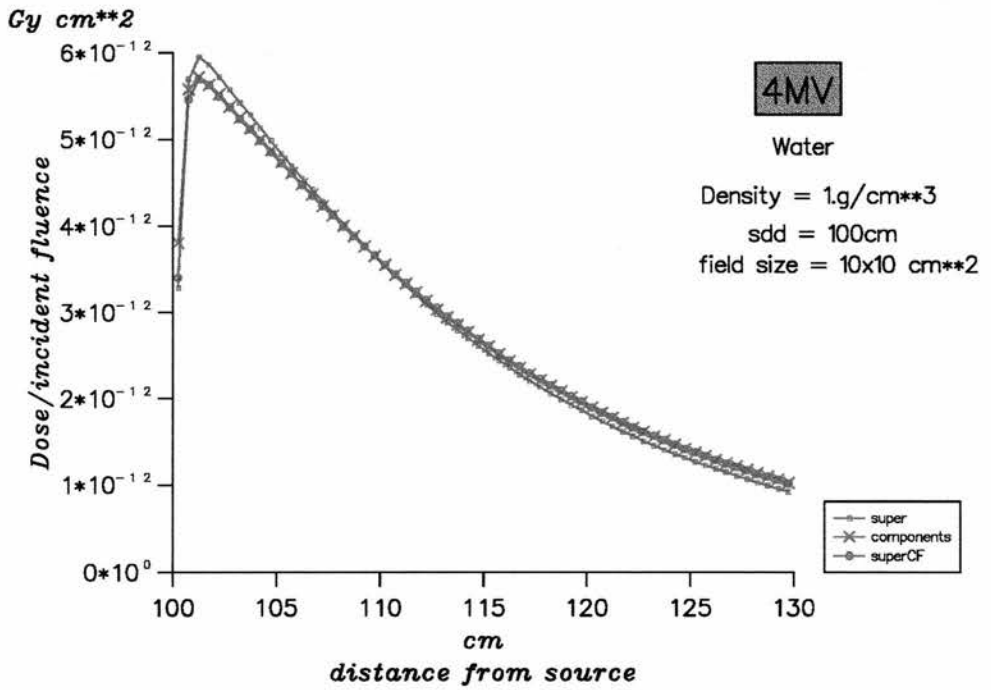

Figure 6.15: The application of a kernel depth hardening correction improves the agreement between the component approach and single polyenergetic superposition.

compares depth dose data from EGS4, superposition and measurements. The curves are normalised at the depth of 10 cm. The differences with measurements are most likely due to differences between the reconstructed spectrum and the actual spectrum of the beam. These results emphasise that superposition is a good but approximate solution to the radiation transport problem. The discrepancies in Figure 6.16 can be eliminated by applying an additional depth hardening correction factor. However, this was not performed in this work, in order to obtain distinguishable results for a clear comparison among the various calculation methods. Finally, not a crucial but a useful test is to examine the performance at positions off axis. Profiles at a series of depths are shown in Figure 6.17. These

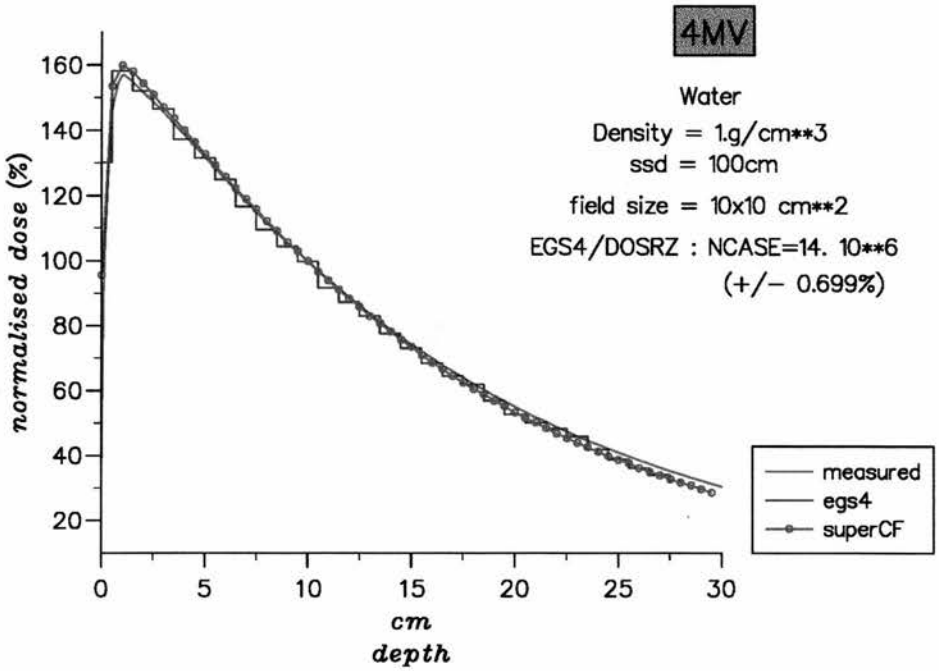

Figure 6.16: *Comparisons of experimentally measured depth dose data with egs4 and superposition*

depths are at 0.5cm, 3.5cm, 10.5 cm, 15.5 cm and 25.5 cm. Superposition data are compared with the Monte Carlo data. The agreement is excellent.

Figures 6.18, 6.19 and 6.20 present the performance of the single polyenergetic superposition model in water for beams with energies higher than 4MV. As expected the agreement with EGS4/DOSRZ is excellent, whereas the discrepancies from measured depth dose data are due to the representation of the spectrum used for superposition.

Dose in a low density medium

The low density medium examined here is waterlike with density $0.3g/cm^3$ simulating lung tissue. Figure 6.21 presents depth dose curves from egs4, the components method and single polyenergetic superposition. Curves *super* and *superCF* differ in the calculation of K_{CF}. As already mentioned, it was realised that K_{CF} should be calculated for the radiological depth along primary photon paths and not just the distance from the surface. Curve *super* is a result of single polyenergetic superposition with K_{CF} obtained using the actual depth of the calculation point, whereas *superCF* is obtained with the method suggested here. Curve *superCF* succeeds in matching very well the data from both the components method and EGS4. Figure 6.22 displays dose profiles from EGS4 and superposition in

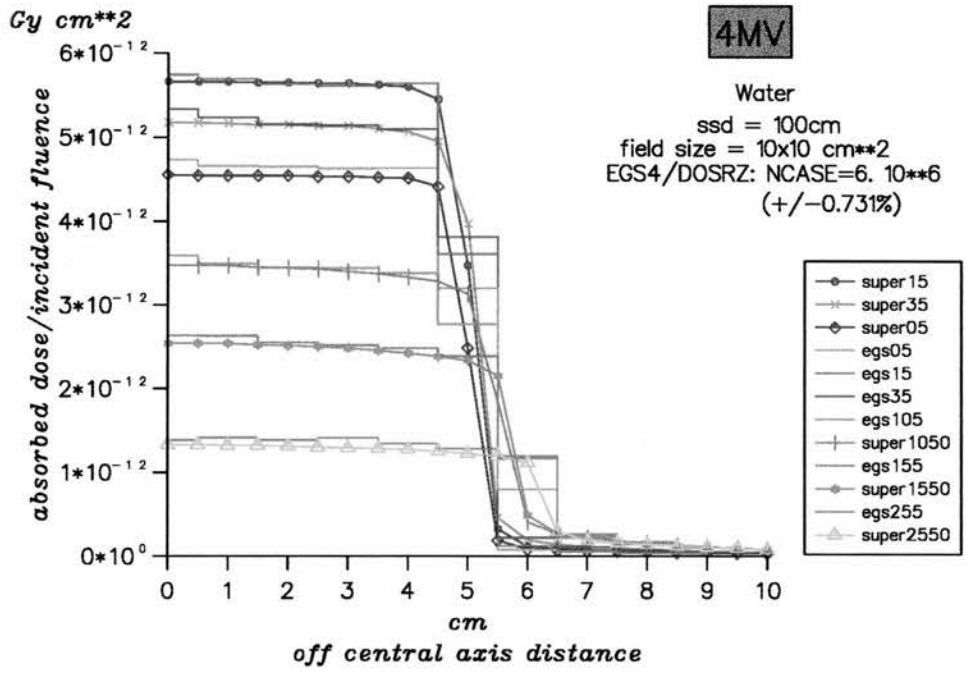

Figure 6.17: *Calculated dose values for various profiles in water.*

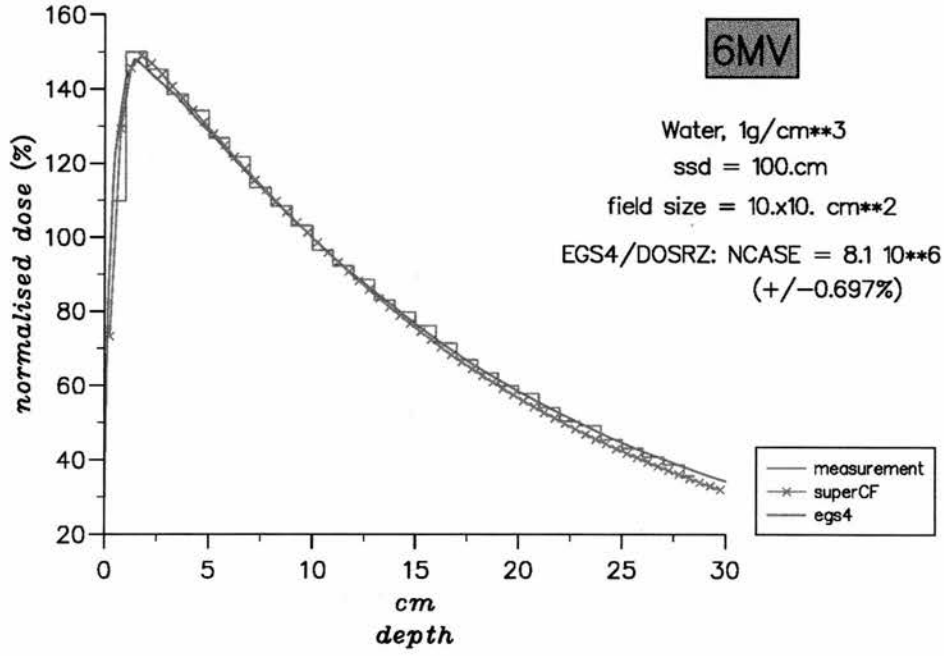

Figure 6.18: *6MV beam in water: Normalised data from EGS4/DOSRZ, superposition and measurements.*

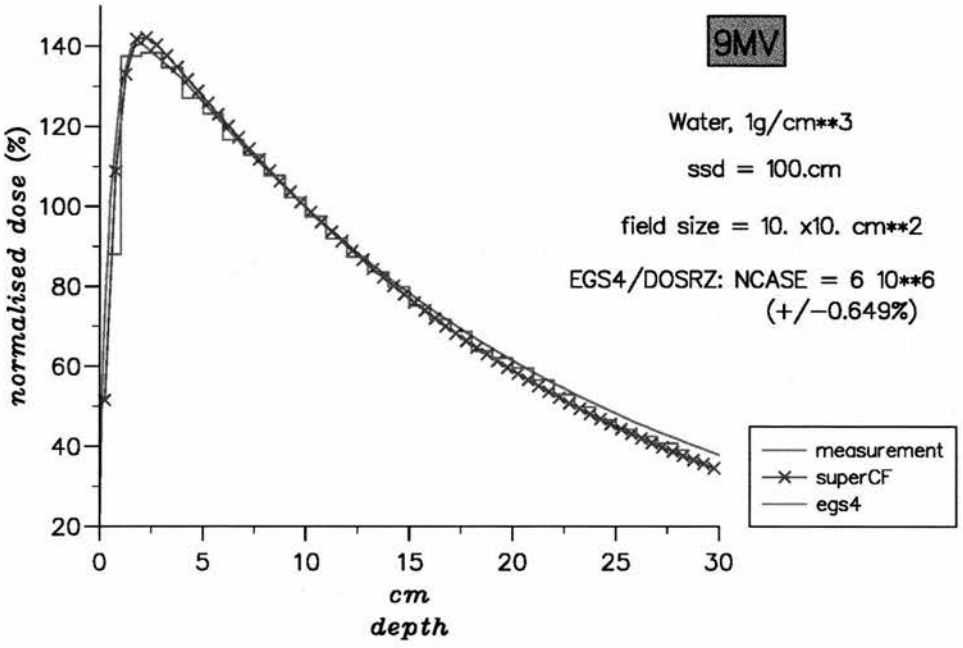

Figure 6.19: *9MV beam in water: Normalised data from EGS4/DOSRZ, superposition and measurements.*

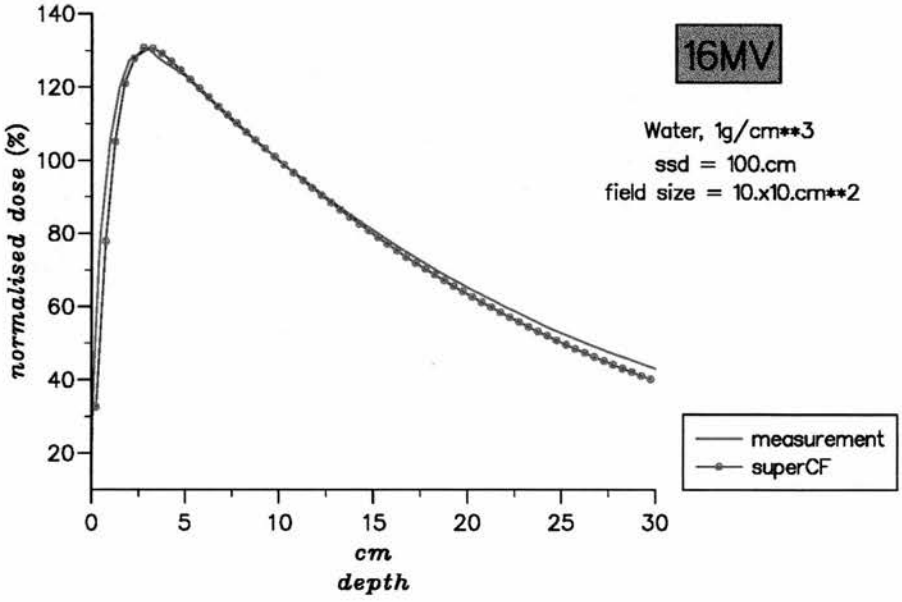

Figure 6.20: *16MV beam in water: Normalised data from EGS4/DOSRZ, superposition and measurements.*

the waterlike low density medium. The agreement is very good, with the most prominent discrepancy in the profile within the build up region. The EGS4 data have an uncertainty of $\approx 1.3\%$ in their maximum dose value (at d_{max}), therefore from this graph we do not have a very good EGS4 result for the build up region.

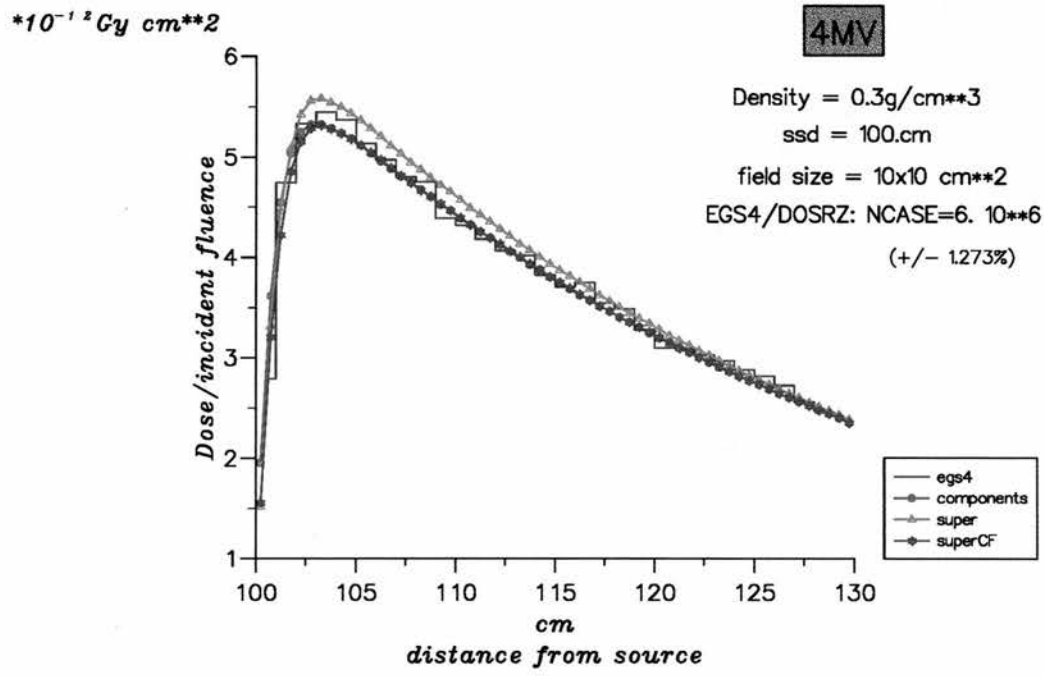

Figure 6.21: *Depth dose variations in a waterlike medium of density* $0.3g/cm^3$ *and a demonstration of the importance of radiological distance in the calculation of factor* K_{CF}.

Dose in a high density medium

A homogeneous medium consisting of Aluminium with density $2.703gcm^3$ simulating bone was used for these verifications. Mass attenuation coefficients for Aluminium were used for the calculation of terma [Hubbell, 1982]. Figures 6.23 and 6.24 demonstrate an excellent performance. These results are very good, considering that discrepancies between egs4 and superposition are to be expected in this case. Aluminium is a material with different atomic number ($Z_{Al} = 13$) than that of water ($\bar{Z}_{H_2O} = 7.51$), and hence, different angular scattering powers and stopping powers for electrons, which affect the shape of the energy deposition kernel. EDKs for Aluminium differ from those in water. The difference at the phantom surface (Figure 6.23) is due to enhanced backscatter in Aluminium compared to water.

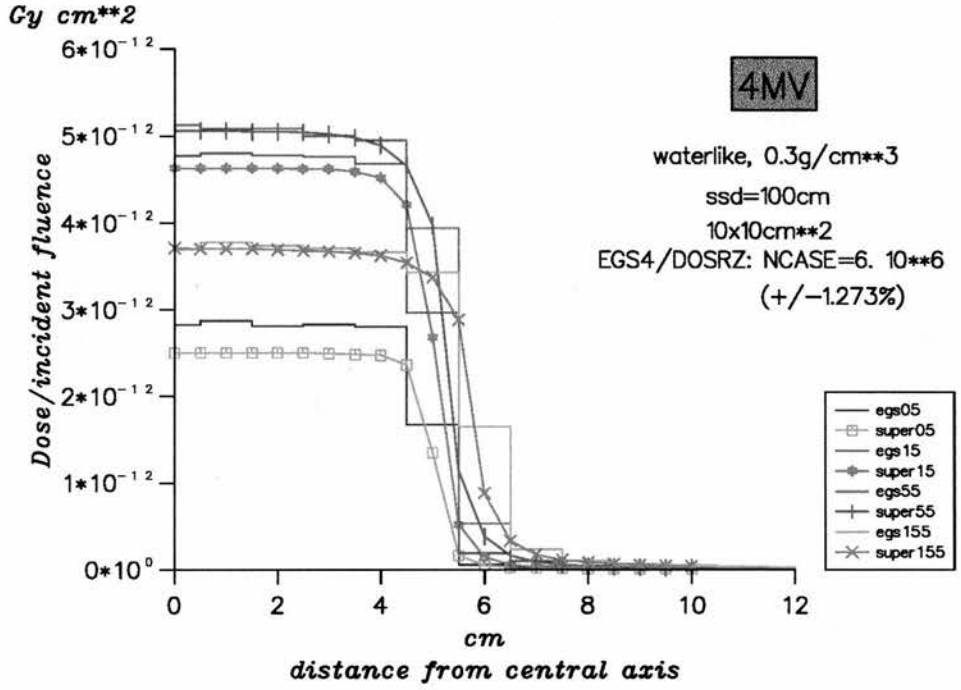

Figure 6.22: *Dose profiles at depths of 0.5cm, 1.5cm, 5.5cm, 15.5cm in the waterlike medium of density* $0.3g/cm^3$.

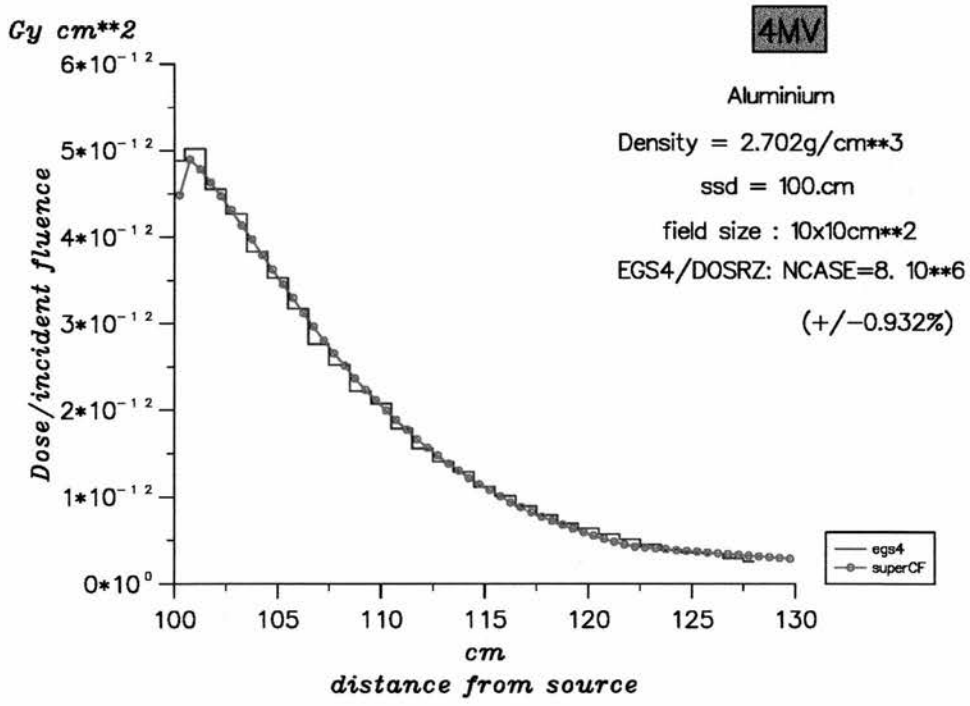

Figure 6.23: *Depth dose curves in Aluminium.*

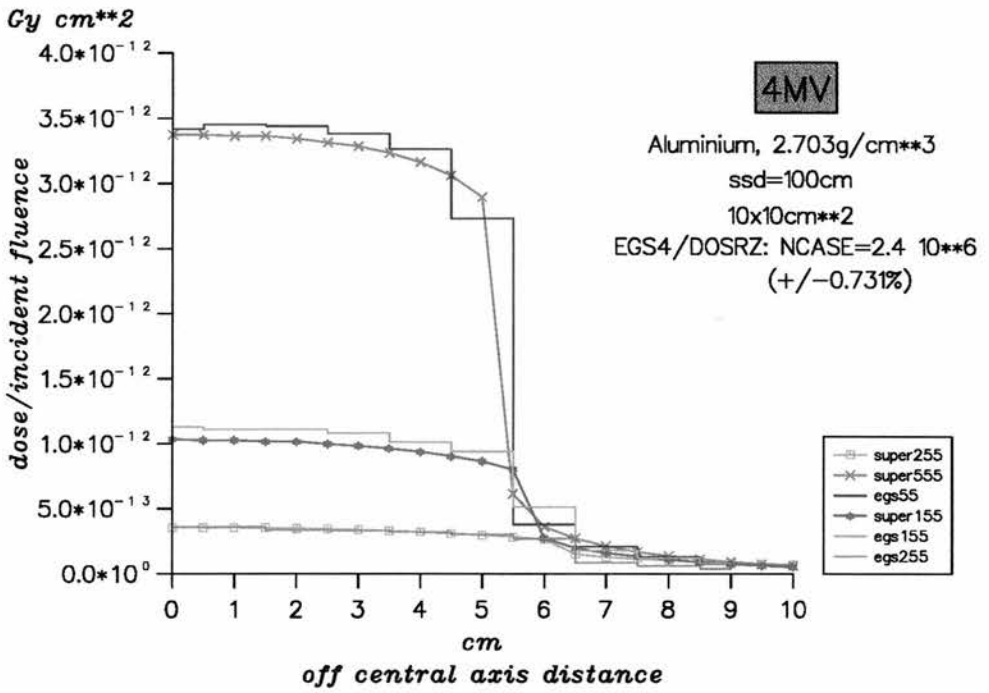

Figure 6.24: *Profiles at depths of 5.5cm, 15.5cm and 25.5cm in Aluminium.*

6.7.3 Polyenergetic beam in heterogeneous media

Slab geometry

Figure 6.25 displays the simple heterogeneous geometry used for this verification. The dimensions of the phantom are $20 \times 20 \times 40 cm^3$. The slab heterogeneity is located at a depth of $10cm$. The phantom is water (density $1g/cm^3$), and the slab consists of a waterlike medium with density $0.3g/cm^3$. The beam is 4 MV, with SSD = 100cm and field size of $10 \times 10 cm^2$. The comparison between superposition and Monte Carlo along the central axis of the beam is shown in Figure 6.26.

The general agreement between Monte Carlo data *egs4* and superposition (curve *superdpo2*) is good. An explanation for the presence of high uncertainty values ($\pm 1.3\%$) in the Monte Carlo data for voxels along the central axis and within the low density region is given in section 5.3.2.

Experiment #1 : tangential irradiation

Following the assessment of the performance of the single polyenergetic superposition model, comparisons were carried out against measured data from two separate experiments. The first experiment simulates a tangential breast irradiation, as shown in Figure 6.27, where the 4MV beam, with field size of

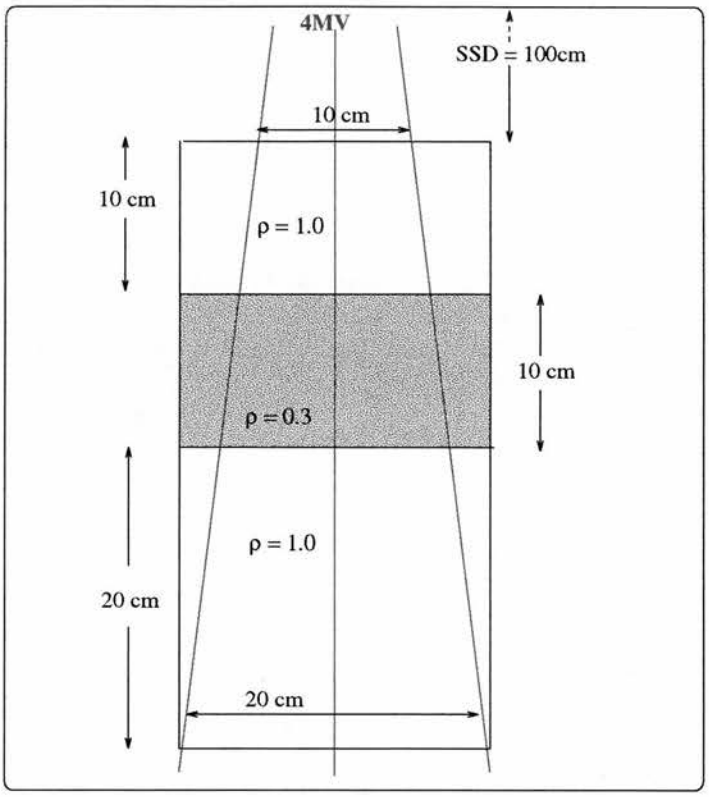

Figure 6.25: *Slab geometry with water and waterlike medium.*

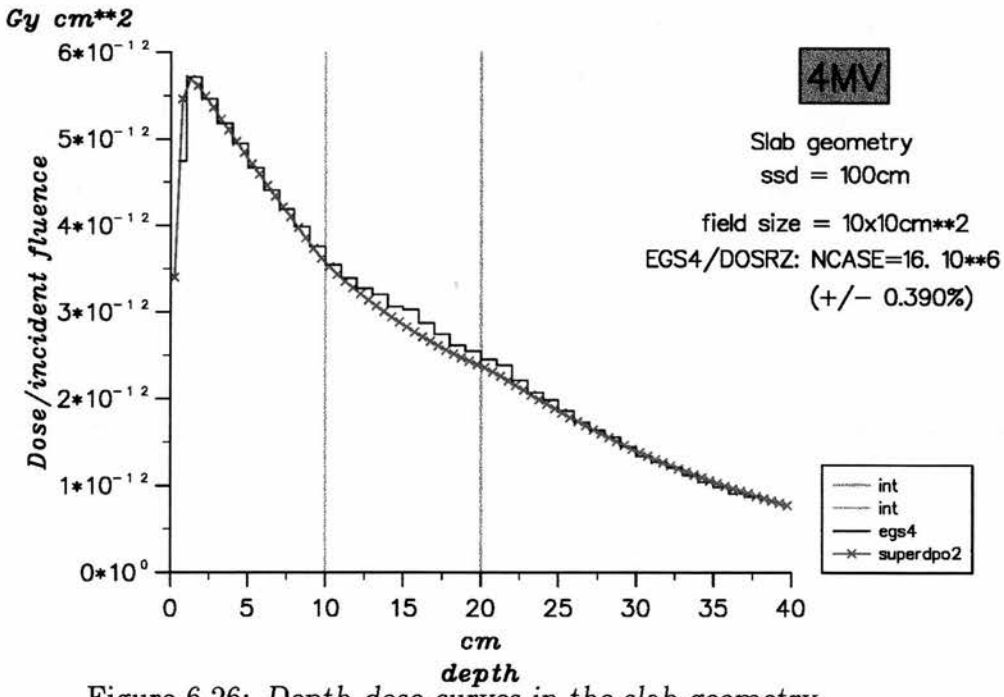

Figure 6.26: *Depth dose curves in the slab geometry.*

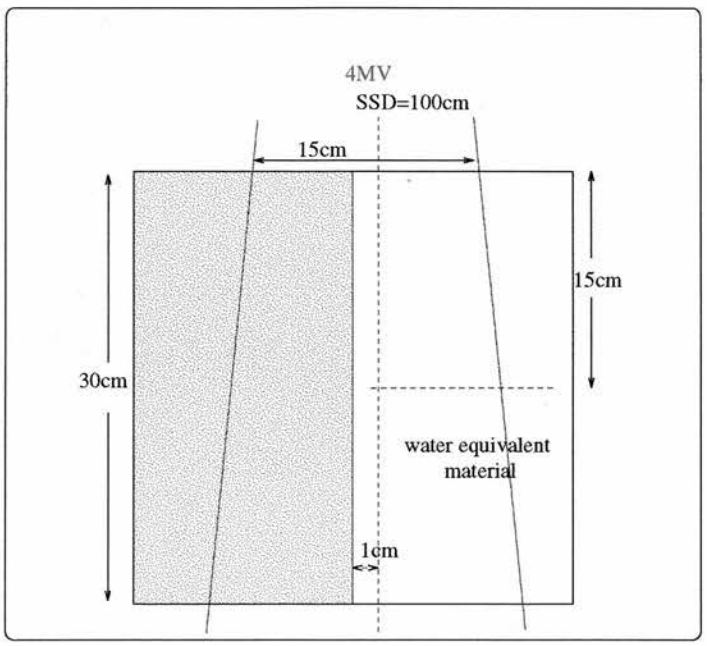

Figure 6.27: *Experiment # 1: The tangential irradiation geometry.*

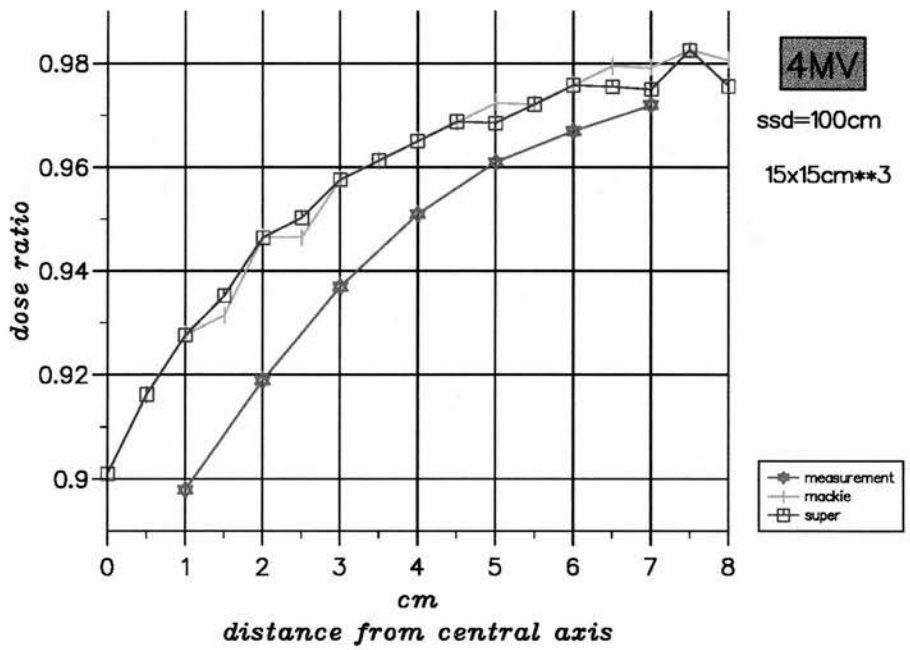

Figure 6.28: *Experiment # 1: Dose ratios (half/full phantom) at 15 cm deep.*

$15 \times 15 cm^2$, normally incident (SSD=100cm) on slabs of tissue equivalent material. The measured data were derived from a publication by Redpath and Thwaites [Redpath and Thwaites, 1991].

Measured data represent ratios of relative dose values at points across the depth of 15cm of a half phantom irradiation (when the shaded region is removed) to a full phantom irradiation (Figure 6.27). The comparison with the corresponding dose ratios derived with the single polyenergetic approach is shown in Figure 6.28. This figure displays three sets of data. The measured data, the dose ratios from the model of this work (denoted as *super*) and the results using the ray-tracing routines developed by Mackie *et al.* [Mackie et al., 1987]. This comparison was carried out in order to eliminate any concerns that the superposition technique developed here, was the reason for the differences with measurements. These two superposition calculations are identical except for their ray tracing procedures (voxel sizes were set to $0.5 \times 0.5 \times 0.5 cm^3$ and terma distributions were the same in both cases). Results in Figure 6.28 display one of the limitations which are related to all convolution/superposition approaches. This here is an example of the inaccuracies involved when kernel arrays are used near the edges of finite phantoms. Spherical EDKs have been generated with the initial assumption that the homogeneous water sphere is almost large enough to represent an infinite medium so that kernels would *not sense* the presence of boundaries. This overestimation of dose is because superposition includes contributions to dose from particles that scatter from the medium into air and would have scattered back into the medium had the medium not been missing. This has also been observed by Mohan *et al.* [Mohan et al., 1985] for a 15MV beam and was considered to be a second-order effect. Here, for a 4MV beam, the kernel is less forward peaked (more isotropic) than the 15MV polyenergetic kernel and this effect is more prominent. The maximum discrepancy is up to 4% at the point closest to the edge of the phantom, but deviations decrease rapidly for points further away. Methods to improve this require separate calculations for the primary, first and multiple scatter components of dose.

Experiment #2 : water with air heterogeneity

Figure 6.29 shows the experimental set up from which dose ratios along the beam's central axis and dose ratios at profiles across depths below a cube of air were measured and calculated. Measurements are again obtained from the publication by Redpath and Thwaites [Redpath and Thwaites, 1991]. The size

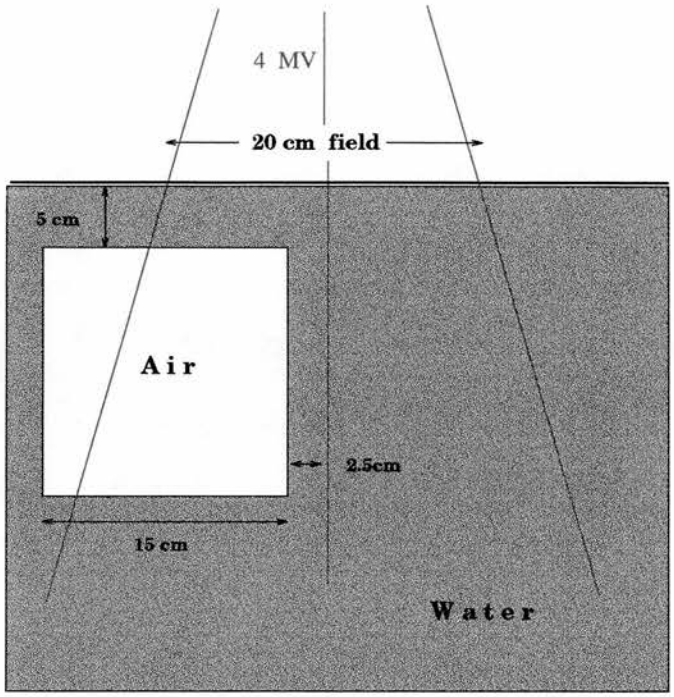

Figure 6.29: *Experiment # 2: Irradiation of a water medium with an inserted cube of air.*

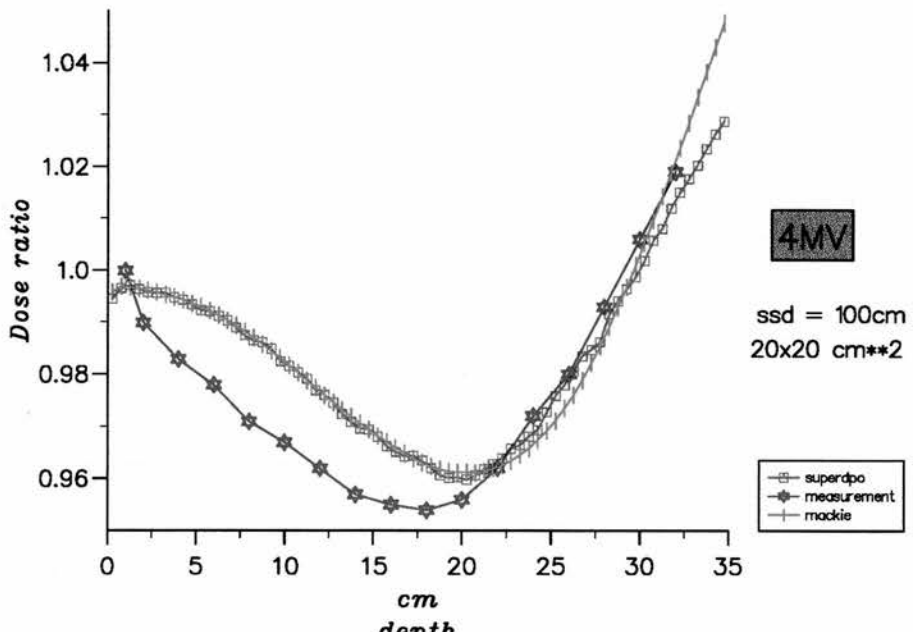

Figure 6.30: *Experiment # 2 : Air heterogeneity in water: dose ratios along the beam's central axis where Dose ratio = Dose(with air cube)/Dose(homogeneous).*

of the phantom is $40 \times 40 \times 40 cm^3$, the cube of air is $15 \times 15 \times 15 cm^3$ placed at a depth of 5cm and 2.5cm off the central axis of the 4 MV beam. The radiation field is $20 \times 20 cm^2$. The SSD is 100cm. Dose ratios are defined as the ratio of dose with the inhomogeneity present in the water to the dose at the same points when the inhomogeneity is replaced with water (homogeneous water medium).

Figure 6.30 displays dose ratios along the central axis from measurements and superposition (curve *superdpo* from this work and curve *mackie* when using the ray tracing routines provided by Mackie *et al.* [Mackie et al., 1987]). For superposition, the density of air was set to $0.0012048 g/cm^3$. As seen from this figure, the agreement between superposition and measured data is very good. Differences occur along the side of the inhomogeneity. At this low energy, the overestimation of dose along the side of the air cube on the central axis is due to the overestimation of the dose originating from multiply scattered particles. At higher energies this overestimation in dose would be enhanced by the inclusion of contributions from secondary electrons which are more likely to enter the air cube and further deposit their energy away from the central axis.

The profiles at depths of 22.5cm (Figure 6.31), 25cm (Figure 6.32) and 30cm (Figure 6.33) compare dose ratios from superposition (this work) with ratios derived from measurements. These ratios have values larger than unity at points below the air heterogeneity because the beam is attenuated less through air, resulting in higher values for terma at these depths. In addition, due to beam divergence, terma values below the air cube increase as the distance from the central axis increases. For the reason discussed previously, superposition overestimates dose below the air heterogeneity mainly because dose from multiply scattered particles is overestimated. In addition, but not as influential for this energy, is the fact that in such cases, rectilinear density scaling results in the inclusion of secondary electrons that would have escaped lateraly in the presence of this large air cube, i.e. rectilinear scaling is obscured by the air to water mass stopping power ratios. Such errors are expected to be more significant in cases of large air heterogeneities, higher energies and under the conditions of narrow beams or boundaries of large beams [Mohan et al., 1985]. The magnitude of these differences seems to increase slightly as the depth below the air cube increases. The dose ratios towards the central axis are in excellent agreement with measurements at all depths. If the size of the air cube was smaller, one would expect that charged particle equilibrium would not be significantly disturbed and that deviations from measurements would be smaller.

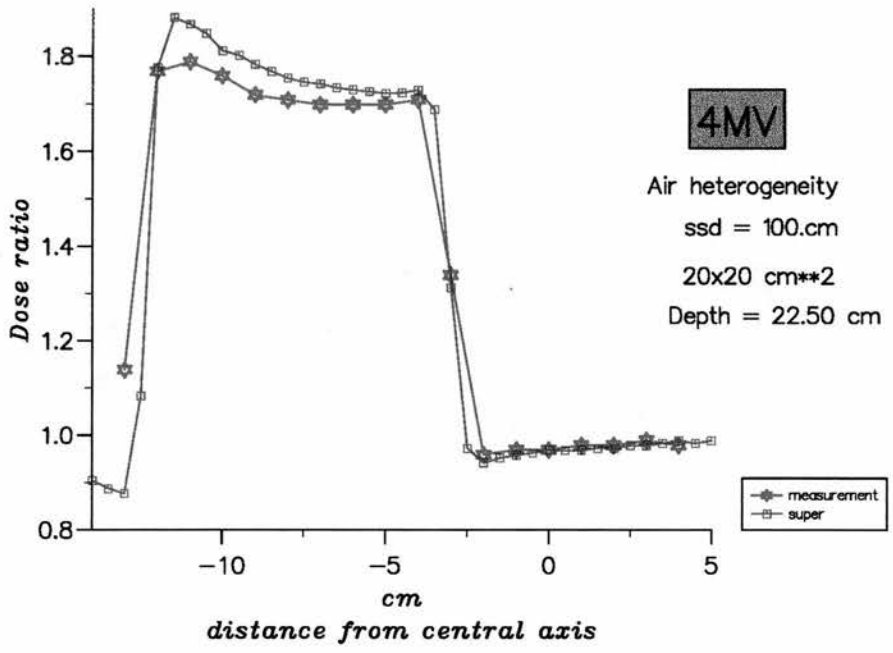

Figure 6.31: *Experiment # 2: Dose ratios across the beam at a depth of 22.5cm; namely 2.5cm below the air heterogeneity.*

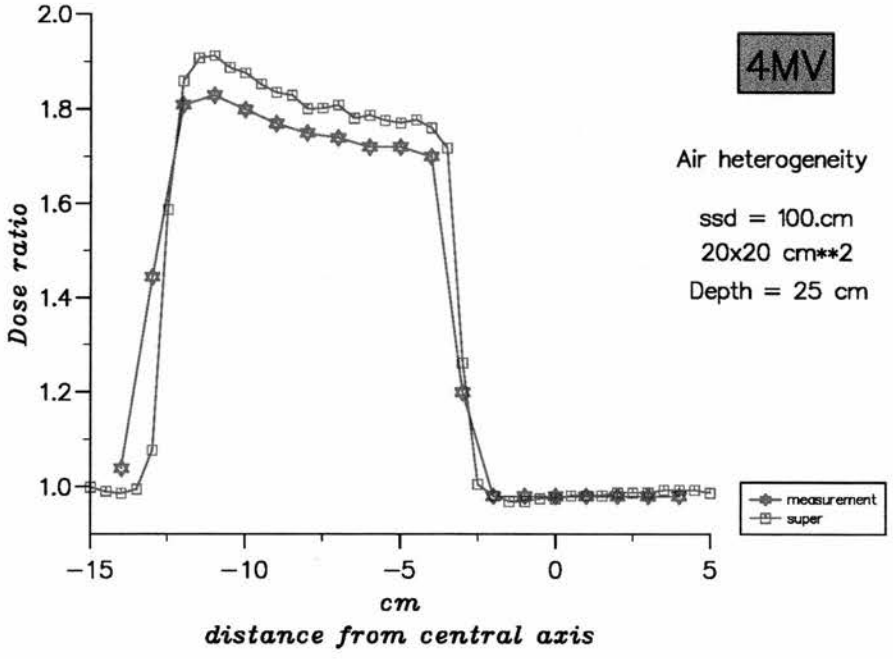

Figure 6.32: *Experiment # 2: Dose ratios across the beam at a depth of 25cm; namely 5cm below the air heterogeneity.*

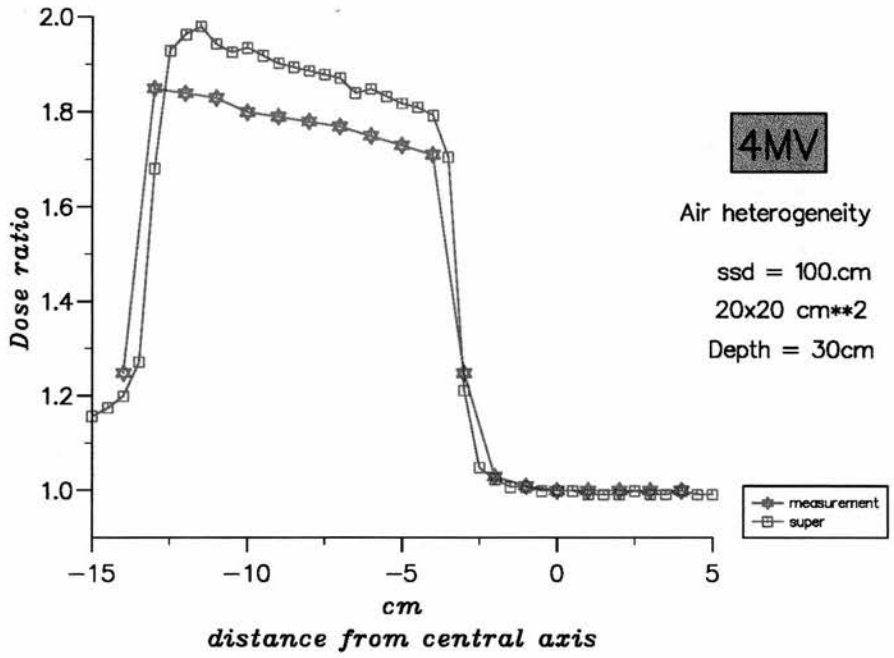

Figure 6.33: *Experiment # 2: Dose ratios across the beam at a depth of 30.cm; namely 10cm below the air heterogeneity.*

Experiment #3 : water with Aluminium heterogeneity

The same experimental set up, phantom size, beam dimensions and SSD were simulated for the case when the air inhomogeneity was replaced by Aluminium. The Aluminium used for the measurements and calculations had density $2.66 g/cm^3$ [Redpath and Thwaites, 1991]. Dose ratios were obtained at the same positions as in the previous experiment.

Figure 6.34 presents the dose ratios along the central axis. Curve *ratio1* is the performance of the superposition calculation when only mass attenuation coefficients for water were used for the calculation of terma. On the other hand, curve *ratio2* is calculated using mass attenuation coefficients for Aluminium at interactions centres within the Aluminium heterogeneity. It is clearly seen that the latter is in closer agreement with the measured data. Curve *ratio2* was plotted as a test to observe the magnitude of differences when only mass attenuation coefficients for water are utilised. For a more complex inhomogeneous medium, a matrix of the effective mass attenuation coefficients and effective energy values along depths should be pre-calculated in accordance with the density information to be used with superposition. In this simple geometry, *ratio2* data were generated by executing conditional statements during the calculation of terma; this is not

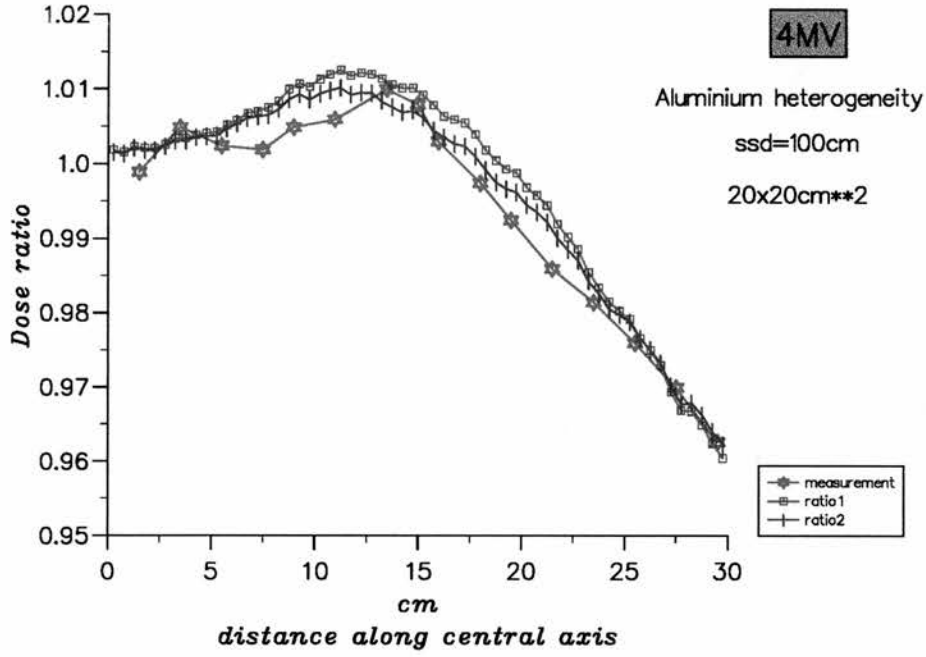

Figure 6.34: *Aluminium heterogeneity in water: dose ratios along the central axis.*

recommended as it slows down terma calculations considerably.

Profiles in Figures 6.35, 6.36, 6.37, show the variation of dose ratios when only mass attenuation coefficients for water are used (curves *ratio1*), or when coefficients for both water and Aluminium are employed (curves denoted as *ratio2*). Since the values of terma play the most significant role in the determination of the shape of the dose distribution, one would expect dose ratios, when Aluminium mass attenuation coefficients are used, to be in closer agreement with ratios derived from measurements. This is verified in these profiles (curves *ratio2*). The ratios from all profiles are smaller than unity because the beam has been attenuated considerably within the Aluminium cube therefore terma values below the cube are less than the corresponding values in the homogeneous water medium. The increase of the ratios at points closer to the central axis of the beam is due to the fact that above these points, a smaller proportion of the beam traverses through the Aluminium cube.

Aluminium has higher electron density than water and a smaller mass stopping power than water. These two factors contribute to an increase in electron fluence within Aluminium. On the other hand, the difference in atomic number from water results in changes in electron multiple scatter and in pair production for the high energy photon beams, which are not incorporated in the water EDKs.

Therefore, in the presence of such an inhomogeneity, the transport of secondary electrons would differ from the case when media are different just in terms of electron density. Here, for the 4MV beam, secondary electrons have relatively small ranges and one does not expect to observe major perturbation effects except very close to the interfaces of the two media. These profiles (curves *ratio2*) do not deviate significantly from measurements. At 22.5cm and 25cm rectilinear density scaling slightly overestimates dose whereas at 30cm the agreement with measured data is improved.

Curves denoted as *ratio1* exhibit a twofold inaccuracy. First and most significantly, terma values at these points are not close to the true values since the primary beam was not attenuated sufficiently within the Aluminium cube. This dominates the magnitude of dose values. Second, as mentioned previously, the polyenergetic EDK does not incorporate any corrections for the changes in stopping power and multiple electron scatter due to the presense of a material with much higher atomic number than that of water.

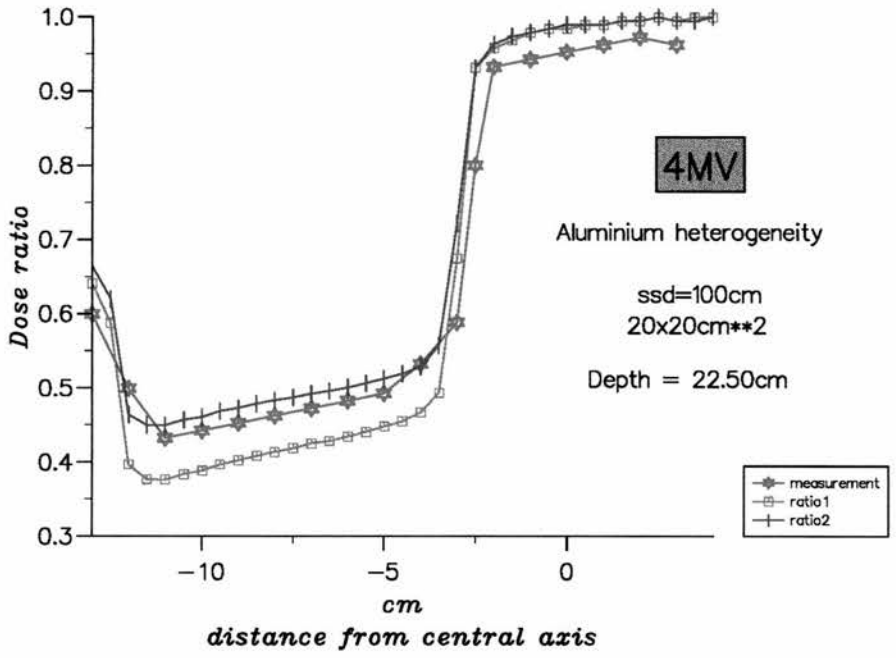

Figure 6.35: *Dose ratios across the beam at a depth of 22.5cm; namely 2.5cm below the Aluminium cube.*

6.7.4 Summary

The previous sections have demonstrated the general performance of the single polyenergetic superposition model developed in this work. Through some of these

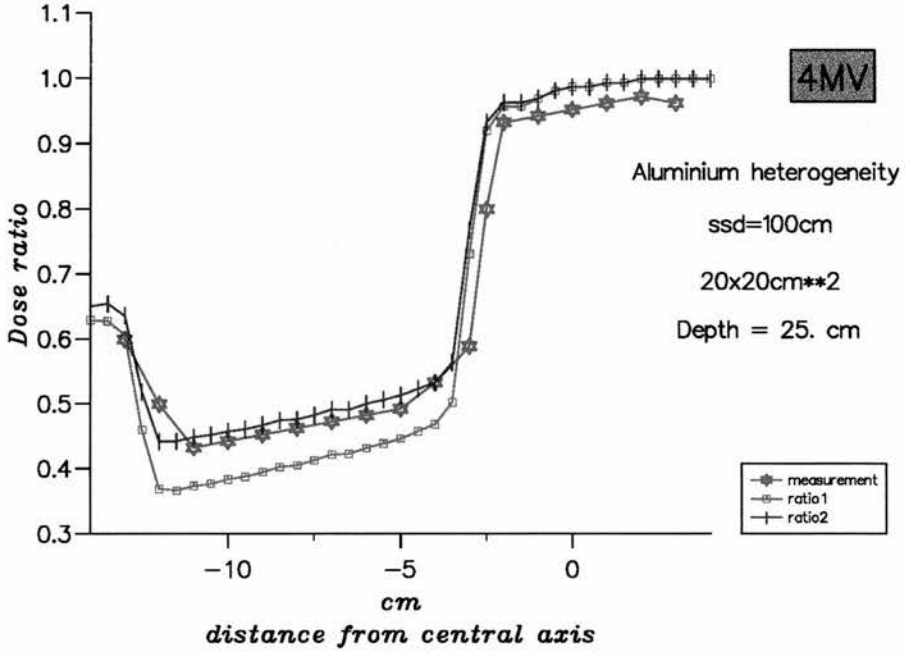

Figure 6.36: *Dose ratios across the beam at a depth of 25cm; namely 5cm below the Aluminium cube.*

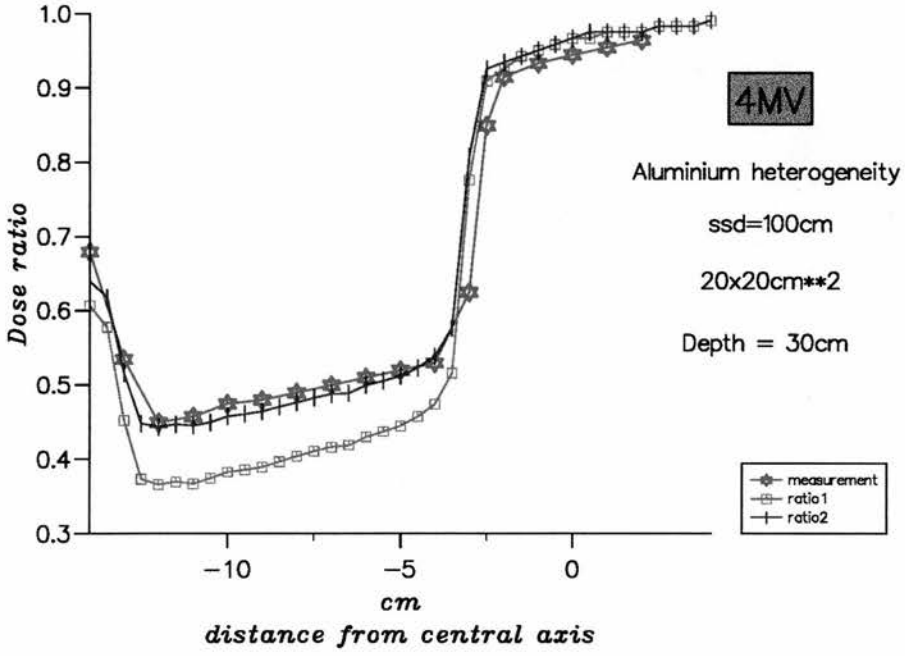

Figure 6.37: *Dose ratios across the beam at a depth of 30cm; namely 10cm below the heterogeneity.*

tests, the inherent limitations of the model, especially when using rectilinear density scaling of EDKs generated in water are demonstrated. The results of dose calculations from a 4MV beam can be summarised as follows:

- *Dose on the central axis in homogeneous media.* Values of dose in water for SSD=100cm and radiation field of $10 \times 10cm^2$ for 4MV, 6MV and 9MV beams are in excellent agreement with Monte Carlo data (Figure 6.14). Discrepancies within the build-up region due to electron contamination or head scatter are not obvious for the 4MV beam (Figure 6.16), whereas for the higher energy beams there are differences between calculated and measured data (Figures 6.18, 6.19 and 6.20). Depth dose variations in the waterlike medium with density $0.3g/cm^3$ are also in good agreement with EGS4 data (Figure 6.21). In Aluminium, the performance against Monte Carlo is very good, since terma is modelled accurately and the beam energy is not high. A 4MV polyenergetic kernel is probably close to isotropic since electrons at this energy would have small ranges, resembling the shape of a kernel generated in Aluminium.

- *Dose off-axis in homogeneous media.* Profiles in homogeneous media are in good agreement with Monte Carlo data. Within the build up region in water, and especially in the low density medium, superposition slightly underestimates dose. This is not a significant error and it could be attributed to the method used for ray tracing in the model (Figure 6.8). Exact radiological paths through voxels are not calculated. Since all off-axis comparisons are carried out against EGS4 generated data, for which the relative energy fluence at the surface is considered constant within the field, in general no discrepancies can be seen due to off-axis softening, the geometry of the source, the flattening filter, the collimating system, and any head scatter.

- *Surface curvature.* Experiment # 1 with the tangential irradiation demonstrates an inherent limitation related to all convolution/superposition methods using kernels generated in infinite water media. The maximum error for the 4MV beam was 4%. For higher beam energies this error is expected to be much less, since energy deposition is less isotropic around the point of primary interaction (i.e high energy kernels are elongated in the forward direction).

– *Inhomogeneous media.* Results from the irradiation of the slab geometry (Figure 6.25) display an underestimation of dose within the low density region in comparison with the data generated from DOSRZ. The increased uncertainty present in the Monte Carlo data are more likely to be the reason for the differences between the two methods. Below and above the low density slab, discrepancies are less than 0.5%.

Experiment #2 in water with the air heterogeneity, confirms the reports from other workers [Mohan et al., 1985], [Yu et al., 1995], according to which dose values are overestimated around regions of air. The shape of the profiles is predicted very well, even using effective mass attenuation coefficients for water instead of the corresponding values for air (the two do not differ significantly). In most clinically encountered situations, air cavities are smaller in size, therefore one does not expect to obtain large errors from superposition calculations.

Finally, experiment #3, tests the performance of the model in water with an Aluminium heterogeneity. It is demonstrated that for materials with atomic composition different from water it is important to use the appropriate mass attenuation coefficients. The energy examined here is low, therefore secondary electrons in Aluminium do not have a long range of travel outside this large heterogeneity. Discrepancies from measurements below the cube are minor, whereas towards the central part of the beam, a slight overestimation of dose contribution from particles originating from Aluminium and scattered laterally is observed.

– *Exit dose.* Another limitation of superposition approaches is the overestimation of exit dose [Mohan et al., 1985], [Woo, 1994]. At the exit surface, dose contributions from backscattered electrons in the kernels cannot be excluded. Due to the low beam energy employed in the above experiments, this effect is negligible for dose values at points on the central axis (Figures 6.14, 6.21, 6.23, 6.26).

6.8 Discussion

Chapter 3 discusses the convolution/superposition approach and analyses the various considerations which introduce approximations to this model. The most prominent problems influencing the performance of a superposition model in terms of accuracy are the effect of beam hardening on the calculation of terma and

the total-kernel changes in heterogeneous media. Beam hardening effects (both on terma and the kernel) and density scaling of total-kernels have been examined and modelled in this work (sections 6.5.3, 6.4, respectively). Beam divergence was only modelled partially (section 6.5.4) to improve agreement with measured data along the central axis. However dose values at off-axis positions do not display any noticeable differences when compared with Monte Carlo generated data. The following summarises the various considerations of superposition which have not been taken into account in this model:

1. *Modelling primary dose.* The model developed here carries out superposition in terms of polyenergetic terma and uses a polyenergetic total-kernel. Primary dose is not calculated separately. Changes in electron fluence caused by scattering in non-water media are not rigorously modelled, and rectilinear density scaling of electron paths is known to be inaccurate [Yu et al., 1995], [Keall and Hoban, 1995],[Keall and Hoban, 1996]. The performance of this model in inhomogeneous media for high energy beams needs further examination.

2. *Atomic number variations.* As discussed in section 3.4.1 of chapter 3, the presence of media with atomic numbers different from those of water should be taken into account. This means that the appropriate values for mass attenuation coefficients should be used for the calculation of terma and that kernels are scaled not only with density variations but also with differences in mean stopping power ratios between the high Z materials and water. This consideration was only carried out for terma (experiment # 3 in section 6.7.3). Further improvement of the model should include appropriate scaling for kernels [Sauer, 1995] or the use of kernels generated for material with different atomic composition than that of water [Papanikolaou and Mackie, 1993].

3. *Off-axis beam softening.* As discussed in chapter 3, photon beam spectra become softer as the off-axis distrance increases due to the nature of the bremsstrahlung spectrum and the shape and material of the flattening filter. In extreme situations, such as in very large irregular field sizes, primary dose calculations with conventional algorithms (using zero area TARs) were shown to lead to significant errors in dose (up to $5\% - 10\%$) at points off the beam's central axis [Kepka et al., 1985]. To allow for off-axis beam softening in this superposition model, would require the use of mass attenuation

coefficient values at off axis points. It has been shown that these can be calculated from the angular distribution of the bremsstrahlung spectra or can be derived from measurements [Mohan et al., 1985], [Zefkili et al., 1994]. Modelling the treatment head of linear accelerators or carrying out transmission measurements is not trivial. Here, off-axis softening is not modelled. The effect of this limitation on dose values at points on the central axis does not seem to be significant. One would expect any inaccuracies to be seen at points off axis.

4. *Beam contamination.* Superposition algorithms calculate dose per unit incident photon fluence (or energy fluence) from first principles. Any contribution to dose from photons or electrons originating from the head of the treatment machine (namely due to scattering in the flattening filter, collimators or beam modulators) should be modelled separately, since terma and kernel distributions do not encompass such information. As secondary collimator scatter accounts for less than 1% of the total dose under common clinical conditions [Ahnesjö, 1995b] and as the inclusion of scatter contributions from beam modulators is not considered critical [Ahnesjö et al., 1995], Ahnesjö essentially contemplates that it is more important to model contributions from photon scattering in the flattening filter [Ahnesjö, 1994]. Errors for failing to model photon and electron contamination are expected to be more prominent on dose values at points near or on the phantom surface. Accounting for head scatter is the next step one should consider for improving the performance of the superposition model in most general irradiation geometries.

6.9 Conclusions

The single polyenergetic superposition model is based on the following significant aspects:

- Polyenergetic terma and polyenergetic total-kernel distributions are used for the calculation of dose at a point.
- Beam hardening is taken into account both in the terma and kernel.
- Kernel alignment to beam divergence is carried out approximately.

- Rectilinear density scaling of the total-kernel is used for the calculation of dose in heterogeneous media.

The performance of the model was verified in both homogeneous and simple heterogeneous media for the 4MV beam and only in water for the higher energy beams. The agreement with results from EGS4/DOSRZ was well within $\pm 2\%$. Discrepancies from measured data were observed in build-up regions for the high energy beams and in the tangential irradiation geometry with the 4MV beam. The former were due to the lack of head scatter and electron contamination modelling, whereas the latter is an inherent modelling deficiency of all models that use kernels generated in the centre of a large phantom when they are used to predict dose close to a surface (sections 3.4.1 and 6.7.3)

This chapter has not discussed the performance of the model in terms of speed. However, several decisions have already been made at early stages of its development in view of the necessity to compromise accuracy for speed. These are:

- The execution of superposition for total dose instead of separately calculating primary and scatter dose components.

- The modelling of beam hardening in terma by using depth dependent effective mass attenuation coefficients, instead of summing up weighted average terma distributions from each spectral component.

The following chapter aims to address the problem of speed in 3D photon dose calculations in general, and presents a novel approach through which 3D models such as superposition can generate results faster.

Chapter 7

The Correction Factor method

7.1 Introduction

Advanced algorithms, such as superposition, which model dose deposition from first principles, achieve the goal of ± 3 % for most clinically encountered situations and generate 3D dose matrices which are necessary for conformation therapy techniques. Such algorithms are generally intensive in terms of memory, mass storage and computation time requirements especially when calculations are performed on a grid of fine resolution. On the other hand, 3D treatment planning systems require computational speeds that enable real-time user interactivity. This chapter is concerned with the problem of improving computation speed of true three dimensional dose calculation algorithms.

While significant efforts have been directed towards the development of accurate models, only limited advances have been made to enable their clinical implementation. The use of special hardware, such as array processors or transputer circuits has already been discussed by some investigators [Krippner et al., 1987], [Wong *et. al.*, 1991], [Murray et al., 1989], [Murray et al., 1991]. The high cost and complexity of such systems are the main reasons that prevent their application into clinical environments.

According to Purdy, the solution to the problem of performance in terms of speed, lies in the use of sophisticated computer systems in conjunction with *software optimisation* [Purdy, 1992]. Purdy refers to techniques that employ variable grid spacing [Rosenberger et al., 1984], [Niemierko and Goitein, 1989b], or random sampling of grid points [Niemierko and Goitein, 1990], [Lu and Chin, 1993]. In addition, software optimisation encompasses techniques such as Siddon's fast ray-tracing [Siddon, 1985] and the "run-length ray-tracing" suggested by Mackie *et al.* [Mackie et al., 1990a]. Methods utilising octree geome-

tries [McShan and Fraass, 1993], quadtrees [Kooy and Kijewski, 1988] or Fast Fourier Transforms [Boyer and Mok, 1984] can also be classified as software optimisation techniques. The limitations on accuracy imposed when employing FFT techniques with the convolution/superposition approach have been discussed in chapter 2. Siddon's software for fast ray-tracing, can be advantageous for calculating the distribution of terma, but offers no improvement in speed if implemented for the superposition of kernels.

The selection of grid spacing for the calculation of accurate dose distributions is an important consideration which involves compromise. In dose calculations with superposition, it relates to computational accuracy, calculation speed and the computer hardware requirements.

Random sampling of dose calculation points has only been investigated for the evaluation of treatment plans (i.e. the calculation of dose-volume histograms, TCP and NTCP) [Niemierko and Goitein, 1990], [Lu and Chin, 1993], but was considered less efficient for the calculation and presentation of an entire dose distribution. This is because the display of dose distributions requires dose values on a regular grid within the display region and interpolation of doses from the randomly distributed points is computationally demanding.

Techniques which allow the calculation of dose on non-uniform but regular grids seem attractive for use with superposition [Niemierko and Goitein, 1989b]. This is because, superposition algorithms implemented from the *dose deposition point of view*, can model accurately dose at individual points, provided terma is obtained on a relatively fine regular matrix. The interesting aspect when using a non-uniform grid is that dose can be calculated on a finer resolution in regions of large dose variations and on a more coarse matrix where dose variations from point to point are small. However, one needs first to identify regions in the medium with non homogeneous composition or non uniform density, where a finer dose resolution is required. Such a task will decrease the overall time required for the completion of a superposition calculation.

An interesting study on the errors involved when linearly interpolating dose values within regular rectangular grids and the relation of these errors to grid size has been provided by Niemierko and Goitein [Niemierko and Goitein, 1989a]. They have shown that dose interpolation between points is acceptable either when the desired dose accuracy is achieved or the distance between the estimated and actual isodose contours does not exceed the maximum acceptable. The difficulty in fulfilling either one of the two criteria, is most apparent in regions of

rapidly varying dose such as at beam margins. Niemierko and Goitein have demonstrated that the required grid size depends on the detailed shape of the penumbra and that linear interpolation between grid points (in both the steepest and slowly varying dose regions) is a good approximation. Regions where the second derivative of the dose profile is large, are those where the greatest errors occur. Another significant conclusion emerging from this work on the choice of grid spacing has been summarised as follows [Dryzmala et al., 1991] : *The best choice of grid spacing to achieve a given accuracy is dominated by the greatest allowable isodose position error, rather than the accuracy of dose estimation at a point. For most practical beams, in order to achieve an isodose positioning error of* $\leq$ *to delta - or a dose accuracy of* $\leq$ *to 2%, a grid spacing of about 2.5 times delta is needed (provided delta is* $\geq$ *to 2mm). Thus 2 % dose accuracy or 2mm isodose positional accuracy (but not necessarily both) will be achieved with a grid spacing of 5mm.* Based on the above, Niemierko and Goitein developed a method of using a nonuniform grid of calculation points [Niemierko and Goitein, 1989b]. It utilises an iterative procedure for reducing an initial large grid size into smaller sizes while dose at points are either calculated or interpolated according to certain predefined criteria. This technique was demonstrated in the case of a wedged profile in a homogeneous medium, but its performance in cases of inhomogeneous media with large heterogeneities is not known.

A method was developed in this thesis, named as the **CF-method**, for improving computation speed in superposition. It is described in section 7.3 and section 7.4 demonstrates the limitations imposed on the accuracy of the results. Prior to the presentation and discussion of this method, section 7.2 offers an analysis on the various parameters which influence calculation speed in the superposition model.

7.2 Calculation times in the superposition method

Section 6.5.2 and Figure 6.8 in chapter 6 describe how the kernel is superimposed on the terma matrix. Dose at a point is calculated from energy contributions originating from volume elements which are defined by spherical coordinates (r, θ, ϕ). The origin of this spherical coordinate system is at the dose calculation point. The values of r depend on the value of variable `radstep`, which determines the voxel size in cm in the radial direction. The values of θ (polar angles) are set equal to those in the kernel array, therefore the number of angles considered in the

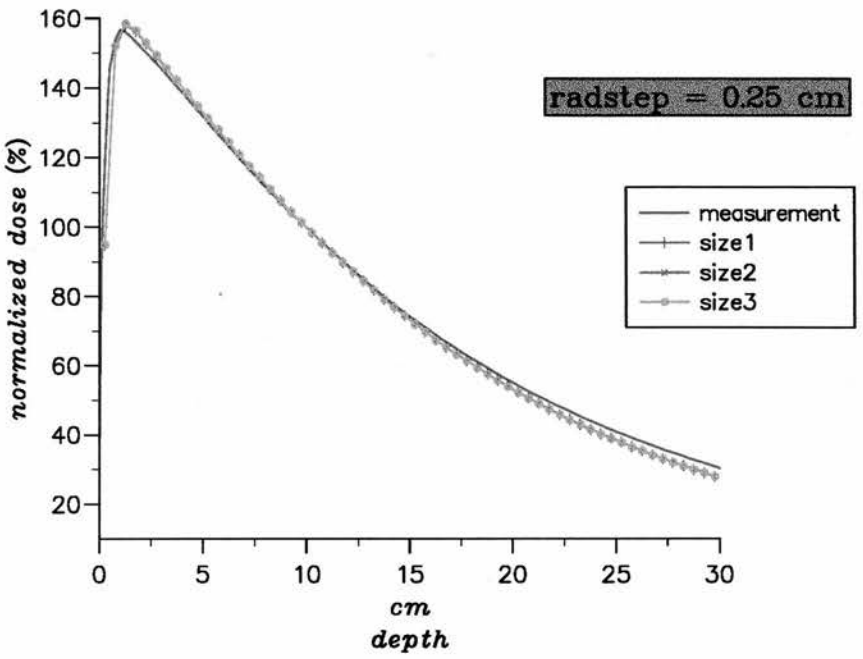

Figure 7.1: *Depth dose curves is water from 4MV beam (SSD=100cm, radiation field=10 $\times$ 10cm^2) with* `radstep=0.25cm` *and varying numbers of steps in the r, θ, ϕ directions.*

polar direction is 48. Due to the symmetry of kernels in the azimuthal direction, one can choose arbitrarily the number of ϕ angles for consideration in the dose calculation. If this number is set to 96, the resolution in the ϕ-direction would be the same as in the θ-direction. All results presented in chapter 6 were obtained using 48 steps in the azimuthal direction. Since these results were in acceptable agreement with Monte Carlo data and measurements, it was considered unnecessary to examine the case of increased resolution in the azimuthal direction. The model presented in chapter 6 does not carry out explicit ray-tracing through voxels lying along the path connecting dose calculation and dose interaction sites Its acceptable performance in the build-up region or at media interfaces is attributed to the fact that variable `radstep` was chosen to be small (0.25cm); smaller than the side of the cubic voxel (0.5cm) in the terma matrix. However, the smaller the value of `radstep`, the larger the computation time.

Table 7.1 displays a comparison of calculation times from different combinations of `radstep` and steps in the ϕ direction (the steps in the r, θ were constant and equal to 24 and 48 respectively). The dimension of the water phantom was $20 \times 20 \times 30cm^3$. Terma and dose matrices comprise of voxels with size equal to $0.5 \times 0.5 \times 0.5cm^3$. The 4MV beam was incident at SSD=100cm with a radiation

radstep (cm)	Number of ϕ steps	Calculation time for depth dose (60 points) (sec)	Calculation time per point (sec)	rel. error at 15cm (%)
0.25	48	100.92	1.68	1.2
	24	50.69	0.84	1.2
	12	25.63	0.42	1.3
0.50	48	79.90	1.33	1.3
	24	40.29	0.67	1.3
	12	20.61	0.34	1.4
0.75	48	70.10	1.16	1.3
	24	35.29	0.58	1.3
	12	17.84	0.29	4.5

Table 7.1: *The influence of kernel dimensions on calculation time for the superposition model developed in this thesis. Relative errors refer to the dose value along the central axis and at the depth of 15cm.*

field of $10 \times 10cm^2$. The third column holds the times required for the calculation of a depth dose (here, 60 calculation points) and the fourth column shows the approximate time for a single calculation point. Column five holds the relative error of the dose calculated at a point on the central axis and at a depth of 15cm. All calculation times quoted in this work are for a Sun/SPARC2 system, while compilation was carried out using the -O4 Fortran optimisation flag. The times could be further reduced by implementing appropriate programming optimisation techniques related to the use of *registers*, *cache* and *virtual memory systems* for frequently accessed data values.

Figure 7.1 presents four depth dose curves. The solid line corresponds to measured data whereas the three other curves display results from superposition when `radstep` was 0.25 cm and the number of steps in the r, θ and ϕ dimension were (24,48,48) in curve denote as *size1*, (24,48,24) in curve *size2* and (24,48,12) in curve *size3*. In the same manner, Figure 7.2 shows comparisons with measurements when `radstep` is 0.50 cm and Figure 7.3 when `radstep` is 0.75 cm.

In all figures, curves *size1*, *size2* and *size3* agree perfectly with each other. In Figure 7.1 the discrepancies from measured data have already been observed and discussed in the previous chapter. As seen from Tables 7.1 a reduction in step size along the ϕ-dimension from 48 to 24 steps does not influence the accuracy of the calculated dose value on the central axis at the depth of 15 cm, whereas it requires approximately half the computation time. A further reduction in size down to

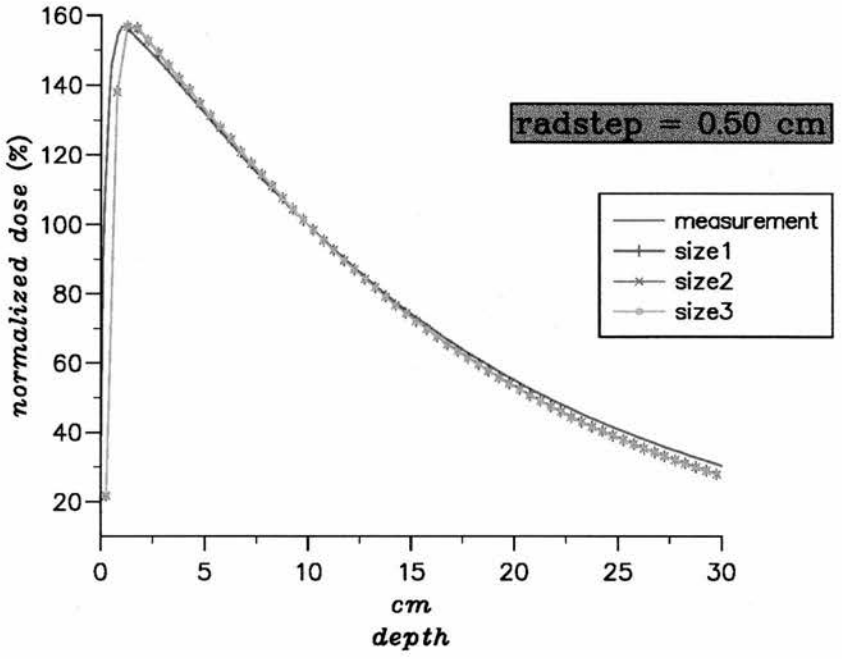

Figure 7.2: *Depth dose curves is water from 4MV beam (SSD=100cm, radiation field=10 × 10cm^2) with* `radstep=0.50cm` *and varying numbers of steps in the* r, θ, ϕ *directions.*

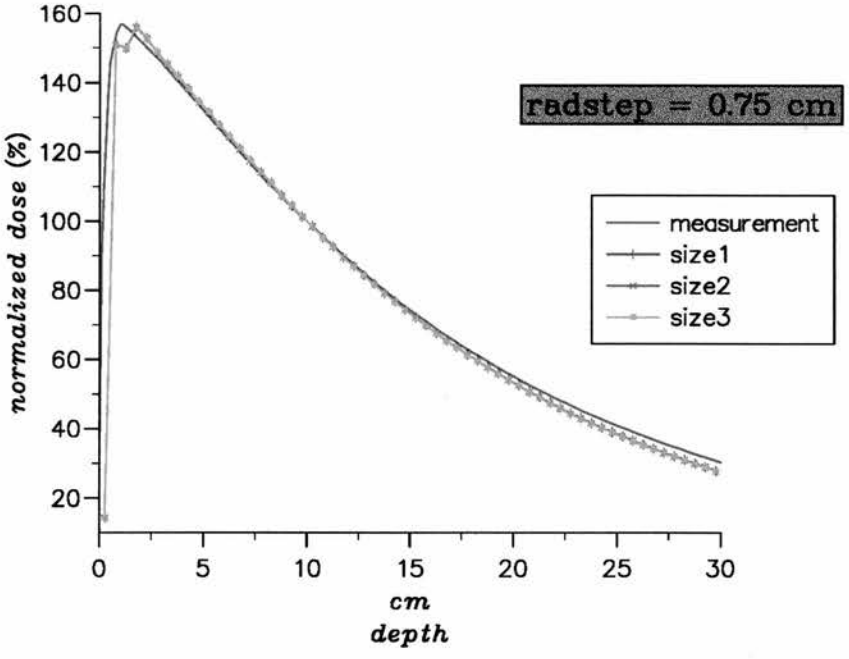

Figure 7.3: *Depth dose curves is water from 4MV beam (SSD=100cm, radiation field=10 × 10cm^2) with* `radstep=0.75cm` *and varying numbers of steps in the* r, θ, ϕ *directions.*

12 steps in the ϕ-dimension introduces a further reduction in computation time with some change of the relative error of dose at a point.

The number of steps in the θ direction were kept the same as in the polyenergetic kernel, which avoids having to interpolate kernel values in the θ direction. Although, this task can be carried out in advance and kernels could be stored for larger angular intervals in this direction, any gains in computational speed will result in loss of accuracy in heterogeneous media. This is because, in the polar direction the kernel exhibits a steep gradient and because the terma values multiplied with the kernel would not be representative of the average primary energy released in the spherical voxel under consideration.

For the superposition model developed in this thesis one observes that calculation time decreases with increasing values of `radstep`. However, with the increase of `radstep` the agreement with measurement gets increasingly worse and this is more obvious around the build up region (Figure 7.3). For large values of `radstep` one expects similar errors at any media interfaces. This is because the density values used for scaling kernels do not have values close to the average density along the path connecting the photon interaction and dose deposition sites. Therefore, the accuracy of results from this software is strongly dependent on the value of `radstep`. This should be set to be smaller than the side of the cubic voxel in the terma matrix. In any case, if terma is calculated on a very coarse grid (the sizes in voxels of the order of units of centimeters) one should also expect inaccuracies in the calculated dose distribution. The generation of accurate dose values depends strongly on the magnitude of values in the terma distribution. The experience from this work, has indicated that a terma matrix (polyenergetic terma matrix in the case of clinical beams) with voxel sizes equal to $0.5 \times 0.5 \times 0.5 cm^3$, together with a `radstep` value of 0.25cm give acceptable dose values. The grid spacing in the terma array is in agreement with the recommendation of Niemierko and Goitein [Niemierko and Goitein, 1989a], [Dryzmala et al., 1991] discussed in the previous section.

From Table 7.1 it is obvious that this implementation of the superposition method is slow for practical use (i.e for 400000 calculation points which represents an example of the number of voxels considered in a patient of average size). The various methods that could achieve an increase in calculation speed have been discussed in the previous section. With the rapid advent of new, faster hardware, it is a matter of a few years before true three dimensional dose calculations are feasible within clinical environments. In the mean time, it is possible to

benefit from the use of accurate three dimensional dose calculations, such as superposition, by implementing the following technique developed in this work and described in the following section.

7.3 Description of the CF-method

The Correction **F**actor method (CF-method) aims to use the single polyenergetic superposition model for dose calculations in three dimensional treatment planning. Current implementations of superposition in interactive treatment planning systems have been possible by performing calculations on very coarse grids and further (linearly) interpolating dose values on finer matrices [Papanikolaou et al., 1995], [Mackie, 1995a], [Schultze, 1995]. This straightforward interpolation from coarse grids runs the risk of producing erroneous results in regions of extreme dose gradients. The aim of the CF-method is to minimise this risk.

The CF-method utilises a true three dimensional dose calculation model such as superposition, in conjunction with a conventional, simpler (fast) algorithm, such as the Batho method, which is implemented to generate 3D dose matrixes. Three dimensional dose calculations with the CF-method are carried out in the following four-step procedure:

1. **Dose calculation on a fine matrix using a fast algorithm.** A conventional algorithm is used for the calculation of the dose distribution on a uniform rectangular Cartesian matrix with a small grid separation (fine calculation matrix).

2. **Superposition dose calculation on a coarse matrix.** Following the calculation of the terma distribution on the same fine matrix, superposition is employed for the calculation of dose at some selected points on this matrix. The distance between these points is larger than the grid separation of the initial fine dose matrix. The selection of this grid separation reflects the accuracy required in the final dose distribution. The use of a single polyenergetic superposition model implemented from the *dose deposition point of view* is clearly an advantage when one needs to test different grid separations. Dose values from superposition are normalised to dose at the same point as those from the conventional calculation.

3. **Derivation of correction factors on a fine matrix.** For those positions

on the fine matrix, where dose values have been calculated by both methods, dose ratios from superposition to the conventional method are derived. With the calculation of these ratios (Correction Factors), two arrays are available. The initial fine dose array generated by the fast algorithm and the coarse matrix of correction factors. A fine matrix of correction factors can be further obtained by linear interpolation among those values on the coarse matrix.

4. **Computation of final 3D dose array**. The last step is the multiplication of the corresponding correction factors with the dose values at points where no superposition calculation has been carried out.

Conventional inhomogeneity corrections which do not use three dimensional density information are known for calculating dose at a point with reduced accuracy. In general though, they predict a realistic shape for the dose distribution within regions of non uniform composition and density [Wong and Purdy, 1990]. For this reason it was realised in this work, that the dose distribution from a conventional calculation could be implemented together with a superposition model for calculating dose distributions on a matrix with fine resolution. This idea can be viewed as a technique for improving the dose distributions produced by fast algorithms [Aspradakis et al., 1995]. In any case, either considering the improvement in the accuracy of fast models or an increase in speed for superposition, the **CF-method** is a simple, fast concept which achieves the desired result. The following section presents examples of the implementation of this technique. Simple arithmetic operations and linear interpolation are much faster than the superposition of a kernel with a terma matrix. Therefore there is no question regarding the advantages in terms of speed. What is of greater concern is the magnitude of errors present in the final dose distribution and in general the limitations imposed by the method.

7.4 Applications of the CF-method

All the following calculations were performed for the 4MV beam. Three irradiation geometries were examined. A homogeneous water medium (section 7.4.1), a geometry of water with a cube of air (section 7.4.2) and a patient geometry (section 7.4.3). The conventional algorithm used was a 3D implementation of the generalised Power-Law (Batho) inhomogeneity correction method [Redpath, 1995].

Superposition calculations were carried out on variable calculation grids. The distribution of terma was calculated once for each irradiation geometry on a fine grid (with voxel size equal to $0.5 \times 0.5 \times 0.5cm^2$). The number of steps in the (r, θ, ϕ) direction was (24,48,48) and `radstep` was set to 0.25cm. The grid separations in superposition were multiples of the separation in the terma matrix. In the following graphs these changes are referred to as the `step` in the calculation. Therefore, `step=1.0 cm` refers to a 1.0 cm separation between calculation points, thus superposition is performed on every two points on the terma matrix. `step = 3.0cm` corresponds to 3.0cm separation, which is at every six points on the the terma matrix. In all figures, the curve denoted as *batho* represents results from the power-law calculation, the curve shown as *super* is from the superposition calculation on the fine grid and the crosses (x) denoted as *super*N, are superposition dose values from the coarse grid calculation with a separation of N/2 cm. Curves denoted as *batho*N are the corresponding dose values calculated by the CF-method. Dose values from both calculation methods are normalised to their respective value at the depth of dose maximum.

7.4.1 Homogeneous water medium

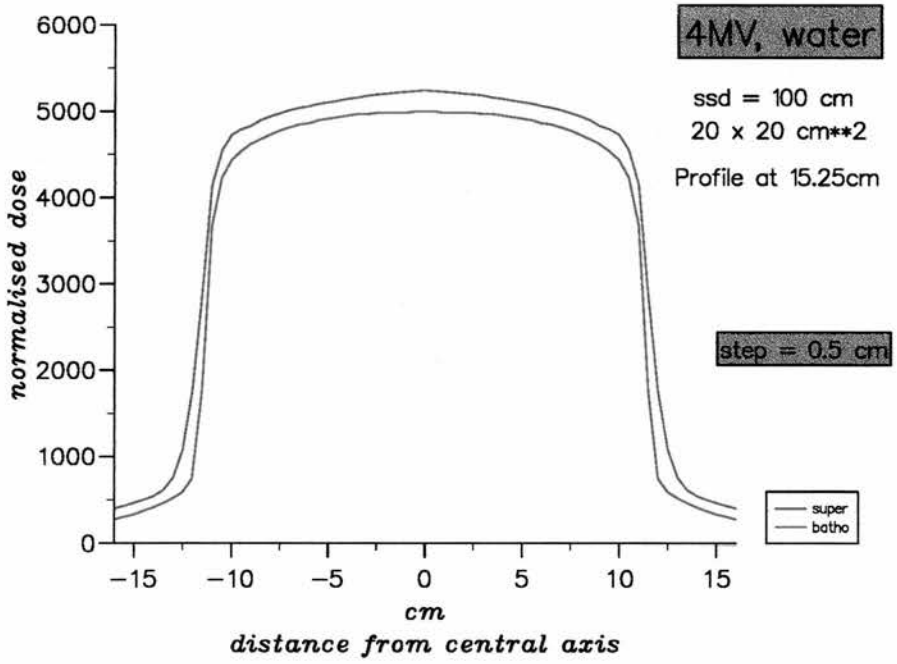

Figure 7.4: *Superposition carried out every 0.5 cm.*

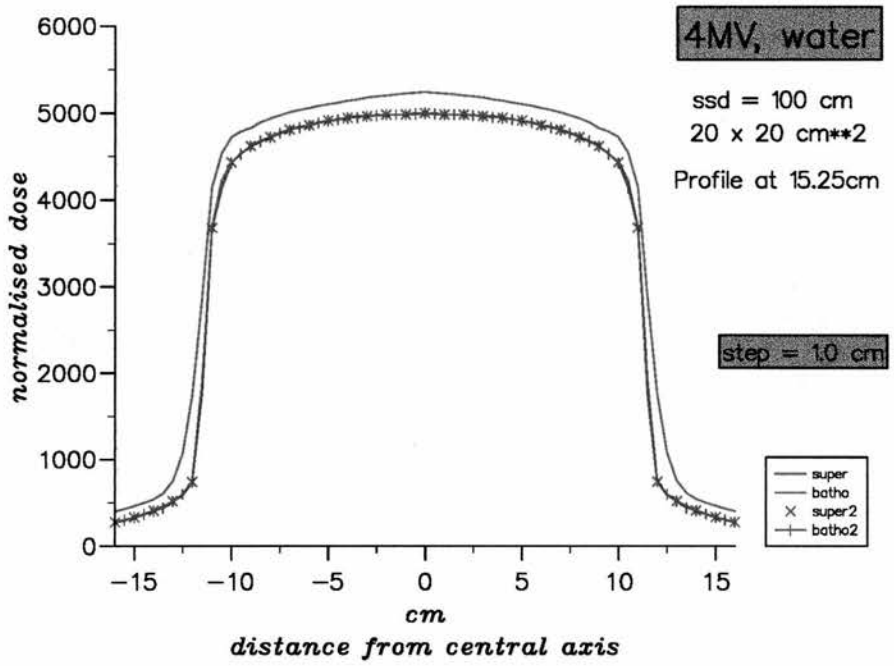

Figure 7.5: *Superposition carried out every 1.0cm.*

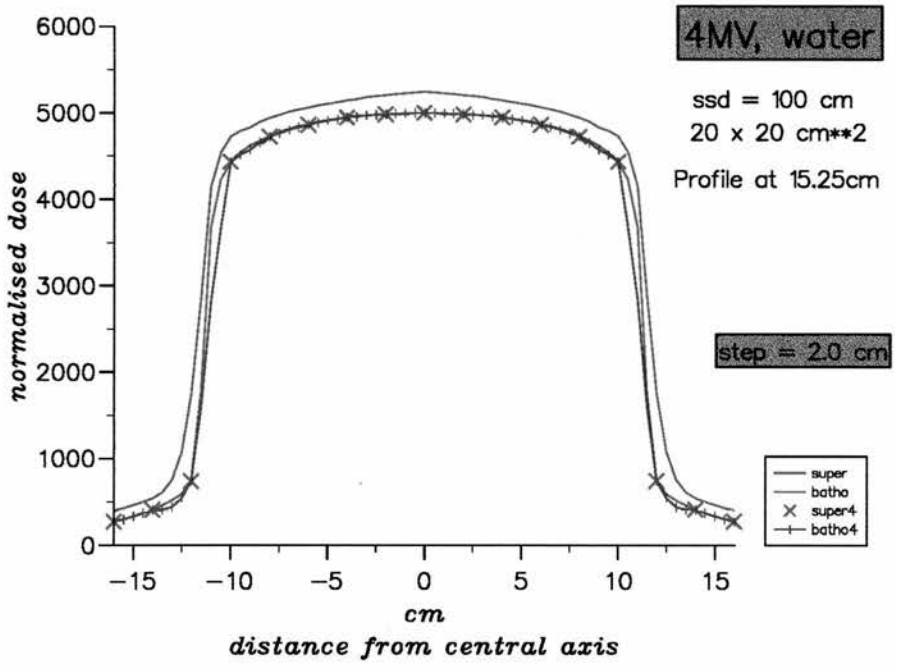

Figure 7.6: *Superposition carried out every 2.0cm.*

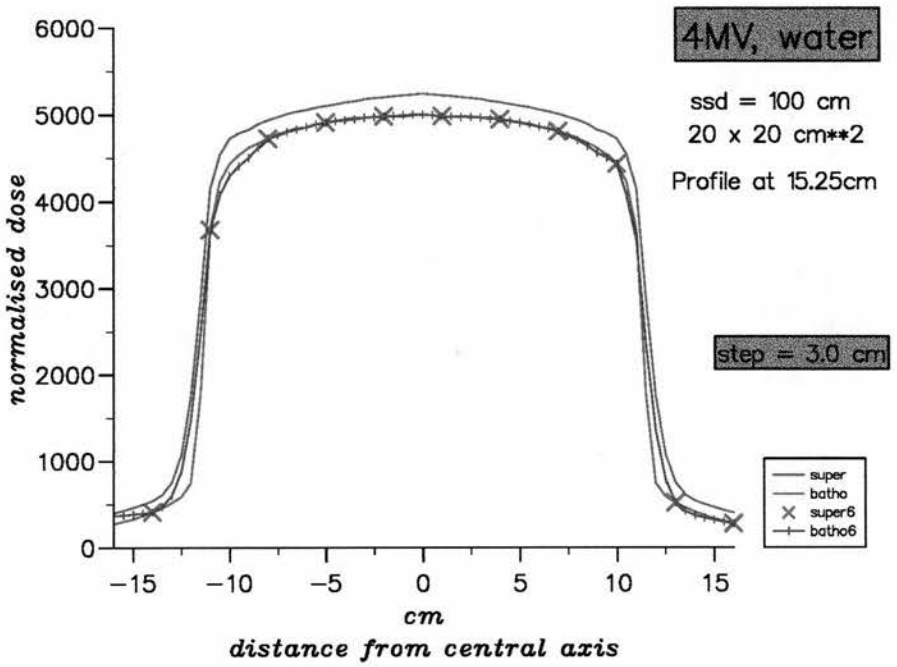

Figure 7.7: *Superposition carried out every 3.0cm.*

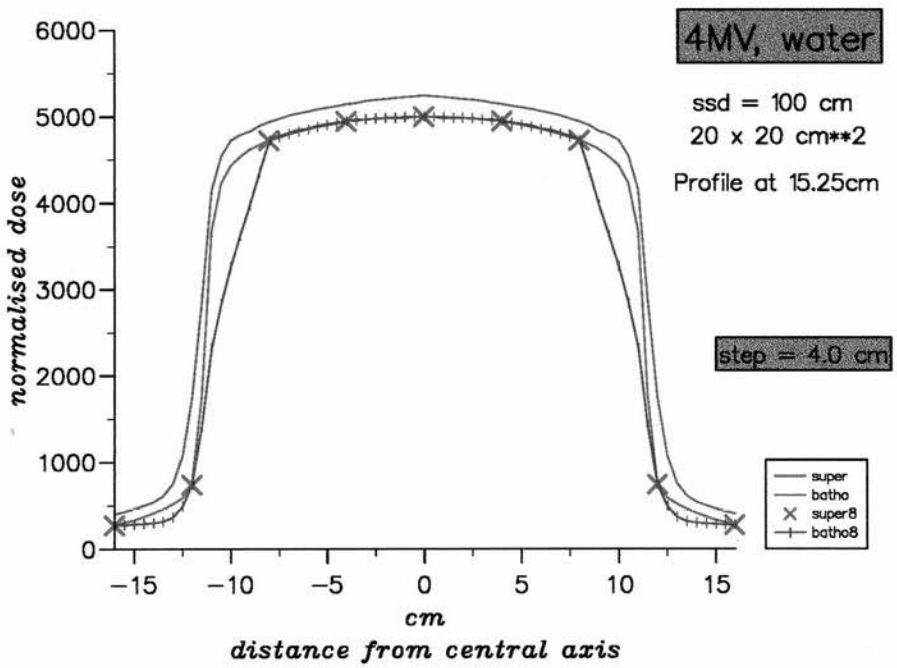

Figure 7.8: *Superposition carried out every 4.0cm.*

The case of a homogeneous medium was examined in order to observe the performance of the CF-method around regions of beam margins where steep dose gradients are present. The phantom dimension was $40 \times 40 \times 40 cm^3$. The incident beam was at SSD=100cm and with radiation field of $20 \times 20 cm^2$. The profiles shown in Figures 7.4 to 7.8 are at a depth of 15.25cm. In a homogeneous medium, the power-law calculation, which is a heterogeneity correction method, simply results in profile data interpolated from stored measured data. These profiles in water from both methods are almost identical in shape if normalised to their respective values on the beam's central axis. The discrepancies in magnitude are attributed to spectral differences, as discussed in the previous chapter. Ignoring these differences due to the spectrum, the aim here is to match, as closely as possible, the results from power law with those from superposition.

The data in Figures 7.5, 7.6 7.7, indicate that a grid spacing up to 3.0 cm introduces deviations from superposition less that 3 %. The time required for calculating a single profile is reduced from about 300 sec for grid separation of 0.5cm (Figure 7.4), to about 50 sec for grid separation of 3.0cm. For grid separations equal or greater than 4.0cm, the accuracy of dose values at points close to the penumbra region depends on the coarse grid distribution from superposition around that region. In such cases, errors are likely to be larger than 10% (Figure 7.8).

7.4.2 Water with cube of air

As discussed in chapter 6, superposition overestimates dose on the central axis of the 4MV beam along the side Figure (6.30) and below the air heterogeneity (Figures 6.31, 6.32 and 6.33). The power-law correction method introduces significantly larger errors in the dose calculation.

Since power-law only takes into account density variations along the primary photon's direction and does not model dose contributions from scattered radiation originating from other directions within the medium, dose values along the central axis are greatly overestimated. The power-law method would not account for the fact that in comparison with the homogeneous water medium, less scattered photons originate from the region of the air heterogeneity.

Depth dose calculations

Figure 7.9 presents a comparison of normalised dose values from superposition and the power-law correction. The grid separation in both calculation methods

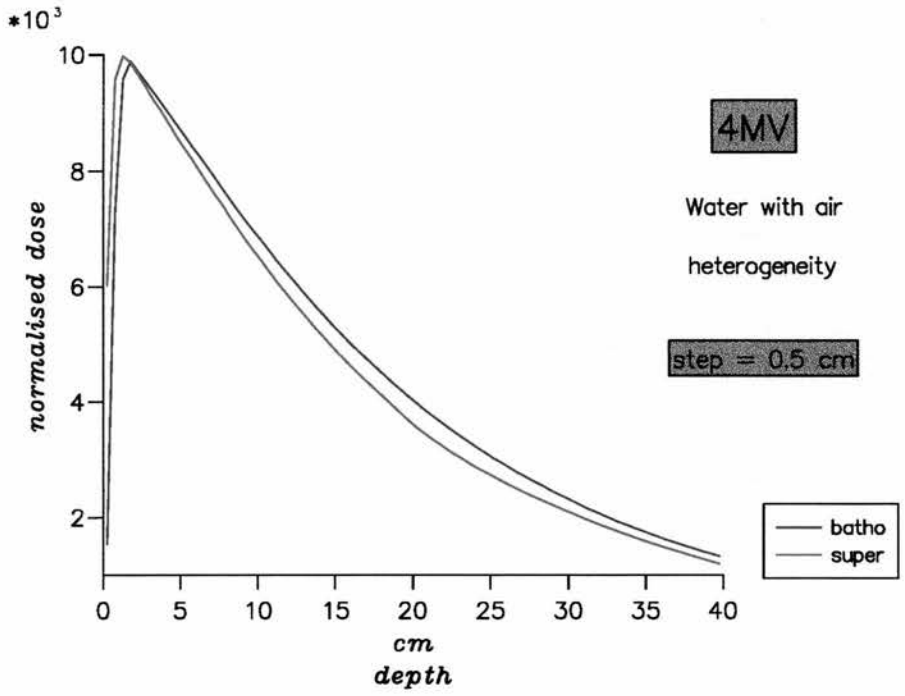

Figure 7.9: *Dose variation along the central axis of a* $20 \times 20cm^2$ *radiation beam in water with an air heterogeneity. Superposition was carried out on a matrix with 0.5cm grid separation.*

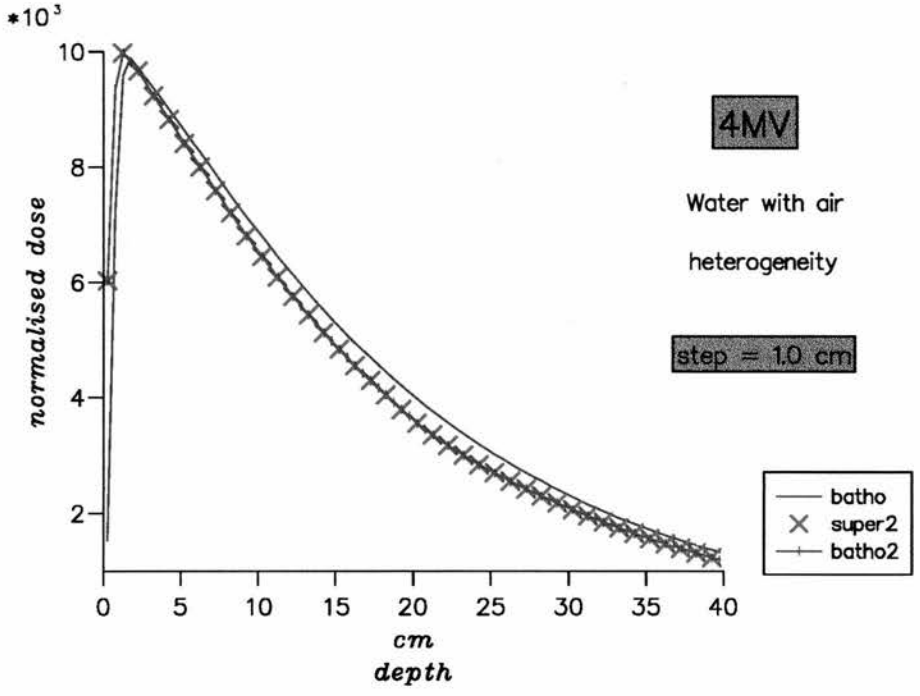

Figure 7.10: *Dose variation along the central axis of a* $20 \times 20cm^2$ *radiation beam in water with the air inhomogeneity. Superposition was carried out on a matrix with 1.0 cm point separation.*

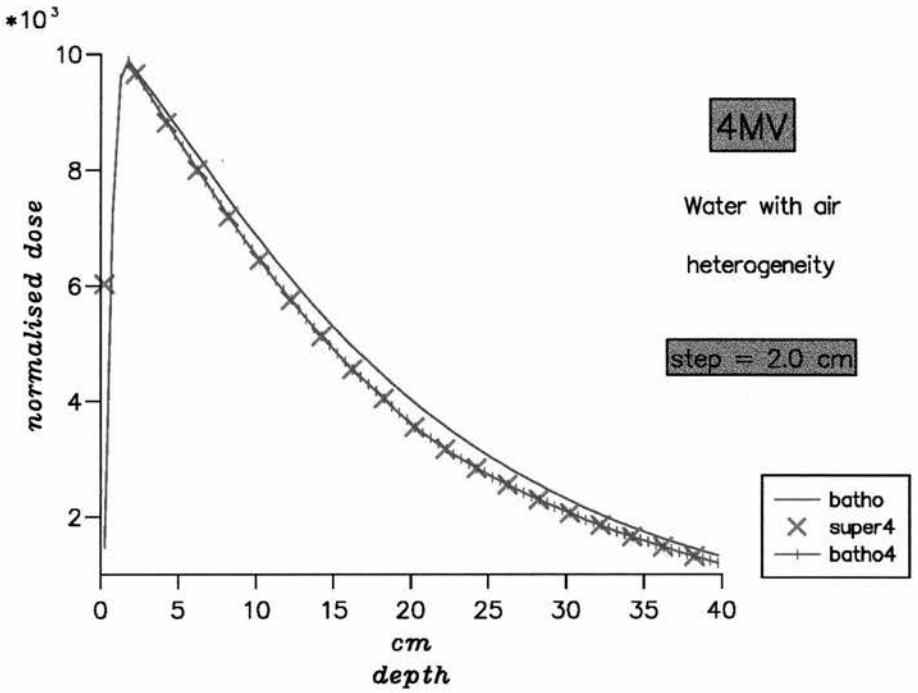

Figure 7.11: *Dose variation along the central axis of a* $20 \times 20cm^2$ *radiation beam in water medium with the air inhomogeneity. Superposition was carried out on a matrix with 2.0 cm point separation.*

is 0.5cm in all dimensions.

Figures 7.10, 7.11, 7.12, 7.13, present the application of the CF-method for grid separations of 1.0cm, 2.0cm, 3.0cm and 4.0cm respectively. As expected, even large grid separations such as 4 cm achieve the computation of dose distribution accurately in regions with no large dose gradients. In this case, the choice of step size in superposition depends on the extent of the build up region. For the 4MV beam, a grid separation of 2.0cm introduces no artefacts in the final depth dose, except that any steps larger than 1.5cm (which is approximately equal to the depth of maximum build up) would result in artefacts apparent at depths less or equal to these steps. For higher energy beams, such problems would be present for larger calculation steps and consequently down to larger calculation depths. If the point of maximum dose is included in the calculation of CF ratios, then any errors within the build-up region would be reduced. The generation of such artefacts is overcome in the CF software by replacing the dose values at the corresponding depths with data from the original power-law calculation.

In terms of speed, in this irradiation geometry, the calculation of a depth dose with superposition on a fine resolution (0.5cm) takes around 160 sec. For a coarser calculation grid (2.0cm) the required time is reduced to 40 sec.

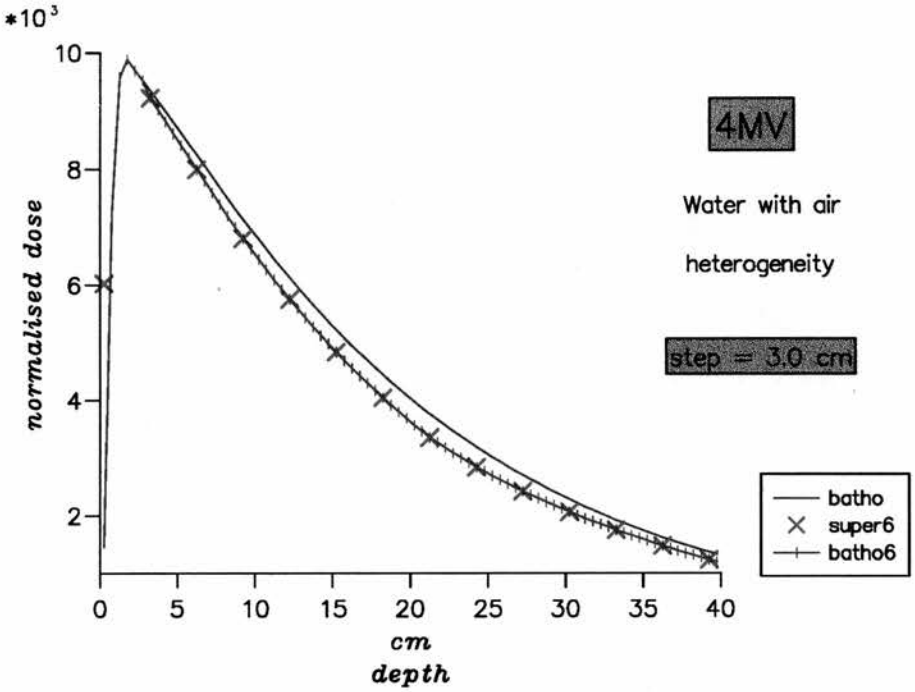

Figure 7.12: *Dose variation along the central axis of a $20 \times 20cm^2$ radiation beam in water medium with the air inhomogeneity. Superposition was carried out on a matrix with 3.0 cm point separation.*

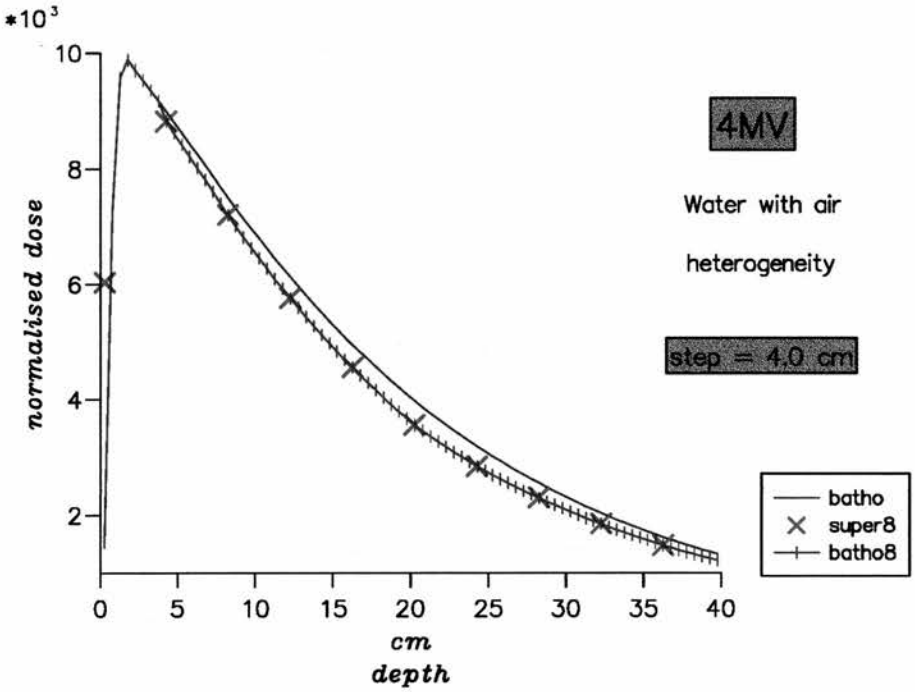

Figure 7.13: *Dose variation along the central axis of a $20 \times 20cm^2$ radiation beam in the water medium with the air inhomogeneity. Superposition was carried out on a matrix with 4.0 cm point separation.*

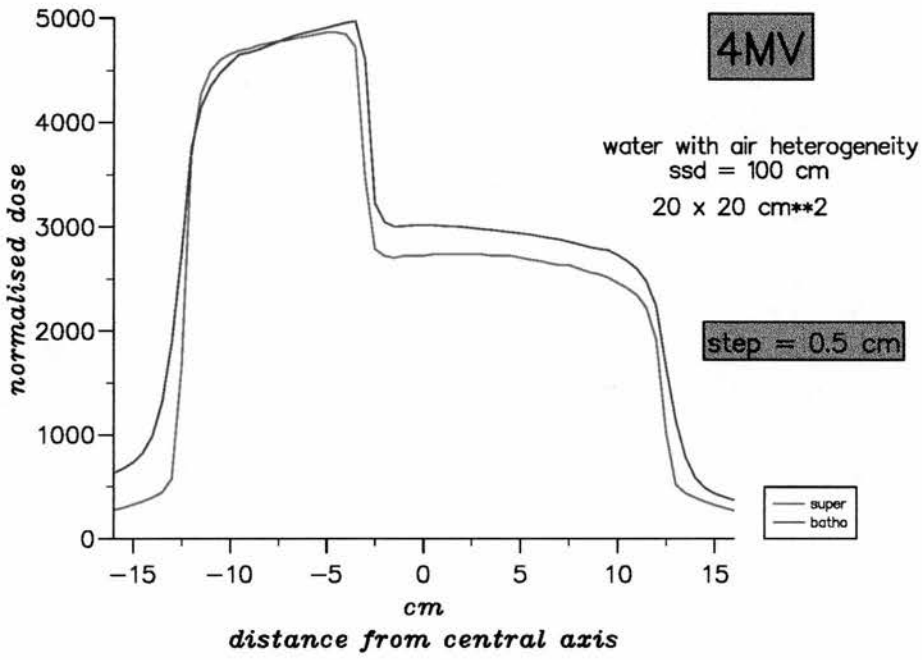

Figure 7.14: *Profiles at 25.25 cm, below the air inhomogeneity. The grid separation in superposition is 0.5 cm.*

Dose profile calculation

The CF-method was applied to the calculation of dose profiles below the air inhomogeneity at the depth of 25.25cm. Figures 7.15 to 7.18 display such profiles for `step` values varying from 1.0cm to 4.0cm. Here, the errors in the dose values are less than 3% for grid separations up to 2.0cm. For larger separations the errors in the vicinity of steep dose gradients are higher than 10%. Calculation time for these curves is around 300 seconds for the fine 0.5 cm resolution (shown in Figure 7.14) and is reduced down to 40 seconds for calculations on a separation of 4.0 cm.

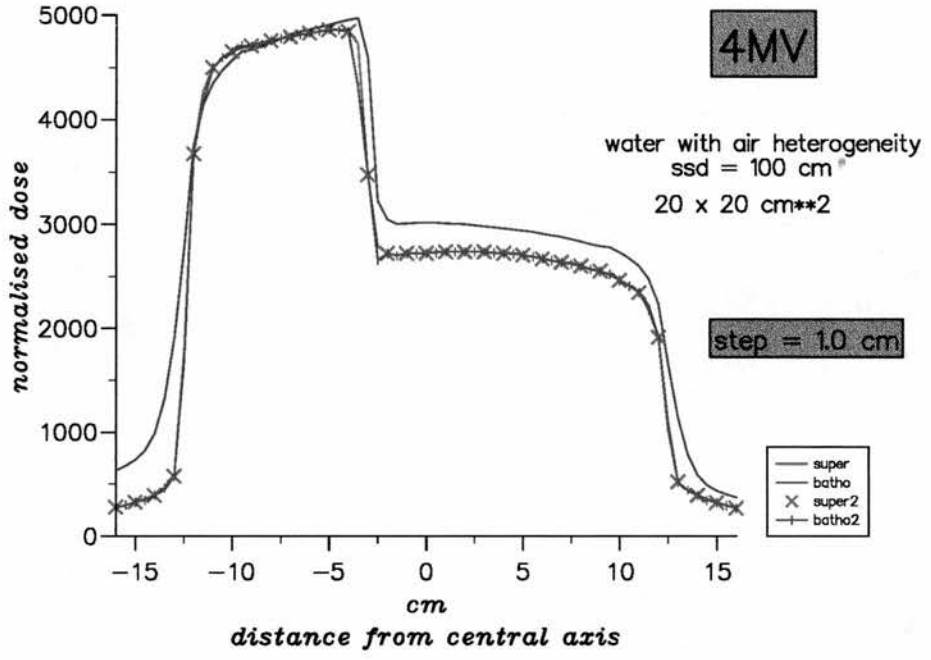

Figure 7.15: *Profiles at 25.25 cm, below the air inhomogeneity. The grid separation in the coarse superposition calculation is 1.0cm.*

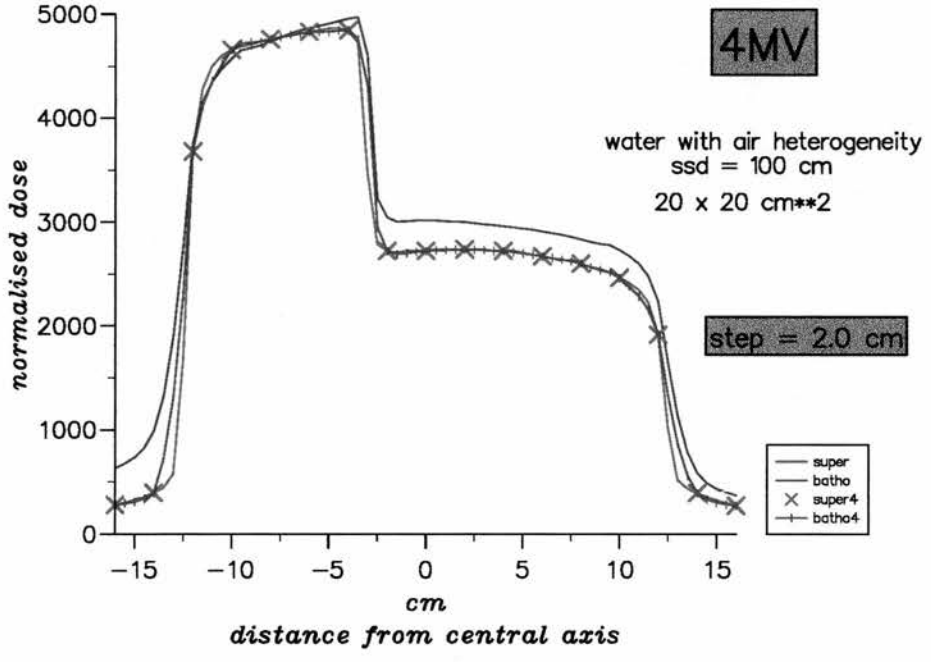

Figure 7.16: *Profiles at 25.25 cm, below the air inhomogeneity. The grid separation in the coarse superposition calculation is 2.0cm.*

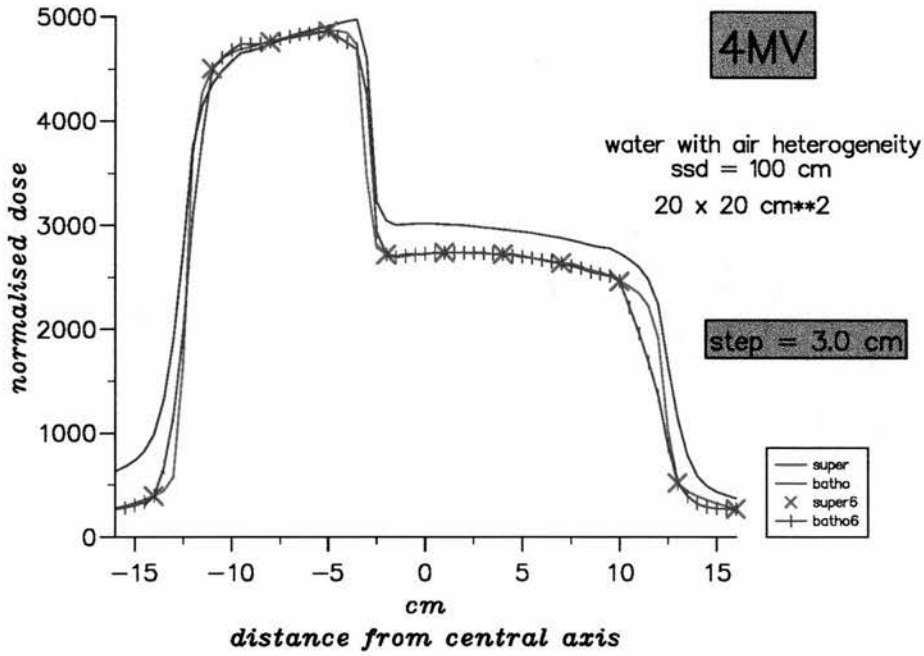

Figure 7.17: *Profiles at 25.25 cm, below the air inhomogeneity. The grid separation in the coarse superposition calculation is 3.0cm.*

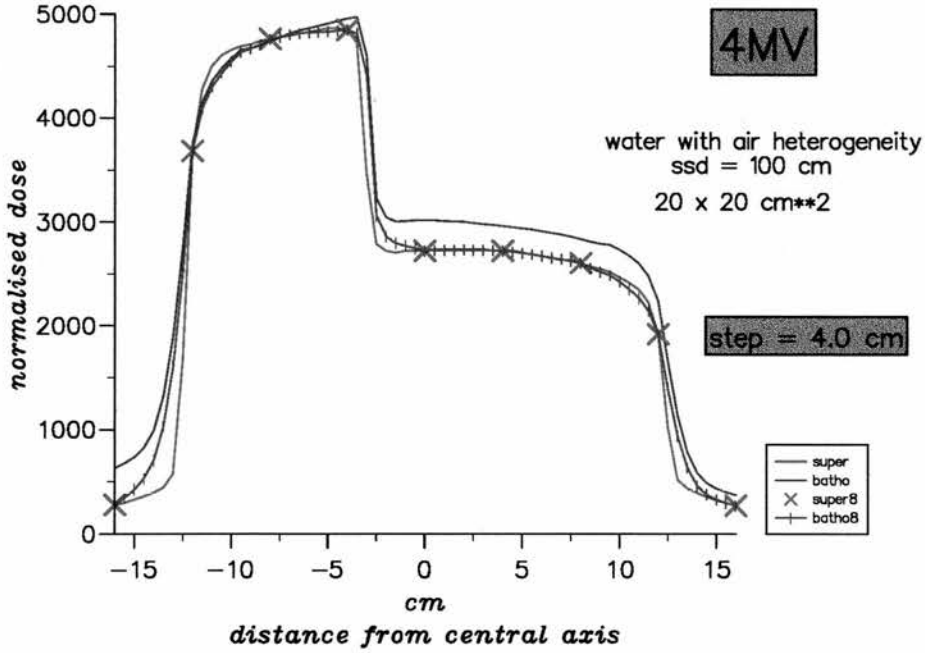

Figure 7.18: *Profiles at 25.25 cm, below the air inhomogeneity. The grid separation in the coarse superposition calculation is 4.0cm.*

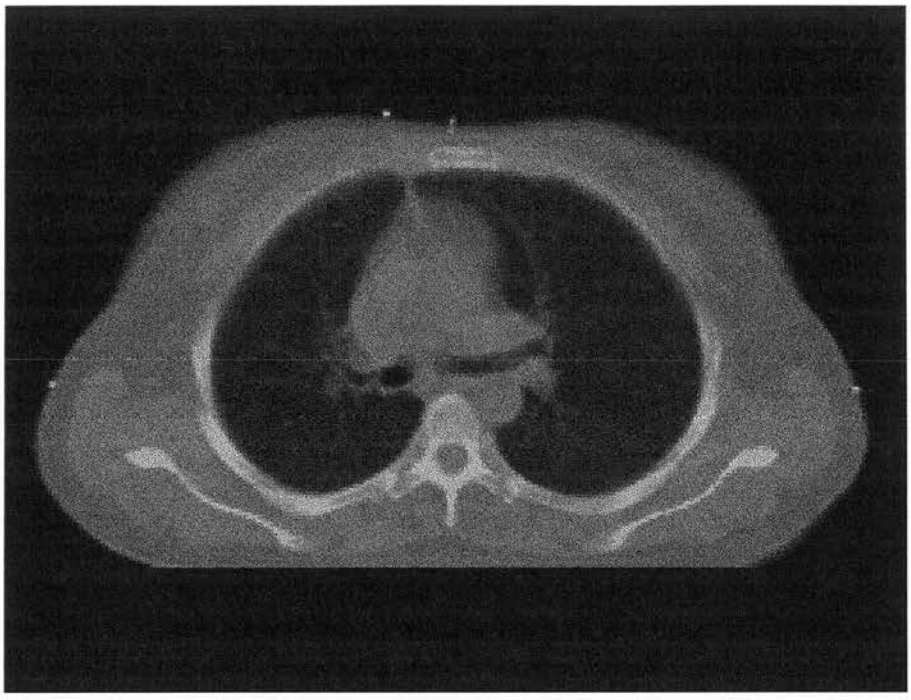

Figure 7.19: *Image of the central CT slice corresponding to the 3D patient density matrix used in this work.*

7.4.3 Application using a patient density matrix

The water with the cube of air is an extreme case of heterogeneous medium. The large dose gradients present, are not usually encountered in actual patient dose calculations. Therefore, the performance of the CF-method was examined in a clinically relevant irradiation geometry. Figure 7.19 displays an image of the central slice from the CT matrix corresponding to the thorax region of a patient. 3D patient density data from CT were utilised for the calculation of depth dose and profile dose variations using both superposition and power-law methods.

The size of the CT density matrix (46 CT slices) is $128 \times 128 \times 46$, with voxel size equal to $0.5 \times 0.5 \times 0.5 cm^3$. The distance from the source to the centre of the density array was set to 100cm (i.e. this is the distance from the source to the isocentre, SAD). The radiation field was set to $15. \times 15. cm^2$ at SAD.

Central axis depth dose calculations

Figure 7.20 illustrates the variation of normalised dose values along the central axis of the beam for a 0.5 cm resolution from the two calculation methods.

Figures 7.21, 7.22, 7.23, 7.24 display depth dose curves obtained using the CF-

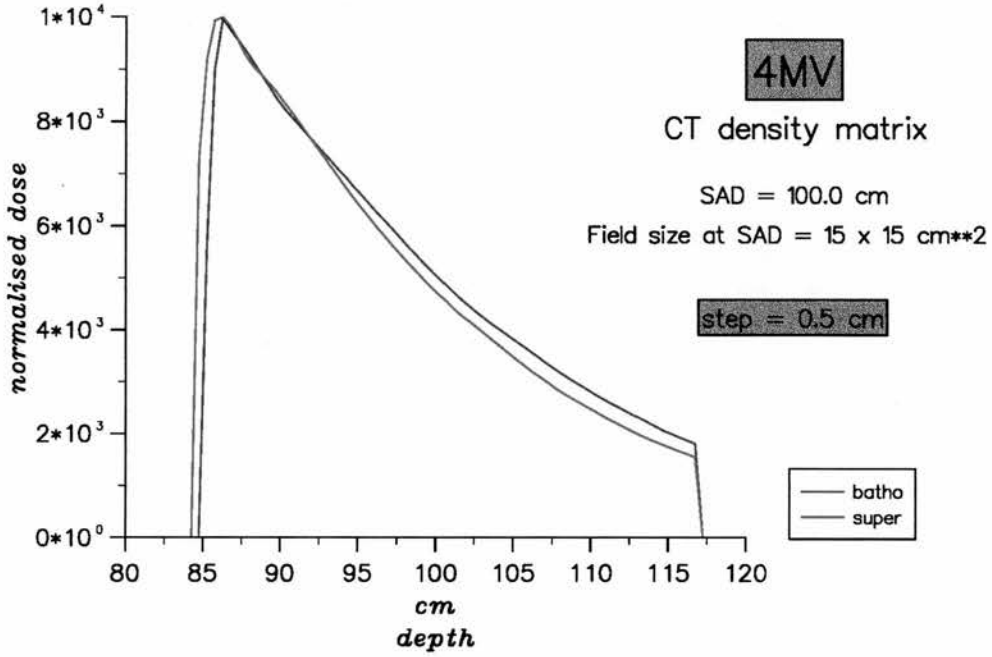

Figure 7.20: Normalised dose values along the central axis of the beam within the patient. The grid separation in the calculations is 0.5 cm.

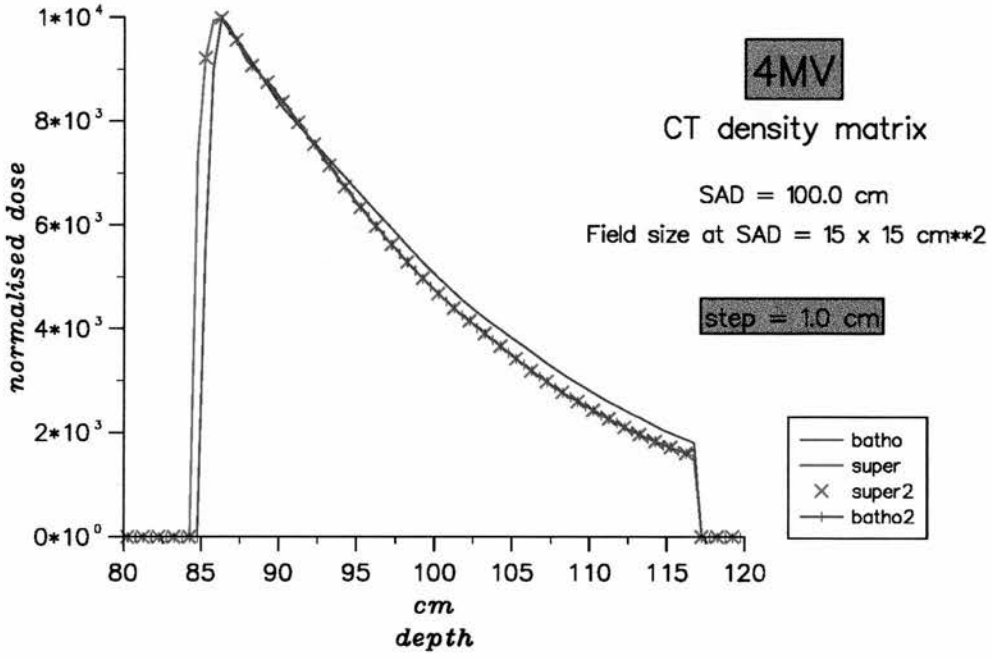

Figure 7.21: *Dose values along the beam's central axis in the patient. Grid separation equal to 1.0 cm.*

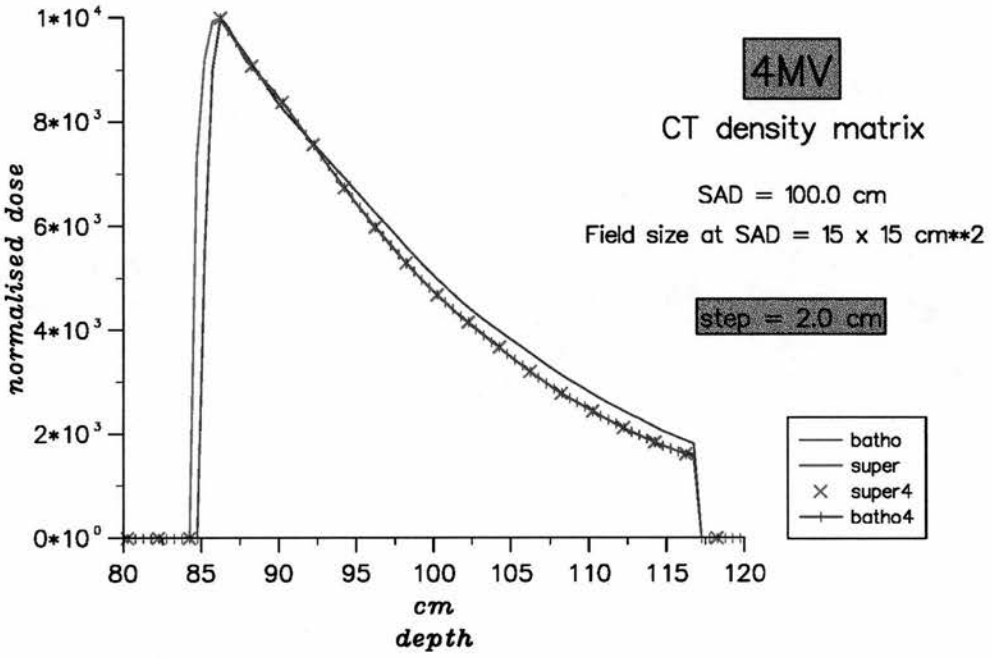

Figure 7.22: *Dose values along the beam's central axis in the patient. Grid separation equal to 2.0 cm.*

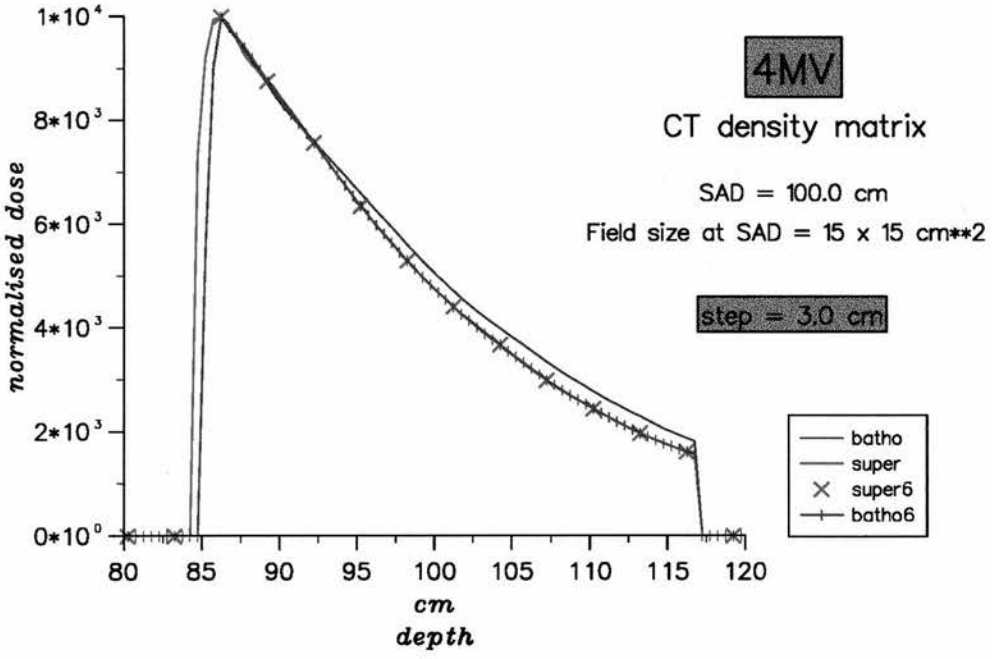

Figure 7.23: *Dose values along the beam's central axis in the patient. Grid separation equal to 3.0 cm.*

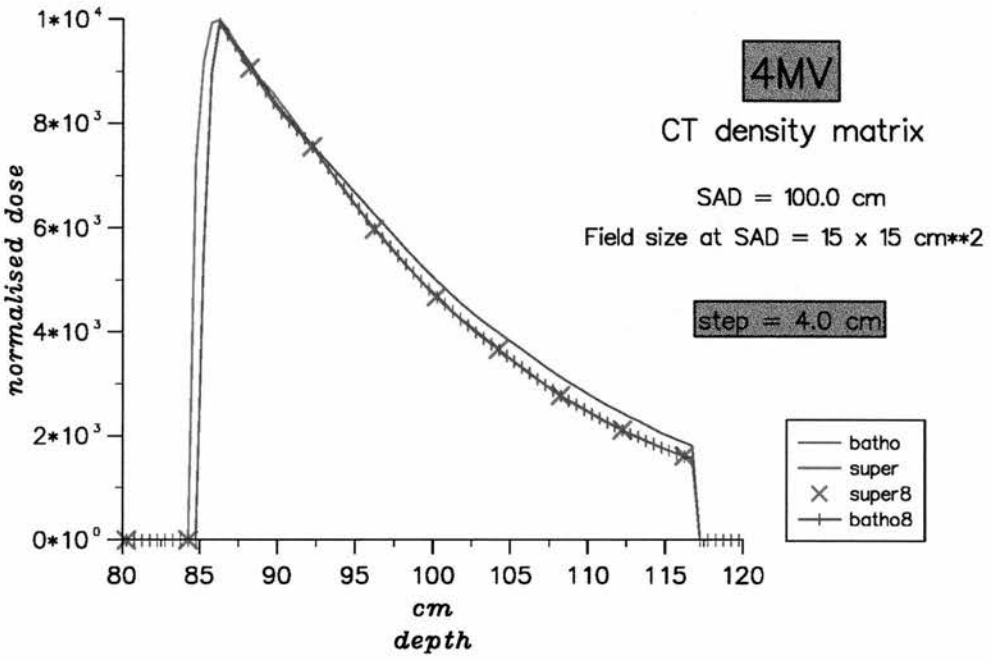

Figure 7.24: *Dose values along the beam's central axis in the patient. Grid separation equal to 4.0 cm.*

method for grid separations of 1.0 cm, 2.0 cm, 3.0 cm and 4.0 cm respectively. The results are excellent. The curves from the CF-method are shown in green and are denoted as *batho*N, where N/2 is the grid separation in cm.

The errors from the calculated dose values in all cases were within $\pm 0.5\%$ at any point along the central axis, except in the build-up region. Realising the difficulties apparent in the build-up region and in order to avoid any artefacts due to the linearly interpolated correction factor, the final dose curve in this region was set to follow the variations predicted by the power-law approach. Ideally, any further advancement to the CF-method, should concentrate in improving the performance in the vicinity of high dose gradient, such as those in the build up region.

Dose profile at a depth

Figure 7.25 displays a comparison between superposition and the power-law calculation. The profiles are taken at the depth of the isocentre, where SAD = 100cm and the field size is $15. \times 15. cm^2$. With the aid of the image illustrated in Figure 7.19, it is clear that both methods predict the increase in primary at the right hand side of the image, since the primary beam traverses a longer distance within lung tissue. The power law method generally appears to overestimate dose

within lung and does not model the increase in scattered dose at both sides of the profile, which is due to the higher intensity of primary photons traversing the lung at lower depths.

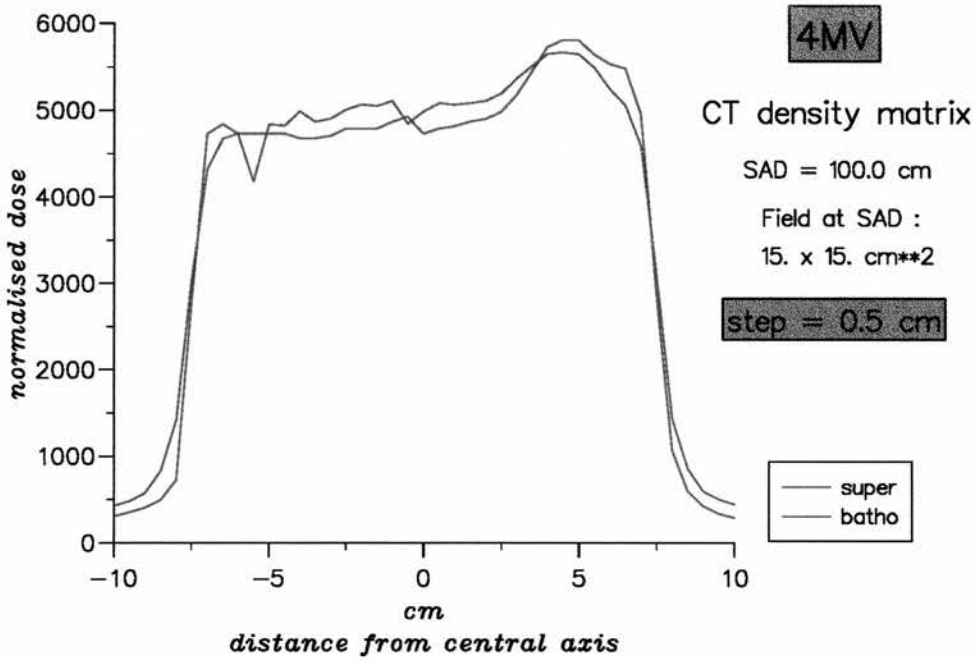

Figure 7.25: *The variation of dose at 100 cm from the source and on the plane incorporating the beam's central axis. Grid separation in calculations is 0.5 cm*

Figures 7.26 and 7.27 show the dose variations across the same depth from the CF-method using 1.0 cm and 2.0 cm grid separations respectively. The grid separation of 2.0 cm introduces errors in the beam margin on the left of Figure 7.27, but it accounts for the increase of dose on the right hand side. An interesting artefact from the method can be seen in these Figures. Between points where the ratios from superposition and power-law are almost equal to unity, the CF-method interpolates correction factors also close to unity, therefore the final dose value equals those from the power-law calculation. If those power-law method dose estimates are not accurate, then the final result would carry the same magnitude of inaccuracies. To avoid this, whenever two contiguous correction factor ratios on the coarse grid are close to unity, it is sufficient to linearly interpolate dose values from superposition for any intermediate points.

Dose errors from the CF-method across the profiles in the CT density matrix were within $\pm 3\%$ for the majority of the points. Individual values displayed higher errors (within $\pm 5\%$) and these were mainly for the case of a 2.0 cm grid separation and at the beam margins.

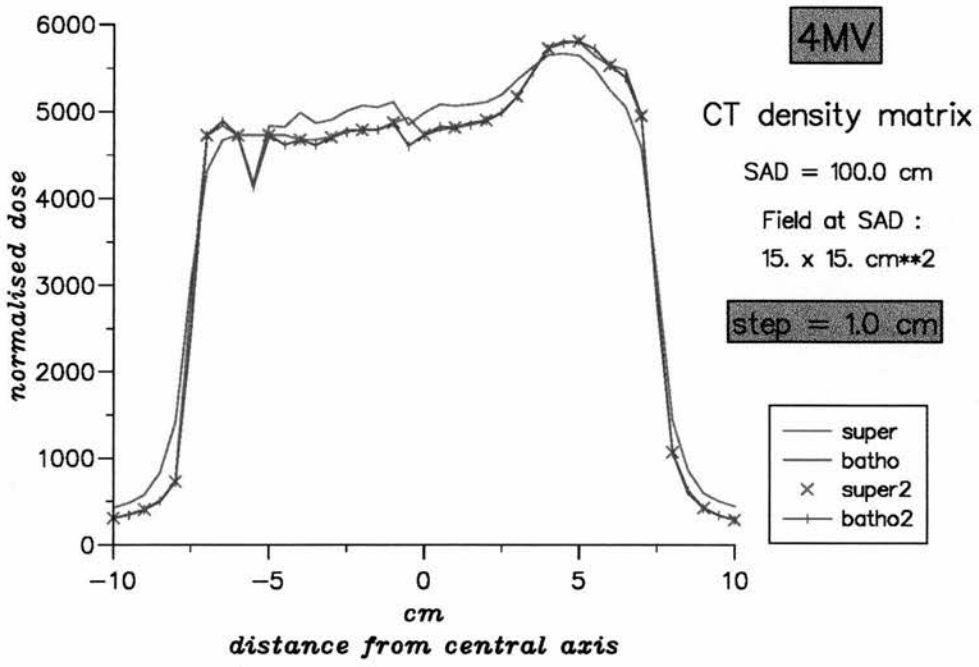

Figure 7.26: *The variation of dose at 100 cm from the source and on the plane incorporating the beam's central axis. Grid separation in calculations is 1.0 cm*

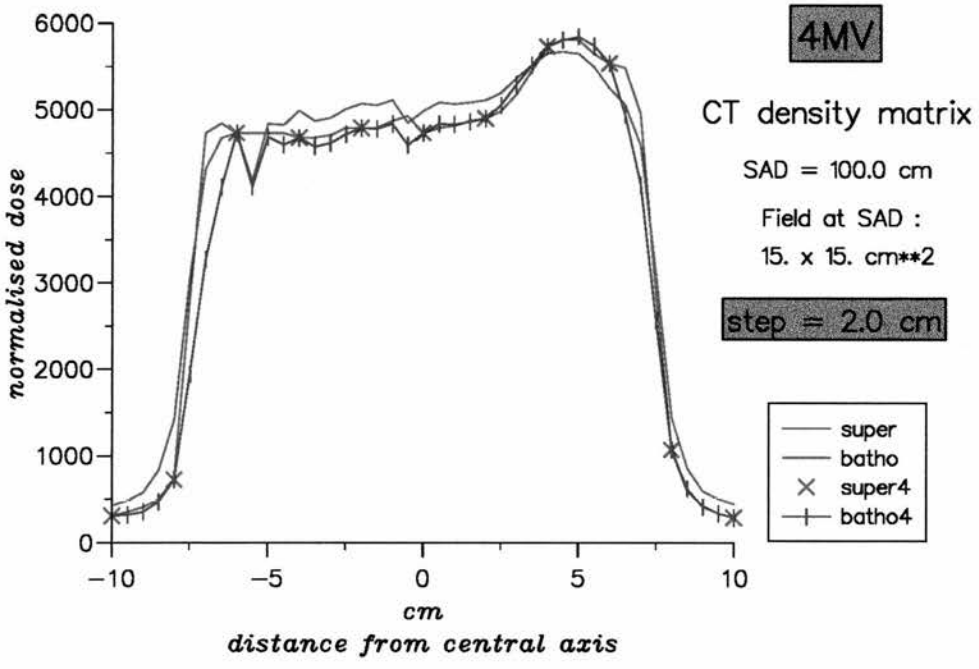

Figure 7.27: *The variation of dose at 100 cm from the source and on the plane incorporating the beam's central axis. Grid separation in calculations is 2.0 cm*

7.5 Summary and Discussion

The previous sections demonstrate the implementation of the CF-method and indicate that this technique can be facilitated to improve the speed of 3D photon dose computations. The use of 1.0 cm, 2.0 cm, 3.0 cm or even 4.0 cm grid separations lead to significant improvements in speed, since the total number of points calculated by superposition is reflected in the time required for the calculation of a true 3D dose array.

Section 7.2 provided an analysis of the various parameters influencing calculation speed in superposition. It was concluded that in heterogeneous media, the value of `radstep` should be set not larger than the grid separation used for the calculation of terma. Namely, for a separation of 0.5cm in the terma distribution, `radstep` should be set to 0.25 cm. A small value of `radstep` is important for sampling terma values around the dose calculation point, i.e. for accurately accounting for energy contributions from secondary electrons and their descendants due to which kernel gradients are steep. Energy contributions from scattered photons, which originate from interaction points outside the extent of the primary kernel, do not influence significantly the dose value at a point. Sampling terma at such radii, would be accurate enough for values of `radstep` larger than 0.25 cm. This is analogous to the way spherical energy deposition kernels have been scored and stored [Mackie et al., 1988b]. In these, the spherical voxel volume increases as the distance from the primary photon interaction site increases. The use of coarser angular spacing in the polar direction was also discussed and is not considered to improve calculation speed without introducing significant losses in accuracy on dose at a point.

Results from the implementation of the CF-method are given in section 7.4. The method was examined initially in a homogeneous water medium. Section 7.4.1 presents dose profiles in water. This test was carried out for assessing the performance of the method in terms of accuracy at the beam margins. It was shown that profiles calculated with grid separations up to 3.0 cm do not deviate significantly from the profiles obtained from superposition calculations on a fine matrix. For larger grid separations, the results are not generally acceptable (errors are outside the range of $\pm 3\%$). Section 7.4.2 demonstrates the performance of the CF-method for a heterogeneous medium. Water with a large air heterogeneity is far from a typical patient geometry and the steep dose gradients present here are not normally encountered in dose distributions within patients, even within regions in the upper body. Therefore, the acceptable performance of

the CF-method in such an extreme case provides the confidence that the technique is a good compromise for clinical applications. The application of the method in a clinically relevant situation is presented in section 7.4.3. Based on the results from previous examples, in this case grid separations along the beam direction were only considered up to 4.0 cm and across the beam the separations were not larger than 2.0 cm. These results clearly demonstrate what was already expected : for these grid separations the CF-method gives very good results. For the variations of dose along the beam central axis a maximum grid separation of 4.0 cm is adequate. In addition, if the value of the dose maximum is also used in the CF-method, then the calculation of the dose distribution in this region can be improved. The calculation of dose profiles using the CF-method is acceptable (i.e. errors within $\pm 3\%$) for grid separations up to 2.0 cm.

In general, the profile data generated using the CF-method indicate that accuracy in the regions of extreme dose values depends on the position of the grid point in relation to the beam width. In the case of rectangular fields one might consider deriving a rule of thumb for choosing the grid step. This should be in accordance with the size of the radiation field, in order to ensure that enough points are calculated in regions of steep dose gradients, namely the beam margins. Such a model though would not be applicable in more general irradiation geometries, i.e. when using irregular fields. For simplicity, all examples shown here are for the calculation of dose variations along one dimension using `step` sizes which are a multiple of the fine grid size. The CF-method software is designed to accept variable `step` lengths in the `x, y, z` directions provided that the conventional calculation method and the terma distribution are obtained on the fine matrix. Finally, to improve further this technique, one may consider using the information from the density matrix for predicting the regions where a larger number of superposition calculations is required. However, it is not clear yet, whether this can be advantageous in terms of computation speed.

In conclusion, for superposition calculations using the CF-method, as implemented and presented in this work, the separation of points in the beam direction were larger (at least a factor of two) than that across the beam. Grid spacing of 4.0 cm in the beam direction and 2.0 cm in the other directions resulted in an improvement of 128 times in calculation time in comparison to the calculation time for grid separations of 0.5 cm in all dimensions.

7.6 Conclusions

This chapter has introduced and verified a novel approach for decreasing computation times in true 3D photon dose calculations.

Prerequisite for the CF-method are two 3D dose matrices. One generated by a simple, thus fast, dose calculation method and the other from a more sophisticated algorithm, such as the superposition model. The software for the CF-method carry out simple arithmetic operations and therefore, can be easily written in-house using any high level programming language.

The use of the CF-method can speed-up the generation of true 3D dose matrices by at least a factor of 100. Depending on the size of the irradiation geometry and the choice of grid spacing this method can enable the routine clinical use of models, like the superposition model, which are generally considered only as research tools.

Chapter 8

Discussion

8.1 Summary

Photon dose calculations for radiotherapy planning are subject to continuous efforts of research and development. *Correction-based models* calculate the distribution of dose within a patient by correcting measured data according to variations due to beam modification and shape, and due to patient shape and composition. These methods are limited by the nature of the dosimetric and patient data they utilise. A critical analysis of *correction-based* methods is provided in chapter 2.

Model-based methods aim to provide more sophisticated and flexible approximations to the *'true'* solution in a wider range of situations. They use analytically calculated fluence or terma distributions together with theoretical data (energy deposition kernels) which are generally obtained using Monte Carlo methods. A comprehensive analysis of convolution/superposition methods is given in chapter 3. Although models based on the superposition principle are faster than Monte Carlo methods, they are generally considered too slow for routine clinical implementation.

Monte Carlo methods have been extensively used as research tools. They can provide accurate estimations of the required solutions to problems of practical interest. However they require considerable programming expertise and long computation times. Chapter 4 reviews the basic concepts related to Monte Carlo techniques, briefly demonstrates the application of this method in radiation transport problems and presents the applications related to radiotherapy. The same chapter includes a description of the EGS4 Monte Carlo Code System [Nelson et al., 1985]. EGS4 comprises a collection of software modules which have been widely used for medical physics and radiotherapy applications. An overview of EGS4 is provided in this chapter not only because the capabilities of

this code were investigated and further developed in this work, but also because this code is one of the few Monte Carlo packages which are likely to dominate future radiotherapy planning systems for generating dose distributions from first principles.

Chapter 5 presented the use of EGS4/PRESTA in this work. Monoenergetic total and total-scatter energy deposition kernels for 1.25 MeV, 6.0 MeV and 20.0 MeV photons were generated on a cartesian coordinate system with usercode `XYZKERN`. The fractional energies in these kernels were compared to the values expected from theory.

Usercode `XYZSIM` is also a descendant of usercode `XYZDOS`. It was developed in this work, to enable the generation of 3D dose distributions (total dose and total-scatter) in heterogeneous media on a cartesian matrix from divergent, polyenergetic photon beams.

A single polyenergetic superposition model was developed and implemented from the *dose deposition point of view*, calculating dose at a point in units of absorbed dose per unit incident photon fluence ($Gy\ cm^2$) (chapter 6). The performance of the model was verified against published data for monoenergetic beams, against Monte Carlo data for polyenergetic beams (4MV, 6MV, 9MV, 16MV) incident on water, and against measured data for the 4MV beam incident on inhomogeneous media.

The requirement of accurate but fast calculation of dose distributions for radiotherapy planning led to the development of a new technique, called the CF-method (chapter 7). The CF-method requires as input a coarse matrix of dose values calculated from superposition and dose values on a fine matrix generated by a fast dose calculation model (i.e. a *correction-based* model). Correction factor ratios are defined as ratios of dose values from superposition to those from the *correction-based* model (here the power-law model was used). These ratios are linearly interpolated on a fine matrix and multiplied by the matrix provided by the power-law calculation. The CF-method succeeds in reducing the number of dose point calculations carried out with the single polyenergetic superposition model with the aid of the *correction-based* model. Calculation times are reduced with no significant losses in accuracy, provided that coarse grid separations are chosen not to exceed 2.0 cm across the beam and that the performance in the build-up region follows that defined by the *correction-based* method.

8.2 Conclusions

The purpose of the work presented in this thesis was to contribute to the improvement of the overall accuracy of radiotherapy treatment by improving the accuracy of photon dose computations. The main outcomes of this study were:

1. A detailed review of photon dose calculations models.
2. An in-depth analysis of the convolution/superposition approach.
3. Usercode `XYZKERN` was developed for generating cartesian energy deposition kernels.
4. Usercode `XYZSIM` was developed for Monte Carlo computations using clinical photon beams.
5. The development of a single polyenergetic superposition algorithm.
6. The development of a new method for speeding up true 3D dose computations.

The review of *correction-based* methods concluded that these methods are generally insufficient to follow-up or develop further for 3D radiotherapy planning.

The discussion on convolution/superposition presented the advantages and limitations of this approach and indicated the requirements for its development. Design criteria which influence the performance of this method essentially are categorised into three groups: those related to the solution of the inhomogeneity problem (i.e density scaling of kernels), those related to the modelling of the nature of x ray beams and those that are introduced in view of the speed requirements for interactive treatment planning.

The use of `XYZKERN` for generating cartesian energy deposition kernels turned out mainly to be an introductory exercise on the use of the EGS4 Monte Carlo code, since a later evaluation of the restrictions imposed when using cartesian EDK scored on a fixed grid size matrix, finally dictated the use of the spherical EDKs. Nevertheless, it is a code readily available to those applications that require the generation and use of cartesian EDKs.

Although it was intended to use `XYZSIM` extensively in this work, time restrictions prevented this. However, this is the type of EGS4 usercode that is appropriate for 3D Monte Carlo Treatment Planning (3D-MCTP).

The single polyenergetic superposition model, using polyenergetic terma and total EDKs, was verified for a variable range of energies in homogeneous media and for 4MV in heterogeneous media and its performance was, in general, very good; any deviations from Monte Carlo measurements or measured data were well within $\pm 3\%$ for the geometries tested.

The new method was shown to significantly increase calculation speed by implementing the superposition model together with the power-law method. Since the CF-method is not a computationally intensive procedure, the work in this thesis concentrated on examining the magnitude of errors introduced by the implementation of the technique. The "worst-case" examined was an irradiation geometry resulting in extreme dose gradients. A further application of the method in a clinically relevant case, using patient density information from CT, provided confidence that the method can be used for clinical implementation. Particularly in low energy beams, the steep dose gradient in the build-up region imposes a limitation on the accuracy of the calculated dose values. In order to avoid any artefacts generated by the CF-method, the values in this region were set equal to those predicted by the conventional dose calculation method. Grid separations of 4.0 cm along the beam's direction were considered adequate, because dose values in this direction are not likely to display extreme variations. The steep dose gradients at the beam margins necessitate a smaller grid separation in the direction across the beam. From the examples examined a value not more than 2.0 cm was recommended, resulting in an improvement of computational speed by at least a factor of 100.

8.3 Future work

Future efforts on the single polyenergetic superposition model should be directed mainly in assessing the model's performance in heterogeneous media irradiated with higher energy beams. In addition, comparisons against measured data might indicate that, especially for high energy beams, head scatter and beam contamination models should be included in this superposition model.

The clinical example studied here on the CF-method was from the upper body region (thorax). Further investigations on the performance of the superposition model together with the CF-method, should concentrate in regions with extreme density variations, such as those of the head with an increased amount of bone present, and the neck where air cavities are expected to introduce steep dose

gradients.

Finally, usercode XYZSIM would benefit greatly from the implementation of more sophisticated variance reduction techniques or even other methods, such as a parallel implementation on a cluster of workstations, that would improve efficiency in the simulations. Thus, there is scope for enhancement of this usercode in order to enable its use in dose deposition studies using real patient data from CT.

Appendix A

Usercode XYZKERN

A.1 Photon interaction forcing macro in XYZKERN

```
REPLACE{$SELECT-PHOTON-MFP;} WITH {
;
IF(NFTIME.EQ.0)[DPMFP=0.0;NFTIME=1;]
ELSEIF ((IFORCE.EQ.0).OR.(NFTIME.GT.NFMAX).OR.(NFTIME.LT.NFMIN))[
$RANDOMSET RNNO35;IF(RNNO35 = 0.0)RNNO35=1.E-30;
DPMFP=-ALOG(RNNO35);]
ELSE[
NFTIME=NFTIME+1;
DUMU=USTEP;
DUMX=X(NP);DUMY=Y(NP);DUMZ=Z(NP);
IRODUM=IROLD;IRNDUM=IRNEW;IRDUM=IR(NP);MEDDUM=MEDIUM;
IDUM=IDISC;
PATHL=0.0;
MEDTMP=0;
LOOP[
 USTEP=VACDST;IROLD=IR(NP);MEDIUM=MED(IROLD);
 IF(MEDTMP.NE.MEDIUM)[MEDTMP=MEDIUM;
 IF(MEDTMP.NE.0)[$SET INTERVAL GLE,GE;
    $EVALUATE DELTAP USING GMFP(GLE);]]
 CALL HOWFAR;
 IF(MEDTMP.NE.0)[PATHL=PATHL+USTEP/DELTAP;]
 IF(IRNEW.EQ.1) EXIT;
 IR(NP)=IRNEW;
```

```
 X(NP)=X(NP)+USTEP*U(NP);
 Y(NP)=Y(NP)+USTEP*V(NP);
 Z(NP)=Z(NP)+USTEP*W(NP);
]
USTEP=DUMU;
X(NP)=DUMX;Y(NP)=DUMY;Z(NP)=DUMZ;
IROLD=IRODUM;IRNEW=IRNDUM;IR(NP)=IRDUM;MEDIUM=MEDDUM;
IDISC=IDUM;
IF(PATHL.LE.1.0E-3)[
     GWAIT=PATHL*(1-0.5*PATHL);]
ELSE[
     GWAIT=1.-EXP(-PATHL);]
GWTOLD=WT(NP);
WT(NP)=GWTOLD*GWAIT;
VIRTGE=GWTOLD*(1-GWAIT)*E(NP);
EPSLON=RNNO35*GWAIT;
IF(EPSLON.LE.1.0E-3)[
     DPMFP=EPSLON*(1.+0.5*EPSLON);]
ELSE[
     ARG=1./(1.-EPSLON);
     DPMFP=ALOG(ARG);] ]}
```

A.2 Subroutine AUSGAB in XYZKERN

```
"*****************************************************************"
"                                                                 "
"                          AUSGAB                                 "
"                          ======                                 "
"                                                                 "
SUBROUTINE AUSGAB(IARG);
"                                                                 "
"*****************************************************************"
;
COMIN/EPCONT,GEOM,MISC,SCORE,STACK,USER,PFORCE/;

"Set flags "
REPLACE{$SET-FLAG1(#);} WITH {LATCH({P1})=LATCH({P1})+1;}
REPLACE{$SET-FLAG2(#);} WITH {LATCH({P1})=LATCH({P1})+1000;}
REPLACE{$SET-FLAG3(#);} WITH {LATCH({P1})=LATCH({P1})+10000;}

REPLACE{$FLAG1} WITH {MOD(LATCH(NP),100)}
REPLACE{$FLAG2} WITH {MOD(LATCH(NP),10000)-$FLAG1};
REPLACE{$FLAG3} WITH {INT(LATCH(NP)/10000)};

IF(IWATCH ~=0)
   CALL WATCH(IARG,IWATCH); "IWATCH PASSED IN COMIN SCORE"

MXNP=MAX(MAXNP,NP); "KEEP TRACK OF HOW DEEP STACK GETS"
IF(NP>=$MXSTACK)[
 OUTPUT61;(
 /
 /' IN AUSGAB, NP=',I3,' >= MAXIMUM STACK ALLOWED WHICH IS',I3/
    1X,79('*')/
 /
 );
 IF(MXNP>$MXSTACK)[STOP 'STACK OVERFLOW'; "MUST INCREASE $MXSTACK"]
 ]

"Set appropriate flags"
```

```
"IF PAIR PRODUCTION:"
IF(IARG=16 & NP=2 & Z(NP)=ZINTPT)[
$SET-FLAG1(NP);$SET-FLAG1(NP-1);]

"IF PHOTOELECTRIC EFFECT:"
IF(IARG=20 & NP=1 & Z(NP)=ZINTPT)[
$SET-FLAG1(NP);]

"IF COMPTON INTERACTION:"
IF(IARG=18 & NP=2 & Z(NP)=ZINTPT)[
IF(IQ(NP)=-1)[$SET-FLAG1(NP);$SET-FLAG2(NP-1);]
IF(IQ(NP)=0)[$SET-FLAG1(NP-1);$SET-FLAG2(NP);]]

"IF BREMSSTRAHLUNG EVENT FROM A PRIMARY CHARGED PARTICLE"
IF(IARG=7 & $FLAG1~=0)[
IF(IQ(NP)=0)[$SET-FLAG3(NP);]
ELSE[$SET-FLAG3(NP-1);]]

"IF ANNIHILATION FROM A PRIMARY CHARGED PARTICLE"
IF((IARG=13 | IARG=14) & $FLAG1~=0)[
$SET-FLAG3(NP);$SET-FLAG3(NP-1);]

IF (IARG = 15 | IARG=17 | IARG=19) [
    IF ( VIRTGE ~= 0.0)[
      EVIRT=EVIRT+VIRTGE;
      VIRTGE=0.0;
    ]
]

IF(IARG >=5 ) RETURN;

FTMP = WT(NP) * EDEP;

IF( IARG = 3 ) [
    ELOST = ELOST + FTMP;
```

```
]

IF (IWATCH.GE.1.AND.EDEP.NE.0.0)[
OUTPUT FTMP,IR(NP),IARG;
(' ***TOTAL ENERGY DEPOSITED =',E15.7,'MeV. IRL= ',I4,' IARG= 'I3);]


IF(IR(NP) > 1  & EDEP~=0.0)[ "SCORE ANY ENERGY IN THE VOLUME"
    $DECODEIR(IR(NP),I,J,K);

"score total energy"
    DOSEIS(I,J,K,IS,1) = DOSEIS(I,J,K,IS,1) + FTMP;

"score scatter..."
    IF($FLAG2~=0)[
            DOSEIS(I,J,K,IS,2)=DOSEIS(I,J,K,IS,2) + FTMP;]

"score brems-annih. from primary charges particles"
    IF($FLAG3~=0)[
            DOSEIS(I,J,K,IS,3)=DOSEIS(I,J,K,IS,3) + FTMP;]
    ]
RETURN;END;
```

A.3 Usercode XYZKERN: example of a simulation record

```
1                    USER CODE XYZKERN(V1.0) USING EGS4 AND PRESTA

 GEOMETRY IS A RECTILINEAR VOLUME, ORIGIN IN BOTTOM LEFT,X-Y PLANE ON
                     THE PAGE AND Z AXIS INTO THE PAGE


       ------------------------------------------------------------
 TITLE: +    6 MeV Kernel
       ------------------------------------------------------------
 NUMBER OF MEDIA: +                1
 MEDIUM  1:  +                    WATER1
 ECUT,PCUT,ESTPE(1 to 1):  +              0.561     0.050     0.010

 # REGIONS IN X,Y,Z DIRECTIONS (IF<0,IMPLIES # GROUPS OF REG): + -1 -1 -1

                     INPUT BOUNDARIES IN THE X DIRECTION
 INITIAL BOUNDARY: +        0.000
 WIDTH IN THIS GROUP, NO. OF REGIONS IN GROUP: +        0.500   47
 BOUNDARIES
       0.000       0.500       1.000       1.500       2.000       2.500
       3.000       3.500       4.000       4.500       5.000       5.500
       6.000       6.500       7.000       7.500       8.000       8.500
       9.000       9.500      10.000      10.500      11.000      11.500
      12.000      12.500      13.000      13.500      14.000      14.500
      15.000      15.500      16.000      16.500      17.000      17.500
      18.000      18.500      19.000      19.500      20.000      20.500
      21.000      21.500      22.000      22.500      23.000      23.500

                     INPUT BOUNDARIES IN THE Y DIRECTION
 INITIAL BOUNDARY: +        0.000
 WIDTH IN THIS GROUP, NO. OF REGIONS IN GROUP: +        0.500   47
 BOUNDARIES
```

```
     0.000     0.500     1.000     1.500     2.000     2.500
     3.000     3.500     4.000     4.500     5.000     5.500
     6.000     6.500     7.000     7.500     8.000     8.500
     9.000     9.500    10.000    10.500    11.000    11.500
    12.000    12.500    13.000    13.500    14.000    14.500
    15.000    15.500    16.000    16.500    17.000    17.500
    18.000    18.500    19.000    19.500    20.000    20.500
    21.000    21.500    22.000    22.500    23.000    23.500

                INPUT BOUNDARIES IN THE Z DIRECTION
 INITIAL BOUNDARY: +       0.000
 WIDTH IN THIS GROUP, NO. OF REGIONS IN GROUP: +      0.500   80
 BOUNDARIES
     0.000     0.500     1.000     1.500     2.000     2.500
     3.000     3.500     4.000     4.500     5.000     5.500
     6.000     6.500     7.000     7.500     8.000     8.500
     9.000     9.500    10.000    10.500    11.000    11.500
    12.000    12.500    13.000    13.500    14.000    14.500
    15.000    15.500    16.000    16.500    17.000    17.500
    18.000    18.500    19.000    19.500    20.000    20.500
    21.000    21.500    22.000    22.500    23.000    23.500
    24.000    24.500    25.000    25.500    26.000    26.500
    27.000    27.500    28.000    28.500    29.000    29.500
    30.000    30.500    31.000    31.500    32.000    32.500
    33.000    33.500    34.000    34.500    35.000    35.500
    36.000    36.500    37.000    37.500    38.000    38.500
    39.000    39.500    40.000
OTOTAL # REGIONS INCLUDING EXTERIOR =         176721
$INPUT WIDTH OF VOXEL ALONG THE Z-AXIS :
+     0.500
OINPUT GROUPS OF REGIONS FOR WHICH DENSITY AND MEDIUM ARE NOT DEFAULTS
 LOWER,UPPER I,J,K, MEDIUM, DENSITY INPUT GROUPS OF REGIONS FOR WHICH
 ECUT AND PCUT ARE NOT DEFAULTS
 LOWER,UPPER I,J,K, ECUT,PCUT ENTER 3 PAIRS DEFINING LOWER,UPPER X,Y,Z
 INDICIES OF DOSE REGIONS  FOR WHICH RESULTS ARE TO BE OUTPUT- IZSCAN
 NON-ZERO FOR Z-SCAN/PAGE
```

```
 ONE SET OF 6 PER LINE, END WITH ALL ZEROS
 : +        1  47     1  47     1  80     0
 :
 SPECIFICATIONS FOR PARALLEL BEAM, INCIDENT ON X-Y SURFACE

 INCIDENT ON WHAT RANGE OF X VALUES? +            11.750    11.750
                                        X INDEX RANGES OVER I= 24 to  24
 INCIDENT ON WHAT RANGE OF Y VALUES? +            11.750    11.750
                                        J INDEX RANGES OVER J= 24 to  24
 ANGLE OF BEAM TO AXES(in deg, 0 IS NORMAL): +   0.00  90.00  90.00 deg
0EIN(K.E.,MeV), IQIN, IWATCH
 : +    6.000         0     0

 *** INPUT OPTION IRSTRT ***


ISTORE(0,1),IRSTRT(0,1),IDAT(0,1):
 DO NOT STORE(0) OR STORE(1) EVERY INITIAL RANDOM #:              0
 FIRST RUN(0),RESTARTED(1):                                       1
 STORE DATA(0) OR NOT(1):                                         0



 *** INPUT HISTORIES  ***


 #HISTORIES,RN SEED #1,RN SEED #2,TIMMAX :
 # OF HISTORIES:                                          250000
 1ST INITIAL RANDOM NUMBER SEED:                              0
 2ND INITIAL RANDOM NUMBER SEED:                              0
 MAXIMUM CPU TIME ALLOWED:                                0.99HRS



 ***START READING PREVIOUS DATA FILE***
```

```
END OF USER DATA FILE READ BEFORE DAT FILE IN


 ********* SUCCESSFUL INPUT ACCOMPLISHED *********


$INPUT THE DEPTH OF FIRST INTERACTION,ZINTPT (IN CM):

    5.250
 DEPTH OF FIRST INTERACTION (IN CM),WIDTH ALONG Z-AXIS :

    5.250    0.500
 INDEX AT DEPTH OF FIRST INTERACTION :

        11
 INPUT REGION IS :

     23196
$FORCE PHOTON INTERACTIONS IN THE TARGET?(0)=>NO,(1)=>YES,
 MIN/MAX PHOTON INTERACTION #/HISTORY TO SWITCH FORCING ON/OFF:
 (max is set equal to NCASE by default) 1 1 4

 FORCED PHOTON INTERACTIONS IN EFFECT FROM  1 TO 4 # INTERACTIONS

 EGS SUCCESSFULLY 'HATCHED' FOR ONE MEDIUM.

 *** PRESTA INPUTS ***
 IPLC,IBCA,ILCA,IOLDTM,BLCMIN:
           0           0           0           0   4.554

 ------------------------------------------------------------

 PRESTA CALCULATED MINIMUM STEP SIZES FOR MAXIMUM ENERGY ELECTRONS

                    MEDIUM NO.          t,prime,min for E=Emax
                       1                     0.125E-01 cm
```

```
------------------------------------------------------------------

CPUTIME SO FAR=       51.420 s


********* RESTARTED INPUT FILE *********
                250000 NEW +      2250000 OLD HISTORIES
                    NEW RN SEEDS=           22           33


********* FINAL RANDOM NUMBER SEEDS:     6    17  *********

FINISHED SIMULATIONS: CPUTIME=898248.9( = 249.51 HR)

CPUTIME PER HISTORY = 0.35930 SEC. # OF HISTORIES PER HOUR = 10019.

END OF RUN           Nov 22 1994 18:41:33

**********************************************************************
**********************************************************************
```

Appendix B

Usercode XYZSIM

B.1 Subroutine AUSGAB in XYZSIM

```
"*****************************************************************************"
"                                                                             "
"                          AUSGAB                                             "
"                          ======                                             "
"                                                                             "
SUBROUTINE AUSGAB(IARG);
                                                                              "
"*****************************************************************************"
;
COMIN/EPCONT,GEOM,MISC,SCORE,STACK,USER/;

"Set flags "
REPLACE{$SET-FLAG1(#);} WITH {LATCH({P1})=LATCH({P1})+1;}
REPLACE{$SET-FLAG2(#);} WITH {LATCH({P1})=LATCH({P1})+1000;}
REPLACE{$SET-FLAG3(#);} WITH {LATCH({P1})=LATCH({P1})+10000;}

REPLACE{$FLAG1} WITH {MOD(LATCH(NP),100)}
REPLACE{$FLAG2} WITH {MOD(LATCH(NP),10000)-$FLAG1};
REPLACE{$FLAG3} WITH {INT(LATCH(NP)/10000)};

IF(IWATCH ~=0) CALL WATCH(IARG,IWATCH);
                    "IWATCH PASSED IN COMIN SCORE"

MXNP=MAX(MAXNP,NP); "KEEP TRACK OF HOW DEEP STACK GETS"
```

```
IF(NP>=$MXSTACK)[
 OUTPUT61;(
     /
     /' IN AUSGAB, NP=',I3,' >= MAXIMUM STACK ALLOWED WHICH IS',I3/
        1X,79('*')/
     /
      );
  IF(MXNP>$MXSTACK)[STOP 'STACK OVERFLOW'; "MUST INCREASE $MXSTACK"]]

"Set appropriate flags"

"IF PAIR PRODUCTION:"
IF(IARG=16 & NP=2 & PEIG=EIN)[
$SET-FLAG1(NP);$SET-FLAG1(NP-1);]

"IF PHOTOELECTRIC EFFECT:"
IF(IARG=20 & NP=1 & PEIG=EIN)[
$SET-FLAG1(NP);]

"IF COMPTON INTERACTION:"
IF(IARG=18 & NP=2 & PEIG=EIN)[
IF(IQ(NP)=-1)[$SET-FLAG1(NP);$SET-FLAG2(NP-1);]
IF(IQ(NP)=0)[$SET-FLAG1(NP-1);$SET-FLAG2(NP);]]

"IF BREMSSTRAHLUNG EVENT FROM A PRIMARY CHARGED PARTICLE"
IF(IARG=7 & $FLAG1~=0)[
IF(IQ(NP)=0)[$SET-FLAG3(NP);]
ELSE[$SET-FLAG3(NP-1);]]

"IF ANNIHILATION FROM A PRIMARY CHARGED PARTICLE"
IF((IARG=13 | IARG=14) & $FLAG1~=0)[
$SET-FLAG3(NP);$SET-FLAG3(NP-1);]

IF (IARG = 15 | IARG=17 | IARG=19)[
    IF ( VIRTGE ~= 0.0)[
      EVIRT=EVIRT+VIRTGE;
```

```
      VIRTGE=0.0; ]]

IF(IARG >=5 ) RETURN;

FTMP = WT(NP) * EDEP;
IF( IARG = 3 ) [
    ELOST = ELOST + FTMP;}

IF (IWATCH.GE.1.AND.EDEP.NE.0.0)[
OUTPUT FTMP,IR(NP),IARG;
(' ***TOTAL ENERGY DEPOSITED =',E15.7,'MeV. IRL= ',I4,' IARG= 'I3);]

IF(IR(NP) > 1  & EDEP~=0.0)[ "SCORE ANY ENERGY IN THE VOLUME"
    $DECODEIR(IR(NP),I,J,K);
"score total energy"
    DOSEIS(I,J,K,IS,1) = DOSEIS(I,J,K,IS,1) + FTMP;
"score scatter..."
    IF($FLAG2~=0)[
            DOSEIS(I,J,K,IS,2)=DOSEIS(I,J,K,IS,2) + FTMP;]
"score brems-annih. from primary charges particles"
    IF($FLAG3~=0)[
            DOSEIS(I,J,K,IS,3)=DOSEIS(I,J,K,IS,3) + FTMP;]]
RETURN;END;
```

B.2 Energy spectrum input in XYZSIM

Subroutine ENSRC.MORTRAN written in NRCC and provided together with EGS4, was slightly modified (MYENSRC.MORTRAN) to accept spectrum information calculated from the spectrum reconstruction software (SPEC_ANA). This subroutine carries out all the work associated with having an input source spectrum. The purpose of this Appendix is to give a brief explanation on how MYENSRC.MORTRAN handles spectral information and describe its implementation within usercode XYZSIM. This subroutine was also used with DOSRZ.

To call MYENSRC.MORTRAN the following common blocks are added in XYZSIM:

```
REPLACE {;COMIN/SOURCE/;} WITH
{;COMMON/SOURCE/SSD,XBEAM,YBEAM,EINSRC,ENFLAG;
INTEGER ENFLAG;
}

REPLACE {;COMIN/SPECTR/;} WITH
{;
COMMON/SPECTR/
CDFINV($INVDIM,2),ENSRCD($NENSRC),SRCPDF($NENSRC),SRCCDF($NENSRC),
NENSRC;
}
```

Common block SOURCE holds variables for modelling beam divergence (SSD,XBEAM,YBEAM), variable EINSRC which is the particle energy returned by the subroutine and integer variable ENFLAG used when pre-generated phase space information are available. In XYZSIM, ENFLAG is set to zero. Common block SPECTR holds the source probability distribution function SRCPDF which represents energy fluence/MeV, the cumulative source probability distribution function SRCCDF, the number of energy bins defining the spectral distribution NENSRC, the tops of the energy bins at which SRCPDF is defined ENSRCD and the inverse of the cumulative source PDF, CDFINV. Within MYENSRC.MORTRAN, array ENVALUE was defined, which holds the energy values at the centre of the energy bins. In addition, the following two macro replacements are in XYZSIM:

```
REPLACE {$NENSRC} WITH {200}

REPLACE {$INVDIM} WITH {1000}
```

The first defines the maximum number of bins that can be considered in the spectral distribution and the latter is the maximum dimension in array CDFINV($INVDIM,2). Integer variable MONOEN (declared and passed on to MYENSRC.MORTRAN from common block USER) is set to zero for a monoenergetic beam and 1 for a polyenergetic beam. MYENSRC.MORTRAN has four entry points:

Entry 1: ENSRC(IEOF) . During the determination of incident particle parameters in MAIN (step 6), the first call to MYENSRC gets spectral information monoenergetic or polyenergetic:

```
IEOF=0;
EIN=0.0;
CALL ENSRC(IEOF);
```

For monoenergetic beams variable EIN is set here.

Entry 2: ENSRC1 . The second call takes place just prior to the call to SHOWER:

```
IF(MONOEN.EQ.0) [
    IF(IQIN.EQ.0)[ETOTIN=EIN;]ELSE[ETOTIN=EIN+RM;]
    EKMAX=EIN;
    ]
ELSEIF (MONOEN.EQ.1) [
    CALL ENSRC1;
    EKMAX=ENSRCD(NENSRC);
    CALL ENSRC0;
```

Here the cumulative probability distribution SRCCDF is calculated from SRCPDF and renormalised. From SRCCDF, CDFINV is also set here. This array holds precomputed energy values on a fine grid.

Entry 3: ENSRC0 . Just after the second call, a summary of the input spectral data is written into standard output by this call.

Entry 4: ENSRCH(ENIN) . The last entry occurs at the beginning of each history (in step 7):

```
IF(MONOEN.NE.0)[
 CALL ENSRCH(EIN);]
```

The energy value ENIN for an incident particle is sampled here from array CDFINV with the aid of two random numbers.

Appendix C

List of routines in spectrum reconstruction software

```
U4:[EPMV04.SPECT]
   |
   |---- [CALC_DATA]    directory with monoenergetic depth dose
                        data
   |---- [RECON_DIR]    directory with 16 FORTRAN routines
   |---- [RESULTS_DIR]  results saved in files in this directory
   |---- [RFA_DATEN]    directory with measured depth dose data

                  -------------------------------------

[CALC_DATA]
   |
   |---- TIKExx.xxT     19 files with monoenergetic depth dose
                        data
                        Numbers xx.xx denote the monoenergetic
                        energy  in MeV

[RECON_DIR]
   |
   |---- ASSIGN_S.COM    file containing  command procedures
   |---- SPEC_ANA.COM    command procedure for compiling and
   |                      linking
   |---- RUN_SPEC.COM    file for non-interactive input
```

```
   |
   |---- SPEC_ANA.FOR     main program
   |
   |---- CONTA.FOR        calculates dose contribution from
   |                      contaminant electrons
   |
   |---- CPHI.FOR         defines  constraints
   |---- DIR.FOR          searching for files with a certain
   |                       name
   |---- FIND_VALUE.FOR   returns the dose for a depth value
   |---- GET_BORDERS.FOR  finds the location of a value in a
   |                      sorted array
   |---- GRADFI.FOR       defines the gradient
   |---- GRGA.FOR         a collection of 26 FORTRAN routines
   |                      for performing optimization
   |---- JACOB.FOR        defines the derivatives of the
   |                      constraints
   |---- LOCATE.FOR       finds the location of a value in a 2D
   |                       array
   |---- PHIX.FOR         defines the chi-square function
   |---- POLINT.FOR       polynomial interpolation and
   |                       extrapolation
   |---- PPPPPP.FOR       reads input parameters
   |---- READ_DDQM.FOR    reads monoenergetic and measured depth
   |                      dose data
   |---- SELECT_FILE.FOR  searches for files of a certain name
   |---- VT100.FOR        selection of 25 routines providing
                          control functions for the VT100 terminal

[RFA_DATEN]
   |
   |---- DYN4MV.DDD       measured depth dose data for Dynaray 4MV
   |---- DYN9MV.DDD           "      "     "    "  for Dynaray 9MV
   |---- ABB6MV.DDD           "      "     "    "  for CH6, 6MV
   |---- ABB16MV.DDD          "      "     "    "  for CH20, 16MV
```

Bibliography

[Ahnesjö, 1987] Ahnesjö, A. (1987). Invariance of convolution kernels applied to dose calculations for photon beams. In Bruinvis, I. A. D., van der Giessen, P. H., van Kleffens, H. J., and Wittkämper, F. W., editors, *9th International Conference on the Use of Computers in Radiation Therapy*, pages 99–102, Scheveningen, The Netherlands.

[Ahnesjö, 1989] Ahnesjö, A. (1989). Collapsed cone convolution of radiant energy for photon dose calculation in heterogeneous media. *Medical Physics*, 16(4):577–592.

[Ahnesjö, 1991] Ahnesjö, A. (1991). *Dose Calculation Methods in Photon Beam Therapy using Energy Deposition Kernels.* PhD thesis, Stockholm University.

[Ahnesjö, 1994] Ahnesjö, A. (1994). Analytic modelling of photon scatter from flattening filters in photon therapy beams. *Medical Physics*, 21(8):1227–1235.

[Ahnesjö, 1995a] Ahnesjö, A. (1995a). Private communication.

[Ahnesjö, 1995b] Ahnesjö, A. (1995b). Collimator scatter in photon therapy beams. *Medical Physics*, 22(3):267–278.

[Ahnesjö, 1995c] Ahnesjö, A. (1995c). Modelling transmission and scatter for photon beam attenuators. *Medical Physics*, 22(11):1711–1720.

[Ahnesjö, 1995d] Ahnesjö, A. (1995d). Photon scattering in treatment heads: A simple formalism for D/M-calculation from first principles. In *Notes from: Workshop on Monitor Unit Calculation and Verification for Therapy Machines*, Gardone Riviera, 6-7 October.

[Ahnesjö and Andreo, 1989] Ahnesjö, A. and Andreo, P. (1989). Determination of effective bremsstrahlung spectra and electron contamination for photon dose calculations. *Medical Physics*, 34(10):1451–1464.

[Ahnesjö et al., 1987] Ahnesjö, A., Andreo, P., and Brahme, A. (1987). Calculation and Application of Point Spread Functions for Treatment Planning with High Energy Photon Beams. *Acta Oncologica*, 26(1):49–56.

[Ahnesjö and Mackie, 1987] Ahnesjö, A. and Mackie, R. (1987). Analytical description of Monte Carlo generated photon dose convolution kernels. In Bruinvis, I. A. D., van der Giessen, P. H., van Kleffens, H. J., and Wittkämper, F. W., editors, *9th International Conference on the Use of Computers in Radiation Therapy*, pages 197–200, Scheveningen, The Netherlands.

[Ahnesjö et al., 1992] Ahnesjö, A., Saxner, M., and Trepp, A. (1992). A pencil beam model for photon dose calculation. *Medical Physics*, 19(1):263–273.

[Ahnesjö et al., 1995] Ahnesjö, A., Weber, L., and Nilsson, P. (1995). Modelling transmission and scatter for photon beam attenuators. *Medical Physics*, 22(11):1711–1720.

[Altschuler et al., 1985] Altschuler, M. D., Sontag, M. R., and Bloch, P. (1985). A clinically operational method for three-dimensional dose calculations. *Physics in Medicine and Biology*, 30(3):217–228.

[Andreo, 1988] Andreo, P. (1988). Electron Pencil Beam calculations. In Jenkins, T. M., Nelson, W. R., and Rindi, A., editors, *Monte Carlo Transport of Electrons and Photons*, chapter 20. Plenum Press. Ettore Majorana International Science Series.

[Andreo, 1991] Andreo, P. (1991). Monte Carlo techniques in medical radiation physics. *Physics in Medicine and Biology*, 36(7):861–920.

[Andreo, 1994] Andreo, P. (1994). Applications of Monte-Carlo techniques in radiotherapy physics. In *Notes from: International course on advances in radiotherapy*, London. Royal Marsden Hospital. March 16th-18th.

[Aspradakis et al., 1995] Aspradakis, M. M., Redpath, A. T., and Sauer, O. A. (1995). Improving the accuracy of fast 3d photon dose calculations with the aid of a superposition algorithm. *Radiotherapy & Oncology*, 37,Supplement 1. Abstract No 108.

[Attix, 1986] Attix, F. H. (1986). *Introduction to Radiological Physics and Radiation Dosimetry*. John Wiley & Sons Inc.

[Batho, 1964] Batho, H. F. (1964). Lung Corrections in Cobalt 60 beam therapy. *Journal of the Canadian Association of Radiologists*, 15:79–83.

[Battista and Sharpe, 1992] Battista, J. J. and Sharpe, M. (1992). True Three-Dimensional Dose Computations for Megavoltage X-Ray Therapy: A Role for the Superposition Principle. *Australasian Physical and Engineering Sciences in Medicine*, 15(4):159–178.

[Beaudoin, 1968] Beaudoin, L. (1968). Analytical Approach to the Solution of the Dosimetry in Heterogeneous media. Master's thesis, University of Toronto.

[Berger, 1963] Berger, M. J. (1963). Monte carlo calculation of the penetration and diffusion of fast charged particles. In *Methods in Computational Physics*, pages 135–215. N. Y. Academic. Volume I.

[Berger, 1969] Berger, M. J. (1969). Beta-ray dosimetry calculations with the use of point kernels. *Medical Radionuclides: Radiation Dose and Effects*, pages 63–89.

[Berger and Seltzer, 1982] Berger, M. J. and Seltzer, S. M. (1982). Tables of Energy Deposition in Water Irradiated by Point Monodirectional Electron Beams with Energies from 1 to 60 MeV, and Applications to Broad Beams. report NBSIR 82-2451, National Bureau of Standards, Washington, D.C.

[Bielajew, 1988] Bielajew, A. F. (1988). Electron Transport in $\vec{E}$ and $\vec{B}$ Fields. In Jenkins, T. M., Nelson, W. R., and Rindi, A., editors, *Monte Carlo Transport of Electrons and Photons*, chapter 19. Plenum Press. Ettore Majorana International Science Series.

[Bielajew, 1990a] Bielajew, A. F. (1990a). An Analytic Theory of the Point-Source Non-Uniformity Correction Factor for Thick-Walled Ionisation Chambers in Photon Beams. *Physics in Medicine and Biology*, 35(4):517–538.

[Bielajew, 1990b] Bielajew, A. F. (1990b). Correction Factors for Thick-Walled Ionisation Chambers in Point-Source Photon Beams. *Physics in Medicine and Biology*, 35(4):501–516.

[Bielajew, 1991] Bielajew, A. F. (1991). Improved angular sampling for pair production in the EGS4 code system. Report PIRS-0287, National Research Council of Canada.

[Bielajew, 1992] Bielajew, A. F. (1992). Running EGS4 on different architectures. Report PIRS-0392, National Research Council of Canada.

[Bielajew, 1993a] Bielajew, A. F. (1993a). The effect of strong longitudinal magnetic fields on dose deposition from electron and photon beams. *Medical Physics*, 20(4).

[Bielajew, 1993b] Bielajew, A. F. (1993b). EGS4 Lecture notes: Efficiency, statistics and sampling. Report PIRS-0395, National Research Council of Canada.

[Bielajew, 1993c] Bielajew, A. F. (1993c). Graphics! Report PIRS-0397, National Research Council of Canada.

[Bielajew, 1993d] Bielajew, A. F. (1993d). How to manage the EGS4 system. Report PIRS-0391, National Research Council of Canada.

[Bielajew, 1993e] Bielajew, A. F. (1993e). Running EGS4 on other machines. Report PIRS-0392, National Research Council of Canada.

[Bielajew, 1994] Bielajew, A. F. (1994). Private communication.

[Bielajew et al., 1994] Bielajew, A. F., Hirayama, H., Nelson, W. R., and Rogers, D. W. O. (1994). History, overview and recent improvements of EGS4. report PIRS-0203/KEK-94-18/SLAC-PUB-6499, National Research Council of Canada and National Laboratory for High Energy Physics and Stanford Linear Accelerator Center.

[Bielajew et al., 1989] Bielajew, A. F., Mohan, R., and Chui, C. (1989). Improved bremsstrahlung photon angular sampling in the EGS4 code system. report PIRS-0203, National Research Council of Canada, Ottawa, Canada.

[Bielajew and Rogers, 1986a] Bielajew, A. F. and Rogers, D. W. O. (1986a). Photoelectron angular distribution inthe EGS4 code system. Report PIRS-0058, National Research Council of Canada.

[Bielajew and Rogers, 1986b] Bielajew, A. F. and Rogers, D. W. O. (1986b). PRESTA :The Parameter Reduced Electron-Step Transport Algorithm for Electron Monte Carlo Transport. Report PIRS-0042, National Research Council of Canada.

[Bielajew and Rogers, 1987] Bielajew, A. F. and Rogers, D. W. O. (1987). PRESTA :The Parameter Reduced Electron-Step Transport Algorithm for Electron Monte Carlo Transport. *Nuclear Instruments and Methods*, B18:165–181.

[Bielajew and Rogers, 1988a] Bielajew, A. F. and Rogers, D. W. O. (1988a). Electron Step-Size Artefacts and PRESTA. In Jenkins, T. M., Nelson, W. R., and Rindi, A., editors, *Monte Carlo Transport of Electrons and Photons*, chapter 5. Plenum Press. Ettore Majorana International Science Series.

[Bielajew and Rogers, 1988b] Bielajew, A. F. and Rogers, D. W. O. (1988b). Variance-Reduction Techniques. In Jenkins, T. M., Nelson, W. R., and Rindi, A., editors, *Monte Carlo Transport of Electrons and Photons*, chapter 18. Plenum Press. Ettore Majorana International Science Series.

[Bielajew and Rogers, 1992a] Bielajew, A. F. and Rogers, D. W. O. (1992a). A standard timing benchmark for EGS4 Monte Carlo calculations. *Medical Physics*, 19(2):303–304.

[Bielajew and Rogers, 1992b] Bielajew, A. F. and Rogers, D. W. O. (1992b). Implications of new correction factors on primary air kerma standards in Co-60 beams. *Physics in Medicine and Biology*, 37(6):1283–1291.

[Bielajew et al., 1993] Bielajew, A. F., Wang, R., and Duane, S. (1993). Incorporation of single scattering in the EGS4 Monte Carlo code system: Tests of Moliére theory. *Nuclear Instruments and Methods in Physics Research*, B82:503–512.

[BJR, 1983] BJR (1983). Central Axis Depth Dose data for use in Radiotherapy. BJR Supplement 17, British Journal of Radiology.

[Bloch and Altschuler, 1995] Bloch, P. and Altschuler, M. D. (1995). *Radiation Therapy Physics*, chapter 3. Springer-Verlag. Edited by A. R. Smith.

[Bond et al., 1978] Bond, J. E., Nath, R., and Schulz, R. J. (1978). Monte Carlo calculation of the wall correction factors for ionization chambers and A(eq) for Co-60 gamma rays. *Medical Physics*, 5(5):422–425.

[Bortfeld et al., 1993] Bortfeld, T., Schlegel, W., and Rhein, B. (1993). Decomposition of pencil beam kernels for fast dose calculations in three-dimensional treatment planning. *Medical Physics*, 20(2):311–318.

[Boyer, 1984] Boyer, A. L. (1984). Shortening the calculation time of photon dose distributions in an inhomogeneous medium. *Medical Physics*, 11(4):552–554.

[Boyer, 1986] Boyer, A. L. (1986). Fourier convolution techniques. In *Proceedings of the Regina Workshop on Convolution*, Regina, Saskatchewan, Canada.

[Boyer, 1988] Boyer, A. L. (1988). Relationship between Attenuation Coefficients and Dose-Spread Kernels. *Radiation Research*, 113:235–242.

[Boyer et al., 1991] Boyer, A. L., Desobry, G. E., and Wells, N. H. (1991). Potential and limitations of invariant kernel conformal therapy. *Medical Physics*, 18(4):703–712.

[Boyer and Mok, 1984] Boyer, A. L. and Mok, E. C. (1984). Photon Beam Modelling Using Fourier Transform techniques. In *8th International Conference on the Use of Computers in Radiation Therapy*, pages 14–16.

[Boyer and Mok, 1985] Boyer, A. L. and Mok, E. C. (1985). A photon dose calculation model employing convolution calculations. *Medical Physics*, 12(2):169–177.

[Boyer and Mok, 1986] Boyer, A. L. and Mok, E. C. (1986). Calculation of photon dose distributions in a inhomogeneous medium using convolutions. *Medical Physics*, 13(4):503–509.

[Boyer et al., 1988] Boyer, A. L., Wackwitz, R., and Mok, E. C. (1988). A comparison of the speeds of three convolution algorithms. *Medical Physics*, 15(2):224–227.

[Bracewell, 1984] Bracewell, R. M. (1984). *The Fourier Transform and Its Applications*. Mc Graw-Hill, NY.

[Brahme, 1984] Brahme, A. (1984). Dosimetric precision requirements in radiation therapy. *Acta Radiologica Oncology*, 23:379–391.

[Brahme, 1987] Brahme, A. (1987). Design principles and clinical possibilities of radiation therapy equipment. *Acta Oncologica*, 26(6):403–412. A Review.

[Brahme, 1988] Brahme, A., editor (1988). *Accuracy requirements and quality assurance of external beam with photon and electrons*, volume vol. 15. Acta Onc., Suppl. 1.

[Burns and Raeside, 1987] Burns, G. and Raeside, D. E. (1987). Monte Carlo simulation of the dose distribution around ^{125}I seeds. *Medical Physics*, 14(3):420–424.

[Carlsson, 1981] Carlsson, G. A. (1981). Effective Use of Monte Carlo Methods for simulating photon transport with special reference to slab penetration problems in X-ray diagnostics. report LiU-RAD-R-049, Department of Radiology, Linköping University.

[Cassell et al., 1981] Cassell, K. J., Hobday, P. A., and Parker, R. P. (1981). The implementation of a generalized Batho inhomogeneity correction for radiotherapy planning with direct use of CT numbers. *Physics in Medicine and Biology*, 26(4):825–833.

[Ceberg et al., 1996] Ceberg, C. P., Bjärngard, B. E., and Zhu, T. C. (1996). Experimental determination of the dose kernel in high-energy x-ray beams. *Medical Physics*, 23(4):505–511.

[Chaney et al., 1994] Chaney, E. L., Cullip, T. J., and Gabriel, T. A. (1994). A Monte Carlo study of accelerator head scatter. *Medical Physics*, 21(9):1383–1390.

[Chui, 1985] Chui, C. S. (1985). *A method for three dimensional gamma ray dose calculations in heterogeneous media and its applications in radiation therapy.* PhD thesis, Columbia University.

[Cook, 1982] Cook, A. J. (1982). Motran3 User's Guide. Computation Research Group Memorandum 209, Stanford Linear Accelerator Center, Computation Research Group 88, SLAC, Stanford, California, 94305.

[Cristy, 1983] Cristy, M. (1983). Applying the reciprocal dose principle to heterogeneous phantoms: practical experience from Monte Carlo studies. *Physics in Medicine and Biology*, 28(11):1289–1303.

[Cunningham, 1972] Cunningham, J. R. (1972). Scatter-Air Ratios. *Physics in Medicine and Biology*, 17(1):42–51.

[Cunningham, 1982] Cunningham, J. R. (1982). Tissue inhomogeneity corrections in photon-beam treatment planning. In Orton, C. G., editor, *Progress in Modern Radiation Physics*, pages 103–131. Plenum, New York.

[Cunningham, 1983] Cunningham, J. R. (1983). Reply to Iwasaki: "Uncertainty of the equivalent tissue-air ratio method". *Medical Physics*, 10(5):717. Communications.

[Cunningham, 1988] Cunningham, J. R. (1988). A summary of dose calculation methods for radiotherapy planning. In Iyer, S. H. . P. S., editor, *Dosimetry in Radiotherapy : Proceedings of a Symposium*, volume 2, pages 3–23, Vienna. IAEA, WHO, International Atomic Energy Agency (IAEA).

[Cunningham and Beaudoin, 1973] Cunningham, J. R. and Beaudoin, L. (1973). Calculations for tissue inhomogeneities with experimental verification. In *Proceeding of the XII International Congress of Radiology*, pages 653–657, Madrid.

[Cunningham et al., 1972] Cunningham, J. R., Shrivastava, P. N., and Wilkinson, J. M. (1972). Program IRREG - Calculation of dose from irregularly shaped radiation beams. *Computer Programs in Biomedicine*, 2(3):192–199.

[Cunningham et al., 1986] Cunningham, J. R., Woo, M., Rogers, D. W. O., and Bielajew, A. F. (1986). The dependance of mass energy absorption coefficient ratios on beam size and depth in a phantom. *Medical Physics*, 13(4).

[Dale, 1982] Dale, R. G. (1982). A Monte Carlo derivation of parameters for use in the tissue dosimetry of medium and low-energy nuclides. *British Journal of Radiology*, 55:748–757.

[Day, 1950] Day, M. J. (1950). A note on the calculation of dose in x-ray fields. *British Journal of Radiology*, XXIII(270):368–369.

[Dean, 1980] Dean, R. D. (1980). A Scattering Kernel for use in True three-Dimensional Dose Calculations. *Medical Physics*, 7(4):429. (Abstract).

[Del Guerra et al., 1991] Del Guerra, A., Nelson, W. R., and Russo, P. (1991). A simple method to introduce K-edge sampling for compounds in the code EGS4 for X-ray element analysis. *Nuclear Instruments and Methods in Physics Research*, A306:378–385.

[Desobry et al., 1991] Desobry, G. E., Wells, N. H., and Boyer, A. L. (1991). Rotational kernels for conformal therapy. *Medical Physics*, 18(3):481–487.

[Dryzmala et al., 1991] Dryzmala, R. E., Mohan, R., Brewster, L., Chu, J., Goitein, M., Harms, W., and Urie, M. (1991). Dose-Volume Histograms. *Int. J. Radiation Oncology Biol. Phys.*, 21:71–78.

[Duane et al., 1989] Duane, S., Bielajew, A. F., and Rogers, D. W. O. (1989). Use of ICRU-37/NBS Collision Stopping Powers in the EGS4 System. Report PIRS-0177, National Research Council of Canada.

[Eklöf et al., 1990] Eklöf, A., Ahnesjö, A., and Brahme, A. (1990). Photon beam energy deposition kernels for inverse radiotherapy planning. *Acta Oncologica*, 29(4):447–454.

[El-Khatib and Battista, 1984] El-Khatib, E. and Battista, J. J. (1984). Improved lung dose calculation using tissue-maximum ratios in the batho correction. *Medical Physics*, 11:279–286.

[Field and Battista, 1987] Field, G. C. and Battista, J. J. (1987). Photon Dose Calculations Using Convolution in Real and Fourier Space: Assumptions and Time Estimates. In Bruinvis, I. A. D., van der Giessen, P. H., van Kleffens, H. J., and Wittkämper, F. W., editors, *9th International Conference on the Use of Computers in Radiation Therapy*, pages 103–106, Scheveningen, The Netherlands.

[Fox and Webb, 1979] Fox, R. A. and Webb, S. A. (1979). A Comparison of inhomogeneity correction methods with Monte Carlo data. *Australasian Physical Sciences in Medicine*, 2-8(85):452–462.

[Geise and McCullough, 1977] Geise, R. A. and McCullough, E. C. (1977). The Use of CT scanners in Megavoltage Photon-Beam Therapy Planning. *Radiology*, 124:133–141.

[Goudsmit and Saunderson, 1940] Goudsmit, S. and Saunderson, J. L. (1940). Multiple scattering of electrons. *Phys. Rev.*, 57:24–29.

[Greene and Stewart, 1965] Greene, D. and Stewart, J. R. (1965). Isodose curves in non-uniform platforms. *British Journal of Radiology*, 38:378.

[Guber et al., 1967] Guber, W., Nagel, J., Goldstein, R., Mettelman, P. S., and Kalos, M. H. (1967). A Geometric Description Technique Suitable for Computer Analysis and for Both the Nuclear and Conventional Vulnerability of Armored Military Vehiles. Report MAGI-6701, Washington DC:MAGI.

[Halbleib and Mehlhorn, 1984] Halbleib, J. A. and Mehlhorn, T. A. (1984). *ITS: The integrated tiger series of coupled electron/photon Monte Carlo transport codes.* (USDOE).

[Hammersley and Handscomb, 1964] Hammersley, J. M. and Handscomb, D. C. (1964). *Monte Carlo Methods.* Methuen, London.

[Hanson and Berkley, 1980] Hanson, W. F. and Berkley, L. W. (1980). Off-axis beam quality change in linear accelerator x-ray beams. *Medical Physics*, 7(2):145–146.

[Hanson et al., 1980] Hanson, W. F., Berkley, L. W., and Peterson, M. (1980). Calculative technique to correct for the change in linear accelerator beam energy at off-axis points. *Medical Physics*, 7(2):147–150.

[Henkelman and Wong, 1981] Henkelman, R. M. and Wong, J. W. (1981). Physics of the Inhomogeneity Problem and the Present Status of Clinical Dosimetry. In Ling, C. C., Rogers, C. C., and Morton, R. J., editors, *Computed Tomography in Radiation Therapy*, pages 187–197. N Y Raven.

[Herring and Compton, 1971] Herring, D. F. and Compton, D. M. J. (1971). The degree of precision required in the radiation dose delivered in cancer therapy. *British Journal of Radiology*, pages 51–58. Special Report no. 5.

[Hirayama et al., 1994] Hirayama, H., Namito, Y., and Ban, S. (1994). Effects of linear polarisation and Doppler broadening on the exposure build up factors of low-energy gamma rays. Report KEK Preprint 93-186, National Laboratory for High Energy Physics, KEK, Japan.

[Hoban, 1995] Hoban, P. W. (1995). Accounting for the variation in collision kerma-to-terma ratio in polyenergetic photon beam convolution. *Medical Physics*, 22(12):2035–2044.

[Hoban et al., 1994] Hoban, P. W., Murray, D. C., and Round, W. H. (1994). Photon beam convolution using polyenergetic energy deposition kernels. *Physics in Medicine and Biology*, 39(4):669–685.

[Holmes et al., 1993] Holmes, M. A., Mackie, T. R., Sohn, W., Reckwerdt, P. J., Kinsella, T. J., Bielajew, A. F., and Rogers, D. W. O. (1993). The application of correlated sampling to the computation of electron beam dose distributions in heterogeneous phantoms using the Monte Carlo method. *Physics in Medicine and Biology*, 38:675–688.

[Hubbell, 1982] Hubbell, J. H. (1982). Photon mass attenuation and energy absorption coefficients from 1 keV to 20 MeV. *Int. J. Appl. Radiat. Isot.*, 33:1269.

[Huizenga and Storchi, 1985] Huizenga, H. and Storchi, P. R. (1985). The use of computed tomography numbers in dose calculations for radiation therapy. *Acta Radiologica Oncologica*, 24(6):509–519.

[ICRU, 1976] ICRU (1976). Determination of Absorbed Dose in a Patient Irradiated by Beams of X or Gamma Rays in Radiotherapy Procedures. Report 24, International Commission on Radiation Units and Measurements, Washington, D. C. 20014,USA.

[ICRU, 1978] ICRU (1978). Dose Specification for Reporting External Beam Therapy with Photons and Electrons. Report 29, International Commission on Radiation Units and Measurements, Washington, D. C. 20014,USA.

[ICRU, 1984] ICRU (1984). Stopping Powers for Electrons and Photons. Report 37, International Commission on Radiation Units and Measurements, 7910 Woodmont Avenue, Bethesda, MD. 20814, USA.

[ICRU, 1987] ICRU (1987). Use of Computers in External Beam Radiotherapy Procedures with High-Energy Photons and Electrons. Report 42, International Commission on Radiation Units and Measurements, Washington, D. C. 20014,USA.

[ICRU, 1993] ICRU (1993). Prescribing, Recording, and Reporting Photon Beam Therapy. Report 50, International Commission on Radiation Units and Measurements, Bethesda, Maryland,USA.

[Inamura et al., 1984] Inamura, K., Abe, S., Ueda, Y., Shigaki, K., and Fujino, S. (1984). An application of Equivalent TAR method to fast reconstructor of three dimensional dose distribution. In *The Eighth International Conference of the Use of Computers in Radiation Therapy*, pages 456–460.

[Iwasaki, 1983] Iwasaki, A. (1983). Uncertainty of the equivalent tissue-air ratio method. *Medical Physics*, 10(5):716–717. Communications.

[Iwasaki, 1985] Iwasaki, A. (1985). A method for calculating high-energy photon primary absorbed dose in water using forward and backward spread dose-distribution functions. *Medical Physics*, 12(6):731–737.

[Iwasaki and Ishito, 1984] Iwasaki, A. and Ishito, T. (1984). The differential scatter-air ratio and differential backscatter factor method combined with the density scaling theorem. *Medical Physics*, 11(6):755–763.

[James, 1980] James, F. (1980). Monte Carlo theory and practice. Technical report, CERN Data Handling Division. DD/80/6.

[Johns and Cunningham, 1983] Johns, H. E. and Cunningham, J. R. (1983). *The Physics of Radiology.* Charles C. Thomas, Springfield, Illinois, USA, Fourth Edition edition.

[Johns et al., 1949] Johns, H. E., Darby, E. K., Haslam, R. N., Katz, L., and Harrington, E. L. (1949). Depth dose data and isodose distributions for radiation from a $22MeV$ betatron. *Am. J. Roentgenol.*, 62:257–268.

[K-A. Johansson, 1982] K-A. Johansson (1982). *Studies of Different Methods of Absorbed Dose Determination and a Dosimetric Intercomparison at the Nordic Radiotherapy Centres.* PhD thesis, University of Götenborg.

[Kahn, 1954] Kahn, H. (1954). Use of different Monte Carlo sampling techniques. In Meyer, H. A., editor, *Symposium on Monte Carlo Methods.* John Wiley & Sons, Inc.

[Karr and Bielajew, 1993] Karr, J. L. and Bielajew, A. F. (1993). PIF [Prepare Input File (for PEGS4). Report PIRS-0365, National Research Council of Canada.

[Karzmark, 1984] Karzmark, G. J. (1984). Advances in linear accelerator design for radiotherapy. *Physics in Medicine and Biology*, 11(2):105–128. Review article.

[Karzmark and Pering, 1973] Karzmark, G. J. and Pering, N. C. (1973). Electron Linear Accelerators for Radiation Therapy: History, Principles and Contemporary Developments. *Physics in Medicine and Biology*, 8(3):321–354. Review article.

[Kawrakow et al., 1996] Kawrakow, I., Fippel, M., and Friedrich, K. (1996). 3D electron dose calculation using a Voxel based Monte Carlo algorithm (VMC). *Medical Physics*, 23(4):445–457.

[Keall and Hoban, 1995] Keall, P. and Hoban, P. (1995). Accounting for primary electron scatter in x-ray beam convolution calculations. *Medical Physics*, 22(9):1413–1418.

[Keall and Hoban, 1996] Keall, P. and Hoban, P. (1996). Superposition dose calculation incorporating monte carlo generated electron track kernels. *Medical Physics*, 23(4):479–485.

[Kepka et al., 1985] Kepka, A. G., Johnson, P. M., and David, J. (1985). The effect of off-axis quality changes on zero area TAR for megavoltage beams. *Physics in Medicine and Biology*, 30(6):589–595.

[Knöös et al., 1995] Knöös, T., Ahnesjö, A., Nilsson, P., and Weber, L. (1995). Limitations of a pencil beam approach to photon dose calculations in lung tissue. *Physics in Medicine and Biology*, 40(9):1411–1420.

[Kooy and Kijewski, 1988] Kooy, H. M. and Kijewski, P. K. (1988). Quadtrees as a representation for irregularly shaped fields in radiotherapy applications. *Int. J. Radiation Oncology Biol. Phys.*, 15:1251–1256.

[Krippner et al., 1987] Krippner, K., Wong, J. W., Harms, W. B., and Purdy, J. A. (1987). The Use of an Array Processor for the Delta Volume Dose Computation Algorithm. In Bruinvis, I. A. D., van der Giessen, P. H., van Kleffens, H. J., and Wittkämper, F. W., editors, *The Ninth International Conference of*

the Use of Computers in Radiation Therapy, pages 533–536, Scheveningen,The Netherlands.

[Larson and Prasad, 1978] Larson, K. B. and Prasad, S. C. (1978). Absorbed dose computations for inhomogeneous media in radiation treatment planning using differential scatter-air ratios. In *2nd Annual Symposium on Ccomputer Applications in Medical Care.*, pages 93–99. IEEE, NY.

[Lax et al., 1983] Lax, I., Brahme, A., and Andreo, P. (1983). Electron beam dose planning using Gaussian beams. Improved radial dose profiles. *Acta Radiol. Supl.*, 364:49–59.

[Loevinger, 1969] Loevinger, R. (1969). *Radiation Dosimetry*, volume III, chapter 18: Distributed Radionuclide Sources, pages 51–90. Academic Press.

[Lovelock et al., 1995] Lovelock, D. M. J., Chui, C. S., and Mohan, R. (1995). A Monte Carlo model of photon beams used in radiation therapy. *Medical Physics*, 22(9):1387–1394.

[Low et al., 1995] Low, D. A., Zhu, X. R., Harms, W. B., and Purdy, J. A. (1995). Measurement of a photon penumbra-generating kernel for a convolution-adapted ratio-TAR algorithm for 3D treatment planning. *Medical Physics*, 22(9):1395–1403.

[Lu and Chin, 1993] Lu, X.-Q. and Chin, L. M. (1993). Sampling techniques for the evaluation of treatment plans. *Medical Physics*, 20(1):151–161.

[Lulu and Bjärngard, 1982] Lulu, B. A. and Bjärngard, B. E. (1982). Batho's correction factor combined with scatter summation. *Medical Physics*, 9(3):372–377.

[Lund, 1981] Lund, T. (1981). An Introduction to the Monte Carlo Method. Technical report, CERN.

[Lutz and Larsen, 1984] Lutz, W. R. and Larsen, R. D. (1984). The effect of flattening filter design on quality variations within an $8 - mv$ primary x-ray beam. *Medical Physics*, 11(6):843–845.

[Lux and Koblinger, 1991] Lux, I. and Koblinger, L. (1991). Monte Carlo transport methods: Neutron photon calculations. Technical report, Boca Raton, Florida 33431 .

[Ma, 1992] Ma, C. M. (1992). *Monte Carlo simulation of dosimeter response using Transputers.* PhD thesis, University of London, UK.

[Ma, 1994] Ma, C. M. (1994). Implementation of a Monte Carlo code on a paraller computer system. *Parallel Computing*, 20:991–1005.

[Ma and Nahum, 1992] Ma, C. M. and Nahum, A. E. (1992). A new algorithm for EGS4 low-energy electron transport to account for the change in discrete interaction cross-section with energy. *Nuclear Instruments and Methods in Physics Research*, B72:319–330.

[Ma and Nahum, 1993] Ma, C. M. and Nahum, A. E. (1993). Effect of the size and composition of the central electrode on the response of cylindrical ionisation chambers in high-energy photon and electron beams. *Physics in Medicine and Biology*, 38(2):267–290.

[Mackie, 1983] Mackie, T. R. (1983). Photon Dose Calculations Using a Convolution Method That Includes Non-Local Electron Energy Deposition. *Medical Physics*, 10(4):536. (Abstract).

[Mackie, 1984] Mackie, T. R. (1984). *A Study of Charged Particles and Scattered Photons in Megavoltage X-ray Beams.* PhD thesis, University of Alberta.

[Mackie, 1990] Mackie, T. R. (1990). Applications of the Monte Carlo Method in Radiotherapy. In Kase, K. R., Bjärngard, B. E., and Attix, F. H., editors, *The Dosimetry of Ionizing Radiation*, volume III, chapter 6. N. Y. Academic Press.

[Mackie, 1993] Mackie, T. R. (1993). Private communication.

[Mackie, 1995a] Mackie, T. R. (1995a). Private communication.

[Mackie, 1995b] Mackie, T. R. (1995b). Status of Monte Carlo dose planning. In *Abstracts of the Third Biennial ESTRO Meeting on Physics in Clinical Radiotherapy*, Gardone Riviera, Italy. European Society for Therapeutic Radiology and Oncology. 8-11 October 1995.

[Mackie et al., 1987] Mackie, T. R., Ahnesjö, A., Dickof, P., and Snider, A. (1987). Development of a convolution/superposition method for photon beams. In *9th International Conference on the Use of Computers in Radiation Therapy*, pages 107–110.

[Mackie and Battista, 1984] Mackie, T. R. and Battista, J. J. (1984). A macroscopic Monte Carlo method for electron beam dose calculations: A proposal. In *The Eighth International Conference of the Use of Computers in Radiation Therapy*, pages 123–127.

[Mackie et al., 1988a] Mackie, T. R., Bielajew, A. F., Rogers, D. W. O., and Battista, J. J. (1988a). Generation of photon energy deposition kernels using the *EGS*4 Monte Carlo code. *Physics in Medicine and Biology*, 33(1):1–20.

[Mackie et al., 1988b] Mackie, T. R., Bielajew, A. F., Rogers, D. W. O., and Battista, J. J. (1988b). Generation of photon energy deposition kernels using the *EGS*4 Monte Carlo code. *Physics in Medicine and Biology*, 33(1):1–20.

[Mackie et al., 1985a] Mackie, T. R., El-Khatib, E., Battista, J. J., Scrimger, J., Dyk, J. V., and Cunningham, J. R. (1985a). Lung dose corrections for 6- and 15-MV x-rays. *Medical Physics*, 12(3):327–332.

[Mackie et al., 1990a] Mackie, T. R., Reckwerdt, P. J., Gehring, M. A., Holmes, T. W., Kubsad, S. S., Thomadsen, B. R., Sanders, C. A., Paliwal, B. R., and Kinsella, T. J. (1990a). Clinical implementation of the convolution/superposition method. In *10th International Conference on the Use of Computers in Radiation Therapy*, pages 322–325.

[Mackie and Scrimger, 1982] Mackie, T. R. and Scrimger, J. W. (1982). Contamination of a $15 - mv$ Photon Beam by Electrons and Scattered Photons. *Radiology*, 144:403–409.

[Mackie et al., 1985b] Mackie, T. R., Scrimger, J. W., and Battista, J. J. (1985b). A convolution method of calculating dose for 15-MV x-rays. *Medical Physics*, 12:188–189.

[Mackie et al., 1990b] Mackie, T. R., Sohn, W., Lindstrom, M., Kubsad, S., Reckwerdt, P. J., Kinsella, T. J., Bielajew, A. F., and Rogers, D. W. O. (1990b). The Ottawa-Madison Electron Gamma Algorithm (OMEGA) project: feasibility of two Monte Carlo techniques. In Iyer, S. H. &. P. S., editor, *The Tenth International Conference of the Use of Computers in Radiation Therapy*, pages 250–252. Lucknow, India.

[Manfredotti et al., 1990] Manfredotti, C., Nastasi, U., Marchisio, R., Onargo, C., Gervino, G., Ragona, R., Anglesio, S., and Sannazzari, G. (1990). Monte Carlo Simulation of Dose Distribution in Electron Beam Radiotherapy Treatment Planning. *Nucl. Inst. Meth*, A:646–654.

[Manfredotti et al., 1995] Manfredotti, C., Nastasi, U., and Zanini, A. (1995). Monte Carlo calculation of dose delivered to patients in radiotherapy treatments. In *Abstracts of the Third Biennial ESTRO Meeting on Physics in Clinical Radiotherapy*, Gardone Riviera, Italy. European Society for Therapeutic Radiology and Oncology. 8-11 October 1995.

[Marsaglia and Zaman, 1991] Marsaglia, G. and Zaman, A. (1991). A New Class of Random Number Generators. *Annals of Applied Probability*, 1:462–480.

[Marsaglia et al., 1990] Marsaglia, G., Zaman, A., and Tsang, W. W. (1990). Toward a Universal Random Number Generator. *Statistics and Probability Letters*, 8:35–39.

[McCracken, 1955] McCracken, D. D. (1955). The Monte Carlo Method. *Scientific American*, 192:90–96.

[McGrath and Irving, 1975] McGrath, E. J. and Irving, D. F. (1975). Techniques for Efficient Monte Carlo Simulation. Oak Ridge National Laboratory report ORNL-RSIC-38, Radiation Shielding Information Center.

[McShan and Fraass, 1993] McShan, D. L. and Fraass, B. A. (1993). Use of an octree-like geometry for 3-D dose calculations. *Medical Physics*, 20(4):1219–1227.

[Medin and Andreo, 1995] Medin, J. and Andreo, P. (1995). Monte Carlo calculated stopping power ratio water/air for clinical proton therapy. In *Abstracts of the Third Biennial ESTRO Meeting on Physics in Clinical Radiotherapy*, Gardone Riviera, Italy. European Society for Therapeutic Radiology and Oncology. 8-11 October 1995.

[Metcalfe et al., 1989] Metcalfe, P. E., Hoban, P. W., Murray, D. C., and Round, W. H. (1989). Modelling polychromatic high energy photon beams by superposition. *Australasian Physical and Engineering Sciences in Medicine*, 12(3):138–148.

[Metcalfe et al., 1990] Metcalfe, P. E., Hoban, P. W., Murray, D. C., and Round, W. H. (1990). Beam hardening of $10MV$ radiotherapy x-rays: analysis using a convolution/superposition method. *Physics in Medicine and Biology*, 35(11):1533–1549.

[Meyer, 1954] Meyer, H. A., editor (1954). *Symposium on Monte Carlo Methods.* John Wiley & Sons, New York.

[Mijnheer et al., 1987] Mijnheer, B. J., Batterman, J. J., and Wambersie, A. (1987). What degree of accuracy is required and can be achieved in photon and neutron therapy? *Radiotherapy & Oncology*, 8:237–252.

[Milan and Bentley, 1974] Milan, J. and Bentley, R. E. (1974). The storage and manipulation of radiation dose data in a small digital computer. *British Journal of Radiology*, 47:115–121.

[Miura, 1987] Miura, K. (1987). EGS4V: Vectorization of the Monte Carlo cascade shower simulation code EGS4. *Computer Physics Communications*, 45:127–136.

[Mobit et al., 1996] Mobit, P. N., Mayles, P., and Nahum, A. E. (1996). The quality dependence of LiF TLD in megavoltage photon beams: Monte Carlo simulation and experiments. *Physics in Medicine and Biology*, 41(5):387–398.

[Mohan, 1987a] Mohan, R. (1987a). *Monte Carlo Transport of Electrons and Photons*, chapter No 26: Dose Calculations for Radiation Treatment Planning, pages 549–571. Etorre Majorana International Science Series. Plenum Press.

[Mohan, 1987b] Mohan, R. (1987b). *Monte Carlo Transport of Electrons and Photons*, chapter No 21: Monte Carlo Simulation of Radiation Treatment Machine Heads, pages 453–468. Etorre Majorana International Science Series. Plenum Press.

[Mohan, 1988] Mohan, R. (1988). Monte Carlo Simulation of Radiation Treatment Machine Heads. In Jenkins, T. M., Nelson, W. R., and Rindi, A., editors, *Monte Carlo Transport of Electrons and Photons*, chapter 21. Plenum Press. Ettore Majorana International Science Series.

[Mohan et al., 1981] Mohan, R., Chui, C., Miller, D., and Laughlin, J. S. (1981). Use of Computerized Tomography in Dose Calculations for Radiation Treatment Planning. *CT: the journal of Computed Tomography, (Special issue)*, 5(3):273–282.

[Mohan and Chui, 1987] Mohan, R. and Chui, C.-S. (1987). Use of fast Fourier transforms in calculating dose distributions for irregularly shaped fields for three-dimensional treatment planning. *Medical Physics*, 14(1):70–77.

[Mohan and Chui, 1988] Mohan, R. and Chui, C.-S. (1988). Extraction of pencil beam kernels by the deconvolution method. *Medical Physics*, 15(2):138–144.

[Mohan et al., 1985] Mohan, R., Chui, C.-S., and Lidofsky, L. (1985). Energy and angular distributions of photons from medical linear accelerators. *Medical Physics*, 12(5):592–597.

[Mohan et al., 1986] Mohan, R., Chui, C.-S., and Lidofsky, L. (1986). Differential pencil beam dose computation model for photons. *Medical Physics*, 13:64–73.

[Molière, 1948] Molière, G. Z. (1948). Theorie der Streuung schneller geladener Teilchen II Mehrfach- und Vielfachstreuung. Z. *Naturforsch.*, A(3A):384–385.

[Morin, 1988] Morin, R. L. (1988). *Monte Carlo Simulation in the Radiological Sciences*. CRC Press, Inc.

[Morin et al., 1979] Morin, R. L., Raeside, D. E., Goin, J. E., and Widman, J. C. (1979). Monte Carlo advice. *Medical Physics*, 6(4):305–306.

[Murray, 1990] Murray, D. (1990). Using EGS4 Monte Carlo in medical radiation physics. *Australasian Physical and Engineering Sciences in Medicine*, 13(3):132–147.

[Murray et al., 1991] Murray, D. C., Hoban, P. W., Round, W. H., Graham, I. D., and Metcalfe, P. E. (1991). Superposition on a multicomputer system. *Medical Physics*, 18(3):468–473.

[Murray et al., 1989] Murray, D. C., Hoban, P. W., Round, W. H., Graham, I. D., and Vel, Y. D. (1989). Radiotherapy Treatment Planning Using Transputers. *New Zealand Journal of Computing*, 1(2):30–38.

[Nahum, 1976] Nahum, A. E. (1976). *Calculations of electron flux spectra in water irradiated with megavoltage electron and photon beams with applications to dosimetry.* PhD thesis, The University of Edinburgh, UK.

[Nahum, 1978] Nahum, A. E. (1978). Water/air mass stopping power ratios for megavoltage photon and electron beams. *Physics in Medicine and Biology*, 23(1):24–38.

[Nahum, 1988a] Nahum, A. E. (1988a). Overview of Photon and Electron Monte Carlo. In Jenkins, T. M., Nelson, W. R., and Rindi, A., editors, *Monte Carlo Transport of Electrons and Photons*, chapter 1. Plenum Press. Ettore Majorana International Science Series.

[Nahum, 1988b] Nahum, A. E. (1988b). Simulation of Dosimeter Response and Interface Effects. In Jenkins, T. M., Nelson, W. R., and Rindi, A., editors, *Monte Carlo Transport of Electrons and Photons*, chapter 25. Plenum Press. Ettore Majorana International Science Series.

[Namito and Hirayama, 1991] Namito, Y. and Hirayama, H. (1991). Improvement of low energy photon transport calculation by EGS4- electron bound effect in Compton ' scattering. Technical report, Japan Atomic Energy Society, Osaka 401.

[Nath and Bond, 1981] Nath, R. and Bond, J. E. (1981). Calculated response and wall correction factors for ionization chambers exposed to ^{60}Co gamma-rays. *Medical Physics*, 8(1):85–93.

[Nelson et al., 1985] Nelson, W. R., Hirayama, H., and Rogers, D. W. O. (1985). The EGS4 Code System. report SLAC-265, Stanford Linear Accelerator.

[Neuenschwander and Born, 1992] Neuenschwander, H. and Born, E. J. (1992). A macro Monte Carlo method for electron beam dose calculations. *Physics in Medicine and Biology*, 37(1):107–125.

[Neuenschwander et al., 1995] Neuenschwander, H., Mackie, T. R., and Reckwerdt, P. J. (1995). MMC-a high-performance Monte Carlo code for electron beam treatment planning. *Physics in Medicine and Biology*, 40(4):543–574.

[Niemierko and Goitein, 1989a] Niemierko, A. and Goitein, M. (1989a). The influence of the size of the grid used for dose calculation on the accuracy of dose estimation. *Medical Physics*, 16(2):357–366.

[Niemierko and Goitein, 1989b] Niemierko, A. and Goitein, M. (1989b). The use of variable grid spacing to accelerate dose calculations. *Medical Physics*, 16(3):357–366.

[Niemierko and Goitein, 1990] Niemierko, A. and Goitein, M. (1990). Random sampling for evaluating treatment plans. *Medical Physics*, 17(5):753–762.

[Nilsson, 1985] Nilsson, B. (1985). Electron contamination from different materials in high energy photon beams. *Physics in Medicine and Biology*, 30(2):139–151.

[Nilsson and Brahme, 1981] Nilsson, B. and Brahme, A. (1981). Contamination of high-energy photon beams by scattered photons. *Strahlentherapie*, 157:181–186.

[O'Connor, 1957] O'Connor, J. E. (1957). The variation of scattered x-rays with density in an irradiated body. *Physics in Medicine and Biology*, 1:352–369.

[O'Connor, 1984] O'Connor, J. E. (1984). The density scaling theorem applied to lateral electronic equilibrium. *Physics in Medicine and Biology*, 11(5):678–680.

[O'Connor and Malone, 1989] O'Connor, J. E. and Malone, D. E. (1989). A cobalt-60 primary dose spread array derived from measurements. *Physics in Medicine and Biology*, 34(8):1029–1042.

[Papanikolaou and Mackie, 1993] Papanikolaou, N. and Mackie, T. R. (1993). Generation of photon convolution kernels using a Monte Carlo code for use in Radiotherapy Treatment Planning and cavity theory. *Medical Physics*, 20(3):901.

[Papanikolaou et al., 1995] Papanikolaou, N., Mackie, T. R., and Gehring, M. (1995). A Convolution based Algorithm for Dose Computation in Radiation Therapy. In *Proccedings of the 10th International Congress of Radiation Research, Würzburg, Germany*, pages 254–255.

[Papanikolaou et al., 1993] Papanikolaou, N., Mackie, T. R., Meger-Wells, C., Gehring, M., and Reckwerdt, P. (1993). Investigation of the convolution method for polyenergetic spectra. *Medical Physics*, 20(5):1327–1336.

[Parker et al., 1980] Parker, R. P., de Frietas, C., Webb, S., Cassell, K. J., and Hobday, P. A. (1980). A method of implementing inhomogeneity corrections in radiotherapy. Treatment planning: Comparison with experiment and Monte Carlo calculations. *J. Eur. Radiotherapy*, 2:93–100.

[Parker et al., 1979] Parker, R. P., Hobday, P. A., and Cassell, K. J. (1979). The Direct Use of CT Numbers in Radiotherapy Dosage Calculations for Inhomogeneous Media. *Physics in Medicine and Biology*, 24(4):802–909.

[Petti et al., 1983a] Petti, P. L., Goodman, M. S., Gabriel, T. A., and Mohan, R. (1983a). Investigation of buildup dose from electron contamination. *Medical Physics*, 10(1):18–24.

[Petti et al., 1983b] Petti, P. L., Goodman, M. S., Sisterson, J. M., Biggs, B. J., Gabriel, T. A., and Mohan, R. (1983b). Sources of electron contamination for the Clinac-35 25-MV photon beam. *Medical Physics*, 10(6):856–851.

[Press et al., 1992] Press, W. H., Teukolsky, S. A., Vetterling, W. T., and Flannery, B. P., editors (1992). *Numerical Recipies in C, The Art of Scientific Computing.* Cambridge University Press, second edition.

[Pruitt and Loevinger, 1982] Pruitt, J. S. and Loevinger, R. (1982). The photon-fluence scaling theorem for compton-scattered radiation. *Medical Physics*, 9(2):176–179.

[Purdy, 1992] Purdy, J. A. (1992). Photon Dose Calculations for Three-Dimensional radiation treatment planning. *Seminars in Radiation Oncology*, 2(4):235–245.

[Purdy and Prasad, 1983] Purdy, J. A. and Prasad, S. C. (1983). Current methods and algorithms in radiation absorbed dose calculation and the role of computed tomography. In Ling, C. C., Rogers, C. C., and Morton, R. J., editors, *Computed Tomography in Radiation Therapy*, pages 187–197. N Y , Raven.

[Raeside, 1976] Raeside, D. E. (1976). Monte Carlo principles and applications. *Physics in Medicine and Biology*, 21(2):181–197.

[Rathee et al., 1993] Rathee, S., McClean, B. A., and Field, C. (1993). An improved method for rebinning kernels from cylindrical to Cartesian coordinates. *Medical Physics*, 20(5):1343–1351.

[Reckwerdt and Mackie, 1992] Reckwerdt, P. J. and Mackie, T. R. (1992). Superposition/Convolution Speed Improvements using Run-Length Raytracing. *Medical Physics*, 19(3):784. (Abstract).

[Redpath, 1995] Redpath, A. T. (1995). Private communication.

[Redpath and Thwaites, 1991] Redpath, A. T. and Thwaites, D. I. (1991). A 3-dimensional scatter correction algorithm for photon beams. *Physics in Medicine and Biology*, 36(6):779–798.

[Redpath and Wright, 1981] Redpath, A. T. and Wright, D. H. (1981). Beam Modelling Techniques for Computerized Therapy Planning. In Burger, G., editor, *Treatment Planning for External Beam Therapy with Neutrons*. Urban and Schwarzenberg.

[Roesch, 1958] Roesch, W. C. (1958). Dose for Nonelectronic Equilibrium Conditions. *Radiation Research*, 9:399–410.

[Roesch, 1968] Roesch, W. C. (1968). Mathematical theory of radiation fields. In Attix, F. H. and Roesch, W. C., editors, *Radiation Dosimetry*, volume 1, chapter 1. Academic Press, N Y.

[Rogers, 1979] Rogers, D. W. O. (1979). Analytic and graphical methods for assigning errors to parameters in non-linear least squares fitting. *Nuclear Instruments and Methods*, 127:253–260.

[Rogers, 1984a] Rogers, D. W. O. (1984a). Fluence to dose equivalent conversion factors calculated with EGS3 for electrons from 100 keV to 20 GeV and photons from 20 keV to 20 GeV. *Health Physics*, 46(4):891–914.

[Rogers, 1984b] Rogers, D. W. O. (1984b). Low energy electron transport with EGS. *Nuclear Instruments and Methods in Physics Research*, 227:535–548.

[Rogers, 1992] Rogers, D. W. O. (1992). Calibration of parallel-plate chambers: resolution of several problems by using Monte Carlo calculations. *Medical Physics*, 19:889–899.

[Rogers, 1993] Rogers, D. W. O. (1993). How accurately can EGS4/PRESTA calculate ion-chamber response? *Medical Physics*, 20(2):319–323.

[Rogers and Bielajew, 1984] Rogers, D. W. O. and Bielajew, A. F. (1984). The Use of EGS for Monte Carlo Calculations in Medical Physics. Lecture Notes for Refresher Course RC7, First Inter-American Meeting of Medical Physics: Report PXNR-2692, National Research Council of Canada, Chicago.

[Rogers and Bielajew, 1988a] Rogers, D. W. O. and Bielajew, A. F. (1988a). 20-MeV Electrons on a Slab of Water. In Jenkins, T. M., Nelson, W. R., and Rindi, A., editors, *Monte Carlo Transport of Electrons and Photons*, chapter 6. Plenum Press. Ettore Majorana International Science Series.

[Rogers and Bielajew, 1988b] Rogers, D. W. O. and Bielajew, A. F. (1988b). A Comparison of EGS and ETRAN. In Jenkins, T. M., Nelson, W. R., and Rindi, A., editors, *Monte Carlo Transport of Electrons and Photons*, chapter 14. Plenum Press. Ettore Majorana International Science Series.

[Rogers and Bielajew, 1990] Rogers, D. W. O. and Bielajew, A. F. (1990). Monte Carlo Techniques of Electron and Photon Transport for Radiation Dosimetry. In Kase, K. R., Bjärngard, B. E., and Attix, F. H., editors, *The Dosimetry of Ionizing Radiation*, volume III, chapter 5. N. Y. Academic Press.

[Rogers et al., 1988] Rogers, D. W. O., Ewart, G. M., Bielajew, A. F., and van Dyk, G. (1988). Calculation of Electron Contamination in a ^{60}Co Therapy Beam. In *Proceedings of the IAEA International Symposium on Dosimetry in Radiotherapy*, volume 1, pages 303–312, Vienna. IAEA.

[Rogers et al., 1995] Rogers, D. W. O., Faddegon, B. A., Ding, G. X., C.-M. Ma, We, J., and Mackie, T. R. (1995). BEAM: A Monte Carlo code to simulate radiotherapy treatment units. *Medical Physics*, 22(5):503–524.

[Rosenberger et al., 1984] Rosenberger, F. U., Krippner, K., D. Stein, J., and Wong, J. W. (1984). Implementation of the Delta-Volume Dose Calculation Algorithm. In *The Eighth International Conference of the Use of Computers in Radiation Therapy*, pages 78–82, Toronto, Canada.

[Rubinstein, 1981] Rubinstein, R. Y. (1981). *Simulation and the Monte Carlo Method.* John Wiley & Sons, London.

[Sakamoto, 1993] Sakamoto, Y. (1993). Photon Cross Section Data PHOTX for PEGS4 Code. In *Proceedings of the Third EGS4 User's Meeting in Japan*, pages 77–82. (KEK Japan).

[Sauer, 1994] Sauer, O. A. (1994). *Dosisverteilungen an Material-Grenzflächen bei energiereichen Röntgenstrahlen.* PhD thesis, Julius-Maximilians- Universität Würzburg.

[Sauer, 1995] Sauer, O. A. (1995). Calculation of dose distributions in the vicinity of high-Z interfaces for photon beams. *Medical Physics*, 22(10):1685–1690.

[Sauer and Neumann, 1990] Sauer, O. A. and Neumann, M. (1990). Reconstruction of high-energy bremsstrahlung spectra by numerical analysis of depth-dose data. *Radiotherapy and Oncology*, 18:39–47.

[Schoknecht, 1966] Schoknecht, G. (1966). Die Bescreibung von Strahlenfeldern durch Separierung von Primäaer und Streustrahlung. i: Relativer Tiefendosisverlauf im Zentralstrahl bei ^{60}co-Feldern. *Strahletherapie*, 131:311.

[Schoknecht, 1971a] Schoknecht, G. (1971a). Die Beschreibung von Strahlenfeldern durch Separierung von Primä und Streustrahlung. *Strahlentherapie*, 141(3):326–331.

[Schoknecht, 1971b] Schoknecht, G. (1971b). Streuverteilungen von Photonen-Nadelstrahlen im Energiebereich von 50 keV bis 1.25 MeV. *Strahlentherapie*, 141(5):561–567.

[Schultze, 1995] Schultze, C. (1995). *Entwicklung schneller Algorithmen zur Dosisberechnung für die Bestrahlung inhomogener Medien mit hochenergetischen Photonen.* PhD thesis, Abteilung Medizinische Physik Deutsches Krebsforschungszentrum, Heidelberg.

[Seltzer, 1988] Seltzer, S. M. (1988). An Overview of ETRAN Monte Carlo Methods. In Jenkins, T. M., Nelson, W. R., and Rindi, A., editors, *Monte Carlo Transport of Electrons and Photons*, chapter 7. Plenum Press. Ettore Majorana International Science Series.

[Seltzer et al., 1978] Seltzer, S. M., Hubbell, J. H., and Berger, M. J. (1978). Some Theoretical Aspects of Electron and Photon Dosimetry. In *National and International Standarization of Radiation Dosimetry.* International Atomic Energy Agency, Vienna. Report: IAEA-SM-222/05.

[Sharpe and Battista, 1993] Sharpe, M. and Battista, J. J. (1993). Dose calculations using convolution and superposition principles: The orientation of dose spread kernels in divergent x-ray beams. *Medical Physics*, 20(6):1685–1694.

[Sharpe et al., 1995] Sharpe, M., Jaffray, D. A., Battista, J. J., and Munro, P. (1995). Extrafocal radiation: A unified approach to the prediction of beam penumbra and output factors for megavoltage x-ray beams. *Medical Physics*, 22(12):2065–2074.

[Siddon, 1984] Siddon, R. L. (1984). Generalised Batho correction factor. *Physics in Medicine and Biology*, 29(12):1575–1579. Technical Note.

[Siddon, 1985] Siddon, R. L. (1985). Fast calculation of the exact radiological path for a three-dimensional CT array. *Medical Physics*, 12(2):252–255.

[Sontag, 1979] Sontag, M. R. (1979). *Photon Beam Dose Calculations in Regions of Tissue Heterogeneity using Computed Tomography.* PhD thesis, University of Toronto.

[Sontag et al., 1977] Sontag, M. R., Battista, J. J., Bronskill, M. J., and Cunningham, J. R. (1977). Implications of Computed Tomography for Inhomogeneity Corrections in Photon Beam Dose Calculations. *Radiology*, 124:143–149.

[Sontag and Cunningham, 1977] Sontag, M. R. and Cunningham, J. R. (1977). Corrections to absorbed dose calculations for tissue inhomogeneities. *Medical Physics*, 4(5).

[Sontag and Cunningham, 1978a] Sontag, M. R. and Cunningham, J. R. (1978a). Clinical application of CT based treatment planning system. *Computed Tomography*, 2:117–130.

[Sontag and Cunningham, 1978b] Sontag, M. R. and Cunningham, J. R. (1978b). The Equivalent Tissue-Air Ratio Method for Making Absorbed Dose Calculations in a Heterogeneous Medium. *Radiology*, 129:787–794.

[Sterling et al., 1964] Sterling, T. D., Perry, H., and Katz, L. (1964). Automation of Radiation Treatment Planning. *British Journal of Radiology*, 37:544.

[Storchi and Woudstra, 1996] Storchi, P. and Woudstra, E. (1996). Calculation of the absorbed dose distribution due to irregularly shaped photon beams using pencil beam kernels from basic beam data. *Physics in Medicine and Biology*, 41:637–656.

[Thatcher and Palti, 1983] Thatcher, M. and Palti, S. (1983). A Simple Equivalent Tissue-Air Ratio Method for Calculating Absorbed Dose in a Heterogeneous Medium. *Radiology*, 146:527–529.

[Thomas, 1991] Thomas, S. J. (1991). A modified power-law formula for inhomogeneity corrections in beams of high-energy x-rays. *Medical Physics*, 18(4):719–723.

[Thwaites, 1988] Thwaites, D. I. (1988). Review and analysis of accuracy required and achievable in radiotherapy. *Physics in Medicine and Biology*, page 639. Abstract from Proceedings of IPSM meeting on Accuracy in Radiotherapy.

[Thwaites, 1994] Thwaites, D. I. (1994). Accuracy Requirements in Radiotherapy. In *Notes from: International course on advances in radiotherapy*, London. Royal Marsden Hospital. March 16th-18th.

[Thwaites, 1995] Thwaites, D. I. (1995). Private communication.

[Thwaites et al., 1992] Thwaites, D. I., Williams, J. R., Aird, E. G., and Klevenhagen, S. C. (1992). A dosimetric intercomparison of megavoltage photon beams in UK radiotherapy centres. *Physics in Medicine and Biology*, 37(2):445–461.

[Turner et al., 1985] Turner, J. E., Wright, H. A., and Hamm, R. N. (1985). Review article: Monte Carlo primer for health physicists. *Health Physics*, 48(6):717–733.

[Udale-Smith, 1988] Udale-Smith, M. (1988). A Monte Carlo investigation of surface doses for broad electron beams. *Physics in Medicine and Biology*, 33(8):939–954.

[Udale-Smith, 1990] Udale-Smith, M. (1990). *A Monte Carlo investigation of high energy electron beams used in radiotherapy.* PhD thesis, University of Leeds, UK.

[Udale-Smith, 1992] Udale-Smith, M. (1992). A Monte Carlo calculation of electron beam parameters for three Philips linear accelerators. *Physics in Medicine and Biology*, 37(1):85–105.

[Urie et al., 1991] Urie, M. M., Goitein, M., Doppke, K., Kutcher, J. G., LoSasso, T., Mohan, R., Munzenrider, J. E., and Wong, M. S. J. W. (1991). The Role of Uncertainty Analysis in Treatment Planning. *Int. J. Radiation Oncology Biol. Phys.*, 21(1):91–107.

[van de Geijn, 1965] van de Geijn, J. (1965). The computation of two and three dimensional distributions in Cobalt-60 teletherapy. *British Journal of Radiology*, 38:369–377.

[van de Geijn, 1972] van de Geijn, J. (1972). Computational methods in beam therapy planning. *Computer Programs in Biomedicine*, 2:153–168.

[van de Geijn, 1987] van de Geijn, J. (1987). The extended net fractional depth dose: Correction for inhomogeneities including effects of electron transport in photon beam dose calculation. *Medical Physics*, 14(1):84–92.

[van de Geijn and Fraass, 1984] van de Geijn, J. and Fraass, B. A. (1984). The net fractional depth dose: A basis for a unified analytical description of FDD, TAR, TMR and TPR. *Medical Physics*, 11(6):784–793.

[van de Geijn and PoCheng, 1980] van de Geijn, J. and PoCheng, C. (1980). Generalization of the Power Law Method To Include Inhomogeneities of Smaller Than Beam Cross Section. *Medical Physics*, 7(4):428. (Abstract).

[Van Dyk, 1983] Van Dyk, J. (1983). Lung dose calculations using computerized tomography: Is there a need for pixel based procedures? *Int. J. Radiation Oncology Biol. Phys.*, 9:1035–1041.

[Walker et al., 1992] Walker, S., Bielajew, A. F., Hale, M., and Jette, D. (1992). Installation of the EGS4 Monte Carlo code on an 80386-based microcomputer. *Medical Physics*, 19(2):305–306.

[Webb, 1993] Webb, S. (1993). *The Physics of Three-Dimensional Radiation Therapy: Conformal Radiotherapy, Radiosurgery and Treatment Planning.* Institute of Physics Publishing, Bristol and Philadelphia.

[Webb and Cassell, 1985] Webb, S. and Cassell, K. J. (1985). Comment on 'Generalised Batho correction factor'. *Physics in Medicine and Biology*, 30(8):859–860. Letters to the Editor.

[Webb and Fox, 1979] Webb, S. and Fox, R. A. (1979). The dose in water surrounding point isotropic gamma-ray emitters. *British Journal of Radiology*, 52:482–484.

[Webb and Fox, 1980] Webb, S. A. and Fox, R. A. (1980). Verification by Monte Carlo methods of power law TAR algorithm for inhomogeneity corrections in photon beam dose calculations. *Physics in Medicine and Biology*, 25(2):225–240.

[Williams and Thwaites, 1993] Williams, J. R. and Thwaites, D. I., editors (1993). *Radiotherapy Physics in Practice.* Oxford University Press.

[Williamson, 1988] Williamson, J. F. (1988). Monte Carlo Simulation of the Photon Transport Phenomena: Sampling Techniques. In Morin, R. L., editor, *Monte Carlo Simulation in the Radiological Sciences.* CRC Press.

[Williamson, 1989] Williamson, J. F. (1989). Radiation transport calculations in treatment planning. *Computerised Medical Imaging and Graphics*, 13:251–268.

[Williamson et al., 1983a] Williamson, J. F., Morin, R. L., and Kahn, F. M. (1983a). Dose calibration response to brachytherapy sources: a Monte Carlo and analytic evaluation. *Medical Physics*, 10(2):135–140.

[Williamson et al., 1983b] Williamson, J. F., Morin, R. L., and Kahn, F. M. (1983b). Monte Carlo evaluation of the Sievert integral for brachytherapy dosimetry. *Physics in Medicine and Biology*, 28(9):1021–1032.

[Wong, 1982] Wong, J. W. (1982). *A New Approach to Photon Dose Calculations in Radiotherapy Treatment Planning.* PhD thesis, Department of Medical Biophysics, University of Toronto.

[Wong and Henkelman, 1982] Wong, J. W. and Henkelman, R. M. (1982). Reconsideration of the power-law (BATHO) equation for inhomogeneity corrections. *Medical Physics*, 9(4):521–530.

[Wong and Henkelman, 1983] Wong, J. W. and Henkelman, R. M. (1983). A new approach to CT pixel-based photon dose calculation in heterogeneous media. *Medical Physics*, 10:199–208.

[Wong et al., 1981a] Wong, J. W., Henkelman, R. M., Andrew, J. W., Dyk, J. V., and Johns, H. E. (1981a). Effect of small inhomogeneities on dose in a cobalt-60 beam. *Medical Physics*, 8(6):783–791.

[Wong et al., 1981b] Wong, J. W., Henkelman, R. M., Fenster, A., and Johns, H. E. (1981b). Second scatter contribution to dose in a cobalt-60 beam. *Medical Physics*, 8(6):775–782.

[Wong and Purdy, 1987] Wong, J. W. and Purdy, J. (1987). Basis of Recent Methods of Photon Dose Calculations. In Bruinvis, I. A. D., van der Giessen, P. H., van Kleffens, H. J., and Wittkämper, F. W., editors, *The Ninth International Conference of the Use of Computers in Radiation Therapy*, pages 319–322, Scheveningen, The Netherlands.

[Wong and Purdy, 1990] Wong, J. W. and Purdy, J. (1990). On methods of inhomogeneity correction for photon transport. *Medical Physics*, 17:807–814.

[Wong and Purdy, 1992] Wong, J. W. and Purdy, J. A. (1992). *Review of methods of inhomogeneity corrections*, pages 887–899. Medical Physics Monograph No 19. Americal Institute of Physics, Inc.

[Wong et al., 1984] Wong, J. W., Slessinger, E. D., Rosenberger, F. U., Krippner, K., and Purdy, J. A. (1984). The Delta Volume for 3-dimensional photon dose calculations. In *The Eighth International Conference of the Use of Computers in Radiation Therapy*, pages 26–30, Toronto, Canada.

[Wong *et. al.*, 1991] Wong *et. al.* (1991). Role of inhomogeneity corrections in three-dimensional photon treatment planning. *Int. J. Radiation Oncology Biol. Phys.*, 21(1):59–69. Photon Treatment Planning Collaborative Working Group.

[Woo, 1994] Woo, M. K. (1994). Analysis of photon beam exit dose using photon point kernels. *Physics in Medicine and Biology*, 39(4):687–702.

[Woo and Cunningham, 1990] Woo, M. K. and Cunningham, J. R. (1990). The validity of the density scaling method in primary electron transport for photon and electron beams. *Medical Physics*, 17(2):187–194.

[Woo et al., 1990] Woo, M. K., Cunningham, J. R., and Jezioranski, J. J. (1990). Extending the concept of primary and scatter separation to the condition of electronic equilibrium. *Medical Physics*, 17(4):588–595.

[Young and Gaylord, 1970] Young, M. E. J. and Gaylord, J. D. (1970). Experimental tests of corrections for tissues inhomogeneities in radiotherapy. *British Journal of Radiology*, 43:349–355.

[Yu et al., 1995] Yu, C. X., Mackie, T. R., and Wong, J. W. (1995). Photon dose calculation incorporating explicit electron transport. *Medical Physics*, 22(7):1157–1165.

[Yu and Wong, 1993a] Yu, C. X. and Wong, J. W. (1993a). Implementation of the ETAR method for 3D inhomogeneity correction using FFT. *Medical Physics*, 20(3):627–632.

[Yu and Wong, 1993b] Yu, C. X. and Wong, J. W. (1993b). A Modification to Equivalent Tissue-air-ratio Method. *Medical Physics*, 20(3):923. (Abstract).

[Zefkili et al., 1994] Zefkili, S., Kappas, C., and Rosenwald, J. (1994). On-axis and off-axis primary dose component in high energy photon beams. *Medical Physics*, 21(6):799–808.

[Zhu et al., 1995] Zhu, X. R., Low, D. A., Harms, W. B., and Purdy, J. A. (1995). A convolution-adapted ratio-TAR algorithm for 3D photon beam treatment planning. *Medical Physics*, 22(8):1315–1327.

[Zhu and Boyer, 1990] Zhu, Y. and Boyer, A. L. (1990). X-ray dose computations in heterogeneous media using 3-dimensional FFT convolution. *Physics in Medicine and Biology*, 35(3):351–368.

[Zhu et al., 1992] Zhu, Y., Boyer, A. L., and Desorby, G. E. (1992). Dose distributions of x-ray fields as shaped with multileaf collimators. *Physics in Medicine and Biology*, 37(1):163–173.

Acknowledgements

I am indebted and deeply grateful to Dr Otto A. Sauer. He has generously provided constructive criticism, guidance and encouragement through a series of long emails, many letters and faxes. I am also grateful for his friendly hospitality during my two week visit to the Universitäts-Frauenklinik in Würzburg, for providing me with the numerical reconstruction software and generally for many stimulating discussions on the convolution/superposition model.

I am also very grateful to Dr Alex F. Bielajew for his advice, help, kindness and patience with an inexperienced but keen EGS4 user.

My thanks are due to Dr A. T. Redpath for providing dose data calculated with the power-law method, CT density data and for providing the necessary computer facilities to carry out this work. Many thanks to Dr Nick C. Nicholson for his system administrator support and help. I also thank them both for proof reading the first draft of the thesis.

I am grateful to Prof. Rock T. Mackie for providing the spherical energy deposition kernels, to Prof. Art L. Boyer for providing the software for manipulating the kernels and Dr Anders Ahnesjö for some good physics advice and generally for teaching me what I know about convolution through his published work.

I am thankful to all staff in the Department of Medical Physics and Medical Engineering and the Directorate of Clinical Oncology for their friendliness during my time here. In particular to Prof. W. N. McDicken for his kindness, Drs Qi Wang and Andrew Nisbet for their kindness and understanding, Dr Carmel M. Moran for her moral support, Dot Marshall and Aileen MacLeod for their kindness and warmth, and Carolyn McKerracher for her encouragement, friendly smile and company during many late nights or weekends in the department. My fellow students deserve a special mention for their support and good advice. Special thanks to Dr Shaofeng Li, Bijan Hashemi-Malayeri and Dr Ali Al-Mejrad.

I thank all those friends with whom I kept in touch these last years. Specially Dr Despina Hatzifotiadou and Tommy Anderberg who have always been on-line, specially during some very difficult times. I have greatly appreciated the friendship of my flatmates John Docherty and Lyn Hand for making 37 Warrender Park Road a home and for being so patient with a very fretful researcher.

Most of all, I am grateful to my family for their continuous love, trust and support through the years and to Kenneth for keeping me sane during this seemingly never ending task.

Financial support from the Commission of the European Communities through the programme of Medical and Health Research, from the Faculty of Medicine and from the Department of Medical Physics and Medical Engineering is also gratefully acknowledged.

Finally, I express my sincere thanks to Drs J. Mills and D. I. Thwaites, the PhD examiners, for their helpful comments and suggestions on the layout and presentation of this thesis.

I declare that this thesis has been composed by myself and that the work contained in it is my own.

Maria Mania Aspradakis

June, 1996